# Magneto-electronic phase separation in doped cobaltites

A DISSERTATION
SUBMITTED TO THE FACULTY OF THE GRADUATE SCHOOL
OF THE UNIVERSITY OF MINNESOTA
BY

**Chunyong He**

IN PARTIAL FULFILLMENT OF THE REQUIREMENTS
FOR THE DEGREE OF
DOCTOR OF PHILOSOPHY

**Chris Leighton**

September, 2009

# Table of Contents

# List of Figures

## Chapter 3

## Chapter 4



## Chapter 5

## Chapter 6

# Chapter 1

# Introduction to magneto-electronic phase separation in magnetic perovskite oxides

## 1.1 Applications of oxides and opportunities for fundamental physics

Oxides refer to a class of oxygen containing materials which are important both from a practical point of view and from a fundamental point of view. From a practical point of view, oxides display a wide spectrum of fascinating properties, which enable them to be utilized in applications. From a fundamental perspective, they serve as excellent candidates for the study of the physics beneath their interesting phenomena.

From a practical perspective, oxides can be utilized in various areas. For example, $SiO_2$ has been playing a dominant role acting as the gate dielectric in the past in MOSFETs (Metal Oxide Semiconductor Field Effect Transistors), which are essential elements of personal computers. Recently, intensive efforts are spurred to find an alternative to $SiO_2$ with high dielectric constant to reduce the expanded power consumptions related to shrinkage of the transistor's dimensions [1]. Perovskite oxides such as lead zirconate titanate PZT **(**$PbZr_{1-x}Ti_xO_3$) and $KNO_3$ can be used for FRAM (ferroelectric Random Access Memory) as reported by Scott *et al.* [2]. Oxides can also be used for the fabrication of solid oxide fuel cells (SOFC) as proposed by Holtappels *et al.* [3]. $La_{1-x}Sr_xMnO_3$, $La_{1-x}Sr_xFeO_3$, and $La_{1-x}Sr_xCo_{1-y}Fe_yO_3$ are reported suitable for the fabrication of the cathode component of SOFC, while $Y_{0.15}Zr_{0.85}O_{1.93}$ and Ni-$Y_{0.15}Zr_{0.85}O_{1.93}$ are suitable materials for the preparation of anode and electrolyte components of SOFC, respectively [3]. Oxides can also be used in a novel type of electronics called spintronics which utilizes the spin in addition to the charge of electrons. For example, heterostructures such as $La_{0.67}Sr_{0.33}MnO_3/SrTiO_3/La_{0.67}Sr_{0.33}MnO_3$, $La_{0.7}Sr_{0.3}MnO_3/SrTiO_3/La_{0.7}Sr_{0.3}MnO_3$ and $La_{0.7}Ca_{0.3}MnO_3/NdGdO_3/La_{0.7}Sr_{0.3}MnO_3$[4-6] have been reported to be used in MTJs with tunneling magneto-resistance (TMR) as high as 1800% [6]. Oxides, such as $TiO_2$, ZnO, and $(La,Sr)TiO_3$ are also found useful in the field of diluted magnetic semiconductors (DMS)[7]. Oxide thin-film heterostructures are

found to be very promising for the creation of novel devices based on the rapid progress of oxide deposition techniques [8].

Besides the wide range of functionality they possess, oxides are also important from a basic science perspective, since they provide an excellent opportunity to study the fundamental physics behind their fascinating phenomena. Among the class of oxides, there is a narrower category called complex oxides, which receives special attention from physicists and material scientists in the past several decades [9-10] due to the fascinating phenomena they illustrate, such as high temperature superconductivity in cuprates [11], colossal magneto-resistance in manganites [12-14], ferroelectricity in titanates [15] and multiferroecity in ferrites [16]. Complex oxides belong to a larger set of compounds referred to as strongly correlated electron systems. In these systems, the charge density is much lower than that of normal metals. Therefore, the interaction between electrons, which is negligible in normal metals due to the large charge density, becomes so important in these systems that the many-body system simply can not be described by the conventional perturbation theory any more [9].

A special set of complex oxides called magnetic perovskite oxides are of interest to us since they are closely related to the properties mentioned above and demonstrate the phenomenon called magneto-electronic phase separation, the theme of this thesis. Driven by the discovery of CMR (colossal magneto-resistance) [9,17], magneto-electronic phase separation has been intensively studied in the past decade and will be discussed in the next section using perovskite manganites as an example.

## 1.2 CMR effect in perovskite manganites

Before introducing the CMR effect, it is worthwhile to introduce the perovskite structure $ABO_3$, as shown in Fig. 1.1, where A represents a lanthanide element (e.g. La, Pr, Nd,…) located at the corner of the cubic structure, B represents a transition metal (e.g. Fe, Mn, Co, Ni,…) positioned at the center of the cubic structure, and O represents the oxygen atom positioned at face center of the cubic structure. It can be seen that the transition metal is surrounded by six oxygen atoms to form an octahedral structure which will induce interesting effects, such as crystal-field spitting, as will be discussed in the later sections.

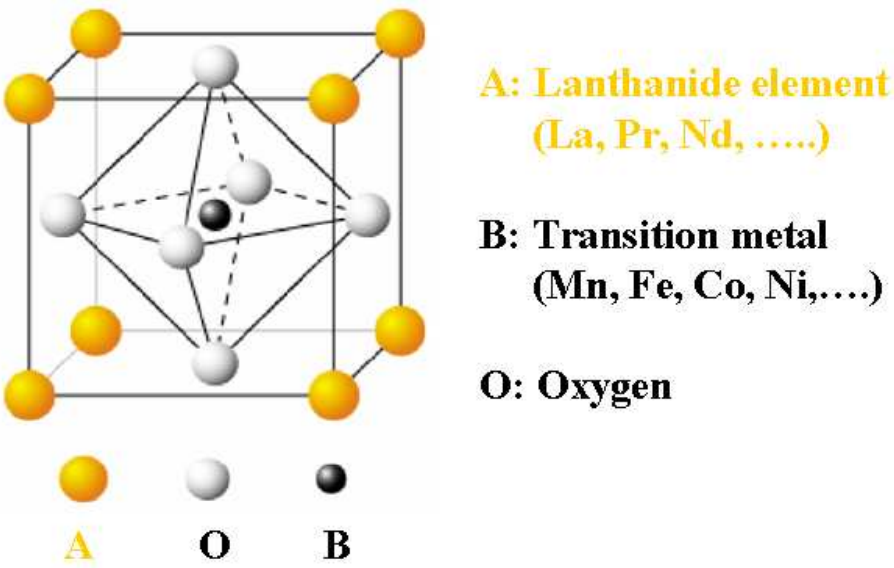


**Fig. 1.1** Schematic picture of perovskite structure $ABO_3$ in a cubic unit cell lattice.

An important structural issue worth addressing in perovskite $ABO_3$ is the tolerance factor. The tolerance factor is introduced to describe the size mismatch between A site cation and B site cation and is therefore used as a measure of the distortion from a cubic structure due to such a mismatch, defined as below [9]:

$$\Gamma = \frac{r_A + r_O}{\sqrt{2}(r_B + r_O)} \qquad (1.1),$$

where $r_A$, $r_B$, and $r_O$ represent the ionic radius of the A site cation, B site cation, and oxygen anion, respectively. For a perfect cubic structure in manganites, $\Gamma = 1$, the perovskite has straight Mn-O-Mn bonds (bond angle $\alpha = 180^0$). When manganites are fabricated with smaller A site cations, it will induce some distortion by rotating the octahedra. Such a distortion from cubic structure results in a lower symmetry structure. The rotation around <111> gives rise to a rhombohedral structure (e.g. $R\bar{3}c$), which is the case for $La_{1-x}Sr_xCoO_3$ and will be discussed in later sections. The rotation around <110> results in an orthorhombic structure (e.g. Pbnm). Therefore, the tolerance factor will be smaller than one and the Mn-O-Mn bond angle deviates away from $180^0$. The impact of the tolerance factor on the properties of materials will be discussed in later sections after the discussion of double exchange.

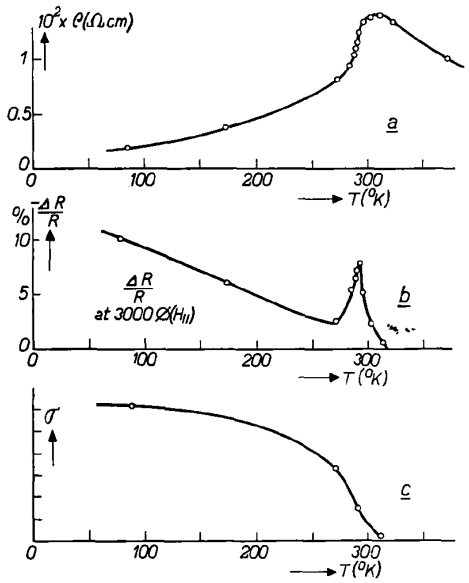


**Fig. 1.2** (a) Resistivity, (b) magnetoresistance in 0.3 T, and (c) magnetization of ceramic form $La_{0.8}Sr_{0.2}MnO_3$. Reproduced from Ref. 18.

Materials of perovskite structure, particularly manganese-based materials, exhibit CMR, which refers to the phenomenon where the application of a magnetic field can dramatically change the electrical resistance of materials, as shown below:

$$MR = \frac{\rho(H) - \rho(0)}{\rho(0)} \tag{1.2},$$

where ρ(0) and ρ(H) refer to the resistivity of materials at magnetic fields of zero and *H*, respectively. The magnitude of MR usually peaks around the Curie temperature of ferromagnetic materials. CMR was first discovered in $La_{0.8}Sr_{0.2}MnO_3$ ceramics by J. Volger in 1954 [18], as shown in Fig. 1.2. However, due to the modest magnitude of magnetoresistance in low fields (only weak electromagnets were used at that time) and limited apparent applications, such a phenomenon did not attract much attention for a long time. It was not until 1993 when the CMR effect was discovered in epitaxial thin film $La_{2/3}Ba_{1/3}CoO_3$ by R. von Helmolt *et al.* [17], as shown in Fig. 1.3, that it received tremendous attention from physicists. In this case, the MR in high fields in high quality samples was very big. Driven by the CMR found in manganites, these materials became a focus of condensed matter physics and materials science in the past two decades.

Although the mechanism of CMR is still unclear, the scientific community believes that the coexistence of different phases in the ground state, and the competition between different phases, must play a key role with regard to the appearance of CMR [9], as discussed in the next section.

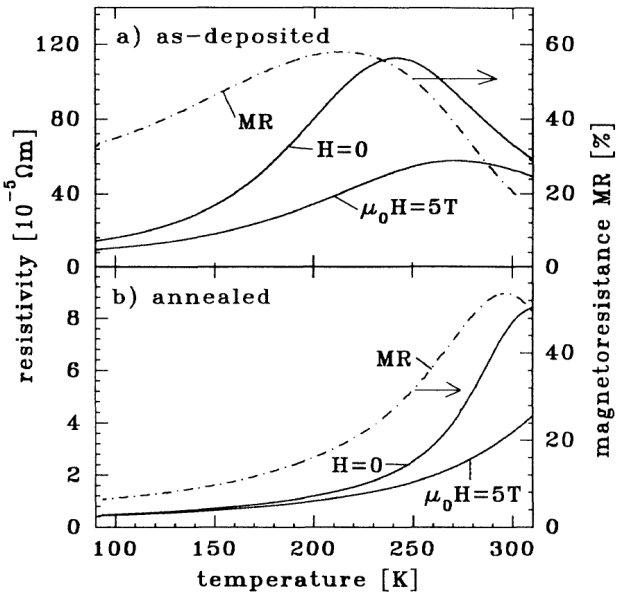


**Fig. 1.3** *T* dependence of the resistivity at magnetic fields of 0 T and 5 T and MR ((ρ(0) - ρ(H))/ ρ(0) ) for an epitaxial film $La_{2/3}Ba_{1/3}MnO_3$ (a) as-deposited at 600 $^oC$ (b) after annealing at 900 $^oC$ for 12 h. Reproduced from Ref. 17.

## 1.3 Magneto-electronic phase separation (MEPS)

Magneto-electronic phase separation (MEPS) refers to the phenomenon where chemically homogeneous materials display inhomogeneous magnetic and electronic properties, i.e. the spatial coexistence of multiple magnetic and electronic phases. In recent years, this phenomenon has been observed in a large number of materials (e.g. manganites and cuprates, cobaltites) [9,10,13] and is believed to play a key role in some of their most attractive properties (e.g. colossal magnetoresistance [12-14] and high temperature superconductivity [11]). Such a phenomenon can be detected by different techniques including direct techniques, such as neutron diffraction (ND), nuclear

magnetic resonance (NMR), small-angle neutron scattering (SANS), inelastic neutron spectroscopy, (INS), scanning tunneling microscopy (STM), etc. as well as bulk probes such as magnetometry and magnetotransport. To demonstrate such a tendency, several examples will be given in the next section.

### 1.3.1 Phenomenology of MEPS

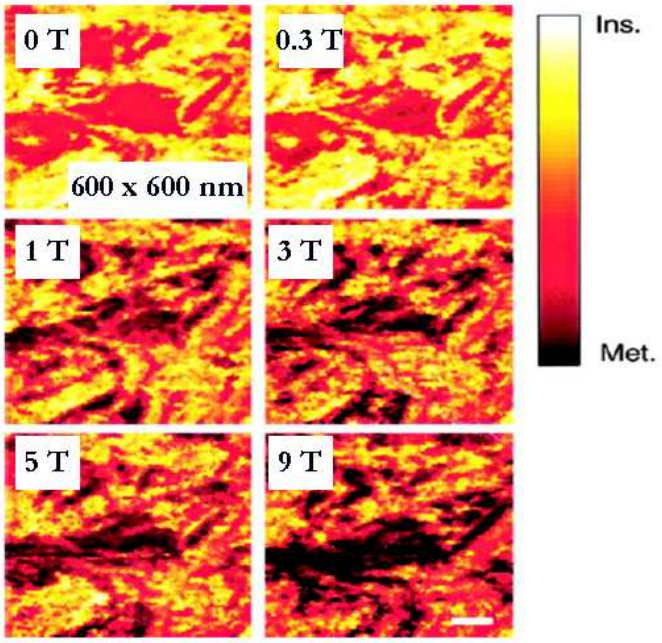


**Fig. 1.4** STM generic spectroscopic images (0.61μm by 0.61 μm; scale bar, 100 nm) of the local electronic structure of $La_{0.7}Ca_{0.3}MnO_3$ thin film taken just below $T_c$ in magnetic fields of 0, 0.3, 1, 3, 5, 9T. Parts of the surface are insulating (light colors), whereas others are metallic (dark colors) or in an intermediate state. The color represents the slope of the local *I-V* spectrum at a bias of 3 V. Reproduced from Ref. 19.

Fig. 1.4 shows an example of MEPS in a $La_{0.7}Ca_{0.3}MnO_3$ thin-film sample using the STM technique performed at a temperature just below the Curie temperature [19]. It can be seen that insulating regions and metallic regions coexist at low magnetic field. With increasing magnetic field, some of the insulating regions are converted into metallic regions, and, when the magnetic field reaches 9 T, the initially isolated metallic regions percolate to form a connected metallic path. Such a percolation behavior driven by

magnetic field is believed to be a major factor in producing CMR around the Curie temperature, which drives the interest in the study of MEPS since the MEPS problem must be solved prior to understanding CMR.

Using the same technique, another example is shown in Fig. 1.5 in high temperature superconductors $Bi_2Sr_2CaCu_2O_{8+\delta}$ [20]. According to the shown differential conductance (d*I*/d*V*) map, for both the normal state (93 K) and superconducting state (50 K), phase inhomogeneity exists in the material. Starting with the normal state, it can be seen that there is a spatial coexistence of metallic regions (red) and insulating regions (blue). For the superconducting state, it can be seen that different areas of the sample possess different superconducting gaps. Therefore, the phenomenon of MEPS is general to oxides.

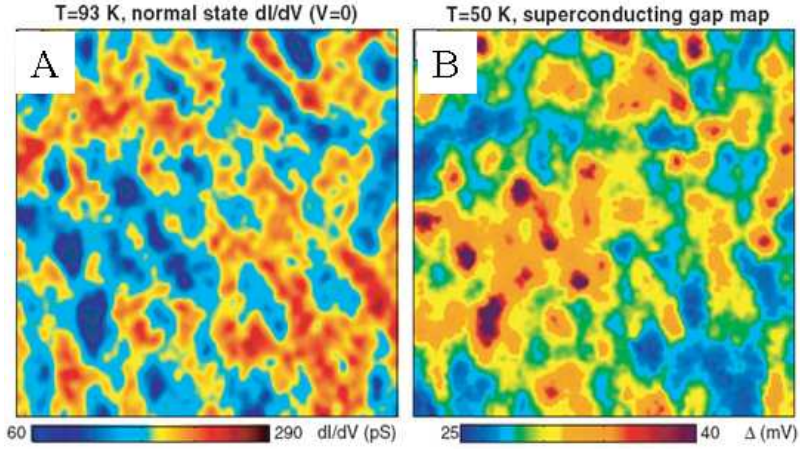


**Fig. 1.5** (A) Differential conductance map (30 x 30 nm) at the Fermi energy obtained at 93 K. (B) Low-temperature (50 K) superconducting gap map obtained on the same area as in (A) in $Bi_2Sr_2CaCu_2O_{8+\delta}$. Reproduced from Ref. 20.

Despite the direct evidence of MEPS shown by direct imaging techniques, it is important to point out there are drawbacks associated with them. For example, direct imaging techniques have statistical issues, meaning different areas of surface might present different phenomena. Also, they are surface sensitive, indicating the phenomena might not represent the bulk properties. Due to the difficulty of cleaving perovskites, the images shown on the surface of these materials could be dubious. Fortunately, MEPS can also be explored by other bulk techniques such as neutron diffraction (ND) and small angle neutron scattering (SANS), which probe the intrinsic properties of bulk materials.

Fig. 1.6(A) shows an example of MEPS in $Pr_{0.65}(Ca_ySr_{1-y})_{0.35}MnO_3$. It plots the ferromagnetic (FM) phase fraction, which is determined from ND analysis by examining the heights of the Bragg peaks of FM phase, vs. temperature for different Sr doping. It can be clearly seen that for all Sr dopings shown, there is a coexistence of a FM phase and the other phase (charge ordered phase with its own separate Bragg peak). With changing temperature, there is a conversion between these two phases. Changing Sr doping also changes the ratio of these two phases in this material.

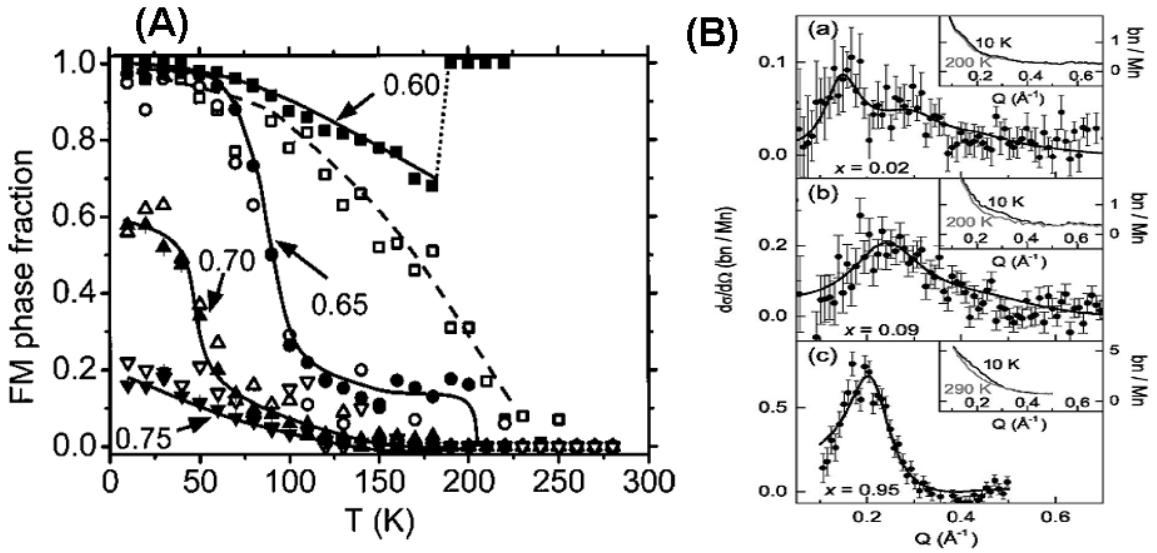


**Fig. 1.6** (A) Temperature dependence of the ferromagnetic phase fraction for $0.6 < y < 0.75$ in $Pr_{0.65}(Ca_ySr_{1-y})_{0.35}MnO_3$. Reproduced from Ref. 21. (B) $Q$ dependence the elastic magnetic cross section of $Ca_{1-x}La_xMnO_3$ for (a) $x = 0.02$, (b) $x = 0.09$, and (c) $x = 0.95$. The solid lines are fitted to a liquid-like distribution model of magnetic droplets. As discussed in the text. Reproduced from Ref. 22.

Fig. 1.6(B) shows one more example of MEPS in $Ca_{1-x}La_xMnO_3$ using SANS. The elastic magnetic cross sections at low temperature for $x = 0.02$, 0.09, and 0.95 are attained by subtracting the high temperature background (shown in the insets). The data clearly show peaks at finite $q$ value corresponding to a distinct size of magnetic clusters. The average size of these clusters was determined to be 1 nm. Such an analysis indicates the existence of FM clusters in the G-type antiferromagnetic (AFM) matrix, which is the

characteristic of the undoped compound $CaMnO_3$. Therefore, for doped materials, they have a signature of FM clusters + G-AFM matrix, i.e. phase separation.

In summary, MEPS occurs quite frequently in complex oxides and is closely related to their interesting properties which, in turn, attract a lot of attention and have become an active research field in the past decade. MEPS can be investigated by numerous techniques including neutron scattering [23-25], nuclear magnetic resonance (NMR) [26-29], inelastic neutron scattering INS [30,31], heat capacity[32-38], and magnetic force microscopy [39,40] etc. A huge amount of work has focused on this theme since its discovery, including some reviews, such as the work focusing on nanoscale phase separation in manganites by E. Dagotto *et al.* [9-10].

### 1.3.2 Ingredients of MEPS

As for the mechanism of MEPS, phase competition is believed to be the major ingredient of MEPS. The following discussion will use perovskite manganites to demonstrate this phase competition tendency. Starting from undoped manganites $TMnO_3$ (T representing a trivalent element) in the perovskite structure, an isolated Mn ion ($Mn^{3+}$) is surrounded by six neighboring oxygen ions, as mentioned earlier in section 1.2 and shown in Fig. 1.1. The octahedral crystal field produced by the octahedral oxygen ions will lift the five-fold degeneracy of the 3d orbital of the Mn ion (located at the center of the octahedral cage) and split them into two sets of energy levels: One lower triplet called the $t_{2g}$ orbital ($d_{xy}$, $d_{yz}$, $d_{zx}$) and the other doublet called the $e_g$ orbital ($d_{x2-y2}$, $d_{3z2-r2}$), as shown in Fig. 1.7 [41]. It can be understood intuitively from the shape of the orbital that the $e_g$ orbital has higher energy than the $t_{2g}$ orbital because the probability density ($|\chi^2|$) points directly towards the oxygen ions, which gives them stronger Coulomb interaction (repulsion between $O^{2-}$ ion and 3d electron from the Mn ion) than the $t_{2g}$ orbital, where the probability density lies between the oxygen ions, resulting in a weaker Coulomb interaction. The energy gap between the $t_{2g}$ orbital and the $e_g$ orbital is usually referred to as the crystal field splitting, represented by $\Delta_{CF}$, as shown in Fig. 1.7. In a perovskite structure, the value of $\Delta_{CF}$ induced by the octahedral crystal field can be determined by [9,42]:

$$\Delta_{CF} = \frac{5}{3}\frac{Zq < r^4 >}{a^5} \quad (1.3),$$

where $Z$ is the atomic number of the ligand ion, $q$ is the charge of an electron, $a$ is the distance between a transition metal ion (in this case, $Mn^{3+}$) and the oxygen ions, $r$ is the radial coordinate of the 3d orbital, and $<r^4>$ is the mean value of $r^4$ for the 3d orbital. In manganites, it has been estimated by K. Yoshida [43] that the crystal field splitting $\Delta_{CF}$ is approximately 1 eV.

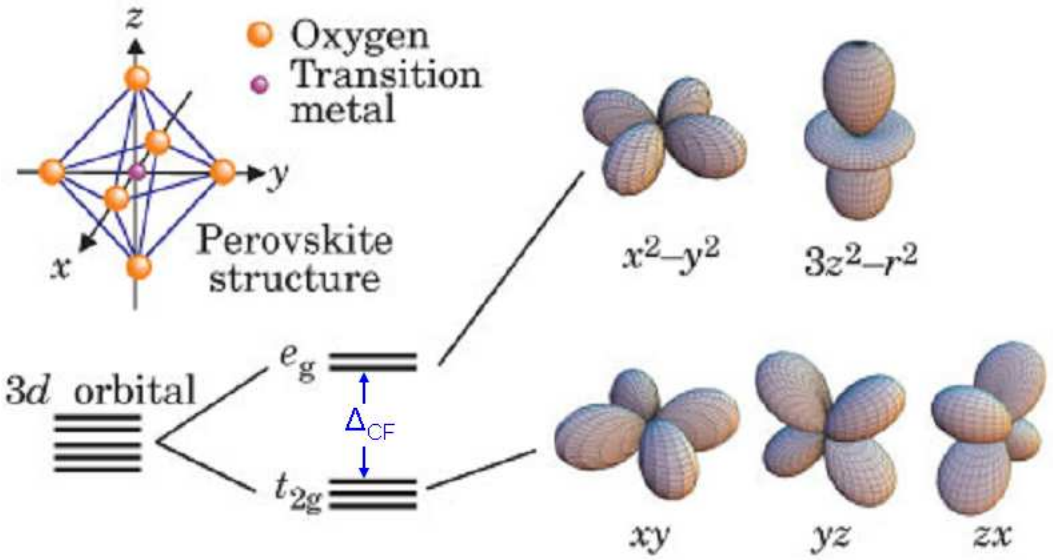


**Fig. 1.7** Schematic diagram of crystal field splitting for a transition metal ion in a perovskite structure. The octahedral crystal field (transition metal surrounded by six neighboring oxygen ions, shown at the top left corner) lifts the degeneracy of 3d orbital for the transition metal ion and splits it into a triplet $t_{2g}$ orbital ($d_{xy}$, $d_{yz}$, $d_{zx}$) and a doublet $e_g$ orbital ($d_{x2-y2}$, $d_{3z2-r2}$). The energy gap between these sets of orbital is usually referred to as crystal field splitting $\Delta_{CF}$. Reproduced from Ref. 41.

Since $Mn^{3+}$ has four 3d electrons in $TMnO_3$, in order to figure out the occupancy for the split 3d orbital, another important energy scale that most be known is the intra-atomic Hund's exchange energy between the 3d electrons. The existence of crystal field splitting has the tendency to let 3d electrons occupy the $t_{2g}$ orbital first (in total 6 states, considering opposite orientations of spins) before occupying the $e_g$ orbital, resulting in a $t_{2g}^4 e_g^0$ configuration. On the other hand, Hund's rule has the opposite tendency, trying to

perfectly align the spins of all 3d electrons, resulting in a $t_{2g}^3e_g^1$ configuration with all spins aligned. The real configuration depends on the comparison of the magnitudes of crystal field splitting $\Delta_{CF}$ and Hund's rule exchange energy $J_H$. In manganites, usually Hund's rule exchange energy easily dominates over crystal field splitting [9,10,44]; therefore, a $t_{2g}^3e_g^1$ configuration is the favored state. Through the optical spectra Y. Okimoto *et al.* estimated that the Hund's rule exchange energy is of the order of 2 eV for $La_{1-x}Sr_xMnO_3$ at $x = 0.175$ [45], which is much larger than the crystal field splitting, of the order of 1 eV, as mentioned earlier. The later analysis of Y. Okimoto *et al.* results carried out by A. J. Millis *et al.* led to an even larger result 2.5 eV [46]. The optical conductivity experiments carried out on $Nd_{0.7}Sr_{0.3}MnO_3$, $La_{0.7}Ca_{0.3}MnO_3$ and $La_{0.7}Ca_{0.3}MnO_3$ by M. Quijada *et al.*[47], and the absorption spectra measurements performed in thin films of the doped manganites $R_{0.6}Sr_{0.4}MnO_3$ (R: Rare earth elements) by A. Machida *et al.*[48], also led to the conclusion that Hund's rule exchange energy is larger than 1 eV. Theoretical calculations using constrained local density approximation (LDA) done in manganites by Satpathy *et al.* [49] also suggest similar results. In summary, because of the dominance of Hund coupling over crystal field splitting, in manganites high spin ionic states ($Mn^{3+}$: $t_{2g}^3e_g^1$) are energetically favorable. Such a scenario is not the case for cobaltites, which will be discussed later in this chapter. The superexchange between neighboring $Mn^{3+}$ ions will lead to the antiparallel alignment of the localized $t_{2g}$ spins, resulting in AFM in undoped manganites, which will be discussed in more detail in section 1.3.3.

Now, if the end member $TMnO_3$ is doped with a divalent element D to form $T_{1-x}D_xMnO_3$, the valences of Mn ions will have a combination of $Mn^{3+}$ and $Mn^{4+}$. Double exchange (DE) starts playing an important role in the magnetic and electronic properties of manganites. As first proposed by C. Zener in 1951 [50] and later expanded by P. G. de Gennes [51] and P.W. Anderson *et al.* [52], DE was used to explain the FM and metallic behavior in doped manganites. The basic idea is shown in Fig. 1.8. It can be seen that there is one $e_g$ electron in the $Mn^{3+}$ 3d orbital. For $Mn^{4+}$, all three 3d electrons are located in the $t_{2g}$ orbital due to the large Hund's coupling, as mentioned earlier. The $e_g$ electron can hop from $Mn^{3+}$ sites to the neighboring $Mn^{4+}$ sites through the oxygen 2p orbital

lying between these sites, as shown in Fig. 1.8(a). After the hopping is complete, it can be seen from Fig. 1.8(b) that $Mn^{3+}$ sites end up being $Mn^{4+}$ sites and $Mn^{4+}$ sites end up being $Mn^{3+}$ sites, i.e. the configuration of the $Mn^{3+}$ site and the $Mn^{4+}$ site is swapped. The states before and after the hopping are degenerate. The phrase "double exchange" comes from the key role the oxygen orbital plays in this hopping mechanism. C. Zener [50] believed that the direct exchange interaction between $Mn^{3+}$ and $Mn^{4+}$ is impossible since they are too far away from each other, therefore, he introduced an indirect exchange interaction between $Mn^{3+}$ and $Mn^{4+}$ and treated the oxygen 2p orbital as the medium for such an indirect exchange. C. Zener [50] believed the hopping of the $e_g$ electron from $Mn^{3+}$ to the oxygen 2p orbital, and the hopping of the oxygen 2p electron to the neighboring $Mn^{4+}$ $e_g$ orbital, occur simultaneously, which is the origin of the phrase "double exchange".

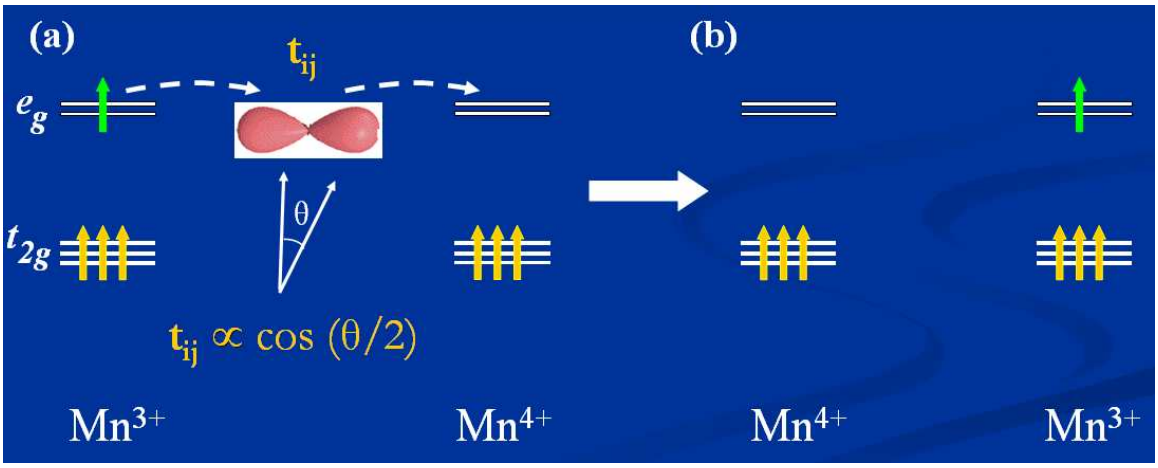


**Fig. 1.8** Schematic diagram of DE mechanism: (a) Configuration of the mixed valences of $Mn^{3+}$ and $Mn^{4+}$ before $e_g$ electrons hop from $Mn^{3+}$ to $Mn^{4+}$, (b) configuration of the mixed valences of $Mn^{3+}$ and $Mn^{4+}$ after $e_g$ electrons hop from $Mn^{3+}$ to $Mn^{4+}$, $Mn^{3+}$ and $Mn^{4+}$ configuration swaps after the hopping of $e_g$ electrons.

Such a hopping mechanism leads to metallic behavior of the system albeit with modest bandwidth and mobility. Meanwhile, as the hopping of $e_g$ electrons occurs, due to the large intra-atomic Hund's rule exchange energy $J_H$ between the spin of $e_g$ electron ($e_g^1$, $s$ = 1/2) and the localized core spin ($t_{2g}^3$, $S$ = 3/2), as mentioned previously, the $e_g$

electron will try to align the localized core spins between neighboring $Mn^{3+}$ and $Mn^{4+}$ sites. In other words, the hopping mechanism will be easiest when the core spin orientation of $Mn^{3+}$ and $Mn^{4+}$ are parallel to each other. If the core spins between cations are antiparallel to each other, a huge energy penalty has to be paid associated with the hopping, which prevents the hopping from occurring. There exists a quantitative relation to describe the hopping amplitude $t_{ij}$ between neighboring $Mn^{3+}$ and $Mn^{4+}$ sites, as shown below [9,10]:

$$t_{ij} = t\cos(\frac{\theta}{2}) \qquad (1.4),$$

where $t$ is the normal transfer integral (hopping amplitude when the core spins of neighboring $Mn^{3+}$ and $Mn^{4+}$ are parallel to each other) and $\theta$ is the angle between the core spin orientation of $\vec{S}_i$ (from $t_{2g}^3$ in $Mn^{3+}$) and $\vec{S}_j$ ( from $t_{2g}^3$ in $Mn^{4+}$), as shown in Fig. 1.8(a). It is obvious from Eq.(1.4) that the hopping is maximized when the localized core spins of $Mn^{3+}$ and $Mn^{4+}$ are parallel to each other, and is reduced to zero when they are antiparallel to each other, i.e. no hopping is allowed. Such a quantitative analysis is in agreement with the earlier conclusion from the intuitive energy perspective. It can be seen that FM enhances the hopping mechanism, and the hopping mechanism, in turn, promotes the FM behavior by aligning the localized core spins of Mn ions in manganites. Therefore DE leads to FM and metallicity in doped manganites.

There are other competing tendencies which give rise to insulating behavior in doped manganites, such as the Jahn-Teller effect. The Jahn-Teller theorem was first developed by H.A. Jahn and E. Teller in 1937 who proved that non-linear degenerate molecules can not be stable [53]. The theorem essentially states that any non-linear molecule with a degenerate electronic ground state will undergo a geometrical distortion that removes the degeneracy to lower the overall energy of the system. The interaction between the electrons and Jahn-Teller modes was later developed by J. Kanamori [54]. We will use doped manganites to illustrate such an effect. As shown in Fig. 1.9, when the perovskite structure is elongated along the *z* axis, the degeneracies of the $e_g$ orbital and the $t_{2g}$ orbital are further lifted by such a Jahn-teller distortion. The $e_g$ orbitals are split into two separate

energy levels $d_{x2-y2}$, $d_{3z2-r2}$, with $d_{3z2-r2}$ being lower in energy, and the $t_{2g}$ orbital are split into a singlet $d_{xy}$, and a lower doublet ($d_{yz}$, $d_{zx}$).

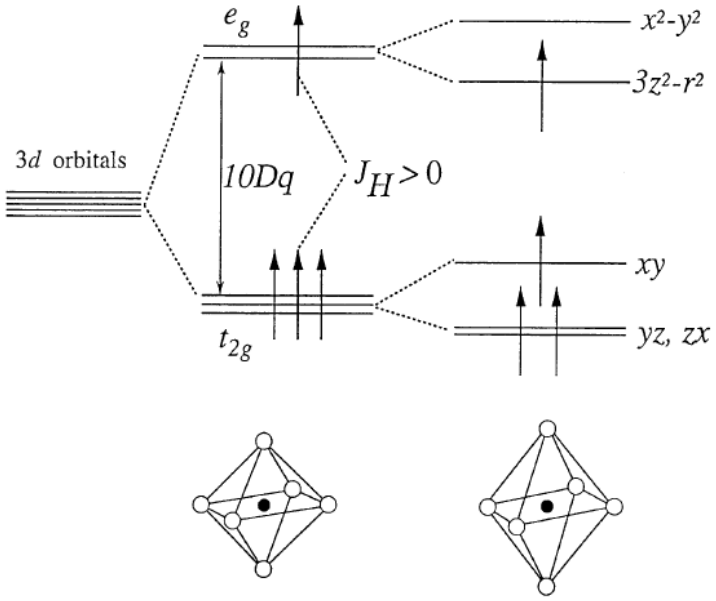


**Fig. 1.9** Schematic diagram of Jahn-Teller distortion in a perovskite structure. The crystal field splits 3d orbital into $e_g$ orbital ($d_{x2-y2}$, $d_{3z2-r2}$) and $t_{2g}$ orbital ($d_{xy}$, $d_{yz}$, $d_{zx}$), as shown earlier in Fig. 1.7. The Jahn-Teller distortion further lifts the degeneracies of $e_g$ orbital and $t_{2g}$ orbital and splits them into two separate levels, and a singlet as well as a doublet respectively. Reproduced from Ref. 10.

Such a distortion can be understood in an intuitive way as below: For a $Mn^{3+}$ ion, single occupancy of the $e_g$ orbital (either $d_{3z2-r2}$ or $d_{x2-y2}$, let us use $d_{3z2-r2}$ for example) will induce a distortion which will minimize the Coulomb repulsion. If the $d_{3z2-r2}$ is the occupied orbital, its orbital (of dumb-bell shape) will elongate along the *z* axis, away from the oxygen ions, in order to reach a lower energy state, which results in the extension along the *z* axis and the contraction in the *x*-*y* basal plane. Such a distortion results in a tetragonal structure for manganites. Similar arguments hold for the occupancy of $d_{x2-y2}$, the only difference is that the distortion will extend in the *x*-*y* basal plane and contract in the *z* axis, giving rise to lower energy level for $d_{x2-y2}$. Such a distortion also gives rise to a tetragonal structure. It can be seen form the above arguments that the Jahn-

Teller distortion is only active for ions with single occupancy of the $e_g$ orbital, i.e. only $Mn^{3+}$ ions, not $Mn^{4+}$ ions, since for double or zero occupancy of the $e_g$ orbital, the distortion will not lower the total energy of the system and will not occur. It can be understood that the elongation occurs in both the basal plane and along the *z* axis, resulting in no net distortion. It can be seen that the Jahn-Teller distortion has the tendency to trap $e_g$ electrons of $Mn^{3+}$ ions in the oxygen octahedral cage and prevent them from hopping. Such a tendency leads to a localization effect, resulting in insulating behavior in these materials, which is opposite to the metallic tendency driven by the DE hopping. The static Jahn-Teller energy was estimated to be 0.25 eV by D.S. Dessau and Z.-X. Shen [55].

Besides the insulating tendency induced by the Jahn-Teller distortion, there are other tendencies including charge/orbital ordering and antiferromagnetism (AFM) (which are quite common in manganites, as shown in Fig. 1.10 in the phase diagrams for four representative perovskite manganites [56]). Charge ordering refers to the phenomenon where $Mn^{3+}$ and $Mn^{4+}$ ions are arranged in an ordered way, such as CE-states, stripes, and bi-stripes [9]. Such an ordered system will prevent $e_g$ electrons from hopping and lead to insulating behavior. Similarly, orbital ordering refers to the phenomenon where the orbitals of $Mn^{3+}$ and/or $Mn^{4+}$ ions are arranged in an ordered way, such as A-type AFM in $LaMnO_3$, where the orbitals of $d_{3x2-r2}$ and $d_{3y2-r2}$ are arranged alternatively in the *ab* plane [9-10], and the hopping between neighboring Mn ions is prevented. As seen from the phase diagrams in Fig. 1.10, rich phases exist in these manganites, indicating multiple ground states are possible. Between these different states, there is a very delicate energy balance which can be modified either by temperature or doping. Using $La_{1-x}Ca_xMnO_3$ as an example, W.E. Pickett *et al.* [57] demonstrated that there are very small differences between different ground states based on the theoretical calculations using the local spin-density approximation. Phase competition is believed to be at the heart of MEPS [9-10], which can be used to help understand the CMR effect mentioned in the previous section. When an external field is applied, the metallic phase grows and the insulating phase shrinks, and at large enough magnetic fields, the metallic phase eventually percolates to form a connected metallic network, as shown in Fig. 1.4. Such a mechanism also explains

why the peak CMR occurs at the boundary of the metal-insulation transition (in the temperature scale), for example, as shown in Fig. 1.3. The coexistence of metallic and insulating phase is indispensible for the existence of sensitive magnetic field dependence of transport, i.e. large CMR. In summary, several other key factors including the interaction between lattice, spin, charge, orbital degrees of freedom, the very small energy difference between different phases, as well as the randomness introduced by doping [9-10] leads to multiple ground states which directly give rise to MEPS.

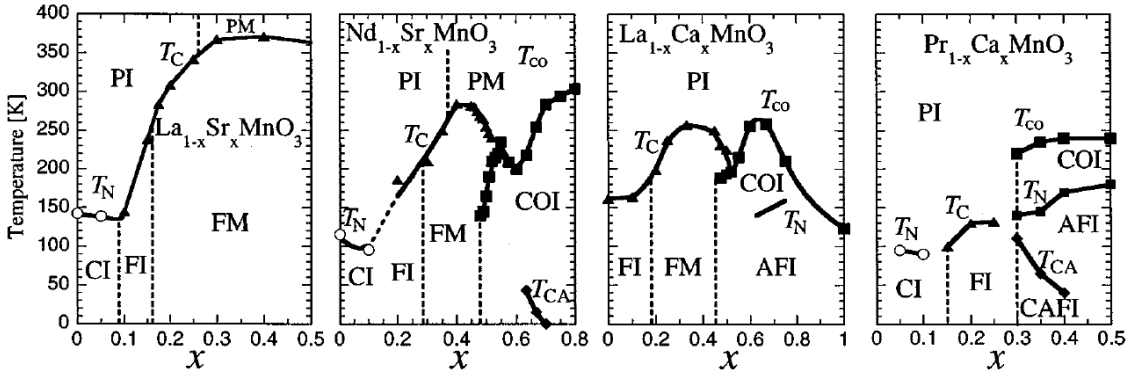


**Fig. 1.10** Phase diagrams plotted as temperature vs. doping *x* for four representative perovskites manganites in the order of decreasing bandwidth: (a) $La_{1-x}Sr_xMnO_3$; (b) $Nd_{1-x}Sr_xMnO_3$; (c) $La_{1-x}Ca_xMnO_3$; and (d) $Pr_{1-x}Ca_xMnO_3$. States denoted by abbreviations. PI: Paramagnetic insulator, PM: Paramagnetic metal, CI: spin-canted insulator, COI: Charge-ordered insulator, AFI: Antiferromagnetic insulator, CAFI: Canted antiferromagnetic insulator. Reproduced from Ref. 56.

Now it is time to discuss how the tolerance factor affects the properties of manganites. As mentioned earlier, when manganites are doped with smaller A site cations, which will induce some distortion, the tolerance factor will be smaller than one and the Mn-O-Mn bond angle α deviates away from $180^0$. Such a factor has a large impact on the properties of manganites since the hopping amplitude *t* between neighboring $Mn^{3+}$ and $Mn^{4+}$, as mentioned earlier, is proportional to cos(α) [9]. It is easy to understand since the hopping mechanism is mediated through the *p* orbital of oxygen, which can not point directly towards both neighboring Mn ions if the bond angle is not $180^0$. While the hopping amplitude is directly related to the bandwidth of manganites, the tolerance factor

therefore directly affects the bandwidth of manganites by impacting the hopping amplitude. A systematic study carried out by H. Y. Hwang *et al.* [58] proved that for $T_{0.7}D_{0.3}MnO_3$ the bandwidth, and thus the Curie temperature, could be tuned by the adjustment of the tolerance factor, as shown in Fig. 1.11. Y. Tomioka *et al.* [59] also performed a similar study for $T_{0.5}D_{0.5}MnO_3$, as shown in Fig. 1.12. It can be seen with decreasing $<r_A>$, the FM state becomes unstable for $T_{0.5}D_{0.5}MnO_3$ and the manganites enter a charge/orbital ordered state. Both of their results indicate that FM is suppressed below some critical tolerance factor $\Gamma_C$.

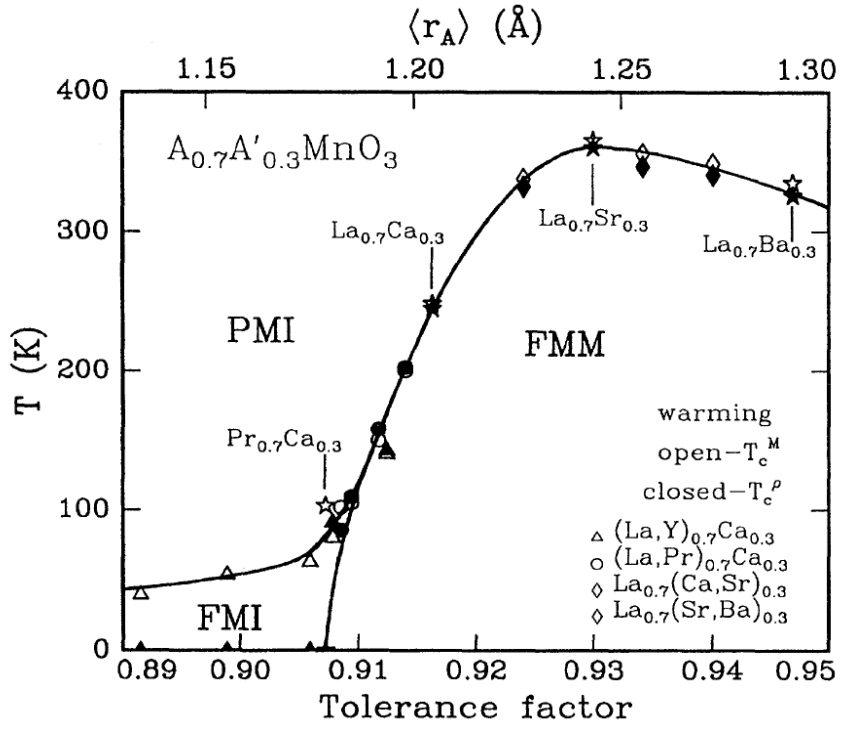


**Fig. 1.11** Phase diagram plotted as temperature vs. tolerance factor for the system $A_{0.7}A'_{0.3}MnO_3$. PMI: Paramagnetic insulator, FMI: Ferromagnetic insulator, FMM Ferromagnetic metal. Reproduced from Ref. 58.

It is important to point out that DE is used for the purpose of simple illustration of phase competition, as discussed in section 1.3.2. It can qualitatively explain why CMR peaks at the insulator–metal transition. However, it fails to *quantitatively* predict the magnitude of CMR [9-10], and fails to qualitatively reproduce the phase diagram of

manganites. For example, a simple calculation based on Eq. (1.4) will predict that the maximum magnitude for CMR is 50 %, which is actually exceeded by most manganites. Another simple example would be the fact that, based on DE, the phase of $T_{1-x}D_xMnO_3$ should be similar to $T_xD_{1-x}MnO_3$, i.e. the phase diagram should be symmetric around $x$ = 0.5 since the DE is active through $Mn^{3+}$-$O^{2-}$-$Mn^{4+}$ and the amount of such a chain should be equal to each other. However, as can be seen from Fig. 1.10, such a prediction does not apply to the real phase diagram. Therefore, more advanced theoretical models which take into account other interactions, such as electron – phonon interactions [60-63], need to be developed to fully understand MEPS in manganites, as will be discussed in the next section.

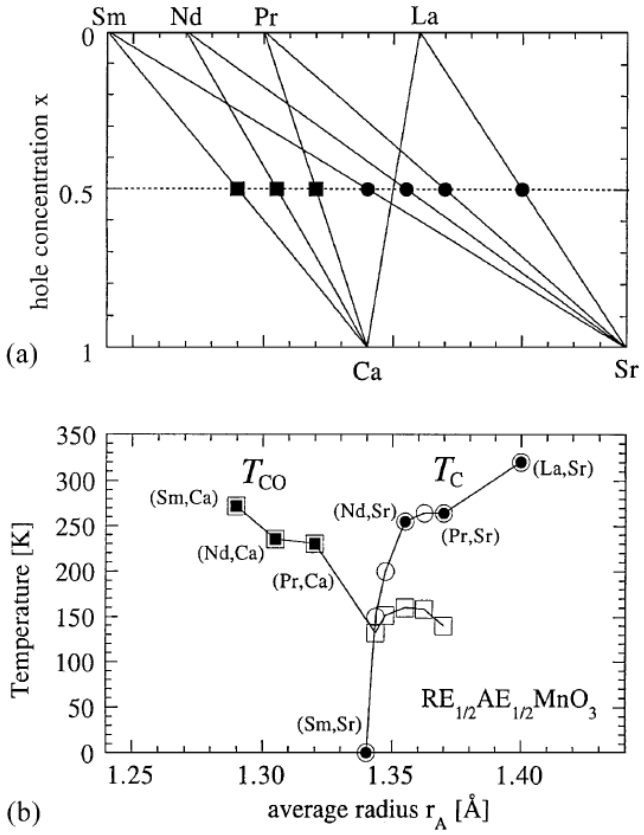


**Fig. 1.12** (a) Average ionic radius at $x$ = 0.5 corresponding to a mixture of trivalent ion and a divalent ion, and (b) the phase diagram plotted as temperature vs. average A-site cation radius for $RE_{0.5}AE_{0.5}MnO_3$. $T_C$: Curie temperature; $T_{CO}$: Charge/orbital ordering temperature. Reproduced from Ref. 59.

### 1.3.3 Theoretical models for MEPS in manganites

Due to the large Hund's rule exchange coupling, as discussed in section 1.3.2, the occupancy of the $t_{2g}$ orbital is fixed regardless of doping, therefore, its charge degree of freedom can be ignored and the only important interaction of relevance between $t_{2g}$ electrons and $e_g$ electrons is due to $t_{2g}$ spins, which can be treated as localized spin. As a result, the Coulomb interaction between $t_{2g}$ electrons and $e_g$ electrons can be dropped [9-10]. After making such a reasonable assumption and taking into account both the electron-phonon interaction (i.e. interaction between Jahn-Teller distortion and $e_g$ electrons), and AFM coupling among nearest neighbor $t_{2g}$ spins (known to occur in doped manganites at doping $x$ = 1, e.g. see $CaMnO_3$ in Fig. 1.10(c)), E. Dagotto proposed a simple but realistic model to describe manganites, as shown below [9-10]:

$$H = H_{kin} + H_{Hund} + H_{AF} + H_{el-ph} + H_{el-el} \quad (1.5),$$

where $H_{kin}$ is the kinetic energy for $e_g$ electrons due to the DE hopping mechanism, $H_{Hund}$ is the intra-atomic Hund's rule exchange energy between the $e_g$ electron spins and localized $t_{2g}$ spins, $H_{AF}$ is the antiferromagnetic exchange coupling between nearest neighboring $t_{2g}$ spins via virtual hopping, $H_{el\text{-}ph}$ is the interaction between $e_g$ electrons and the Jahn-Teller distortion of the $MnO_6$ octahedron, and $H_{el\text{-}el}$ is the Coulomb interactions between $e_g$ electrons. Each individual component is demonstrated in the schematic diagram, as shown in Fig. 1.13 [64]. However, such a Hamiltonian after making many simplifications is still too complicated to solve in practice in spite of modern many-body techniques. Some further simplifications have to be made to produce simpler models that can still contain the basic physics of manganites.

One useful and widely used model is called the one-orbital DE model. Its Hamiltonian is expressed as below [9]:

$$H = -t\sum_{\langle ij\rangle,\sigma}(a_{i,\sigma}{}^{\dagger}a_{j,\sigma} + H.c.) - J_H\sum_i \boldsymbol{s_i}\cdot\boldsymbol{S_i} + J_{AF}\sum_{\langle ij\rangle}\boldsymbol{S_i}\cdot\boldsymbol{S_j} \quad (1.6),$$

where $a_{i,\sigma}$ and $a^{\dagger}_{i,\sigma}$ are the annihilation and creation operators at site $i$ with spin $z$-projection $\sigma$, $t$ is the nearest-neighbor hopping amplitude for the electrons, $J_H$ is the Hund's coupling between the mobile electron spin ($e_g$ electron) $\boldsymbol{s_i}$ and localized electrons

($t_{2g}$ electrons) spin $\boldsymbol{S_i}$ at the same site i, and $J_{AF}$ is the antiferromagnetic coupling between nearest neighboring $t_{2g}$ spins. <ij> denotes nearest-neighbor lattice sites. By comparing Eq. (1.6) to Eq. (1.5), it can be seen that one-orbital model is obtained by dropping the electron and phonon coupling as well as the Coulombic interaction among $e_g$ electrons. The reason such a model is called the "one-orbital" model is because only one active orbital in $e_g$ electron is kept after assuming uniform splitting of degenerate $e_g$ due to static Jahn-Teller distortion, as discussed by E. Dagotto [9]. In spite of such drastic simplifications, such a model still captures the essence of the FM mechanism as well as phase competition in manganites, which is why it is accepted as reasonable [9].

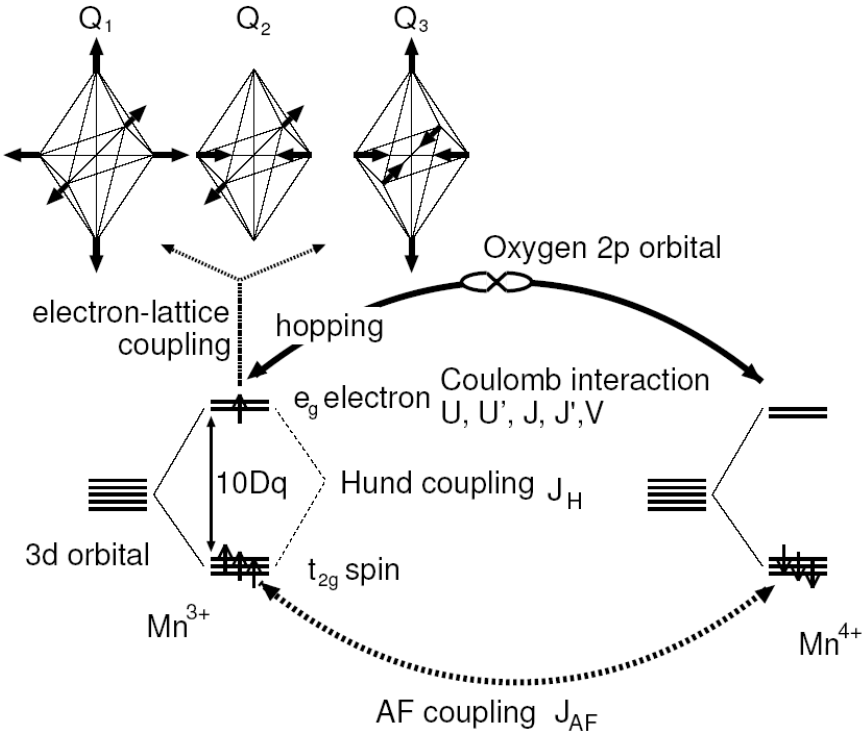


**Fig. 1.13** Schematic diagram for each individual type of interactions included in the hamiltonian for manganites. Reproduced from Ref. 64.

The Monte Carlo simulations based on the one-orbital model performed by S.Yunoki and E. Dagotto *et al.* [65-67] can compute the electron density $e_g$ <n>, which should vary between 0 and 1 according to the definition, as a function of the chemical potential μ.

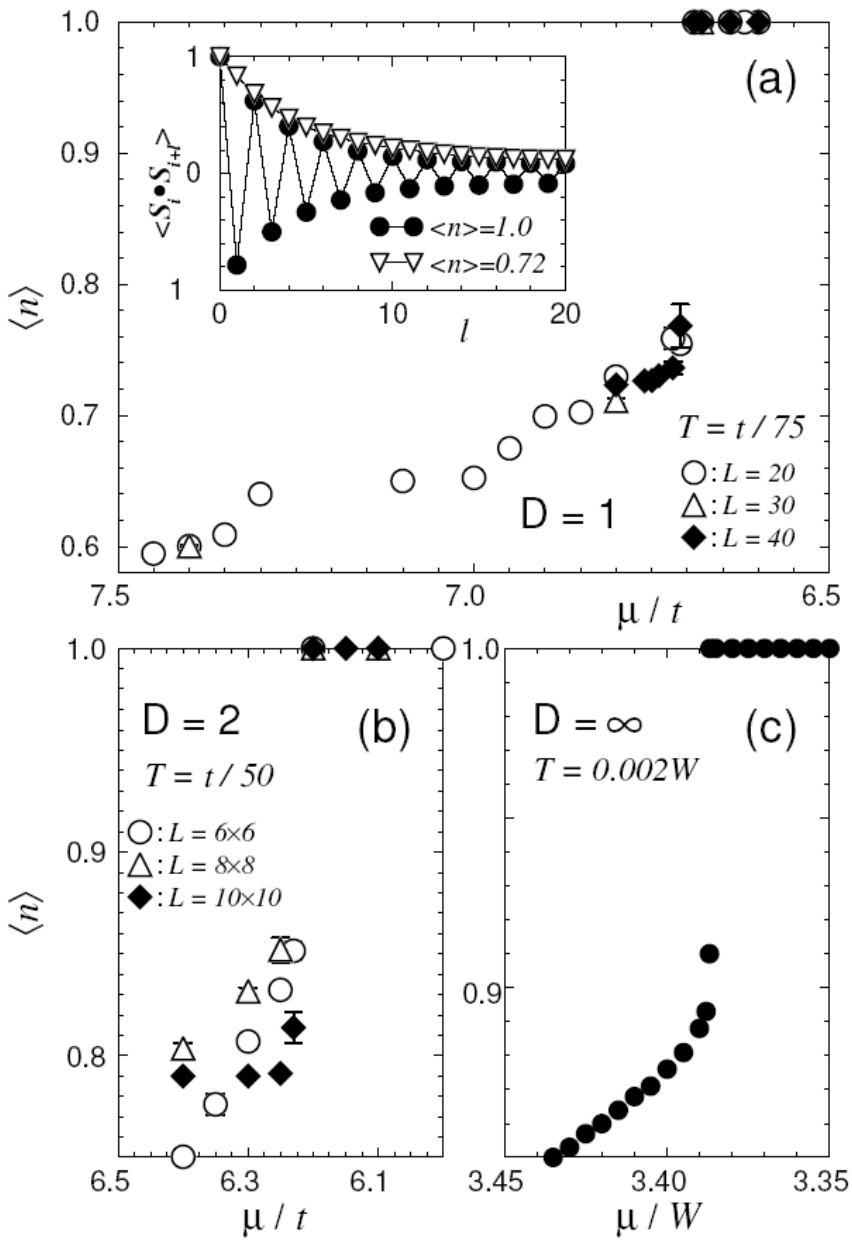


**Fig. 1.14** Electronic density <*n*> as a function of chemical potential μ for (a) D = 1, (b) D = 2, and (c) D = ∞ based on Monte Carlo simulations. Cluster size, *L*, and temperature, *T*, are indicated. *t*: The hopping amplitude, *W*: The half-width of the density of states. Inset of (a): Spin correlations in real space at *n* = 1.0 and 0.72, showing phase separation occurred between FM and AF regions. Reproduced from Ref. 65.

The calculated results for one-dimensional (D = 1), two-dimensional (D = 2), and infinite dimensional (D = ∞) systems are shown in Fig. 1.14 [65]. It can be seen for all three cases, that there exists a region of electronic density discontinuity, clear evidence of first-order abrupt transition and phase separation [65]. Using the D = 1 study as an example, as shown in Fig. 1.14 (a), it can be seen that the electronic density between 0.78 and 1 is inaccessible, regardless of how the chemical potential μ is tuned. Such a result indicates that the electronic density between 0.78 and 1 is unstable, i.e. any global electronic density in this region is not possible. For example, n = 0.9, will have the tendency to spontaneously separate into two regions which are stable, say, n = 1 and n = 0.72. It can also be seen from the spin correlation functions, as shown in the inset of Fig. 1.14(a) that these two macroscopically phase separated regions have different or competing coupling mechanisms, i.e. FM coupling at low density n = 0.72, and AFM coupling at higher density n = 1.

It is important to point out that such a phase separation occurs on macroscopic scales, as predicted by the simulation. Such a macroscopic phase separation will have the problem of paying a huge energy penalty due to electrostatics. This unreasonable element is due to the simplifications of dropping the Coulombic interaction when deriving the model, as mentioned earlier. After taking into account the long-range Coulombic interaction, it is expected that phase separation can only occur on the nanoscopic scale, as a result of the balance of phase separation tendency and the long-range Coulombic interaction [9-10]. Such an expectation is confirmed by the theoretical calculation carried out by K.I. Kugel *et al.* after taking into account Coulombic interactions [68]. The calculated size of the clusters can be expressed as below [68]:

$$\left[\frac{\xi}{a}\right]^3 = \frac{15E_{Con}(x_F)}{4\pi U(x_F - x_{NF})^2(2-3f^{1/3}+f)} \qquad (1.7),$$

where $\xi$ is the size of the FM clusters, $a$ is the lattice parameter, $U$ is the Coulomb energy scale ($e^2/4\pi\kappa\varepsilon_0$), $E_{Con}$ is the part of the Coulombic energy penalty due to confinement , $f$ is the FM phase fraction, $x_F$ is the effective doping in FM phase, and $x_{NF}$ is the effective doping in non-FM phase. According to Eq. (1.7), a simple calculation based on

reasonable assumptions leads to a ξ value about 5-10 Å (about 2-3 unit cells) in manganites, meaning the phase separation really occurs on nanoscopic scales.

Such a nanoscopic phase separation is the key issue to be discussed in this thesis. It is worthwhile to mention that other theoretical calculations, including the mean-field approximations and variational calculations, etc. also lead to phase separation. For example, the existence of phase separation is also observed by M. Kagan *et al.* using approximate analytical techniques [69], by D. Arovas *et al.* using the Schwinger boson formalism [70], and in some other calculations [71,72]. Therefore, phase separation seems to be a universal effect in manganites, regardless of the specific simulation method.

There is another type of phase separation in manganites that can occur on larger length scales, on the order of micrometers, called mesoscopic phase separation. Such a phase separation is usually driven by disorder near a first order transition [9,10,73] or elastic effects [74]. For example, M. Uehara *et al.* have used electron microscopy to demonstrate that in $La_{5/8-y}Pr_yCa_{3/8}MnO_3$ systems, there is submicron scale coexistence of insulating regions with a specific type of charge-ordering and FM metallic regions [75]. K. Kim *et al.* demonstrated that such a large length scale phase separation is usually associated with the long-range strain due to the fact that different phases possess different crystal symmetries [76].

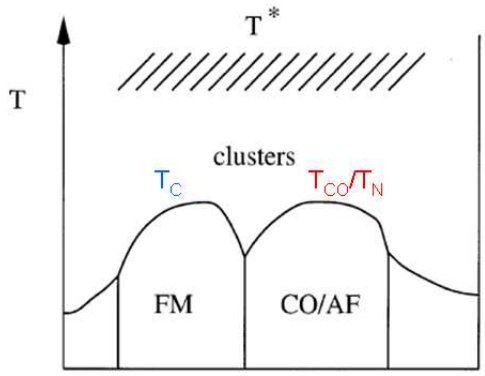


**Fig. 1.15** Schematic illustration of a new temperature scale *T** in system possessing a first order transition. Such a model is specifically developed for manganites. Above the Curie temperatures $T_C$, charge/orbital ordering temperature $T_{CO}$, and Neel temperature $T_N$, and below *T**, a region with coexisting clusters could exist. Reproduced from Ref.10.

Although such a mesoscopic phase separation is not the focus of this thesis, it is worthwhile to point out that such a phase separation usually occurs at the boundary of the first order transition, as shown in Fig. 1.15, according to the simple model developed specifically for manganites by E. Dagotto *et al.* [10]. According to this model, in the materials possessing a mesoscopic phase separation near the first order transition, there exists a new temperature scale $T^*$ above the ordering temperatures, as shown in Fig. 1.15, indicating the onset of coexisting clusters, which will be discussed in Chapter 4.

## 1.4 Physics of cobaltites ($La_{1-x}Sr_xCoO_3$)

Compared to the resurgent tremendous attention manganites have attracted since the re-discovery of the CMR effect in thin films in 1990's [17], the cobaltites have received somewhat less attention, in spite of the earlier studies carried out as early as the 1950's [77-79]. The major reason is that in cobaltites, the CMR effect is significantly smaller than in manganites, and from the practical point of view, the Curie temperature of cobaltites is slightly lower than that of manganites, which will favor manganites as the promising application candidates. However, cobaltites can offer several fascinating properties, which make them attractive in the study of fundamental physics. One reason is that doped $La_{1-x}Sr_xCoO_3$ is a model system to study nanoscopic phase separation, which will be discussed in detail in section 1.4.2. Another important property is the extra spin degree of freedom that undoped $LaCoO_3$ offers, which is absent in manganites due to large Hund's rule exchange coupling, as discussed in section 1.3.2. Due to the slight dominance of crystal field splitting over Hund's rule exchange in $LaCoO_3$, which is due to the ionic radius difference between Mn ions and Co ions, the spin state transition can be thermally excited and become an interesting property to study, as will be discussed in the next section.

### 1.4.1 Spin state transitions in $LaCoO_3$

In spite of its discovery over 40 years ago [80], the spin state transition (SST) in $LaCoO_3$ remains a controversial issue. Before looking into the details of SST, it is important for one to gain an intuitive picture of how the SST behaves magnetically and

electronically, say, in terms of magnetic susceptibility and electronic resistivity. Fig. 1.16 shows an example of the temperature dependence of such data gained by S. R. English *et al.* [81]. It can be seen that at low temperature, the susceptibility is very small. With increasing temperature, two noticeable anomalies show up, which is in agreement with previous observations [82-89]. The first anomaly occurs around 100 K, which increases sharply with increasing temperature below 100 K and then decreases with increasing temperature above 100K, resulting in a sharp peak centered around 80 K. This is associated with the transition from low spin to intermediate spin, as will be discussed in more detail later. With further increase of temperature, the susceptibility follows the Curie-Weiss behavior, i.e. linear behavior in the plot of inverse susceptibility vs. temperature (e.g. as shown in Fig. 1.17 by V.G. Bhide *et al.* [82]). The second anomaly shows up around 500 K, which corresponds to a plateau or a broad peak. It can be seen that the slopes of Curie-Weiss behavior are different below and above 500K, indicating an effective magnetic moment change (e.g. as determined by R. R. Heikes *et al.* [78], $\mu_{eff}$ changes from 3.1 $\mu_B$ for T < 400 K to 4.0 $\mu_B$ for T > 600 K) associated with a second SST occurred at this temperature, as shown in Fig. 1.17 [82].

Accordingly, these two anomalies are also reflected in electronic transport measurements. A major change occurs around 500 K where the transport behavior evolves from an insulating or semiconducting behavior into a fairly conducting state with the resistivity on the order of $1\times10^{-2}\Omega$ cm, as shown in Fig. 1.16(b). A similar behavior is observed by S. Yamaguchi *et al.* [85], with even smaller resistivity on the order of $1\times10^{-3}\Omega$ cm, for T > 500 K on a $LaCoO_3$ single crystal. Such a metal-insulator-transition is apparently associated with the second anomaly observed in susceptibly at 500 K. The first anomaly observed around 80 K in susceptibility is also reflected in transport in terms of the slope change of the resistivity curve near 100K, as shown in Fig. 1.16(b), as well as the magneto-transport (reaches a negative magneto-resistance minimum at about the temperature as the first susceptibility peak), as reported by S. R. English *et al.* [81].

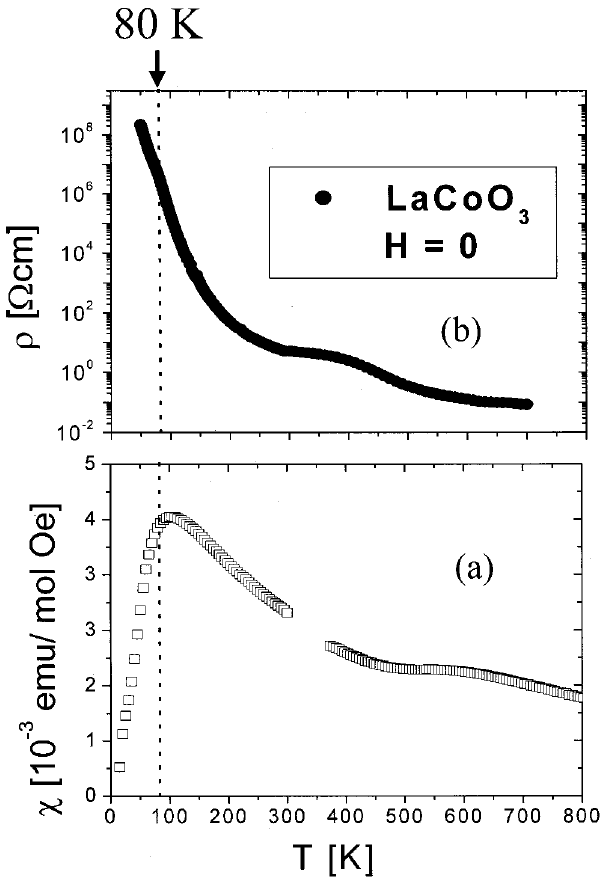


**Fig. 1.16** *T* dependence of (a) the magnetic susceptibility at 50 kOe after subtraction of low *T* "Curie tail" and (b) the resistivity of $LaCoO_3$ at zero field. The dotted line indicates the 80 K spin-state transition. Reproduced from Ref. 81.

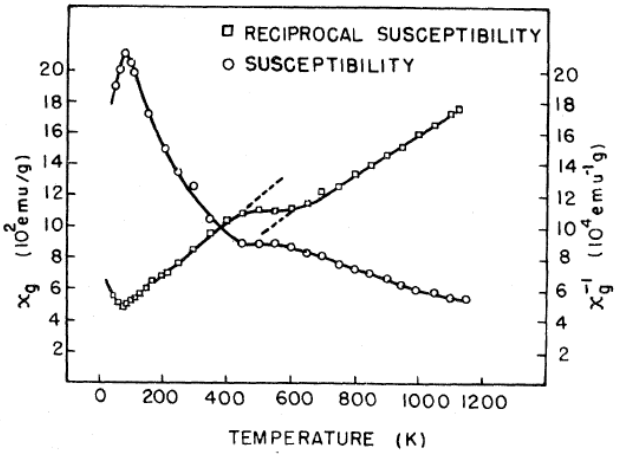


**Fig. 1.17** *T* dependence of the magnetic susceptibility ($\chi_g$) and inverse of magnetic susceptibility ($\chi_g^{-1}$) for of $LaCoO_3$. Reproduced from Ref. 82.

The origin of the thermally excited SST in $LaCoO_3$ is the subtle energy balance of $Co^{3+}$ in $LaCoO_3$, i.e. there is only a slight dominance of the crystal field splitting $\Delta_{CF}$ over Hund's rule exchange energy $\Delta_{EX}$, which results in a very small "spin gap" ($\Delta_{CF}$ - $\Delta_{EX}$), usually on the order of a few meV [81, 84]. Therefore, at $T$ = 0 K, all $3d^6$ electrons of $Co^{3+}$ reside in $t_{2g}$ states, resulting in a nonmagnetic low spin $t_{2g}^6$ $e_g^0$ (LS, S = 0) ground state, as shown in Fig. 1.18. Such a scenario is quite different from the picture in manganites, as discussed in section 1.3.2, where the dominance of Hund's coupling energy over crystal field splitting always gives rise to parallel spin alignment for the 3d electrons of the Mn ion, thus the high spin state configuration. With increasing temperature, the small energy barrier of $\Delta_{CF}$ - $\Delta_{EX}$ can be overcome by thermal energy, which excites the non-magnetic ground state into a finite spin state, either an intermediate spin $t_{2g}^5$ $e_g^1$ (IS, S = 1) or a high spin $t_{2g}^4$ $e_g^2$ (HS, S = 2), as shown in Fig. 1.18.

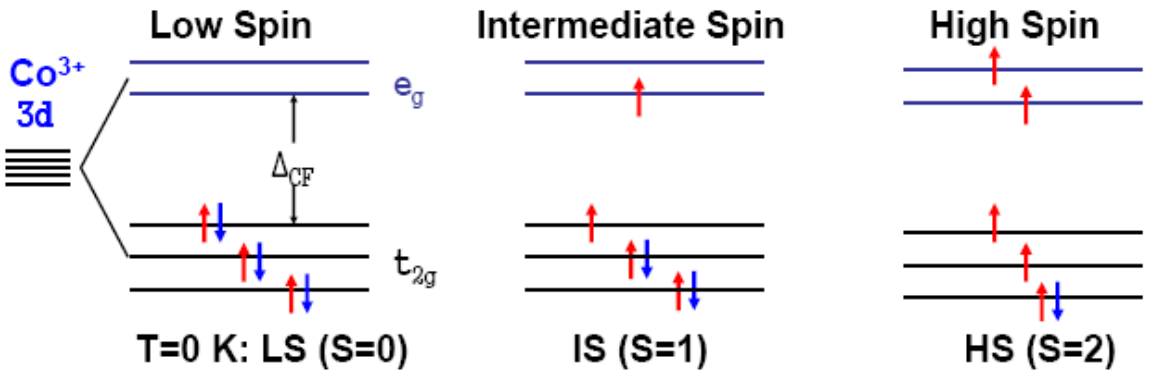


**Fig. 1.18** Schematic diagram of crystal field splitting of $Co^{3+}$ 3d orbital and all possible spin states for $Co^{3+}$ in $LaCoO_3$.

Although it is generally believed that in $LaCoO_3$, slight dominance of the crystal field splitting over Hund's rule exchange energy leads to a $t_{2g}^6e_g^0$ ($S$ = 0) low spin (LS) non-magnetic ground state [84]. The nature of the SST observed around 100 K by different groups [81-90], i.e. whether it is a LS → IS or a LS → HS transition, or a mixture of both, remains highly controversial. In the 1960's, according to the Tanabe-Sugano diagrams based on an atomic picture, P.M. Raccah *et al.* proposed HS as the first excited state [80]. In the 1990's, based on the LDA+U band structure calculation, M.A. Korotin

*et al.* interpreted the first crossover as an LS → IS transition indicating stabilization of IS by Co $e_g$ – O 2p orbital hybridization [91], which is radically different from LS→ HS transition and is very rare in nature. Such a picture was supported by the evidence obtained through different experimental techniques such as infrared spectroscopy [87], magnetic susceptibility [92], thermal expansion [92], X-ray diffraction [93], x-ray absorption near-edge structure spectroscopy [94], and electron energy-loss spectroscopy [95], etc. However, recent experiments via electron spin resonance (ESR) [96,97], x-ray absorption spectroscopy (XAS)/magnetic circular dichroism (MCD) [98], and inelastic neutron spectroscopy (INS) [99] provide evidence for LS → HS transition. In light of these conflicting reports, the nature of the SST thus remains highly debatable.

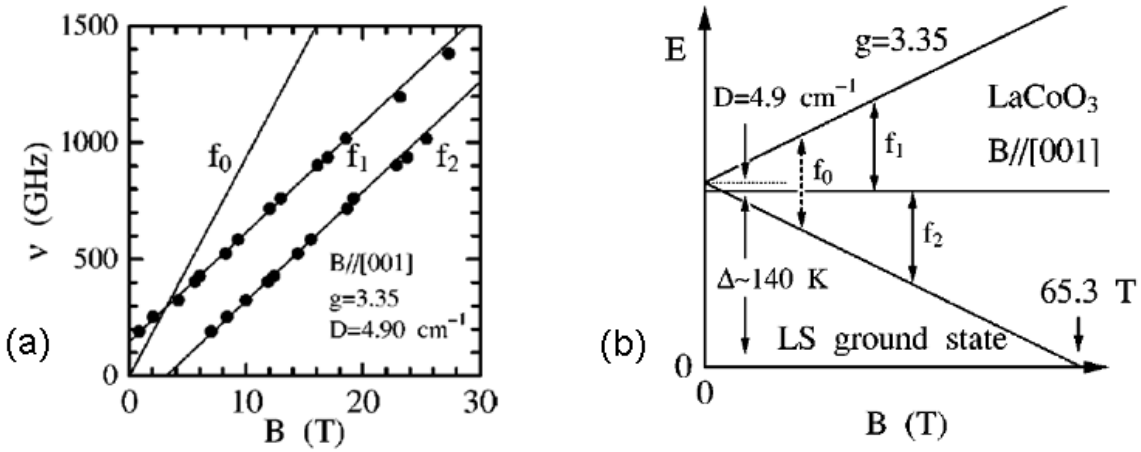


**Fig. 1.19** (a) ESR signal plotted as frequency vs. field for [001] of a $LaCoO_3$ single crystal at 50 K. The solid lines correspond to calculated results. (b) Schematic diagram of the zero-field-splitting triplet nature of the first excited spin state for $Co^{3+}$ for [001] of a $LaCoO_3$ single crystal. Reproduced from Ref. 96.

Recently, another important issue that received much attention is the zero field-split triplet nature of the first excited finite spin state. Through ESR on a $LaCoO_3$ single crystal, S. Noguchi *et al.* first determined the zero field-split nature of the excited spin state with a *g*-factor ~3.35 [96] as well as zero field-splitting $\Delta = 4.9\ cm^{-1} \approx 0.6$ meV [96], as shown in Fig. 1.19(a), which shows the field dependence of the excitations within the triplet excited states when the applied field is along the [001] axis of a $LaCoO_3$ single

crystal (for simplicity purposes, we treat $LaCoO_3$ as a cubic system although it actually possesses a rhombohedral structure, as discussed above). The meaning of each individual excitation is illustrated in Fig. 1.19(b) [96]. It can be seen that at zero field, there is a splitting (represented by *D*) between the lower energy singlet and the higher energy level doublet which will further split in the presence of a magnetic field due to Zeeman splitting. Similar results were found for other high symmetry crystallographic directions and the g-factor was found to be weakly-dependent on the crystallographic directions with a *g*-factor of 3.45 [96]. Such an experimental observation was later perfectly reproduced by Z. Ropka *et al.* based on theoretical calculations within the localized electron atomic-like approach [100] and thus became the strong evidence of HS.

Later two independent INS experiments carried out by A. Podlesnyak *et al.* [99] and D. Phelan *et al.* [30], respectively, almost simultaneously revealed the direct evidence of the thermally excited 0.6 meV excitation, as shown in Fig. 1.20, although these two groups came up with different interpretations. Podlesnyak *et al.* interpreted such an excitation within a HS triplet picture due to spin-orbit coupling partly because the determined *g*-factor (~ 3) is in agreement with the HS spin state picture [99]. The 0.6 meV excitation was ascribed to the transition from a singlet to a doublet in this HS triplet, which lies about 10 meV above the ground states. The absence of direct excitation to this HS first excited state was attributed to the selection rules [99]. On the contrary, the excitation observed by D. Phelan *et al.* was interpreted within an IS first excited state scheme [30]. This was supported by local dynamic Jahn-Teller (JT) distortions [101], and simultaneous ferromagnetic (FM) and antiferromagnetic (AF) spin correlations [30], i.e. dynamic A-type AF ordering (AF coupling between FM sheets) induced by dynamic orbital ordering associated with JT active IS states. However, the latter interpretation is questioned by recent work carried out by Sundaram *et al.* via extended x-ray absorption fine structure and neutron pair distribution function analysis [102]. They claimed few, if any, JT active states exist in $LaCoO_3$ [102]. In light of these conflicting arguments based on similar observed phenomena, the sequence of excited states thus remains highly controversial. More discussions on the SST will be provided in Chapter 3, particularly on

an excitation of similar magnitude found at low temperature with non-thermally driven character.

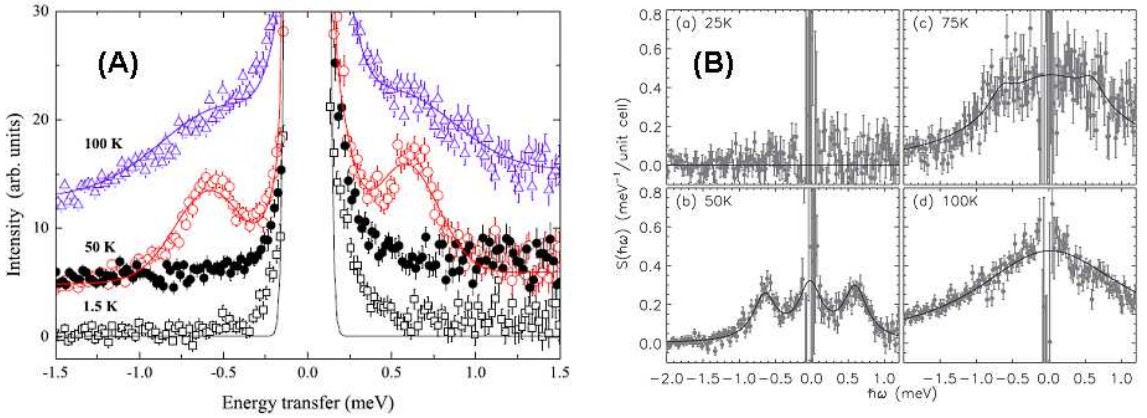


**Fig. 1.20** (A) Temperature dependence of INS signals in a $LaCoO_3$ polycrystal. The closed circles refer to signals from a nonmagnetic reference material $LaAlO_3$ at 50 K. Various curves were offset for clarity purpose. Reproduced from Ref. 99. (B) Temperature dependence of INS signals on power samples of $LaCoO_3$: (a) T = 25 K, (b) T = 50 K, (c) T = 75 K, and (b) T = 100 K. Reproduced from Ref. 30.

### 1.4.2 Magneto-electronic phase separation in doped $La_{1-x}Sr_xCoO_3$

MEPS occurs as $LaCoO_3$ is hole doped. Before investigating MEPS, it is important to address the structure of $La_{1-x}Sr_xCoO_3$. Via x-ray powder diffraction and neutron diffraction, J. B. Goodenough *et al.* determined the structure of $La_{1-x}Sr_xCoO_3$ at low dopings ($x < 0.5$) to be the rhombohedrally distorted pseudo-cubic perovskite structure with space group $R\bar{3}c$ [80, 103]. When the Sr doping ($x$) is above 0.5, the structure of $La_{1-x}Sr_xCoO_3$ evolves into a cubic structure with space group $Pm\bar{3}m$ [104]. The schematic structure of $La_{1-x}Sr_xCoO_3$ and one example of the doping-dependent lattice parameters determined by P. Ravindran *et al.* is shown in Fig. 1.21 [104]. Similar results are found by other groups, for example, J. Wu *et al.* carried out a systematic study on $La_{1-x}Sr_xCoO_3$ ($0 \leq x \leq 0.70$) polycrystals and found the similar structure transition from rhombohedral structure to cubic symmetry occurred at $x \approx 0.5$ within the resolution of X-ray diffraction [105]. The lattice parameters (e.g. a = 5.42 Å, c = 13.26 Å for $x$ = 0.3)

[105] are also consistent with earlier reported data [80,103,104]. The structural characterization of our samples will be discussed in more detail in section 2.2.1.

(a)

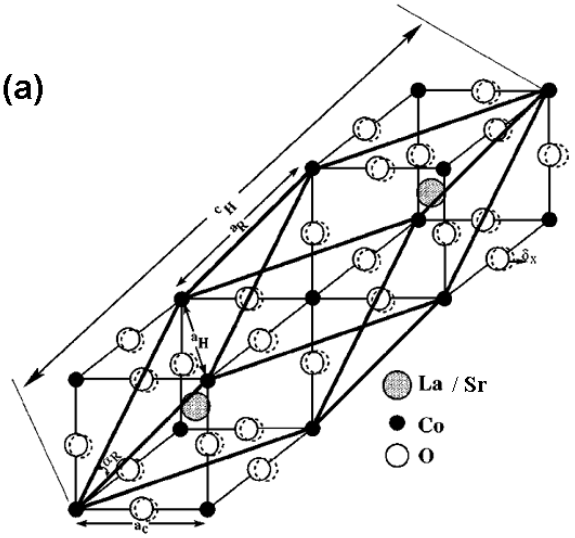


(b)

| Sr content ($x$) | $a_R$ | $\alpha$ | $x$ | $y$ | $z$ | $a_C$ |
|---|---|---|---|---|---|---|
| 0 | 5.37 | 60.79 | 0.3021 | 0.1978 | 0.75 | 3.805 |
| 0.1 | 5.32 | 60.49 | 0.292 | 0.208 | 0.75 | |
| 0.2 | 5.36 | 60.45 | 0.289 | 0.211 | 0.75 | |
| 0.25 | 5.34 | 60.46 | 0.2835 | 0.2165 | 0.75 | 3.789 |
| 0.3 | 5.32 | 60.47 | 0.278 | 0.222 | 0.75 | |
| 0.4 | 5.35 | 60.30 | 0.274 | 0.226 | 0.75 | |
| 0.5 | 5.35 | 60.27 | 0.264 | 0.236 | 0.75 | 3.791 |
| 0.75 | 5.41 | 60.00 | 0.25 | 0.25 | 0.75 | 3.827 |
| 1.0 | 5.424 | 60.00 | 0.25 | 0.25 | 0.75 | 3.836 |

**Fig. 1.21** (a) Schematic structure of $La_{1-x}Sr_xCoO_3$. $a_R$ and $\alpha_R$ refers to the lattice parameter and the rhombohedral angle in a rhombohedral unit cell. $a_H$ and $c_H$ corresponds to the hexagonal index system. $a_C$ is the lattice parameter indexed by a cubic structure. Dotted circles represent displacement $\delta x$ of oxygen atoms with respect to cubic structure. (b) Lattice parameters for $La_{1-x}Sr_xCoO_3$. ($x$, $y$, $z$) are coordinates for 6(e) oxygen atom (1/4 - $\delta x$, 1/4 + $\delta x$, 3/4). Reproduced from Ref. 104.

The general picture of phase separation in $La_{1-x}Sr_xCoO_3$ (LSCO) was first proposed by J. B. Goodenough *et al.* based on the studies of the crystallographic, magnetic, and electric properties [79]: At low Sr dopings ($x < 0.18$), hole rich FM clusters mediated by DE between $Co^{3+}$ and $Co^{4+}$ form in a hole poor non-FM matrix, which possesses the super-exchange interaction between $Co^{3+}$ and $Co^{3+}$, as shown in Fig. 1.22. Such a picture has now been confirmed by the intensive studies on the phase separation in LSCO via numerous probes including direct techniques such as neutron diffraction (ND) [103], nuclear magnetic resonance (NMR) [29, 106-108], small-angle neutron scattering (SANS) [109,110], and inelastic neutron spectroscopy (INS) [30,31,101], as well as bulk probes such as magnetometry [105,111-115], magnetotransport [105,110,115,116], a.c. susceptibility [103,105,112,113], and thermopower [111,116]. The direct experimental evidence for phase separation will be returned to later in this section.

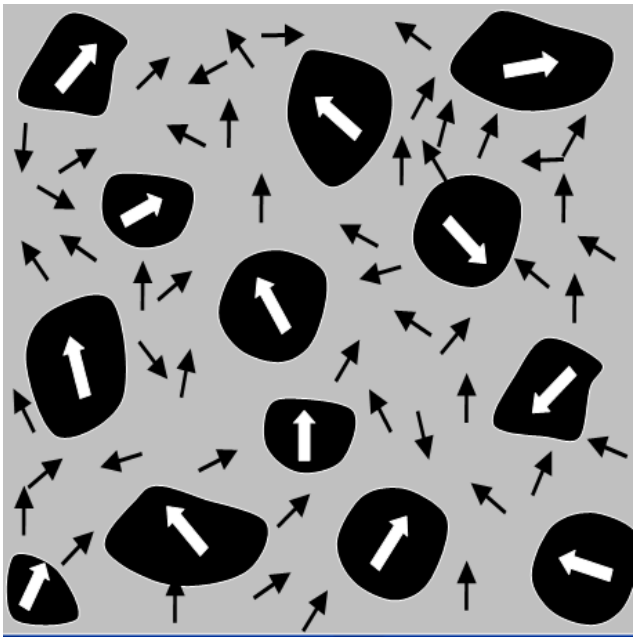

**Fig. 1.22** Schematic diagram of phase separation in $La_{1-x}Sr_xCoO_3$ at low dopings ($x < 0.18$): FM clusters (black bubbles, white arrows represent its spontaneous magnetization) are embedded in non-FM matrix (black arrows represent the spin orientation of each individual Co ion).

Before illustrating the experimental evidence of phase separation, it is important to show the phase diagram of LSCO determined on bulk polycrystalline samples. One

example determined by J. Wu *et al.* is shown in Fig. 1.23 [105]. Starting from zero doping, it can be seen there is a temperature scale representing the SST, as discussed in section 1.4.1, which quickly dies out at very low dopings (≈ 0.01). At low dopings ($x$ < 0.18), FM clusters form in a non-FM matrix. With increasing doping, the size of the FM clusters weakly increases. At $x$ ≈ 0.18, the FM clusters percolate and the system transforms into FM metallic state from the SG insulating state. $x_C$ ≈ 0.18 is the critical doping marking the SG to FM transition as well as the insulator to metal transition.

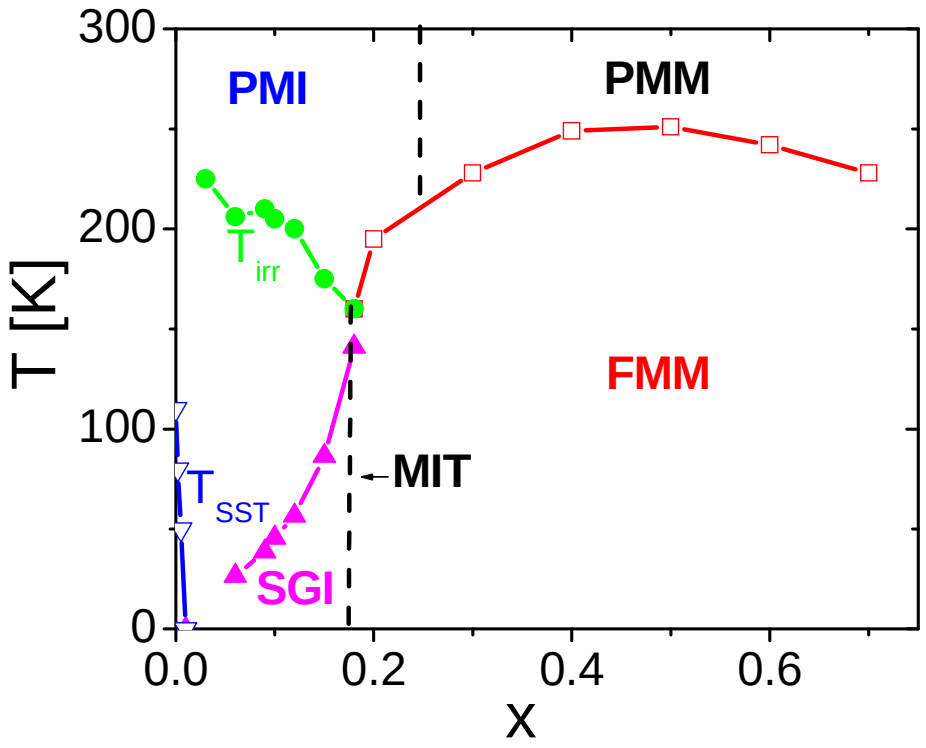


**Fig. 1.23** Magnetic phase diagram of $La_{1-x}Sr_xCoO_3$. PMI: Paramagnetic (PM) insulator, PMM: PM metal, FMM: FM metal, SGI: Spin glass insulator, MIT: Metal-insulator-transition, $T_{irr}$: Irreversible temperature, i.e splitting between zero field cooling (ZFC) and field cooling (FC) magnetization. $T_{SST}$: SST temperature. Reproduced from Ref. 105.

A similar phase diagram was also established by D. Louca *et al.* [117], which shared a lot of similarities at low doping as well as at high doping. However, the latter phase diagram illustrated quite an unnatural transition of the ordering temperature around the

critical doping range, i.e. $x \approx 0.18$. Nevertheless, it can be seen from both phase diagrams that the phase behavior of LSCO may be simpler than those of parallel manganites in certain aspects, as shown in Fig. 1.10. It can be seen that the phases of charge ordering, ferromagnetic insulating, as well as the long-range AF ordering are absent in LSCO, which makes it much easier to detect FM clusters in this system. This advantage together with other characteristics in LSCO, which will be discussed later in this section, makes LSCO a model system for the study of phase separation.

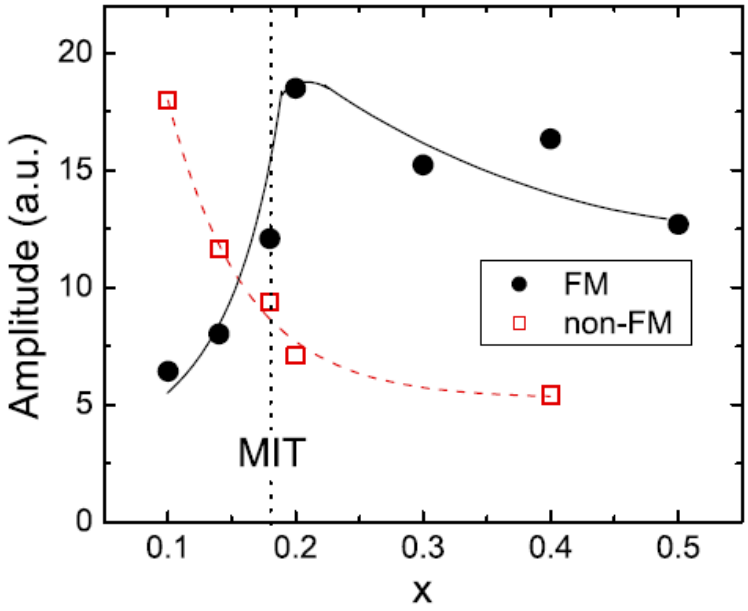


**Fig. 1.24** Doping dependence at 1.9 K of the integrated area of zero field NMR spectra (black closed circles), which corresponds to FM phase, and 102 MHz Gaussian 9.97 T NMR spectra (red open squares), which corresponds to non-FM phase, in $La_{1-x}Sr_xCoO_3$ Reproduced from Ref. 29.

The experimental evidence of phase separation can be explored by different techniques, as mentioned earlier. Fig. 1.24 shows the evidence obtained by P.L. Kuhns *et al.* via $^{59}$Co NMR [29] at low temperature (1.9 K) on bulk polycrystalline samples. The zero-field integrated signal of the NMR spectra probe only the FM phase since the internal magnetic field in FM phase will split the nuclear levels, which can be detected in the NMR spectra. The high field integrated area corresponds to the non-FM phase. It can be seen that there is coexistence of FM and non-FM phase at all dopings shown ($0.10 \leq x$

≤ 0.50). Starting from $x$ = 0.10, it can be seen that the non-FM phase dominates, however, there still exists some FM phase, indicating the possible presence of FM clusters. With increasing doping, the FM phase grows and the non-FM phase shrinks. At $x$ = 0.18, there is a crossover from dominant non-FM phase to dominant FM phase. At high dopings ($x$ > 0.18), the FM phase totally dominates. The phenomena of two-phase coexistence as well as the phase conversion tuned by doping are very well illustrated and also consistent with the phase diagram, as shown in Fig. 1.24.

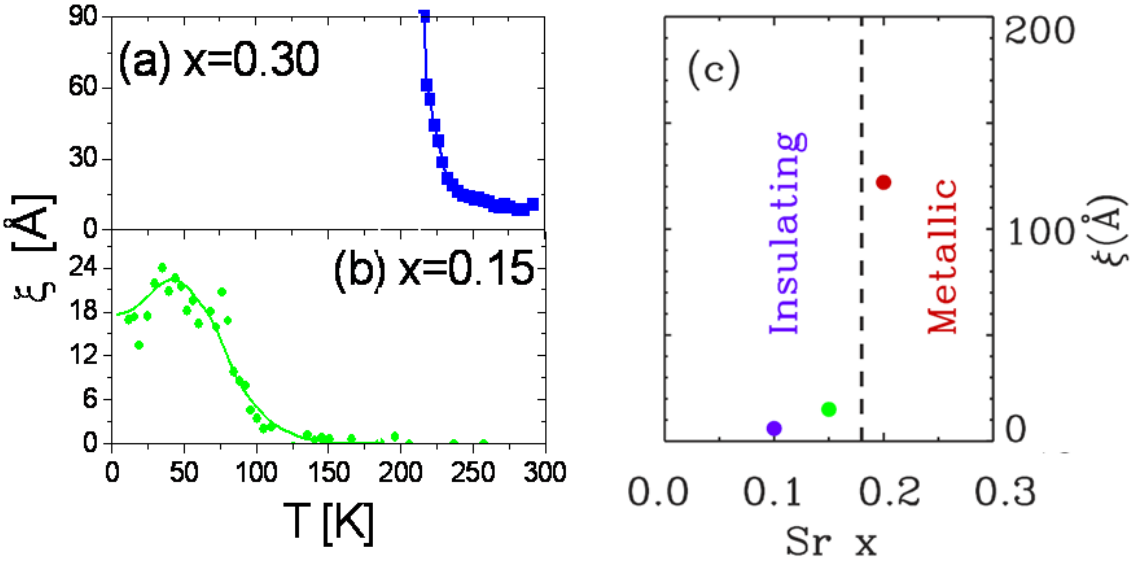


**Fig. 1.25** Temperature dependence of magnetic correlation length determined from SANS on (a) $x$ = 0.30, and (b) $x$ = 0.15 $La_{1-x}Sr_xCoO_3$ polycrystals. (c) Doping dependence of magnetic correlation length determined from INS at 8 K on $La_{1-x}Sr_xCoO_3$ single crystals. (a) and (b) are reproduced from Ref. 110. (c) is reproduced from Ref. 30.

Despite the clear evidence demonstrated by NMR, the information about the length scale of the MEPS in LSCO, or the size of FM clusters, is still missing. Such essential information was provided by SANS carried out on bulk polycrystalline samples by J. Wu *et al.* [110] and INS performed by D. Phelan *et al.* [30], as shown in Fig. 1.25. It can be seen from Fig. 1.25(a) that the magnetic correlation length (ξ) diverges at the Curie temperature at the high doping end of LSCO ($x$ = 0.30), indicating the system truly enters a long-range FM ordered regime, also confirmed by ND [103]. However, on the low doping end of LSCO ($x$ = 0.15), as can be seen from Fig. 1.24(b), ξ, a measure of the size

of the FM clusters, doesn't diverge. Instead, it persists to low temperature with a constant value about 2 nm. Such a result is validated by independent measurements by INS where ξ is directly determined through the inverse of the half width at half maximum of the diffraction peak in reciprocal space [30], as shown in Fig. 1.25(c) at low dopings, which also suggests the weak doping dependence of ξ. Such a fact, as well as the tunable density through doping, is another attractive feature of LSCO for the study of phase separation. Also, the isotropic scattering in the reciprocal space at the Bragg peak via INS by D. Phelan *et al*. [31], as shown in Fig. 1.26(a), indicates the shape of FM clusters is approximately spherical, i.e. they are "droplets". It can be seen that for $x$ = 0.15, the FM peak at (001) is isotropic, branching out along the (111) direction. Four satellite peaks along (111) are found, incommensurate with the lattice, which was ascribed by D. Phelan *et al*. to the seven-site cluster or magnetopolaron. This describes a hole introduced by Sr doping at a specific Co ion site, resulting in $Co^{4+}$, which is not fully localized at that site, instead, it is more or less shared by six nearest neighboring $Co^{3+}$ ions, forming a seven-site cluster, as shown in Fig. 1.26(b) [31]. Such a sharing mechanism leads to a slight dislocation of the hole from the Co sites and gives rise to magnetic peaks incommensurate with the lattice [31].

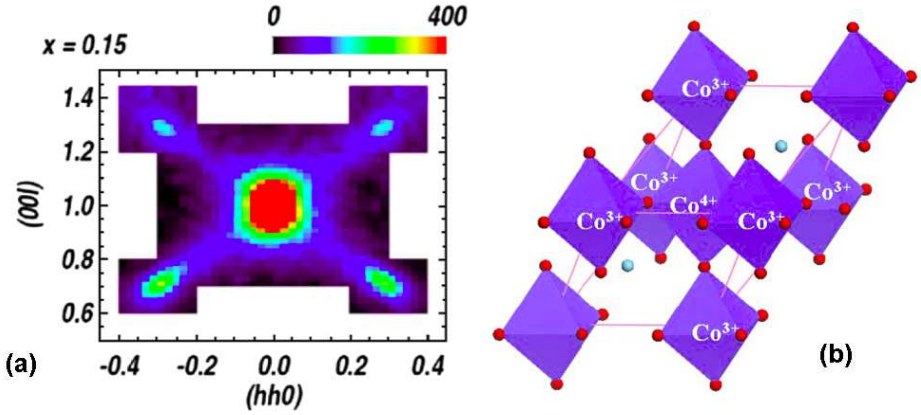


**Fig. 1.26** (a) Contour plot of neutron scattering at 8 K (after subtracting room temperature scattering background) in the (*hhl*) plane around (001) for an $x$ = 0.15 $La_{1-x}Sr_xCoO_3$ single crystal. The center peak corresponds to (001) Bragg peak and four weak satellite peaks along (111) corresponds are incommensurate with lattice, as discussed in the text. (b) Schematic illustration of seven-site magnetopolaron in real-space. Reproduced from Ref. 31.

The phenomenon of phase separation in LSCO, i.e. spontaneous formation of nanoscale FM metallic clusters in a non-FM insulating matrix at low dopings, is expected to have profound effects on the physical properties of LSCO. Fig. 1.27 shows one example of the many consequences: Intergranular giant magnetoresistance (GMR) was observed in $x = 0.15$ $La_{1-x}Sr_xCoO_3$ single crystals, as reported by J. Wu *et al*. [110]. It can be seen that a hysteretic MR effect persists to high field while demonstrating distinct differences between the virgin curve and the following field sweeps. The examination of the MR curve by the authors illustrates that the peak of the MR resides at almost exactly the coercive field determined from $M(H)$, suggesting close correlation between the transport and the magnetization. As hinted by the similar behavior in MR reported in artificial heterogeneous materials composed of FM clusters in a nonmagnetic matrix, such as Co-$SiO_2$ [118-120], spin dependent transport between FM clusters was proposed as the origin of such a MR effect in LSCO [110]. Such a hypothesis was confirmed by the temperature dependence of the MR, which is closely related to the formation the FM clusters as indicated by $\xi(T)$ [110], as well as the doping dependence of the MR at low temperature, which indicated such an MR approaches zero once the doping exceeds the MIT (all isolated clusters percolate) [110]. Two quantitative analyses carried out by the authors also arrived at the same conclusion. One of them is the scaling behavior of MR with magnetization $\{[\rho(H) - \rho(H_C)] / \rho(H_C)\} \propto -(M(H)/M_S)^2$ [120, 121], with $M_S$ being the saturation magnetization. The square of normalized magnetization is shown as the red line in Fig. 1.27 and the agreement of such a form is self-evident [110]. The other analysis performed is to test the $\rho = \rho_0 \exp(T_0/T)^{1/2}$ form of the insulating resistivity, which is also verified [110]. Therefore, such an MR effect is due to spin dependent inter-granular transport, which is dictated by the MEPS in LSCO, i.e. nanoscale FM metallic clusters embedded in an insulating nonmagnetic matrix. Unlike the artificial heterogeneous materials mentioned above, such a magnetic and electronic heterogeneity is spontaneously developed. Besides this, other consequences of MEPS are also observed experimentally, such as glassy magnetism at low dopings [105], glassy transport at low doping [122], FM cluster growth percolation at high magnetic field via INS [123], and the giant anomalous Hall effect [124,125].

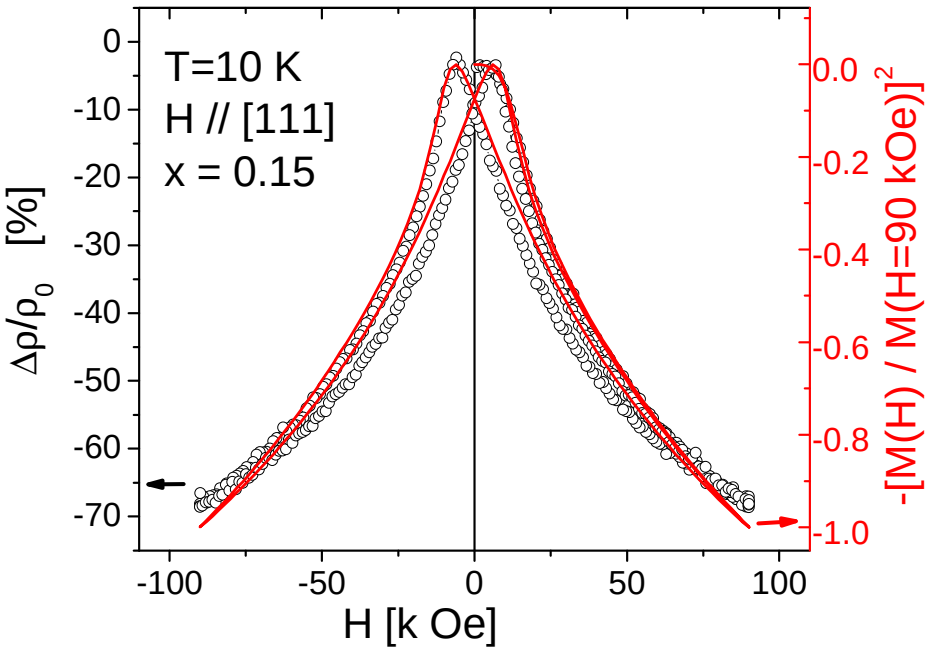


**Fig. 1.27** Magnetoresistance (MR) of an $x$ = 0.15 $La_{1-x}Sr_xCoO_3$ single crystal measured at 10 K with H parallel to [111] and perpendicular to the measuring current, after zero field cooling. Black open symbols represents the MR, while the red solid line represents M(H), as discussed in the text. Reproduced from Ref. 110.

In summary, LSCO forms nanoscopic (1-3 nm) hole rich clusters with strong FM intra-cluster correlations due to $Co^{3+}/Co^{4+}$ DE in a hole-poor non-FM insulating matrix at low $x$. The key advantages of such a system for the study of MEPS include: (a) the absence of long-range AF ordering at low doping, which simplifies the detection of FM cluster formation, (b) crystallographic simplicity, (c) the adoption of the same rhombohedra crystal structure ($R\bar{3}c$) for both the clusters and the matrix, (d) tunable FM phase fraction ($f_{FM}$) via doping, (e) the simple percolation nature of the metal-insulator transition (MIT) at $x \approx 0.18$, and (f) the phase separation always occurs on nanoscopic length scales. These attractive properties make LSCO an ideal model system for the study of nanoscopic MEPS.

In spite of the intensive studies on the MEPS in LSCO in the past decade, most of them focused on the phase separation and its evolution with doping at low temperature. Little work has placed an emphasis on the phase separation at high temperature. The discovery of a high temperature scale above the Curie temperature in manganites, which represents preformation of clusters, leads us to wonder if a similar temperature scale exists in LSCO. Caciuffo *et al*. [109] did report an observation of a high temperature anomaly (about 305 K) at a specific doping ($x$ = 0.3 powder) via the deviation from Curie-Weiss behavior, which was interpreted as entry into a "cluster-fluctuation regime". The subsequent SANS data were unfortunately dominated by chemical scattering but revealed a weak magnetic Guinier component, attributed to magnetic polarons [109]. However, such an experiment was limited to a specific doping and was not done to high enough temperature to illustrate the onset temperature of such a phase separation scenario, the systematic work on multiple doping measured to high enough temperature is still missing. In this thesis, efforts to try to fill such a gap by carrying out a systematic study of phase separation at high temperatures for the FM region of LSCO through multiple techniques, including transport, magnetometry, and SANS are made, which is discussed in detail in Chapter 4.

More importantly, and fundamentally, aside from the well established picture of phase separation in such a model system (through intensive phenomenological studies by different groups), a systematic study on all range of dopings aiming to uncover the origin of such a nanoscopic phase separation is lacking. In our group, the accessibility of complimentary experimental techniques, such as magnetometry, electrical and magneto transport, heat capacity, small angle neutron scattering, nuclear magnetic resonance (by collaboration), and scanning transmission electron microscopy (by collaboration), and the accessibility of the high quality single crystals at a wide range of dopings, provides us a unique opportunity to systematically study the phase evolution with doping in LSCO with the possibility of determining the origin of phase separation in LSCO. This will be thoroughly explored in the later chapters.

# Chapter 2

# Experimental considerations

## 2.1. Materials Fabrication

### 2.1.1 Polycrystalline materials fabrication: Solid state reaction

Polycrystalline bulk perovskite $La_{1-x}Sr_xCoO_3$ ($0.0 \leq x \leq 0.5$) was fabricated using a solid state reaction method. $La_2O_3$ (Alfa Aesar: 99.9%), $SrCO_3$ (Alfa Aesar: 97.5%), and $Co_3O_4$ (Sigma Aldrich: 99.8%, particle size < 10 micron) were used as starting materials. For $La_{1-x}Sr_xCoO_3$, the reaction proceeds as follows:

$$\frac{1-x}{2}La_2O_3 + xSrCO_3 + \frac{1}{3}Co_3O_4 + (\frac{1}{12}+\frac{x}{4})O_2 \rightarrow La_{1-x}Sr_xCoO_3 + xCO_2 \qquad (2.1).$$

Stoichiometric amounts of each reactant were weighed carefully on an electronic balance with a resolution of 0.1 mg. These reactants were then mixed together and ground thoroughly before being heated to and dwelling at 1000 $^oC$ for one week. To achieve homogeneous single-phase materials, intermediate grindings (2-3 times) were employed during this reaction period. The mixtures were then cooled and pressed into disks of thickness ~ 1 mm using a 0.5 inch diameter die under a 40,000 Lbs force at room temperature. The disks were then sintered in air at 1200 $^oC$ for 24 hrs and cooled to room temperature at a slow cooling rate of 0.5 K/min. X-ray diffraction was then used to ensure the materials prepared were single phase before and after the sintering process. Note that since $La_2O_3$ is hygroscopic, it is important to weigh prior to $H_2O$ absorption. This is accomplished through the standard procedure: Annealing for one day at 1000 $^oC$ and weighing before cooling to room temperature.

Fick's second law describes how materials diffuse over time in general. By solving such a diffusion equation, the diffusion length $l$ in solid state reaction can be determined, shown as below [1]:

$$l = 2\sqrt{Dt};\ D = D_0 \exp(-\frac{Q_d}{RT}) \qquad (2.2),$$

where $D$ is the diffusion coefficient and $t$ is the reaction time. $D$ can be calculated by the second part of Eq. (2.2), where $D_0$ is a temperature-independent constant, varying from material to material and usually falling in the range $10^{-5}$~$10^{-4}$ $m^2/s$ [2]. $Q_d$ is the activation energy, usually in the range 100 kJ/mol [2], $R$ is the gas constant, and $T$ is the reaction temperature. Thus the defined diffusion length provides a measure of over what extent intermixing occurs over a time period $t$. It can be seen from Eq. (2.2) that high reaction temperature $T$ is much more efficient than reaction time $t$ in increasing the diffusion length, justifying our choice of high reaction temperature (1000 $^oC$) and sintering temperature (1200 $^oC$). The criterion to determine appropriate reaction temperature and time interval is that the diffusion length should be larger than the particle size for each individual reactant. For example, as reported by M. Palcut [3], Co diffusion coefficient in $LaCoO_3$ was $1.40\times10^{-11}$ $cm^2s^{-1}$ at 1200 $^oC$, which results in diffusion length about 69.6 micron for one day sintering. Such a diffusion length is much larger than the particle size of $Co_3O_4$. As the materials have the tendency to develop oxygen deficiency under heating conditions, higher reaction and sintering temperature is avoided since it accentuates the problem of oxygen deficiency. Empirical reaction/sintering temperatures were chosen to be 1000 $^oC$/1200 $^oC$ since the fabricated materials under these conditions had been proved to be single phase.

It is important to address the issue of oxygen stoichoimetry in the sample preparation as it becomes a more and more severe problem with higher Sr doping. It is known that for $x$ = 1.0 $La_{1-x}Sr_xCoO_3$, it is impossible to fabricate fully oxygenated $SrCoO_3$ samples under ambient conditions [4-5]. Instead, it forms oxygen-deficient $SrCoO_{3-\delta}$ [4-5]. Oxygen stoichoimetry is important for two reasons. First of all, it will change the valences of Co ions. Compared to fully oxygenated $La_{1-x}Sr_xCoO_3$, oxygen deficiency will decrease the nominal ratio of $Co^{4+}/Co^{3+}$ from $\frac{x}{1-x}$ to $\frac{x-2\delta}{1-x+2\delta}$ in oxygen deficient sample $La_{1-x}Sr_xCoO_{3-\delta}$. Lower ratio of $Co^{4+}/Co^{3+}$ in oxygen deficient cobaltites will affect both their magnetic and electronic properties. For $x$ < 0.5, with increasing oxygen deficiency, the double exchange interaction between $Co^{3+}$ and $Co^{4+}$ will decrease, resulting in smaller saturation magnetization and Curie temperature. For $x$ = 1.0, oxygen

deficiency will drive a stoichiometric cubic structure $SrCoO_3$ (FM) to a BrownMillerite-type $SrCoO_{2.5}$ (antiferromagnet) [6], therefore, increasing oxygen deficiency will also lower the saturation magnetization and Curie temperature. It is observed that the Curie temperature and saturation magnetization are systematically lowered from 280 K and 2.1 $\mu_B$/Co for $\delta = 0$ [4-5] to 180 K and 0.67 $\mu_B$/Co for $\delta = 0.255$ [6]. H. Taguchi *et al.* observed from electrical resistivity measurements between 77 K and 300 K that, with increasing oxygen deficiency from $\delta = 0.04$ to 0.30, all samples showed metallic behavior with decreasing Curie temperature and monotonically decreased resistivity [5]. P. Bezdicka *et al.* found that the metallic behavior ($\delta = 0.0$) evolved into semiconducting behavior when more oxygen vacancies are introduced ($\delta = 0.5$) [6]. Second, oxygen deficiency in materials will change their lattice parameters. It has been reported that in $x = 1.0$ $La_{1-x}Sr_xCoO_3$, lattice constants linearly increase with increasing oxygen deficiency due to the decreasing ratio of $Co^{4+}$ concentration [3].

The reaction product $La_{1-x}Sr_xCoO_3$ has the tendency to evolve into an oxygen deficient sample under certain temperature and oxygen conditions, as expressed below:

$$La_{1-x}Sr_xCoO_3 \xrightarrow{T,P(O_2)} La_{1-x}Sr_xCoO_{3-\delta} + \delta/2\ O_2, \qquad (2.3).$$

It is important to control the reaction condition such that the net reaction goes in the desired direction (from right to left). High oxygen pressure and slow cooling rate favors such a net reaction, which justifies the procedure of slow cooling rate after the sintering process. It is also evident from the Eq. (2.1) that the higher the Sr doping, the more oxygen the ambient environment has to provide, therefore, the more severe the oxygen deficiency could potentially be. This suggests slower cooling rate for higher Sr doping or alternative method of using oxygen flow in the sintering procedure to increase the amount of oxygen the reaction needed. As a matter of fact, the claimed fully-oxygenated samples $x = 1.0$ $La_{1-x}Sr_xCoO_3$, can only be made by electrochemical oxidation [6-7] or under high oxygen pressure (e.g. several hundred atmospheres) [8].

### 2.1.2 Single crystal fabrication: Floating zone method

The single crystals of $La_{1-x}Sr_xCoO_3$ ($0.0 \leq x \leq 0.3$) were grown using the floating zone method in an NEC SC-15 HD optical mirror furnace at Argonne National Laboratory [9]. In the floating zone technique, polycrystalline samples are supplied in the form of a rod with one small fraction exposed to optical heating to form a floating molten zone, as shown in Fig. 2.1[10]. Since the small liquid molten zone is surrounded by two solid parts of the rod, like a floating drop, it is called the floating zone method [10]. By moving the heater with the sample rod fixed or moving the sample rod with the heater fixed, the molten zone can be moved along the rod. A single crystal can either be grown by spontaneous nucleation or by using a single crystal seed located at the bottom of the rod as the starting point of the growth.

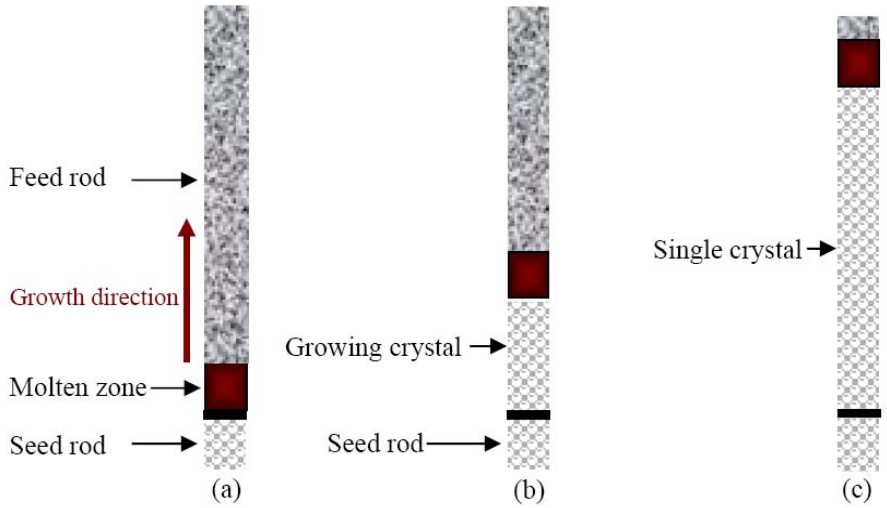


**Fig. 2.1** Schematic diagram of floating zone method: (a) Initial stage: Formation of the molten zone, (b) middle stage: Growth of single crystal along the rod, and (c) final stage: Molten zone moved to the end of the feed rod [10].

Fig. 2.2 shows the schematic experimental set up of crystal growth in an NEC SC-15 HD optical mirror furnace [11]. Two hemi-ellipsoidal mirrors are used to focus the light from the two high power Halogen lamps (1.5 kW) onto the sample to produce the molten zone, making the technique suitable for both conducting and non-conducting materials. The use of optical heating is particularly convenient and efficient for oxides and

semiconductors that absorb infrared easily [10]. During the crystal growth, the sample rod is rotated counter-clockwise to get uniform heating in the molten zone. Inside the image furnace, the sample is protected from air by a quartz tube, which also makes it possible to control the growth atmosphere and gas pressure around the growing crystal. The advantages of utilizing such a technique to grow single crystals include no crucible contaminations, high reaction temperature in the molten zone (up to 2100 $^{o}$C), controllability of growth atmosphere composition and pressure (usually using pure oxygen up to 10 bar), etc [11]. More details on the growth method can be found in ref.12.

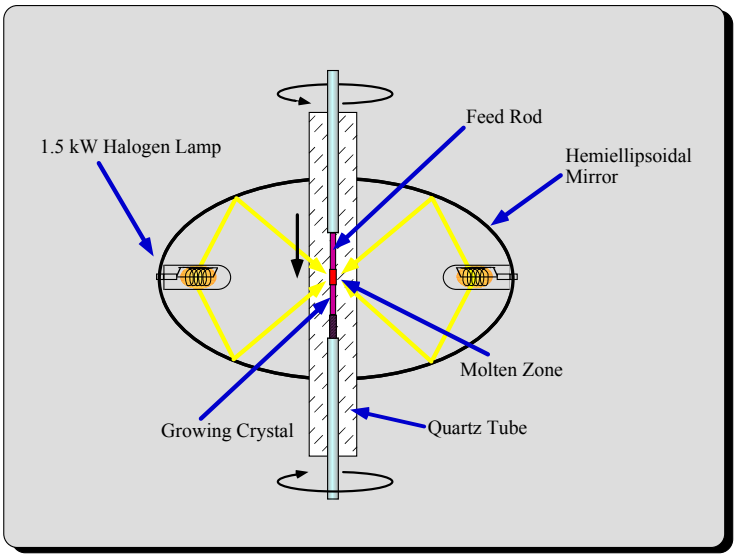


**Fig. 2.2** Schematic diagram of floating zone method in an optical mirror furnace with two hemi-ellipsoidal mirrors [11].

## 2.2 Structural and chemical characterization

The samples were characterized by x-ray and neutron diffraction, scanning electron microscopy (SEM), energy dispersive spectroscopy (EDS), and thermo-gravimetric analysis (TGA) [9]. Low resolution XRD was performed on the Bruker-AXS (Siemens) D5005 diffractometer with a 2.2 kW sealed Cu X-ray Source. High resolution XRD was taken on the Panalytical X'pert Diffractometer, and single crystal characterization was done on the Bruker-AXS Microdiffractometer with a 2.2 kW sealed

Cu X-ray Source at the Institute of Technology Characterization Facility at the University of Minnesota. TGA experiments were done at Argonne National Laboratory [9].

### 2.2.1 XRD: X-Ray Diffraction

#### (a) Bragg's law and powder diffraction

Being a form of electromagnetic radiation possessing a wavelength between 0.01nm to 10 nm, X-rays are useful tools to probe the structure of crystals, which usually have a spatial lattice periodicity on the order of angstroms. Bragg's law is shown as below:

$$2d\sin(\theta) = n\lambda \qquad (2.4),$$

where $d$ is the spacing between the planes in the atomic lattice, θ is the angle between the incident X-ray and the scattering planes, $n$ is the order of diffraction (an integer), and λ is the wavelength, as shown in Fig. 2.3. A peak emerges in the diffraction pattern when Bragg's law is satisfied and there is no systematic absence, which will be discussed later.

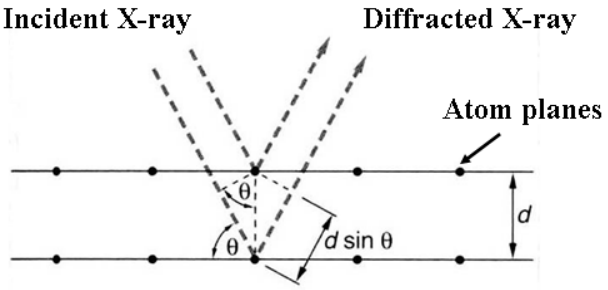


**Fig. 2.3** Schematic illustration of Bragg's law in X-ray diffraction

X-ray diffraction can be used to determine crystal structure since crystals are composed of periodic arrangement of atoms, i.e., scattering centers. Diffraction is the consequence of constructive interference (corresponding to maximum diffraction intensity), and destructive interference (corresponding to minimum diffraction intensity) from multiple sources. Using Bragg's law, the inter-planar spacing can be determined and the crystal structure can be deduced. First let us introduce the atomic form factor $f$, which is used to describe the ratio of the amplitude of the wave scattered by an atom to the amplitude of wave scattering by a single electron. In general, for X-rays, $f$ is proportional to $Z$, the atomic number, which leads to the difficulty of detecting light atoms like oxygen

atoms in X-ray diffraction. What is more important to reconstruct the crystal structure is the structure factor, which is directly related to the diffraction pattern. If the atoms in a unit cell are not identical, the structure factor is given by [13]:

$$S_K = \sum_{j=1}^{n} f_j(K)\, e^{iK\cdot d_j} \qquad (2.5),$$

where $n$ is the number of atoms in a unit cell, $f_j$ is the atomic form factor for the $j^{th}$ atom in the unit cell with the corresponding coordinates $d_j$, and $K$ is the reciprocal lattice vector ([h k l]**)**, which is the scattered wave vector when Bragg's condition is satisfied. Such a quantity describes the interference effect of scattered waves from different atoms within a unit cell. The scattering intensity is proportional to $|S_K|^2$. For some crystals with certain symmetry, it is possible for some reciprocal lattice vector [h k l] that the structure factor will just be zero, which produces systematic absences in the diffraction pattern, and will help to determine the crystal symmetry. Consider a body centered cubic material for example; if its unit cell is made of two atoms of one type, the structure factor can be calculated as $f(1+e^{i\pi(h+k+l)})$**,** which indicates the condition for a systematic absence will be $h + k + l$ = odd integers.

The structure of $La_{1-x}Sr_xCoO_3$ at low dopings ($x$ < 0.5) was determined to be rhombohedral with space group $R\bar{3}c$ by x-ray powder diffraction and neutron diffraction by J. B. Goodenough et *al.* [14, 15]. The standard procedures to determine the crystal structure in practice proceed as follow: (a) Measure the scattering intensity/position for each Bragg peak by XRD or neutron diffraction, (b) calculate the scattering intensity/position for each Bragg peak for possible crystal structures, (c) compare the calculated data with the measured data in terms of normalized scattering intensity and position, (d) the crystal structure is refined to the structure which gives the smallest discrepancy between the calculated data and the measured data. The parameter to describe the discrepancy between the calculated data and the measured data is called the crystallographic discrepancy index $R$, as expressed below [16, 17]:

$$R = \frac{\sum_{h\,k\,l} \left| I_{abs}(h\ k\ l) - I_{calc}(h\ k\ l) \right|}{\sum_{h\,k\,l} \left| I_{obs}(h\ k\ l) \right|}; I_{calc}(h\ k\ l) = Cm(h\ k\ l)P(\theta)\left|S(h\ k\ l)\right|^2 \qquad (2.6),$$

where $I_{abs}$ (*hkl*) and $I_{calc}$ (*hkl*) are the observed relative intensity and the calculated relative intensity at (*hkl*) Bragg peak, *C* is the scaling factor, *m*(*hkl*) is the peak multiplicity, *P*(θ) is the Lorentzian-polarization correction at Bragg angle θ, and *S*(*hkl*) is the structure factor. The lowest *R* indicates the best match between the symmetry used for the calculation and the real structure of the sample. In the case of $La_{1-x}Sr_xCoO_3$, the space group was shown to be $R\bar{3}c$ in $LaCoO_3$ using X-ray diffraction [14], and the same symmetry was shown in doped $La_{1-x}Sr_xCoO_3$ with doping up to 0.3, by neutron diffraction [15].

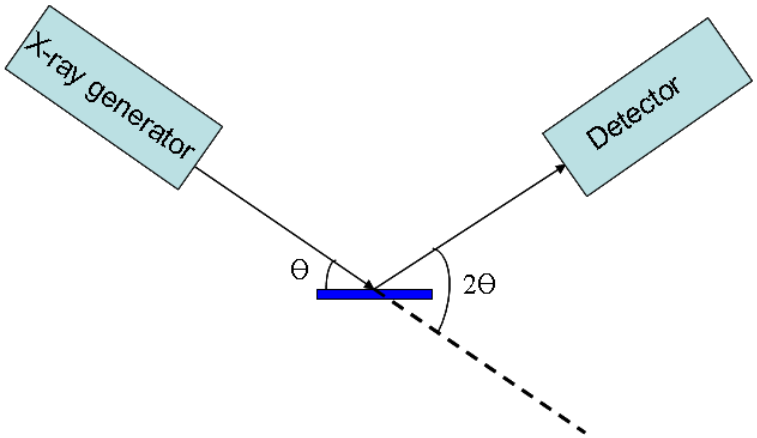


**Fig. 2.4** Schematic diagram of wide angle x-ray diffraction: θ-2θ coupled scan

In practice, wide angle X-ray diffraction of powder samples was done on the Bruker-AXS (Siemens) D5005 diffractometer with a 2.2 kW sealed Cu X-ray source (λ = 1.5406 Å). The θ-2θ coupled scan mode was used. Fig. 2.4 shows the schematic setup of a θ-2θ scan. In this scan mode, the sample and the detector rotate in a coupled fashion to ensure the X-ray scattering angle is twice the angle between the incident X-ray and the scattered plane in the samples. For powder and polycrystalline samples, because each grain has different orientation, when θ is scanned continuously. It is possible to probe all atomic planes in the samples, which show up as peaks in the diffraction pattern if no systematic absence is present.

The diffraction pattern is usually plotted as diffracted intensity versus 2θ angle. For example, the top two panels of Fig. 2.5 show the diffraction pattern of $LaCoO_3$ both before and after sintering. The standard way to check the phase purity of the samples is to

compare the pattern with the reported X-ray pattern of the same materials. For example, the third panel of Fig. 2.5 shows the X-ray pattern of $LaCoO_3$ reported by Closset *et al.* [18]. The excellent agreement between the two sets of the experimental data in terms of the position and the relative height indicates the single phase of the samples within the resolution of X-ray diffraction. It is important to check the possible existence of unreacted binary materials, i.e. $La_2O_3$ and $Co_3O_4$ in this case, and the most thermally stable oxides, CoO in this case. No peaks of $La_2O_3$, $Co_3O_4$, and CoO observed in the samples rule out the existence of unreacted binary materials within the detection limits of XRD.

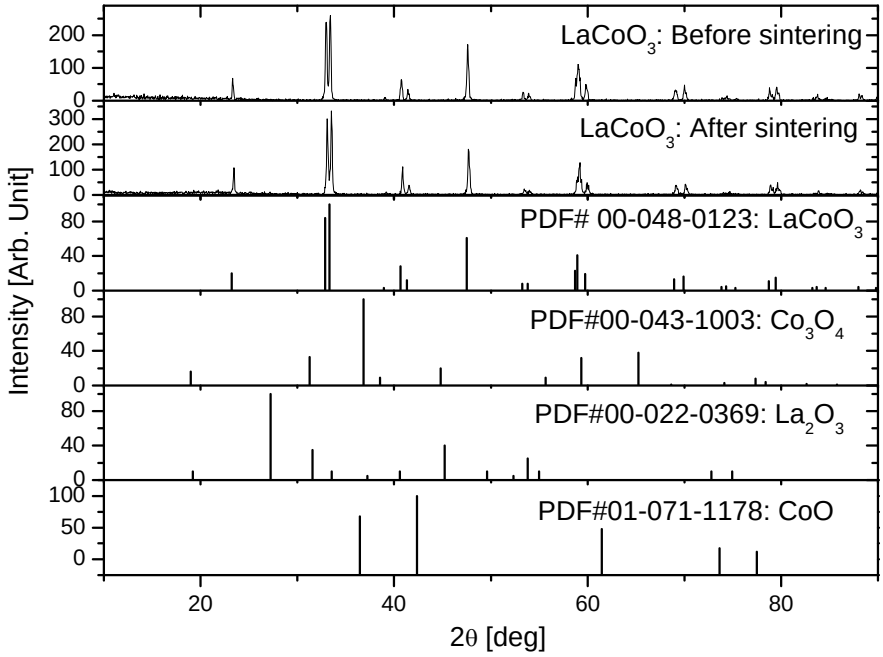


**Fig. 2.5** XRD patterns of $LaCoO_3$ powder samples in comparison with reported $LaCoO_3$ and binary materials XRD pattern [18].

In Fig. 2.6, evolution of X-ray diffraction with Sr doping is plotted for three different dopings $x$ = 0.1, 0.3, and 0.5. As mentioned in Chapter 1, $La_{1-x}Sr_xCoO_3$ is a rhombohedral structure material with space group $R\bar{3}c$ at low doping, which evolves into cubic structure with space group $Pm\bar{3}m$ when Sr doping $x$ is above 0.5, which is clearly

seen in Fig. 2.6. For example, (110) and (104) peaks, corresponding to two sets of d-spacings at low dopings $x$ = 0.1, and 0.3, eventually merges into a single peak (110) when $x$ = 0.5, which indicates only one set of d-spacing exists, a clear evidence of evolution from rhombohedral structure to cubic structure.

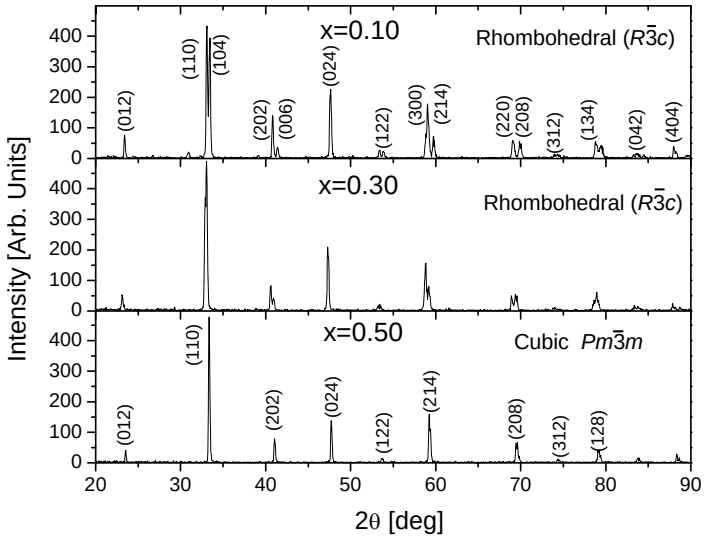


**Fig. 2.6** Evolution of XRD pattern with Sr doping in $La_{1-x}Sr_xCoO_3$

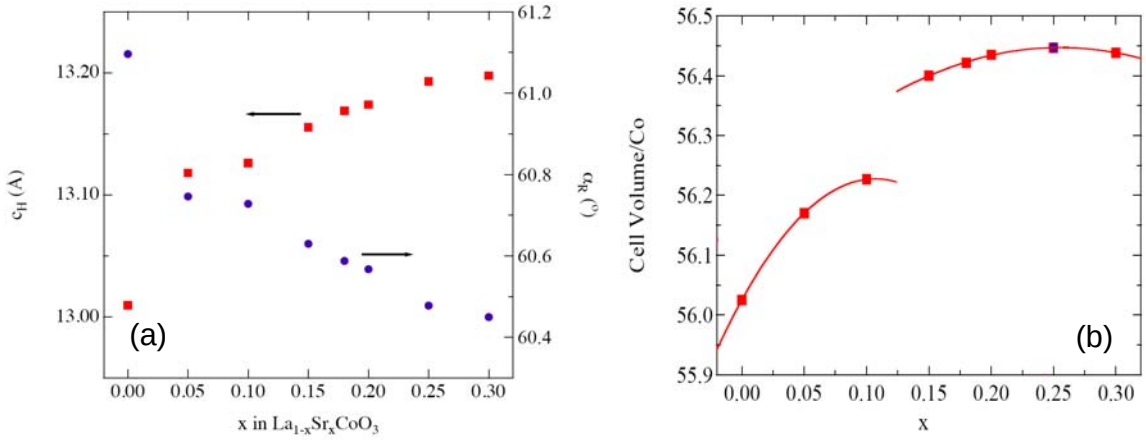


**Fig. 2.7** $x$ dependence of (a) $C_H$ axis of a hexagonal cell and rhombohedral angle $\alpha_R$, and (b) cell volume, in $La_{1-x}Sr_xCoO_3$ single crystals.

The crystallographic data in $La_{1-x}Sr_xCoO_3$ single crystals are shown in Fig. 2.7 [19]. The general trend of $x$ dependence of $C_H$ axis of a hexagonal cell as well as the rhombohedral angle $\alpha_R$ is in agreement with the data reported by Raccah and Goodenough [20]. It can be seen from Fig. 2.7(a), that $\alpha_R$ decreases and approaches to

$60^o$ (the value for cubic structure) with increasing $x$, clear evidence of structural evolution from rhombohedral structure into cubic structure. The most surprising feature is the discontinuity in slope between $x$ = 0.10 and 0.15, as observed from Fig. 2.7(b), suggesting a significant change in lattice structure around $x$ = 0.125. This will be returned later.

**(b) Microdiffraction**

In order to carry out magnetic anisotropy studies on $La_{1-x}Sr_xCoO_3$ single crystals, samples were aligned on the Bruker-AXS Microdiffractometer at the Institute of Technology Characterization Facility at the University of Minnesota, as shown in Fig. 2.8 [21].

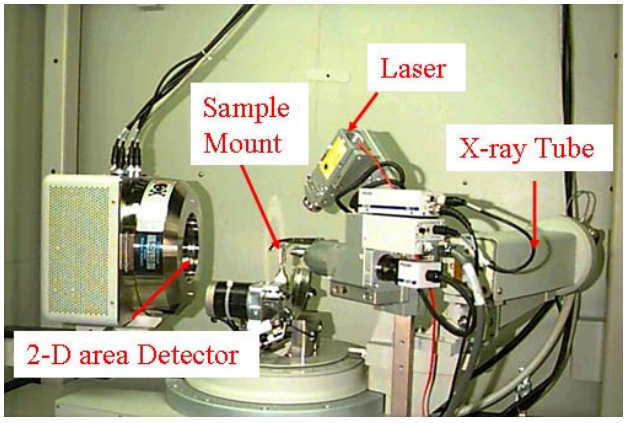


**Fig. 2.8** Bruker-AXS Microdiffractometer at IT Characterization facility at UMN [21]

One advantage of microdiffraction over wide angle X-ray diffraction is that it can measure small area samples. For this specific Bruker-AXS Microdiffractometer, the X-ray beam can be focused down to 50 micron in size with precise positioning through the combination of a video-microscope and laser pointer [21]. This microdiffractometer is operated with the 2.2 kW sealed Cu X-ray Source ($\lambda$ = 1.5406 Å), which includes an incident Beam Monochromater, a 1/4 circle Eulerian cradle sample holder and a Hi-Star 2-D area detector. The 2-D area detector allows for quick data acquisition and orientation information. General Area Detector Diffraction System (GADDS) is used to detect the diffracted signal. Being the key element of GADDS, the 2-D Area Detector is equipped with a large photon counter area. In the 2-D detector, the polycrystalline samples and

single crystals will be shown as Debye rings and spots respectively in terms of the diffraction pattern according to the Bragg's Law. As shown in Fig. 2.9, when a $La_{0.7}Sr_{0.3}CoO_3$ single crystal is aligned along [202] orientation, which indicates (202) planes are chosen as scattering planes, a single dot should be expected in the 2-D area detector at the expected 2θ value, 40.6 deg. The observed single dot at the expected 2θ value in the 2-D detector, as shown in Fig. 2.10, indicates the $La_{0.7}Sr_{0.3}CoO_3$ sample is perfectly aligned along the [202] orientation.

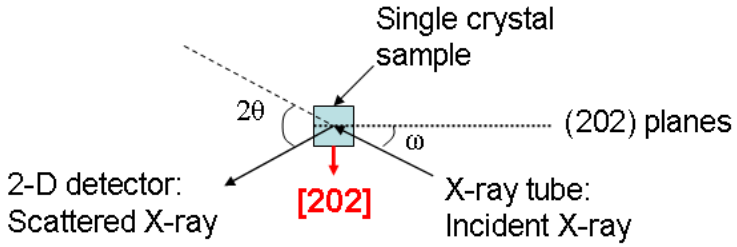


**Fig. 2.9** Schematic diagram of experimental setup (top view) when a $La_{0.7}Sr_{0.3}CoO_3$ single crystal is aligned along [202], which corresponds to (202) scattering planes.

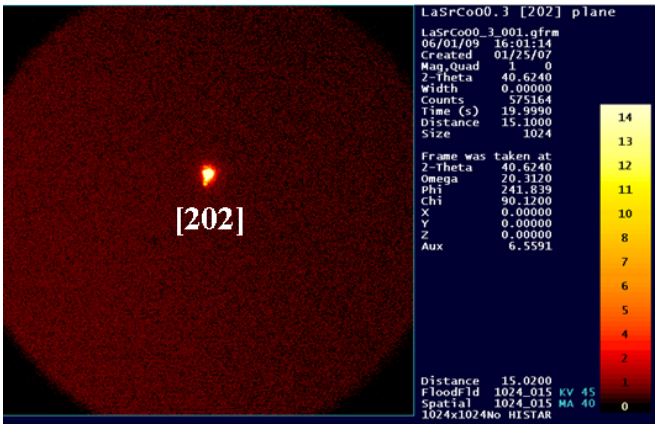


**Fig. 2.10** [202] diffraction patterns of a $La_{0.7}Sr_{0.3}CoO_3$ single crystal when (202) are chosen as scattering planes.

### 2.2.2 TGA: Thermogravimetric analysis

Thermogravimetric analysis (TGA) is an analytical technique used to determine the composition of materials and to predict their thermal stability by monitoring the weight change, and the related rate of change, as a function of temperature when the sample is heated in a controlled atmosphere. It is a useful technique to characterize materials

exhibiting weight changes. As materials are heated, some can lose weight due to drying, decomposition, evaporation, desorption, and dehydration; others can gain weight because of oxidation or absorption. These are kinetic processes associated with some weight change rates, which can be monitored and used to determine the materials compositions.

In practice, the samples of interest are placed into a sample pan that is supported on an analytical balance located outside a furnace chamber. The sample pan is heated inside the furnace with controlled atmosphere according to a preselected thermal cycle. The recorded weight signal measured from the balance as well as the sample temperature and the elapsed time is recorded and the TGA curve plots the TGA signal, in terms of the percent weight change on the Y-axis, against the sample temperature, or the elapsed time with a fix ramp rate, on the X-axis. Since each individual material corresponds to its own characteristic weight change curve, the sample composition can be determined by fitting the experimental data.

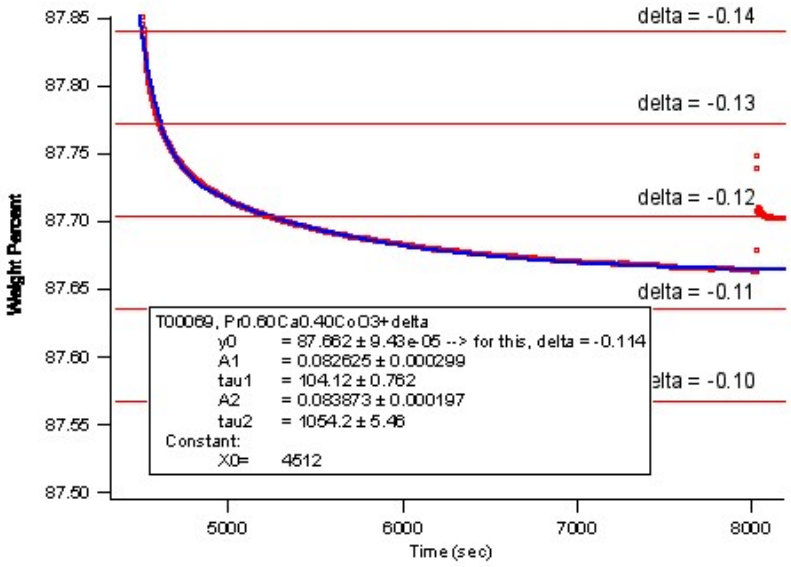


**Fig. 2.11** TGA fitting curve of a $Pr_{0.60}Ca_{0.40}CoO_3$ polycrystalline sample [19]

TGA was used to determine the oxygen content of cobaltites. The TGA curve of $Pr_{0.60}Ca_{0.40}CoO_{3+\delta}$ is shown in Fig. 2.11 as an example [19]. After heating to 900 $^oC$, $Pr_{0.60}Ca_{0.40}CoO_{3+\delta}$ will decompose into binary materials, which can be identified by XRD. In this case, the decomposed materials are $Ca_2O_3$, $Pr_6O_{11}$, and Co, shown as below:

$$Pr_{0.6}Ca_{0.4}CoO_{3+\delta} \xrightarrow{Heating} \frac{1}{5}Ca_2O_3 + \frac{1}{10}Pr_6O_{11} + Co + (\frac{13}{20} + \frac{\delta}{2})O_2 \quad (2.7),$$

By monitoring the weight loss (in terms of percentage) during the heating process, the oxygen content can be determined. It can be seen that the weight loss (oxygen in this case) is directly related to the oxygen content in this materials. Therefore, each individual oxygen content corresponds to a specific ending mass (the steady mass over a long time of heating), as marked as red lines in Fig. 2.11. The double exponential was only used to extract the ending mass. In this specific sample, it can be seen that δ lies between -0.11 and -0.12. Similar TGA measurements are done on $La_{1-x}Sr_xCoO_3$ crystals to ensure the samples used for experiments are oxygen stoichiometric.

## 2.3 Measurement techniques

### 2.3.1 SQUID magnetometry

Magnetometry measurements were done on a commercial Quantum Design system (MPMS XL model) with temperature ranging from 1.8 K to 800 K (with a sample space oven) and fields varying from ± 0.05 Oe (accomplished via a 10 Oe fluxgate) to 70 k Oe. The sensitivity can reach $10^{-8}$ emu when measurements are done on the AC susceptibility option or the Reciprocating Sample Option (RSO). Being the key element of the MPMS XL sample magnetometer, the Superconducting Quantum Interference Device (SQUID) technology utilizes the Josephson effect via the Josephson junction to measure the magnetic moments of samples as described below.

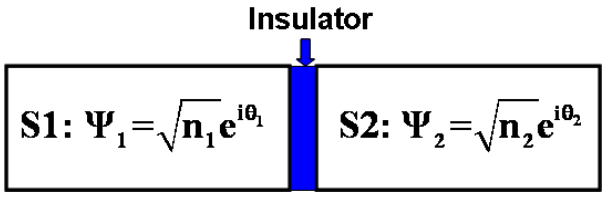


**Fig. 2.12** Schematic diagram of a Josephson junction

The Josephson effect refers to the phenomenon of current flow across two weakly coupled superconductors, separated by a very thin insulating barrier. This corresponding setup, two superconductors (S1 and S2) linked by a thin insulating layer, is known as a

Josephson junction, as shown in Fig. 2.12. The supercurrent tunneling across the insulating layer is called the Josephson current. These terms are named after Brian David Josephson, who predicted the effect in 1962 [22]. This effect was first confirmed experimentally in 1963 by P. W. Anderson and J. M. Rowell [23].

The Josephson effect is a macrospcopic effect of quantum mechanical nature, which includes two types: the DC Josephson effect and the AC Josephson effect. In the DC Josephson effect, a DC supercurrent will be induced across the junction without any application of voltage across the junction. The supercurrent is the tunneling of cooper pairs in the superconducting state. As shown in Fig. 2.12, the wave function in each individual superconductor, represented by $\Psi_1$ and $\Psi_2$, can be coupled to each other as long as the insulating layer is thin enough, which will introduce a phase difference in the wavefunctions across the junction. Using two identical superconductors for the purpose of simplicity, the DC supercurrent will be expressed as, $J = J_0 \sin(\Delta\theta)$ ($\Delta\theta = \theta_2 - \theta_1$). In the AC Josephson effect, an applied DC voltage $V$ across the junction will produce an AC supercurrent, $J = J_0 \sin[\Delta\theta(0) - 2eVt/\hbar]$, which is oscillatory with a frequency $\omega = 2eV/\hbar$.

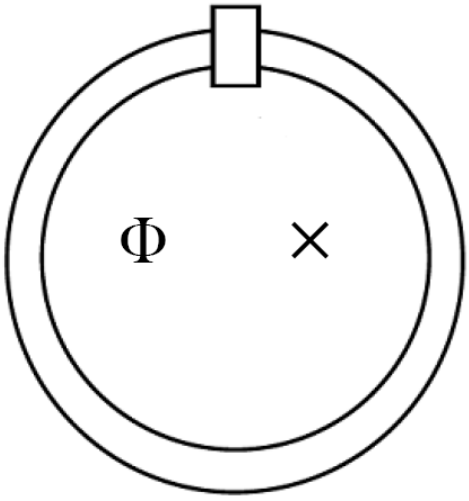


**Fig. 2.13** Schematic diagram of an r.f. SQUID made of one Josephson junction

In an r.f. SQUID, a Josephson junction is connected into a loop, as shown in Fig. 2.13. When a magnetic field is applied perpendicular to the loop, the phase of the supercurrent will depend sensitively on the magnetic flux Φ, as expressed below [13]:

$$J = J_0 \frac{\sin(\pi\Phi/\Phi_0)}{\pi\Phi/\Phi_0} \qquad (2.8),$$

where $\Phi_0 = h/2e$ is the quantum flux, and $J_0$ depends on the temperature and the structure of the junctions, but not on magnetic field. Such an equation means that the current will oscillate with the magnetic flux and enable a SQUID to be used as a sensitive measure of magnetic field. If the current is kept constant, the voltage across the circuit $V$ will be a periodic function with any flux applied to the SQUID. Using a locked-flux loop circuit [24], the $V$-$\Phi$ can be linearized and the magnetic flux can be directly determined from the output voltage $V$. Since the quantum of flux is extremely small ($2.07 * 10^{-15}$ Wb), the sensitivity of a SQUID can be high.

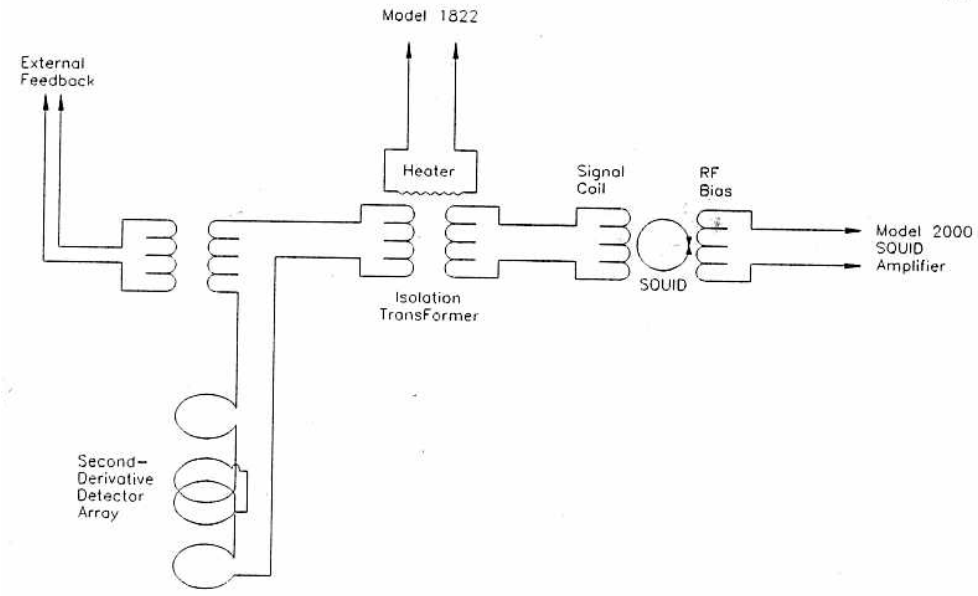


**Fig. 2.14** Schematic diagram of longitudinal SQUID detector system in MPMS

In the MPMS XL model system, the SQUID detection system is shown in Fig. 2.14, which includes the SQUID sensing loops, a superconducting transformer with a radio frequency interference (RFI) shield, the SQUID sensor, and control electronics [25]. The SQUID detection loops is a second-derivative coil set, which has the advantage of maximizing the field gradient from the signal of samples and minimizing distant noise sources such as power line noise, RFI, the earth's field, etc. The signals detected in the

second-derivative coils are coupled into the SQUID sensor through a superconducting RFI isolation transformer with a 3 dB rolloff frequency of about 20 kHz, which can screen very noisy RFI environments while performing a measurement [25]. During a measurement, the sample is moved inside the second-derivative coil and the detected signal is converted into SQUID voltage, as shown in Fig. 2.15. The magnitude of the sample moment can be calculated based on the amplitude of the SQUID voltage signal.

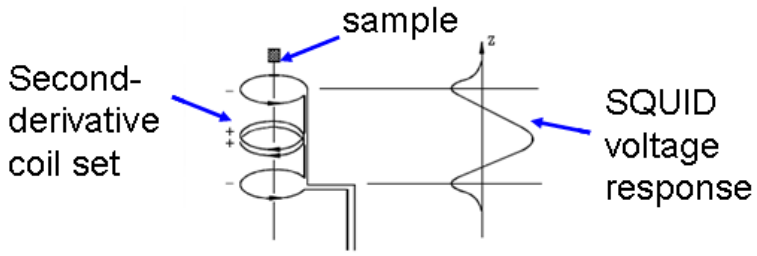


**Fig. 2.15** Sample measurement and measured SQUID response

### 2.3.2 Transport and magneto-transport measurements

Transport and magneto-transport measurements were done in a commercial Janis superconducting magnet (NbTi magnet) system using an AC resistance bridge at 13.7 Hz with fields up to 9 T and temperature ranging from 1.8 K to 500 K (using a home-made high temperature oven insert operating in the Janis system [26]).

#### 2.3.2.1 Temperature control

The temperature control is accomplished by the Janis Research SuperVariTemp (SVT) system [27], as shown in Fig. 2.16. Along the radial direction, from outside to inside, there is a vacuum jacket, a liquid nitrogen reservoir, another vacuum jacket, the liquid helium reservoir, the isolation tube and the sample tube. Such a design achieves low temperature in the sample tube by reducing the temperature gradient step by step and therefore reduces liquid helium boil-off. The vacuum jackets and the isolation tube has pressures down to $10^{-5}$ Torr to reduce the conductive heat load. The sample tube is linked to the liquid helium reservoir through a needle valve, and at the bottom of the sample tube there is a vaporizer incorporating with a heater. There are two thermometers in the

sample tube: One located close to the vaporizer, the other close to the sample mount reflecting the real sample temperature.

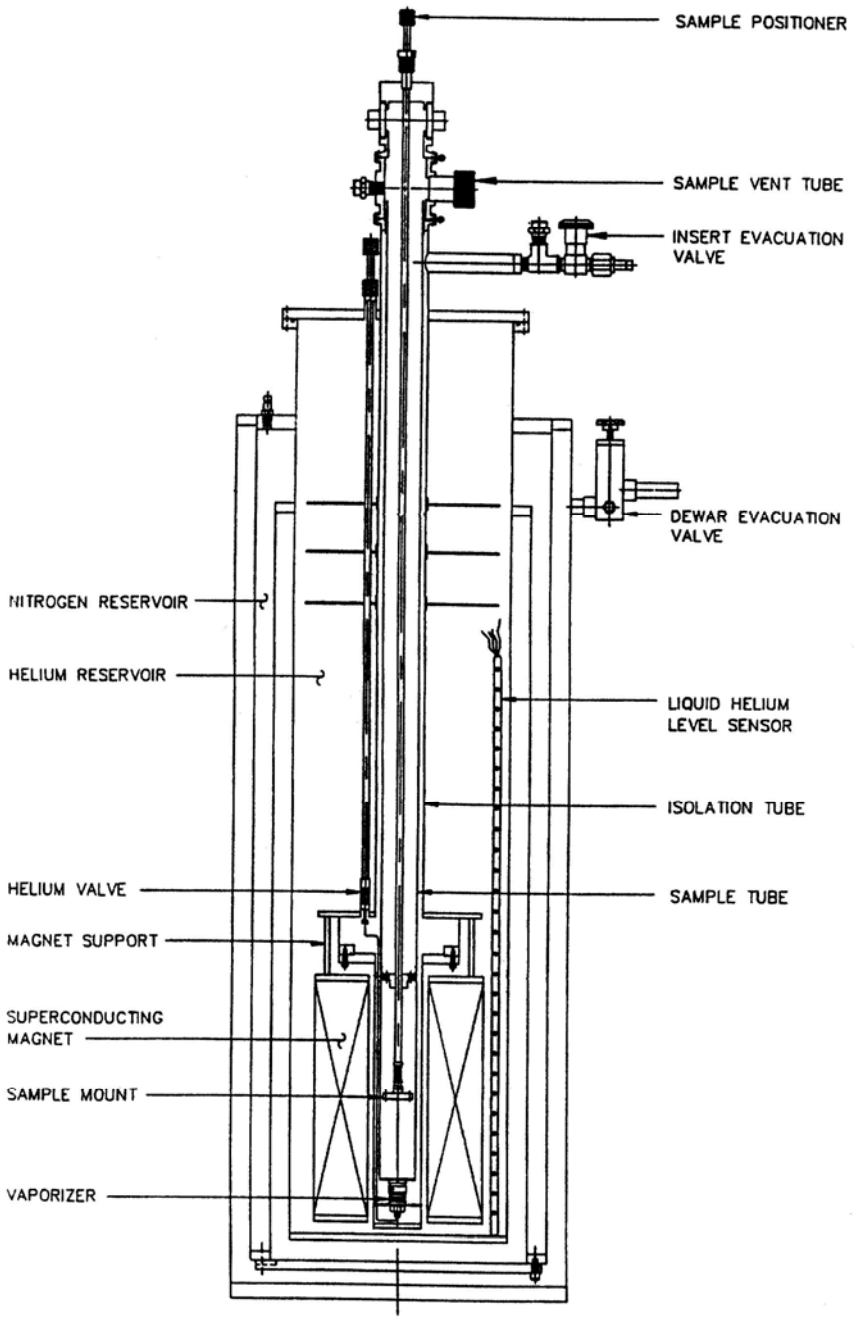


**Fig. 2.16** Cross sectional diagram of a Janis superconducting magnet system [27].

The temperature regulation is different for temperature below and above 4.2 K. For $T$ > 4.2 K, the temperature is controlled by adjusting the flow rate of helium vapor through a needle valve, the heater power in the vaporizer, as well as the heater power in the sample mount. For $T$ < 4.2 K, the needle valve is opened and the sample tube is filled with liquid helium until the sample is immersed in the liquid helium. Then the needle valve is closed. Temperature regulation is achieved by controlling the boiling temperature of liquid helium via controlling the pressure inside the sample tube through the mechanical pump attached to the sample tube. For temperature above room temperature, the high temperature oven insert needs to be used [26].

Below 200 K, a temperature sweep is achieved by controlling the vaporizer temperature, reflected from the vaporizer thermometer. About 2 K/ min ramp rate can be accomplished by turning on the heating power (about 20 % of 2.5 W power) in the vaporizer, therefore heating the helium vapor in the sample chamber, which in turn heats the sample. The sample temperature can then be read from the sample thermometer. Usually there is a lag between the vaporizer temperature and the sample temperature, the former being higher than the latter. Temperature sweep between 200 K and 300K is achieved by the combination of vaporizer heater power and the sample heater power. In this temperature range, the vaporizer heater power can be increased to about 20% of 25 W, and the sample heater can be adjusted within 1 W based on the difference of the set temperature and the actual temperature.

**2.3.2.2 Field control**

The field up to 9 T is generated by a NbTi magnet in the Janis superconducting magnet system, which stays in the superconducting state at 4.2 K in magnetic fields up to 9 T, as shown in Fig. 2.16 [27]. The field control is accomplished by a circuit made of a NbTi magnet and a persistent current switch (PCS), which contains a small length of superconducting wire wrapped with a heater, as shown in Fig. 2.17 [28]. The mechanism of field control goes as follows [28]: (1) Turn on the PCS by applying current to the heater, which will heat the PCS and drive it to the normal state, (2) charge the magnet (corresponding to the desired magnetic field) by ramping the power supply current, (3) turn off the PCS by removing the current through the heater, (4) turn off the power

supply. Now since both the PCS and magnet work in the superconducting state, they form a closed circuit without Joule heating, therefore without any current decay, resulting in a stable field once the persistent mode is entered. To remove or change the magnetic field, what needs to be done is to repeat step (1)-(4) and change the corresponding charging current in step (3).

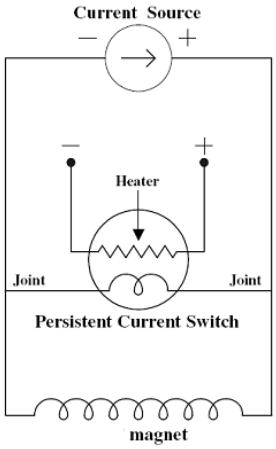


**Fig. 2.17** Schematic diagram of the circuit of a magnet with a PCS [28]

The field sweep can be achieved via the magnet power supply. The field to current ratio is 2236.3 G/A. For the field sweep below 67089 G, which corresponds to a 30 A charging current, the maximum current charging rate is 0.042 A/s (93.92 G/s) and the maximum charging voltage can reach 1.75 V. In practice, the charge voltage is usually smaller than 1 V. For the field sweep above 67089G, the maximum current charging rate is 0.024 A/s (53.67 G/s) and the maximum charging voltage is 1.0 V. In practice, for a field sweep up to 9 T, usually the sweep rate is fixed at 0.024 A/s to avoid changing the sweep rate at 6.7 T. The maximum field that Janis superconducting system can reach is 90011 G, corresponding to a charging current 40.25 A.

### 2.3.2.3 The van der Pauw method

The resistivity measurements were done using the four-terminal van der Pauw method [29-30]. For a sample with arbitrary shape with four contacts A, B, C, D on it (Fig. 2.18 (a)), it was shown that the resistivity of the sample can be calculated by [29]:

$$\rho = \frac{\pi d}{\ln 2}\left(\frac{R_{AB,CD} + R_{BC,DA}}{2}\right) f\left(\frac{R_{AB,CD}}{R_{BC,DA}}\right) \quad (2.9),$$

where ρ is the resistivity of the sample, $d$ is the sample thickness, $R_{AB,\,CD}$ ($R_{BC,\,DA}$) is the resistance when channel AB (BC) is used as the current path and channel CD (DA) is used to measure the voltage difference, $f\,(R_{AB,\,CD}/R_{BC,\,DA})$ is a function of $R_{AB,\,CD}/R_{BC,\,DA}$, as shown in Fig. 2.18 (b). In practice, $R_{AB,\,CD}/R_{BC,\,DA}$ should be smaller than 2 such that $f\,(R_{AB,\,CD}/R_{BC,\,DA})$ is larger than 0.95, very close to one. Such an equation holds for any sample as long as the sample has uniform thickness, a connected surface, i.e., no isolated holes or cracks, with small contacts, being one order of magnitude smaller than the sample size, located on the circumferences of the sample surface [29]. The advantage of the van der Pauw method is that it can measure the resistivity of a sample of arbitrary shape and can be used to check the anisotropy of the measurement.

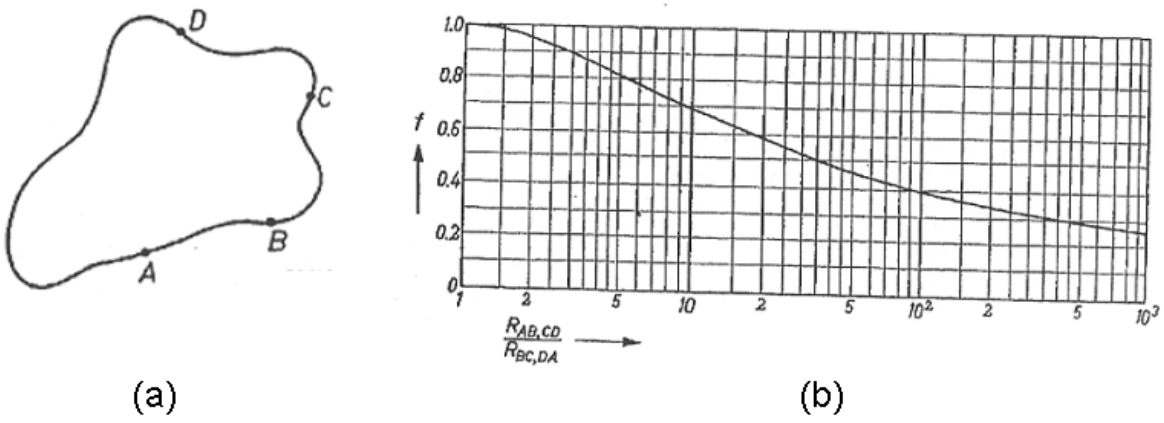


**Fig. 2.18** (a) Schematic diagram of a sample of arbitrary shape with four small contacts at arbitrary places along the circumferences, (b) $f$ plotted as a function of $R_{AB,\,CD}/\,R_{BC,\,DA}$ [29].

In practice, indium contacts (low $T$) or silver-loaded epoxy contacts (high $T$) were used when the van der Pauw geometry was employed. One important criterion for good contacts is that the two-terminal resistances should be very small and dominated by the wire resistances (around 40 Ω). For each two-terminal pair configuration, the resistances should be very close to each other. Ohmic behavior was checked down to low

temperature by checking the linearity of *I-V* curve. The measuring current should be chosen within the linear region of the *I-V* curve. Depending on samples, the measuring current is usually chosen to be smaller than 1mA to avoid self-heating effect by controlling the heating power below 1 μW, as a rule of thumb. For the measurement done above room temperature (with high temperature oven insert [26]), cooling and warming measurements were done to rule out the possibilities of introduction of oxygen deficiency due to heating, and an excellent agreement was achieved.

### 2.3.3 PPMS: Physical Property Measurement System

A commercial Quantum Design PPMS is used for heat capacity and torque magnetometry measurements. The PPMS used is a cryogenic system incorporated with a 9 T superconducting magnet, which accommodates different types of measurements, including heat capacity, torque magnetometry, AC transport, AC susceptibility, etc., with temperature ranging from 1.8 K to 400K and fields up to 9 T. Fig. 2.19 shows the schematic diagram of the PPMS probe [31]. In the sample chamber, a 12-pin connector is pre-wired to the system electronics at the bottom of the sample chamber. A removable sample insert or sample "puck" can be plugged and locked in the bottom connector for all types of measurement with the connection to the system hardware and software. Each specific type of measurement will be discussed in more detail in the following sections.

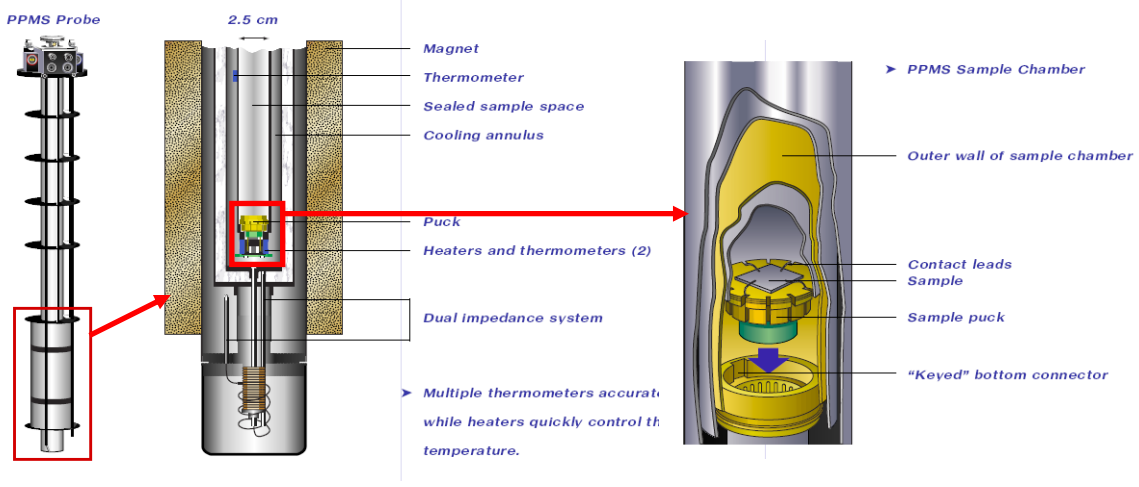


**Fig. 2.19** Schematic diagram of PPMS (Quantum Design) probe [31].

### 2.3.3.1 Heat capacity measurement

Heat capacity measurements were done on a Quantum Design PPMS with a heat capacity option, using the relaxation method [32]. Heat capacity of samples was measured with temperature down to 0.35 K (using a $He^3$ refrigerator) and fields up to 9 T. Heat capacity measurements are very useful to explore the lattice, electronic, and magnetic properties of materials and are particularly powerful for the study of bulk samples, as will be discussed in detail later.

#### 2.3.3.1.1 Experimental setup

The heat capacity at constant pressure is expressed as below:

$$C_P = (\frac{dQ}{dT})_P \qquad (2.10),$$

where $Q$ is the heat energy put into the sample system and $T$ is the sample temperature at fixed pressure $P$. The PPMS heat capacity option controls the heat applied to and removed from the sample while monitoring its temperature change. A measurement cycle includes a heating stage at a constant heating power for a fixed time length and a cooling period of the same duration without any heating power. For both the heating and cooling cycle, the monitored temperature of the sample can be fitted to the model that takes into account the thermal relaxation between a sample and the platform as well as the thermal relaxation between the platform and the thermal bath [32], which will be discussed in detail in the next section. Such a measurement technique is called *the relaxation method*.

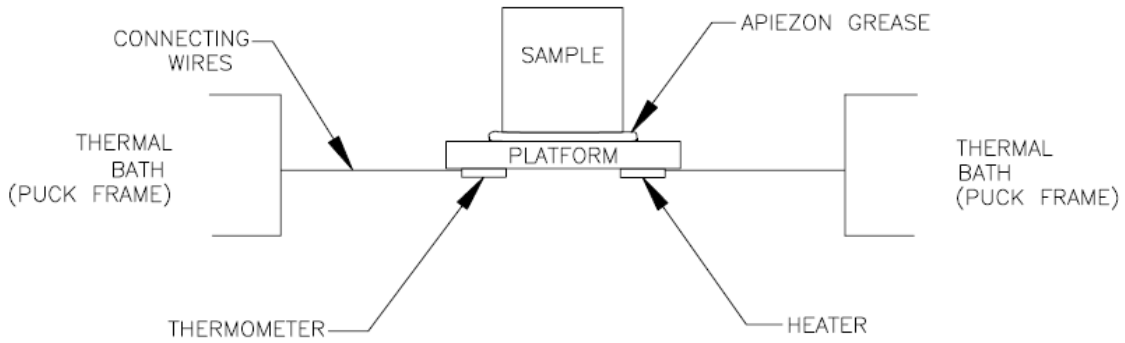


**Fig. 2.20** Schematic thermal connections to sample and sample platform of the heat capacity option in PPMS [32]

As shown in Fig. 2.20, a platform heater and a platform thermometer are incorporated to the bottom of the calorimeter chip that functions as the sample platform and the sample is mounted to the platform by using a thin layer of Apiezon N grease serving as the thermal contact to the platform due to its good thermal conductivity and adhesive quality. For measurements above room temperature, Apiezon H grease is recommended since Apiezon N grease melts above room temperature. Small wires provide the electrical connection to the platform heater and the platform thermometer and also provide the thermal connection and structural support for the platform [32]. The PPMS Cryopump High-Vacuum option provides a high vacuum (base pressure about 0.01 mTorr when high vacuum is activated) so that the conductance of the wires dominates the thermal conductance between the platform and the thermal bath. Therefore, it builds a reproducible heat link to the bath with a large time constant, which enables both the platform and the sample to achieve good thermal equilibrium during the measurement [32].

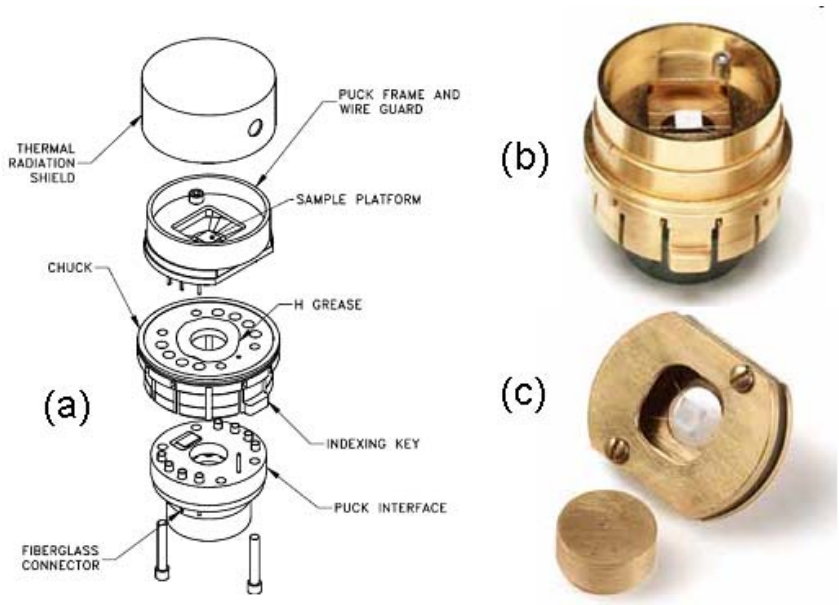


**Fig. 2.21** (a) Schematic view of a calorimeter puck, (b) picture of a regular puck, and (c) picture of a $He^3$ puck [32].

Fig. 2.21 (a) shows the structure of a calorimeter puck, which contains a resistive platform heater, a platform thermometer, and a puck thermometer [32]. Incorporated

within the puck, the puck thermometer is used to measure the puck temperature, the reflection of the calorimeter's thermal bath. The sample platform temperature and thus the sample temperature are measured by the platform thermometer. The sample platform is suspended in the middle of the puck by eight small wires, as can be seen from the picture of a regular calorimeter puck shown in Fig. 2.21 (b). Besides structurally supporting the platform, these wires also serve as the electrical channel as well as the thermal connection between the platform and the puck frame. In the case of the $He^3$ puck, only four smaller wires (compared to $He^4$ puck) support the platform, as shown in Fig. 2.21(c). Serving as the thermal contact to the bottom of the sample chamber, the chuck is positioned below the puck frame. The indexing key of the chuck is designed to drop into the indexing notch at the bottom of the sample chamber to lock the puck.

For a regular calorimeter puck, the temperature range of the measurement covers from 1.8 K to 400K. When even lower temperature measurements are required, a closed cycle $He^3$ refrigerator is used, which can reach temperature down to 0.35 K. This is because $He^3$, a different isotope to $He^4$, condenses at a lower temperature (about 3 K) than $He^4$, which condenses at 4.2 K. Through evaporative cooling, lower temperature (as low as 0.35 K) can be reached if the pressure above the liquid $He^3$ is maintained in the range of mTorr and the warmer surroundings are sufficiently isolated from the sample chamber [33]. The mTorr pressure is provided by the turbo pump mounted at the top of He-3 insert, which is backed by a small diaphragm pump. By sealing the He-3 insert into the sample chamber, good thermal isolation is accomplished when the high vacuum option is activated.

At low temperatures, it is difficult to accomplish good thermal contact between materials. Therefore, the contact wires are designed to reduce the thermal connection between the platform and the surroundings. As shown in Fig. 2.21(c), the calorimeter puck for the He-3 insert only has four wires possessing half the cross section area of the regular puck. Such a design effectively slows down the measurement and thus provides enough time for the system to accomplish better thermal equilibrium within a sample [33]. As a side effect, these extremely delicate wires are very easy to break. In practice, smaller samples were chosen to reduce the potential possibility of breaking a wire.

#### 2.3.3.1.2 Theoretical models for heat capacity measurement

Thermal models need to be employed to extract the heat capacity of the sample once one cycle of measurement is performed.

**(a) Simple model (single τ model)**

When good thermal contact between the sample and the sample platform is achieved, it can be assumed that the sample has the same temperature as the platform. The thermal diffusion equation can be expressed as [32]:

$$C_{Tot}\frac{dT}{dt} = -K_w(T - T_b) + P(t) \qquad (2.11),$$

where $C_{Tot}$ is the total heat capacity of the sample and sample platform, $T$ is the sample (platform) temperature, $t$ is the measurement time, $K_w$ is the thermal conductance of the wires, $T_b$ is the temperature of the thermal bath (puck), and $P(t)$ is the power supplied by the heater. The heater power $P(t)$ is a step function, which is fixed at $P_0$ during the heating stage and is removed during the cooling period, as shown in Fig. 2.22 (a).

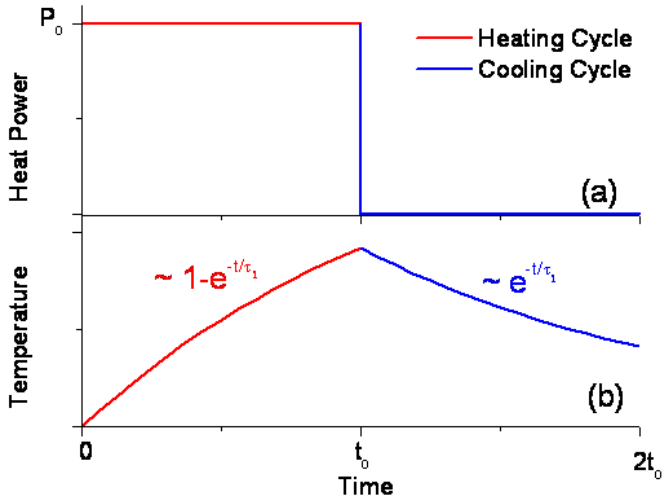


**Fig. 2.22** Time evolution of (a) heating power, (b) sample temperature during a cycle.

The solution to this equation is given by exponential functions with a characteristic time constant $\tau_1$ equal to $C_{Total}/K_w$, as shown in Fig. 2.22 (b). By fitting the recorded

platform temperature to the solution to Eq. (2.11), time constant $\tau_1$ can be extracted. Combined with the $K_w$ value obtained during a calibration, the total heat capacity can be determined. By subtracting the contribution from the addenda coming from the platform and the grease, the sample heat capacity can be calculated. Such a simple model is usually employed during the addenda measurement and for samples that possess good thermal contact with the sample platform. Fig. 2.23 (a) shows a typical addenda heat capacity data prior to a sample measurement.

**(b) Two-tau model.**

Such a model is usually used when poor thermal contact between the sample and the platform exists or when a large sample results in a temperature difference between the sample and the platform [32]. By considering the heat flow between the sample and sample platform as well as the heat flow between the sample platform and the puck, the thermal diffusion equation can be expressed as below [32]:

$$C_P \frac{dT_P(t)}{dt} = P(t) - K_w(T_P(t) - T_b) + K_g(T_S(t) - T_P(t)) \quad (2.12),$$

$$C_S \frac{dT_S(t)}{dt} = -K_g(T_S(t) - T_P(t)) \quad (2.13),$$

where $C_S$ ($C_P$) is the heat capacity of the sample (sample platform plus the grease), $T_S$ ($t$) ($T_P$ ($t$)) is the temperature of the sample (sample platform), $K_w$ is the thermal conductance of the wire, and $K_g$ is the thermal conductance between the sample and sample platform. It can be seen that when there is no temperature difference between the sample and the sample platform, the two-tau model is reduced to the simple model containing just one time constant $\tau_1$.

By fitting the recorded platform temperature with the two-tau model, two time constants can be extracted as below [32]:

$$\tau_1 = \frac{1}{\alpha + \beta}; \tau_2 = \frac{1}{\alpha - \beta} \quad (2.14),$$

$$\alpha = \frac{K_w}{2C_P} + \frac{K_g}{2C_P} + \frac{K_g}{2C_S} \quad (2.15),$$

$$\beta = \frac{\sqrt{(K_g C_S)^2 + 2K_g{}^2 C_P C_S + (K_g C_P)^2 + (K_w C_S)^2 + 2K_g C_S{}^2 K_w - K_g K_w C_P C_S}}{2C_P C_S} \quad (2.16).$$

The heat capacity of samples can then be derived from the obtained two tau values by subtracting the heat capacity of the addenda, which is obtained using the simple model during addenda measurement and will be discussed in the next section. Fig. 2.23(b) shows an example of heat capacity of a $La_{0.76}Sr_{0.24}CoO_3$ crystal.

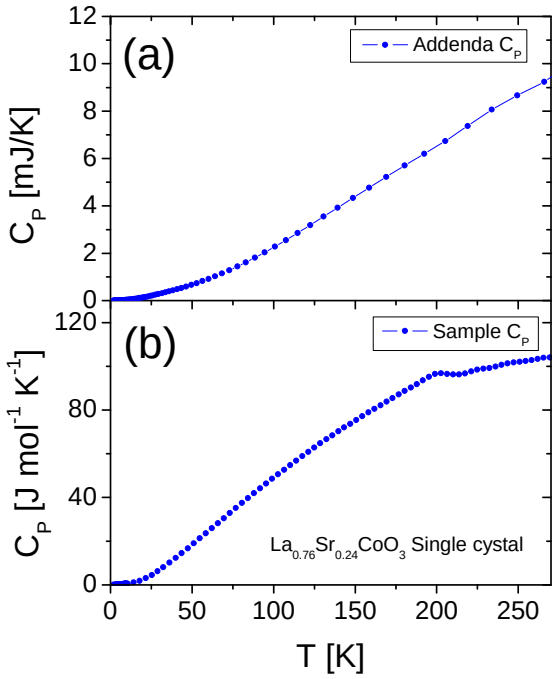


**Fig. 2.23** Example of (a) addenda $C_P(T)$ prior to the sample measurement, and (b) sample $C_P(T)$ of a $La_{0.76}Sr_{0.24}CoO_3$ crystal during a typical sample measurement cycle.

#### 2.3.3.1.3 Heat capacity measurement procedures

To determine the heat capacity of a sample, three procedures need to be performed: Puck calibration, addenda measurement, and sample measurement.

The puck calibration only needs to be done once for a specific puck, regardless of the type of calorimeter (He-3 or regular puck). During the calibration, the conductivity of the puck wires and the temperature-dependent resistance of the platform heater, the platform thermometer, and the puck thermometer are measured. The measured values are stored in

a calibration table, which will be used for every single measurement associated with the same puck. These parameters are indispensible for solving the thermal diffusion equation. If a measurement is performed in a magnetic field, the puck has to be calibrated in the same field if it has not been done before, since the corresponding parameters, such as the conductivity of the wires, and the resistances of heater and the thermometers are not only temperature dependent, but also field-dependent.

Once puck calibration is done, the addenda measurement needs to be performed prior to a sample measurement. During an addenda measurement, a small amount of grease is applied on the center of the platform and the total heat capacity of that small amount of grease and the sample platform is measured. The addenda heat capacity limits the size of the smallest sample. Measurement accuracy is also affected when the sample heat capacity is small compared to the addenda heat capacity. So it is important to adjust the amount of grease applied in practice, which should be dictated by the size and geometry of the sample. Too much grease leads to poor thermal diffusivity and thus a poor addenda measurement, which results in inaccurate sample heat capacity afterwards. Unlike the calibration process, for every sample measurement, a new addenda measurement is required.

After the addenda measurement is done, the sample measurement can be continued. Before mounting the sample on the platform, it is important to examine the sample and locate its flattest side since any surface irregularities will influence the thermal contact between the sample and the sample platform and therefore the measurement accuracy. The flattest side should be used as the surface in contact with the grease since it can get the best thermal contact. It is important to polish the flattest side of the sample if necessary and weigh the mass of the sample before performing the measurement. It is critical to preserve the exact amount of grease during an addenda measurement when mounting the sample, which requires extreme care.

#### 2.3.3.2 Torque magnetometry

Torque measurements were done on a commercial Quantum Design PPMS torque magnetometer option. Torque magnetometry is a useful tool for determining the magnetic

properties of materials, especially for the magneto-crystalline anisotropy study of materials, which will be discussed in chapter 4.

**2.3.3.2.1 Experimental setup**

The torque magnetometer is based on the principle that the torque experienced by a sample in a magnetic field $\vec{B}$ is proportional to its magnetization $\vec{\tau} = \vec{m} \times \vec{B}$ and the derivative of the anisotropy energy towards the angle θ between the magnetic field and the moment. Fig. 2.24 shows the schematic view of a torque-lever chip used in PPMS [34]. For the PPMS torque magnetometer, a piezoresistive technique is employed during which the torsion of the torque lever about its symmetry axis is measured [34]. In the presence of a magnetic field, the torque felt by the sample, which is mounted on the chip, will twist the torque lever. The torque lever possesses a continuous piezoresistive path, which includes two grids patterned on the legs of torque lever in the region of high stress. By measuring the resistance change of the piezoresistive grids, $\Delta(R_2\text{-}R_1)$, via a Wheatstone bridge circuit integrated on the chip, the torque signal can be detected. Originated from the mechanical stress driven by the magnetic torque in each leg, the resistance change can be converted to the torque, which will be discussed in the next section.

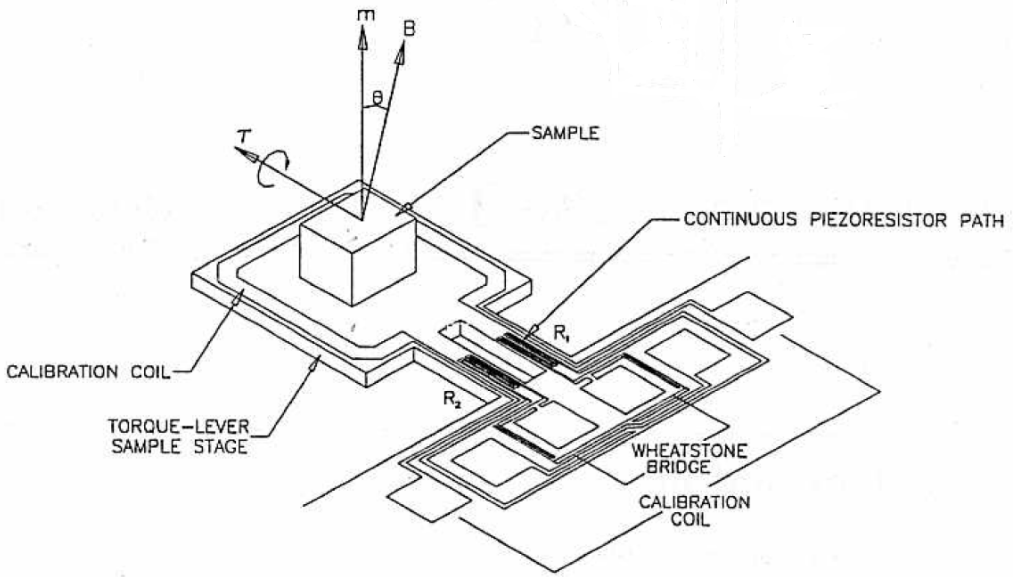


**Fig. 2.24** Components on a torque-lever chip in the Quantum Design PPMS torque magnetometer option [34]

Fig. 2.25 shows the detection circuit incorporated in the torque lever chip via a Wheatstone bridge configuration [34]. By comparing the resistance of the two piezoresistive grids with the two precision resistors possessing closely matching resistance values, the resistance of the grids can be measured. By driving a current into the bridge and measuring any out-of-balance resistance developed across the bridge, the differential resistance in the piezoresistor grids can be measured, which is induced by a magnetic torque. To reduce the noise level and the magneto-resistive effect, a ratiometric measurement of the Wheatstone bridge is used. Such a measurement measures the imbalance and the absolute total resistance of the bridge and calculates the ratio of those two (imbalance resistance to total resistance). Then the torque can be derived by the combination of the resistance ratio and the torque coefficient obtained during a calibration run, which will be discussed in the next section.

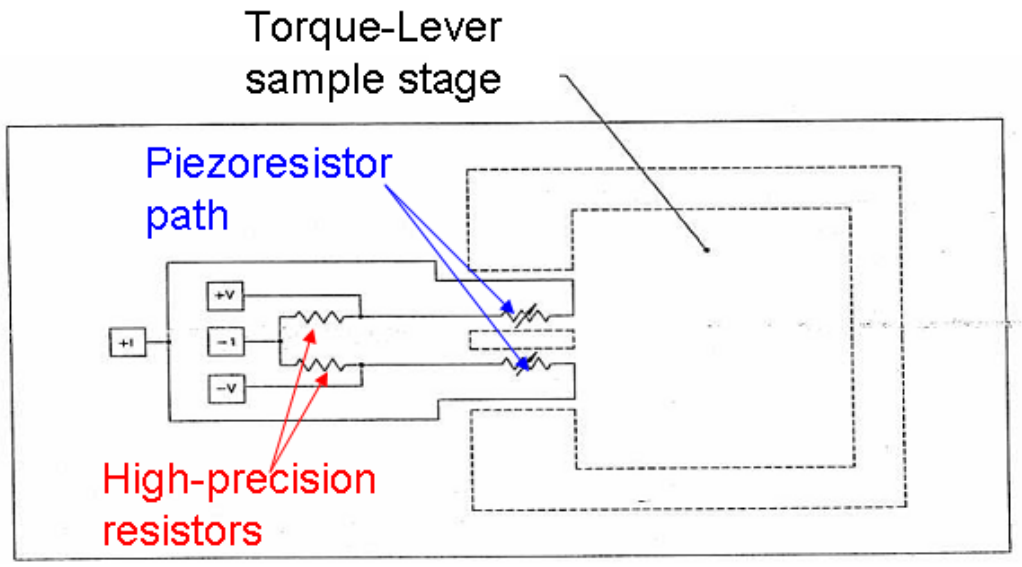


**Fig. 2.25** Circuit diagram of a Wheatstone bridge in a torque-lever chip [34]

Before doing a measurement, a small amount of Apiezon N grease or Apiezon M grease is applied to the center of the torque-lever sample stage and the sample is mounted on the torque lever chip, as shown in Fig. 2.26 (a). The chip with sample is then mounted on the platform board assembly, as shown in Fig. 2.26 (b), by loosening the brass screws

to lower the backing supporting plate and position the chip on the plate such that the six electrical pads are in good contact with the six copper contact springs on the platform board assembly. Once the chip is mounted on the platform board assembly, the backing supporting plate can be tightened. Then the platform board assembly can be mounted on the horizontal rotator, as shown in Fig. 2.26(c). Then the horizontal rotator can be installed in the sample chamber to do the measurement.

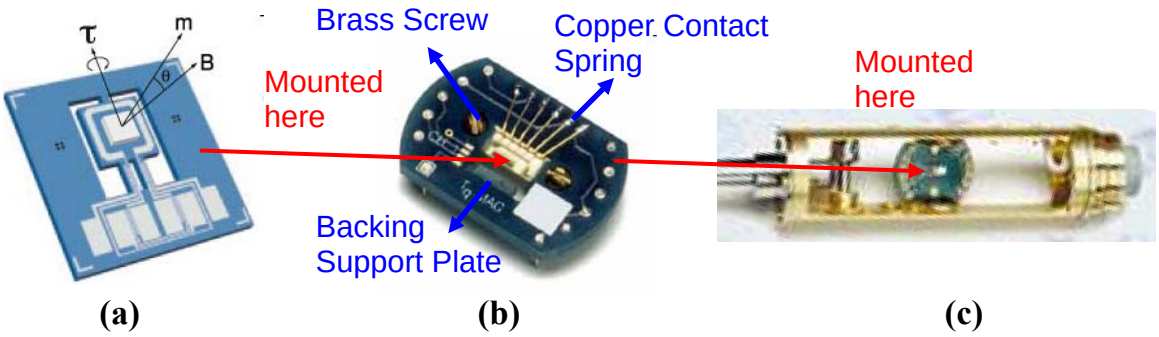


**Fig. 2.26** Mounting procedures: (a) Mount a sample on the torque-lever chip, (b) mount the torque lever chip on the platform board assembly, and (c) mount the platform board assembly on the horizontal rotator.

#### 2.3.3.2.2 Theory of calibration and measurement

During a calibration, a magnetic torque $\tau_{coil}$ produced by the calibration coil, i.e., a copper coil loop on top of the torque-lever chip, as shown in Fig. 2.24, can be used as a calibration standard for the torsion of the torque lever. The torque-lever chip is positioned so that the calibration coil is perpendicular to the applied magnetic field to reach the maximum torque at a given temperature and a given current (typically ±1.96 mA). The recorded resistance ratio can be used to calculate a torque coefficient. The magnetic moment associated with the calibration coil and the torque produced is expressed as [34]:

$$m_{coil} = I_{coil} A_{coil}; \tau_{coil} = I_{coil} A_{coil} B \sin(\theta) \qquad (2.17),$$

where $I_{coil}$ and $A_{coil}$ are the current through the calibration coil and the area of the calibration coil, and $B$ is the applied magnetic field, and θ is the angle between the

magnetic moment of the calibration coil and the applied field. The torque coefficient is determined as [34]:

$$C_{\tau}(T) = \frac{2\tau_{coil}}{\Delta\left(\frac{R_1(T) - R_2(T)}{R_{bridge}(T)}\right)} \tag{2.18}.$$

The excitation current is usually limited to < 2mA during a typical calibration to avoid heating the torque lever. As can be seen from Eq. (2.18), torque coefficient is temperature dependent due to the temperature dependence of piezoresistor grids and the total resistance of the bridge. During a calibration, the calibration temperature range should be chosen with minimum temperature down to 1.8 K and maximum temperature up to 300 K. Maximum field strength is recommended to use during a calibration since it produces the maximum torque.

Once the torque coefficient is determined during the calibration, the imbalance-to-resistance ratio is recorded during the sample measurement, which can be converted into the torque of the sample:

$$\tau_{sample}(T) = C_{\tau}(T) \times \left(\frac{R_1(T) - R_2(T)}{R_{bridge}(T)}\right)_{sample} \tag{2.19}.$$

It is worthwhile to point out the imbalance-to-resistance ratio of the sample is zero-torque background resistance ratio subtracted, which will be discussed in detail in the next section. Fig. 2.27 shows an example of torque curve for a $CoS_2$ crystal (1.5 mg). It can be seen that at high magnetic field, the torque saturates. More discussions of the data analysis will be returned in Chapter 4.

**2.3.3.2.3 Torque measurement procedures**

As mentioned earlier, during a calibration, a small amount of grease is applied to the chip. Special attention has to be taken to avoid getting grease on the copper contact springs. All these procedures are done under a microscope. A calibration process includes two stages: One measures the imbalance-to-resistance ratio of the Wheatstone bridge at zero field during the cooling down process, the other measures the differential ratio of

bridge at the set maximum field during the warming up process and calculates the torque coefficient at each temperature. During the first stage, the imbalance-to-resistance ratio is recorded while cooling, which serves as the background and will be subtracted from the resistance ratio during a sample measurement. Such a procedure is done to minimize the temperature and magneto-resistance effects caused by the wires in the rotator and the PPMS probe. The second stage starts during a warming up measurement once the base temperature is reached and the maximum field is stable. At each sampling temperature, both a negative and a positive excitation current with magnitude 1.96 mA is driven through the calibration coil, the resistance ratio can be recorded and the differential ratio is calculated, which is the origin of the factor 2 in the expression of torque coefficient calculation, as shown in Eq. (2.18).

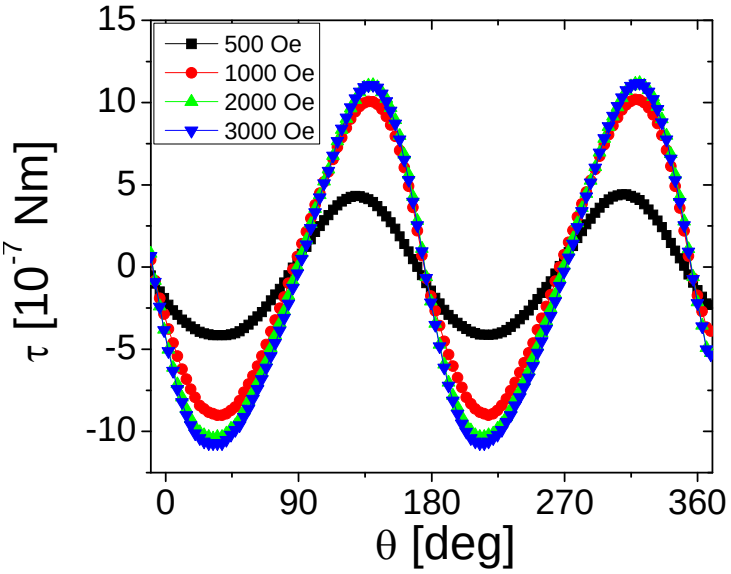


**Fig. 2.27** Field dependence of torque magnetometry data at 10 K of a $CoS_2$ crystal (mass: 1.5 mg)

During the sample measurement, the imbalance-to-resistance ratio is measured at each temperature, then this ratio is subtracted from the background ratio recorded during a calibration and the net ratio coming from the sample is obtained. By multiplying the torque coefficient determined in the calibration, the sample torque can be obtained.

Depending on the situation, sometimes it is worthwhile to calibrate the background resistance ratio after the sample is mounted on the chip to get more accurate baseline resistance ratio than employing the values from the calibration run considering the slight difference the sample will produce in the background resistance ratio. Such a calibration is done at zero field, according to definition. Considering how delicate the torque-lever chip is, it is also important to make sure sample dimensions smaller than $1.5\text{mm} \times 1.5\text{mm} \times 0.5\text{mm}$ and total mass smaller than 10 mg [34]. It is extremely important not to exceed the upper measuring limit, which is $5 \times 10^{-5}$ N·m since such large signal might break the chip [44]. In fact, it is recommended to constrain the signal to below $10^{-5}$ N·m since larger signals will produce a nonlinear response and result in inaccurate measurements [34]. It is important to choose the right size of a sample and to estimate the maximum magnetic moment of the sample before performing a measurement. To avoid exceeding the upper torque measuring range, extreme caution is needed when determining the maximum applied field. Small field is recommended to start with and the field can be gradually increased with a small increment with care.

### 2.3.4 SANS: Small-angle neutron scattering

#### 2.3.4.1 Introduction

Neutron scattering is widely used in different disciplines including, but not limited to, physics, materials science, biology, chemistry, and chemical engineering [35]. Compared with other techniques to probe the structure of materials, neutron scattering offers a variety of advantages. Neutrons are charge neutral and only interact weakly with materials via short-range nuclear forces (on the order of fm), which enables them to penetrate materials far better than charged particles with much less scattering, leading to larger penetration depth usually on the order of cm, much larger than X-ray and electrons in most cases, as shown in Fig. 2.28 [35]. Neutrons also have spin, which enables them to probe magnetic structure of materials. Also, neutrons scatter irregularly with nuclei, unlike X-ray, where the form factor is proportional to *Z*. Such a fact makes neutron scattering an excellent tool to probe light elements with large neutron cross-sections such as C, H, O, and N, as shown in Fig. 2.29 [36], which plays such an important role in the

disciplines of chemistry, polymers, biology, magnetic oxides, etc., since such light elements are almost invisible to X-ray. In addition, neutron cross-sections can vary a lot between isotopes, which makes isotope substitution an excellent tool for labeling. For example, neutron interactions from hydrogen (H) and deuterium (D) are quite different, which makes deuterium labeling method an important probe in structure determination. Another advantage of neutron scattering is that neutrons have similar energy scale to thermal vibration energy of the lattice. For example, thermal neutrons of wavelength 1 Å possess energy 85 meV, which is comparable to room temperature energy scale $k_BT$~ 25 meV. Such a property can be used to probe the dynamic properties of materials including lattice vibration, magnons, non-equilibrium properties, etc.

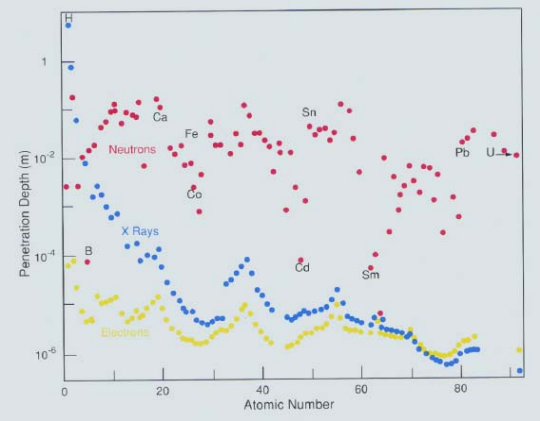


**Fig. 2.28** Penetration depth of neutrons (λ = 1.4 Å), X-rays, and electrons [35].

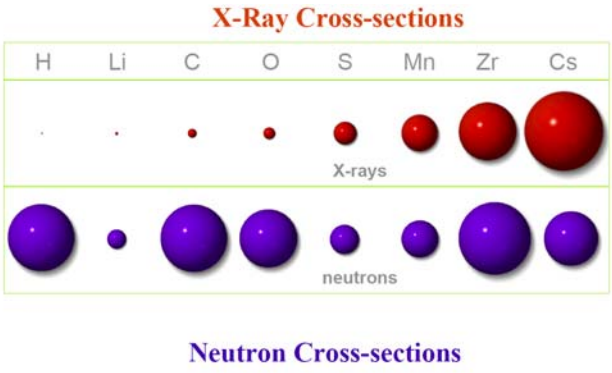


**Fig. 2.29** Comparison of X-rays and neutrons Cross-sections [36].

SANS is a type of neutron scattering where the scattering occurs at very small angles, which can be used to probe the structure of materials on the length scale varying from 1nm to 1000 nm [37]. As shown in Fig. 2.30 (a), a highly collimated neutron beam with wavelength λ is scattered by the sample by a small angle 2θ. The scattered intensity recorded in a 2-D detector can be reduced to the absolute cross-sections of the sample, which will be discussed later. As shown in Fig. 2.30 (b), $k_i$ ($k_f$) is the incident (scattered) wave vector, and $q = k_f - k_i = 4\pi \sin(\theta)/\lambda$ is the transfer wave vector. Since SANS occurs as very small scattered angle, it is quasi-elastic scattering ($|k_i| \approx |k_f| \approx \frac{2\pi}{\lambda}$) with scattering intensity integrated over a small energy window centered at zero energy transfer. The length scale that SANS can probe is,

$$d = \frac{2\pi}{q} = \frac{2\pi}{|k| 2\sin(\theta)} = \frac{2\pi}{4\pi \sin(\theta)/\lambda} \approx \frac{\lambda}{2\theta} (\theta \text{ is small}) \qquad (2.20).$$

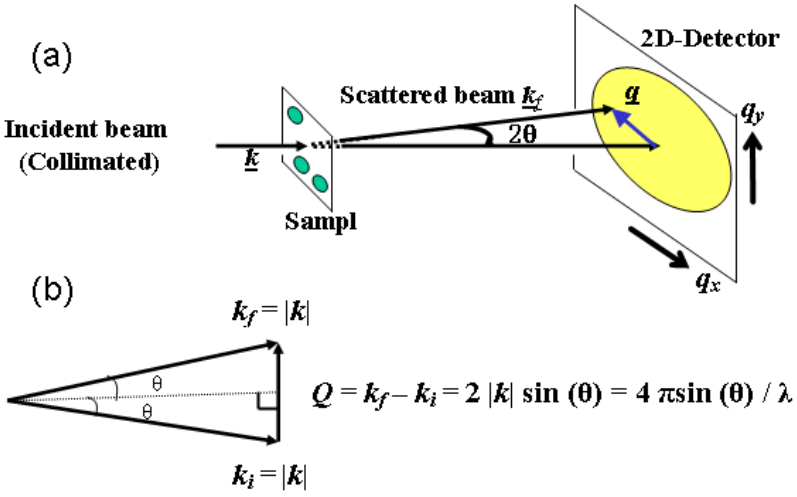


**Fig. 2.30** (a) Schematic diagram of SANS setup, (b) Schematic diagram of incident, scattered, and transfer wave vector in SANS.

Fig. 2.31 (a) shows a real picture of the 30 m SANS instrument NG7 located at the Guide Hall of NCNR at NIST [38]. As shown in Fig. 2.31 (b), the velocity selector is used to determine the wavelength of neutrons (5~8 Å in our experiments). The selected

neutrons then travel through a 16-m long pre-sample neutron guide to form a highly collimated neutron beam before being scattered by the sample. The 128×128 pixel 2-D detector is installed inside the scattering vessel (about 15 m long), as shown in Fig. 2.31(b), which can be adjusted by moving toward or away from the sample with sample to detector distance ranging from 1m to 12 m. Therefore the scattering angle θ can be changed accordingly, which enable SANS to probe large scale objects as well as small scale objects in materials.

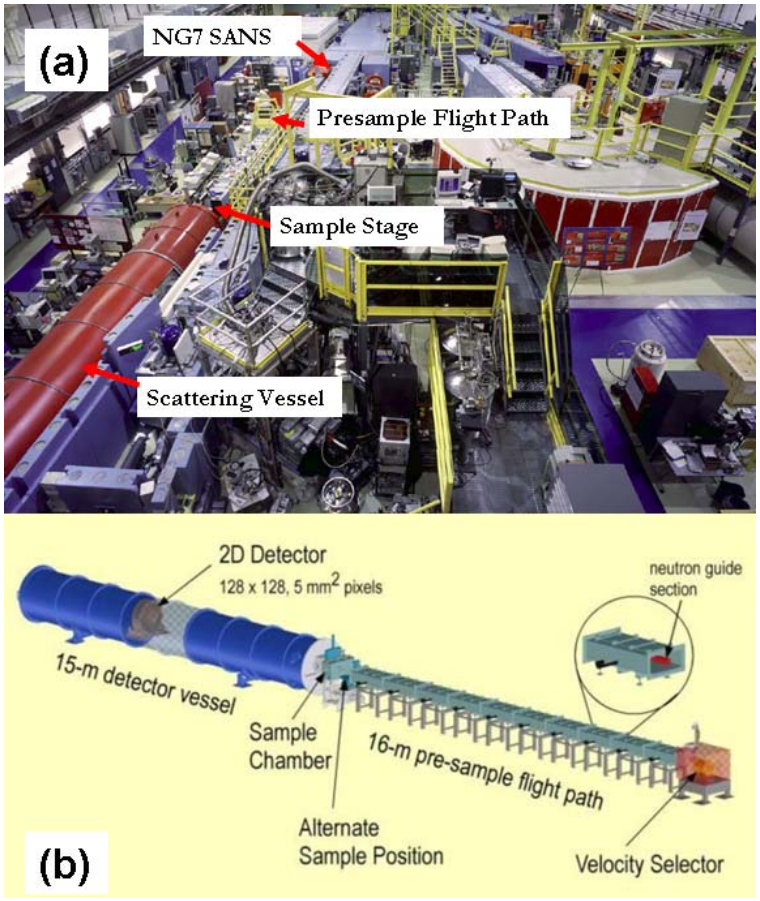


**Fig. 2.31** (a) Real picture and (b) schematic diagram of the 30m SANS instrument NG7 taken at NCNR at NIST [38]

Before exploring the conversion between the scattering intensity directly recorded from the detector and the absolute cross section, it is important to first introduce the neutron scattering length density $\rho_{SLD}$, defined as below [39, 40]:

$$\rho_{SLD} = \frac{\sum_{i}^{n} b_i}{V} = N_A \left( \frac{\rho_{mass}}{M_W} \right) (\sum_i b_i)_{molecule} \text{ or } \rho_{SLD}(\vec{r}) = b_i \delta(\vec{r} - \vec{r}_i) \quad (2.21),$$

where $b_i$ is the bound scattering length of atom $i$, $V$ is the volume containing $n$ atoms, $N_A$ is Avogadro constant, $\rho_{mass}$ is the mass density, and $M_W$ is the molecular weight. The absolute cross section can be expressed via Van Hove's scattering law [37, 40]:

$$\frac{d\Sigma}{d\Omega}(q) = \frac{1}{V} \left| \sum_i^N b_i \exp(i\vec{q} \cdot \vec{r}) \right|^2 = \frac{1}{V} \left| \int_V \rho(\vec{r}) \cdot \exp(i\vec{q} \cdot \vec{r}) \right|^2 \quad (2.22).$$

The number of neutrons scattered by a sample is then related to the absolute cross section, expressed as follows [39, 41]:

$$I(q) = \phi A d T \frac{d\Sigma(q)}{d\Omega} \Delta\Omega \varepsilon t \quad (2.23),$$

where $\phi$ is the total incident neutron flux on the sample, $A$ is sample area, $d$ is sample thickness, $T$ is the measured sample transmission, $\Delta\Omega$ is the solid angle for each pixel, $\varepsilon$ is the detector efficiency, and $t$ is the measuring time. Once the raw intensity is recorded, the absolute cross section can be calculated using the reduction software [41].

Since neutrons interact with magnetic materials not only through short-range nuclear force, but also through magnetic interaction, the scattering includes two parts: One coming from structural scattering due to nuclear interaction, the other arising from magnetic contribution due to magnetism. The part of interest to us is the magnetic part, which can be extracted by subtracting the structural/chemical background at temperature far above the Curie temperature. For most of the samples we measured, since the Curie temperature is lower than room temperature, as an approximation, room temperature scattering is used as the structural/chemical background. The exception to this will be discussed in Chapter 4 for high doping samples, where the Curie temperature is close to room temperature. The magnetic contribution is discussed in detail below.

**2.3.4.2 SANS in ferromagnets**

In ferromagnetic (FM) materials, neutrons not only interact with the materials through nuclear forces, but through magnetic forces as well, since neutrons have spin.

Generally, possible sources of magnetic scattering include: Domains, domain walls, spin waves, spin fluctuations, etc. Two major types of magnetic scattering of interest to us are present for conventionally long-range ordered FM materials: Porod scattering and Lorentzian scattering. Porod scattering occurs at low $q$, and arises from long-range magnetic ordering below the Curie temperature $T_C$. On the other hand, Lorentzian scattering occurs at higher $q$ and originates from short-range magnetic ordering when the temperature approaches the Curie temperature due to the critical scattering. These two types of scattering will be discussed in more detail below.

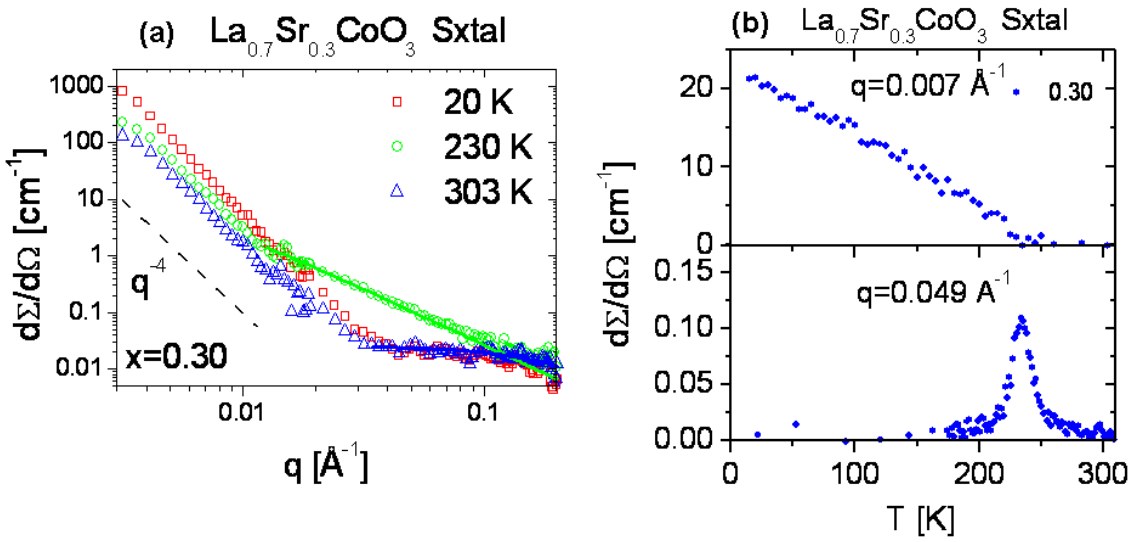


**Fig. 2.32** (a) $q$ dependence at $T$ = 20 K, 230 K, and 303 K, and (b) $T$ dependence at $q$ = 0.007 Å$^{-1}$ and 0.049 Å$^{-1}$ of SANS intensity for a $La_{0.7}Sr_{0.3}CoO_3$ crystal.

Below $T_C$, magnetic low $q$ scattering due to FM domains and domain walls typically dominates, which, in some case, quite often, obeys the well-known Porod form [42]:

$$I(q) = 6\pi(\Delta\rho)^2 / (Rq^{-4}) \qquad (2.24),$$

where $\Delta\rho$ is the scattering length density contrast, arising from the spin reorientation in the domain walls, $q$ is the transfer wave factor, and $R$ is the radius of the scattering centers. Such a form ($I$ proportional to $q^{-4}$) comes from the 3 dimensional distributions of "hard spheres" when $q >> 1/R$, which is due to the scattering from magnetic domains/

walls and corresponds to long length scale objects. Using a $La_{0.7}Sr_{0.3}CoO_3$ single crystal as an example, as shown in Fig. 2.32 (a), the low $q$ scattering possesses the form $q^{-4}$. The low $q$ scattering of the $La_{0.7}Sr_{0.3}CoO_3$ crystal is observed at $q$ down to 0.003 $Å^{-1}$, indicating the domain size is larger than 2000 Å, which is truly long-range ordering. Such a type of scattering is often observed in FMs [43-45], and is thus a good probe of long-range-ordered FMs. As shown in the top panel of Fig. 2.32 (b), the low q scattering related to long-range magnetic ordering at a representative $q$ value 0.007 $Å^{-1}$ turns on abruptly below $T_C$, which is around 230 K for $La_{0.7}Sr_{0.3}CoO_3$.

When temperature approaches $T_C$ from above ($T \rightarrow T_C^+$), another type of scattering will be observed at high $q$, which is called Lorentzian scattering [42]:

$$I(q) = I_0 / (\kappa^2 + q^2) = I_0 / ((\frac{1}{\xi})^2 + q^2) \qquad (2.25),$$

where $I_0$ is a constant, and $\xi$ is the spin correlation length. Such a form is the Fourier transformation of the real space instantaneous spin correlation function for spins at 0 and $r$ possessing the Ornstein-Zernike form:

$$< S_0(0) S_r(0) > \propto \frac{e^{-\kappa r}}{r} \qquad (2.26),$$

where $\kappa$ is inverse of the spin correlation $\xi$. Such a type of scattering is called Lorentzian scattering, which is observed in many FM materials [43, 46]. As shown in Fig. 2. 32 (a), the high $q$ scattering in $La_{0.7}Sr_{0.3}CoO_3$ can be fitted with the Lorentzian scattering form and can be used to extract the correlation length $\xi$.

When temperature approaches $T_C$ from below ($T \rightarrow T_C^-$), more and more spin waves (magnons) are excited, and among those are the ones with short wavelength. The combination of the Lorentzian scattering (above $T_C$) and the scattering due to spin waves (below $T_C$) forms a peak at $T_C$ for conventional FMs. Fig. 2.32 (b) shows an example of this "critical scattering" for a $La_{0.7}Sr_{0.3}CoO_3$ crystal at $q$ =0.049 $Å^{-1}$, which exhibits a peak around $T_C$ (230 K).

Starting from $T$ (well above $T_C$), all electron spins are randomly distributed and are not correlated to each other, so there is no spin correlation at all. As $T$ decreases, the

material gradually approaches the second order transition from paramagnetic phase to FM phase. Spin fluctuations start to slow down and the electrons start to communicate to each other via short-range spin correlations. When $T$ is decreased even closer to $T_C$, the range of the spin correlations (represented by ξ) grows. When $T$ is decreased to $T_C$, the system enters a long-range magnetic ordering state. ξ is found to diverge for conventional FMs [43, 46] and Porod scattering often takes over in SANS.

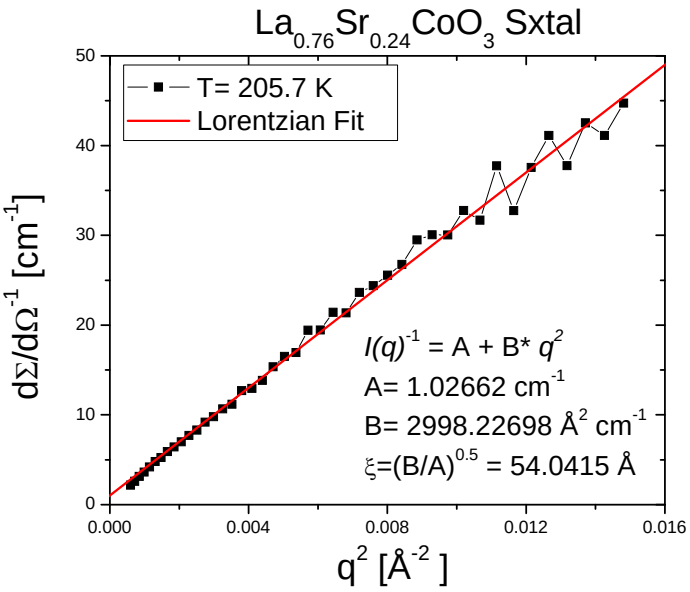


**Fig. 2.33** Extraction of spin correlation length for a $La_{0.76}Sr_{0.24}CoO_3$ single crystal at $T$ = 205.7 K by plotting $I^{-1}$ vs $q^2$.

It can be seen from Eq. (2.25) that Lorentzian scattering can be utilized to determine the spin correlation length, indicative of the size of the FM clusters above $T_C$:

$$I(q)^{-1} = \frac{1}{I_0}((\frac{1}{\xi})^2 + q^2) = A + Bq^2; \xi = \left(\frac{B}{A}\right)^{0.5} \qquad (2.27).$$

Thus the standard procedure is to plot the inverse of $I(q)^{-1}$ versus $q^2$ for each specific temperature, which should be a linear form in the regime of Lorentzian scattering, and from the slope and intercepts of the fitting, ξ can be extracted from the second part of Eq.(2.27). As shown in Fig. 2. 33, for a $La_{0.76}Sr_{0.24}CoO_3$ single crystal at $T$ = 205.7 K, the

linearity of $I^{-1}$ versus $q^2$ (in the high $q$ Lorentzian scattering regime) is evident. The linear fitting gives rise to the spin correlation length about 54 Å at this temperature for the $La_{0.76}Sr_{0.24}CoO_3$ single crystal. The same procedure can be done at other temperatures and the temperature dependence of the spin correlation length can be determined for FMs.

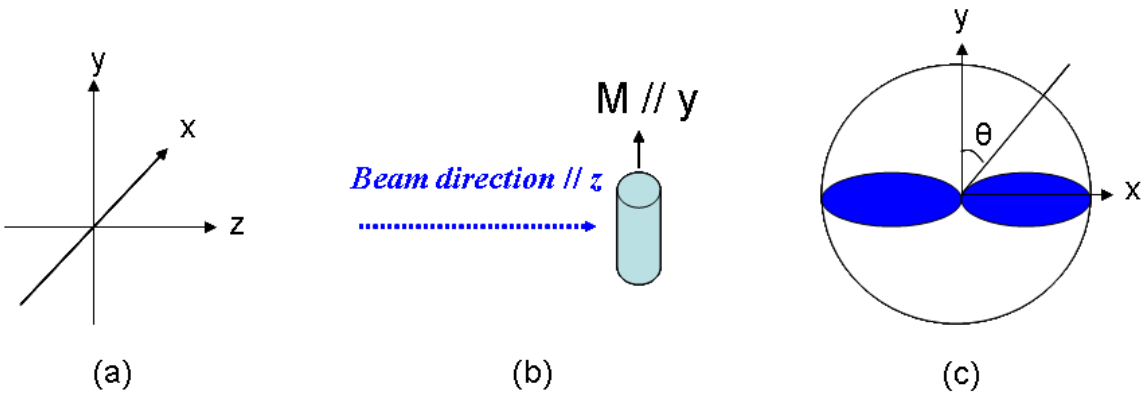


**Fig. 2.34** Schematic diagram of angular dependence of SANS intensity on the detector due to the magnetic correlations: (a) Coordinate system, (b) sample with magnetization along *y* axis and the neutron beam along *z* axis, (c) SANS intensity pattern due to sample magnetization on the detector, maximized along *x* axis and minimized along *y* axis. The θ is the angle between sample magnetization and some specific orientation on the detector.

According to the micromagnetic theory [47-48], due to the interaction of neutron spins and magnetization through torque, the angular dependence of SANS intensity on the two dimensional detector from magnetic correlations has the form of $\sin^2(\theta)$, where θ is the angle between magnetic correlations (along *y* orientation) in the sample, which is also perpendicular to the neutron beam (along *z* orientation), and some specific orientation on the detector, as shown in Fig. 2.34. It can be seen that the peak position of SANS intensity (along *x* orientation) on the detector is rotated by 90° from the magnetization position in the sample (*y* orientation). In essence, the scattering becomes "lobed" along the *x* axis. More details can be found on Ref. 49. Such an angular dependence will be used for the anisotropy analysis, as will be discussed in Chapter 6.

# Chapter 3

# Spin State Transition in $LaCoO_3$

As discussed in Chapter 1.3.1, despite its long history of discovery, the spin state transition in $LaCoO_3$ remains a controversial issue. In this chapter, it will be shown that the low temperature specific heat of $LaCoO_3$ single crystals reveals a previously unobserved Schottky anomaly with an energy level splitting, 0.5 meV, that is associated with the first excited spin-state of the $Co^{3+}$ ion. These states persist well below 2 K and have a *g*-factor around 3.5, consistent with the high-spin spin-orbit triplet. A close examination of such a Schottky anomaly indicates the existence of a low density (approximately 0.1 % of the sites) of finite-spin Co ions even in the $T = 0$ limit, which we propose are trapped at defects (e.g. oxygen vacancies). Such a discovery will cast a new perspective on the studies of low temperature spin states in $LaCoO_3$.

## 3.1 Spin State Transition in $LaCoO_3$

The magnetism of $LaCoO_3$ remains controversial, despite its discovery over 40 years ago [1] and intense recent activity [2-14], as discussed in chapter 1.3.1. It is generally accepted that slight dominance of the crystal field splitting over Hund's rule exchange energy leads to a $t_{2g}^6e_g^0$ ($S = 0$) low spin (LS) ground state [2]. Thermal excitation populates excited spin states, the $t_{2g}^5e_g^1$ ($S = 1$) intermediate spin (IS) and the $t_{2g}^4e_g^2$ ($S = 2$) high spin (HS) both being possible [1-14]. HS was initially favored as the first excited state according to the calculated energy diagram based on an atomic picture [1], an interpretation that was later questioned by LDA+U electronic structure calculations [4] indicating stabilization of IS by Co $e_g$ – O 2p hybridization. Several experimental studies via infrared spectroscopy [5], susceptibility [6], thermal expansion [6], X-ray diffraction [7], x-ray absorption near-edge structure spectroscopy [8], and electron energy-loss spectroscopy [9] found evidence in support of this picture. However, recent electron spin resonance (ESR) [10,11], x-ray absorption spectroscopy (XAS)/magnetic circular dichroism (MCD) [12], and inelastic neutron spectroscopy (INS) [13] provide evidence for HS. ESR demonstrated that the first excited state is a zero field-split triplet (as in XAS/MCD [12]) with a *g*-factor ~3.45 [10], while INS [13] revealed a thermally excited

0.6 meV excitation, which was ascribed to a spin-orbit HS triplet, due to the transition from a singlet to a doublet in this triplet about 10 meV above the ground states [13,14]. The *g*-factor from INS is ~ 3 (roughly consistent with ESR), the absence of direct excitation to the first excited state being accounted for by selection rules [13]. However, the 0.6 meV excitation was also found by Phelan *et al* [15], and interpreted in terms of an *IS* first excited state. This was supported by local dynamic Jahn-Teller (JT) distortions [16], and simultaneous ferromagnetic (FM) and antiferromagnetic (AF) spin correlations [15], i.e. dynamic A-type AF ordering (AF coupling between FM sheets), which is induced by dynamic orbital ordering associated with JT active IS states. Recent work via extended x-ray absorption fine structure and neutron pair distribution function analysis by Sundaram *et al.* [17] has even questioned this conclusion, claiming few, if any, JT active states. In light of these conflicting reports, the sequence of excited states thus remains highly controversial.

Remarkably, the magnetic properties in the "non-magnetic" low *T* region dominated by the $S = 0$ LS state are also debated, due to observation of paramagnetism or weak FM. Although originally dismissed as a "Curie tail" due to impurities, detailed studies provided evidence either of surface FM due to higher spin states of surface Co ions, since reduced oxygen coordination changes the energy balance between crystal field splitting and Hund's rule exchange energy [18], or formation of high spin local magnetic entities. Evidence for the latter is strong. As predicted by Nagaev [19] and observed via magnetometry [20-23] and muon spin relaxation (μSR) [21,22], non-stoichiometries (e.g. oxygen point defects) create localized carriers that stabilize HS states on neighboring $Co^{3+}$ ions, creating a "magnetic polaron" or, more accurately, "magnetic exciton". This is similar to the "spin-state polaron" in lightly doped $La_{1-x}Sr_xCoO_3$ [24], where dilute LS $Co^{4+}$ ions stabilize the IS state on neighboring $Co^{3+}$ ions generating a spin polaron via double exchange (DE). This has also been proposed as an explanation for the incommensurate magnetism competing with DE FM to higher *x* [25]. The motivation for this work in this chapter is the anticipated Schottky anomalies that should occur due to the various predicted energy level splittings. We therefore studied specific heat to low temperature.

## 3.2 Schottky anomaly in heat capacity

As mentioned in Chapter 2, heat capacity measurements are useful to explore the magnetic and electronic properties of materials. In general, the heat capacity of materials includes four contributions, expressed as follows [26]:

$$C_p(T) = \frac{\partial U}{\partial T} = C_{Lat} + C_{Elec} + C_{Mag} + C_{Nuc} \quad (3.1),$$

where $C_{Lat,}$ $C_{Elec,}$ $C_{Mag,}$ and $C_{Nuc}$ refers to the lattice contribution, electronic contribution, magnetic contribution, and nuclear contribution respectively. At low temperatures, based on the Debye model and the free-electron model, the lattice and electronic contribution can be expressed as [27]:

$$C_{Lat} = \beta T^3;\ \beta = 234(\frac{1}{\Theta_D})^3 N_{total} k_B \quad (3.2),$$

$$C_{Elec} = \gamma T;\ \gamma = \frac{\pi^2}{3} k_B{}^2 N(E_F) \quad (3.3),$$

where $N_{total}$ is the number of ions/mole, $\Theta_D$ is the Debye temperature, and $N(E_F)$ is the density-of-states at the Fermi level. More discussions will be covered for each contribution in detail in Chapter 5. The low temperature heat capacity is often plotted as $C_P(T)/T$ vs. $T^2$, to test for a temperature dependence of the form:

$$C_P(T) = \gamma T + \beta T^3 \quad (3.4),$$

i.e. only electronic ($\gamma T$) and lattice ($\beta T^3$) contributions to heat capacity.

Schottky anomaly in heat capacity refers to a peak in $C_P(T)$ due to a multi-level energy spectrum. For example, consider $N$ particles in a 2 level system with energy separation $\varepsilon$, $C_P(T)$ will be given by [28]:

$$C_P(T) = Nk_B \times \left(\frac{\varepsilon}{k_B T}\right)^2 \times \left(\frac{\nu_0}{\nu_1}\right) \frac{e^{\varepsilon/k_B T}}{(\nu_0/\nu_1\, e^{\varepsilon/k_B T} + 1)^2} \quad (3.5),$$

where $\nu_0, \nu_1$ is the degeneracy for the low and high energy levels respectively. Such an expression will give rise to a peak in heat capacity. It can be understood intuitively as follows: At $T << \varepsilon$, since thermal excitation is too small due to the *"huge"* energy gap, almost all particles stay in the lower energy level, which gives rise to little contribution to heat capacity; on the other hand, at $T >> \varepsilon$, since the energy gap is *"tiny"*, two energy

levels are almost equally occupied, which also results in small thermal excitation and little contribution to heat capacity. However, when $T \approx \varepsilon$, the excitation will be large since the thermal energy is large enough to overcome the energy barrier and there are also enough "*available"* states in the higher energy level, which eventually gives rise to a large contribution to the heat capacity. The combination of these three temperature regions leads to a peak in the heat capacity at a temperature comparable to ε. Fig. 3.1 shows an example of $\nu_0 / \nu_1 = 1$ for the purpose of illustration. In this simple case, the peak is located at about 0.4 $k_B T/\varepsilon$ and the peak height is on the order of $R$ for one mole of material, depending on the number of ions per mole. Therefore, by exploring the Schottky anomaly in heat capacity, one can determine the energy separation as well as the degeneracy ratio associated with the energy separation in materials.

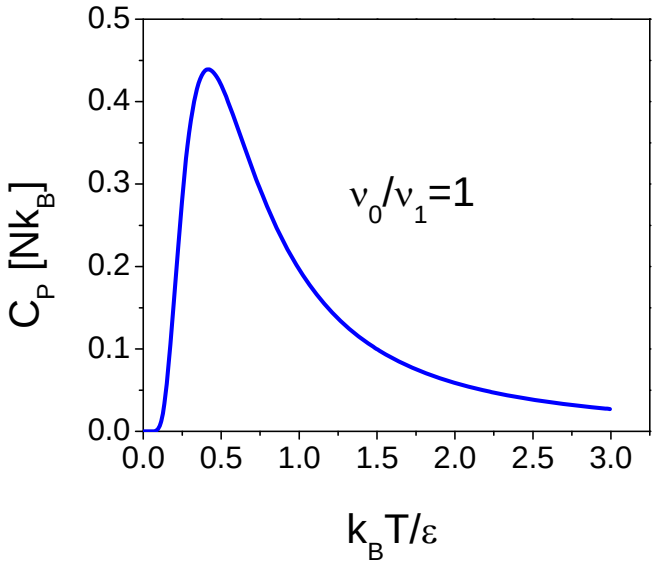


**Fig. 3.1** Schottky anomaly in heat capacity for a two-energy level system containing $N$ particles with energy separation ε and degeneracy ratio $\nu_0 / \nu_1 = 1$

In the case of $LaCoO_3$, as mentioned in chapter 1, the slight dominance of crystal field splitting over the Hund's rule exchange energy results in a nonmagnetic, low spin ($S$ = 0) ground state for $Co^{3+}$. With increasing temperature, thermal excitation will overcome such a small spin gap (about 10 meV) and result in finite spin states (either intermediate

spin $S = 1$ or high spin $S = 2$). The spin gap associated with such a spin state transition is expected to show up in the form of a Schottky anomaly in heat capacity.

## 3.3 Global temperature behavior in the specific heat of $LaCoO_3$

Two single crystals were used for the specific heat measurements of $LaCoO_3$: One provided by Cava's group at Princeton (Labeled as Princeton) and one provided by Mitchell's group at Argonne National Laboratory (Labeled as Argonne). The global temperature behavior (1.8 K < $T$ < 270 K) of the specific heat for a $LaCoO_3$ single crystal (Argonne) is shown in Fig. 3.2. It is noticed that with increasing temperature, the specific heat approaches the classical limit 3$R$, as predicted by Dulong-Petit's Law. In the high temperature range (10 K < $T$ < 270 K), the data are consistent with earlier reports [11,29,30]: A weak, broad bump centered around 50 K exists, which is associated with a modest magnetic contribution [11] from the 10-15 meV splitting of the ground and first excited states of $Co^{3+}$. Such a bump becomes more obvious when plotted as a net magnetic contribution vs. $T$ after subtracting the lattice contribution via the reference materials, e.g., the combination of $LaGaO_3$ and $LaAlO_3$ [30]. This is not, however, the central focus of this chapter. As will be shown below, more attention will be placed on the previously unobserved Schottky anomaly detected at low temperature.

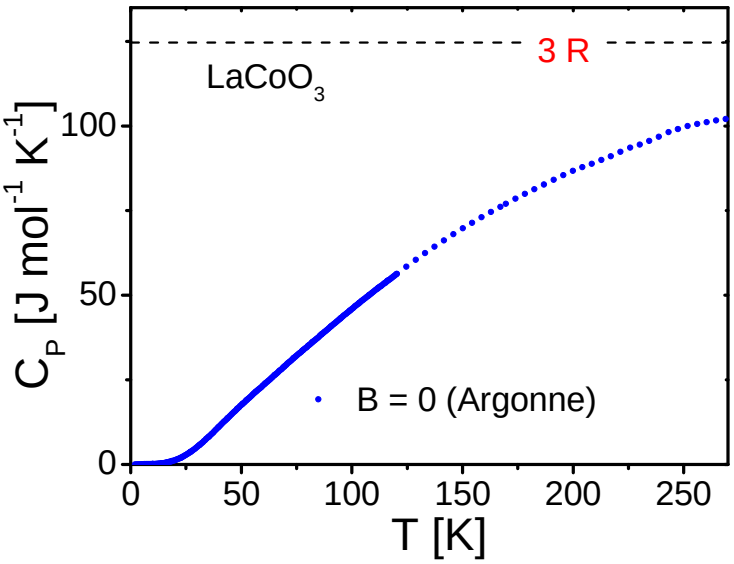


**Fig. 3.2** $T$ dependence (1.8 K < $T$ < 270 K) of the specific heat of a $LaCoO_3$ single crystal (Argonne) at fields of 0 T plotted as $C_P$ vs. $T$.

## 3.4 Low temperature Schottky anomalies in the specific heat of $LaCoO_3$: Defect-stabilized finite spin-states

The low $T$ (0.35 K < $T$ < 8 K) $C_P(T)$ is shown in the inset to Fig. 3.3. The most interesting aspect is the hump around 2 K, followed by further enhancement below 0.6 K. Such a discovery is observed for the first time. These features are seen more clearly on the $C_P/T$ vs. $T^2$ plot in the main panel of Fig. 3.3. Measurements in applied fields, $B$, of 3 and 6 T reveal strong field dependence, indicative of a magnetic origin for the excess $C_P$.

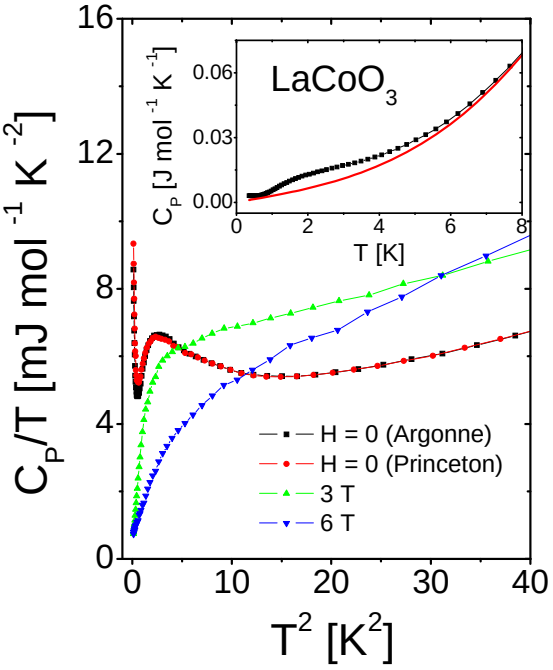


**Fig. 3.3** $T$ dependence of the specific heat of $LaCoO_3$ single crystals at fields of 0, 3, and 6 T plotted as $C_P/T$ vs. $T^2$ (main panel) and $C_P$ vs. $T$ (inset). The solid line in the inset is the non-magnetic contribution to $C_P$ as described in the text. The zero field data are shown for two crystals (Argonne and Princeton), the field data for one (Argonne).

The overall form of this magnetic contribution to $C_P(T)$ around 2 K (i.e. a steep increase at low $T$ and a long tail at high $T$) is consistent with a Schottky anomaly [3], as shown in Fig. 3.1. In order to quantify this we fitted the data (up to 10 K) to $C_P(T) = \gamma T + \beta T^3 + C_P^{Mag}(T)$, i.e. electronic, lattice, and magnetic contributions. The non-magnetic

(electronic + lattice) contribution (solid line in the inset to Fig. 3.3) gives a 480 K Debye temperature, consistent with an *x*-dependent study [31], which will be discussed in detail in Chapter 5, and an electronic contribution that is negligible in comparison to that seen in the metallic phase at high *x* [31].

Any nuclear contribution is insignificant at these temperatures below $x \approx 0.04$ [31] due to the small hyperfine field, which will be discussed in detail in Chapter 5. The extracted $C_P^{Mag}(T)$ is plotted in Fig. 3.4(a) along with a fit to a modified Schottky form [28],

$$C_P^{Mag}(T) = \left(\frac{n}{N_{Co}}\right) R \left(\frac{\Delta E}{k_B T}\right)^2 \frac{\nu_0}{\nu_1} \frac{\exp(\Delta E / k_B T)}{\left[1 + \left(\frac{\nu_0}{\nu_1}\right)\exp(\Delta E / k_B T)\right]^2} \qquad (3.6),$$

where $R$ is the gas constant, $\Delta E$ is the energy level splitting, $\nu_0$ and $\nu_1$ are the degeneracies of the lower and upper levels, and $n/N_{Co}$ is the fraction of contributing Co sites.

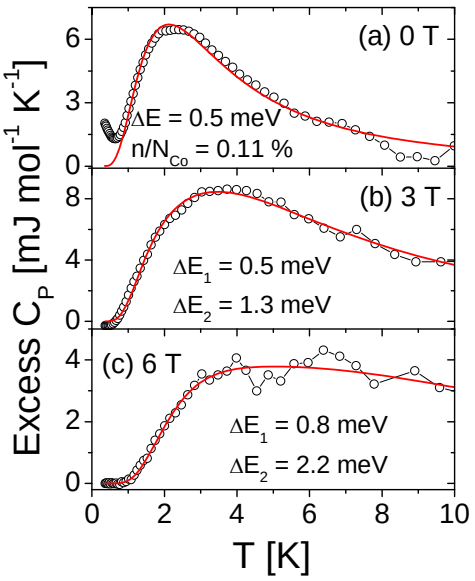


**Fig. 3.4** *T* dependence of the excess magnetic specific heat (0.35 K < *T* < 10 K) of $LaCoO_3$ in fields of **(a)** 0 T, **(b)** 3 T, and **(c)** 6 T. The solid lines are fits to the model described in the text, resulting in the fit parameters shown.

The modification is done by adding one prefactor, $n/N_{Co}$, to take into account the fact that only a small fraction of lattice sites contributes to the Schottky anomaly, which can easily be seen by comparing the much smaller height of excess $C_P$ to the typical height (on the order of $R$) of a Schottky anomaly, as shown in Fig. 3.1. With the exception of the tail at $T < 0.6$ K (see below) this provides a good fit (Fig. 3.4(a)) with $\nu_0/\nu_1$ set to 1/2 (the first excited states are composed of a singlet at the low energy level and a doublet at a higher energy level), $\Delta E = 0.5$ meV, and $n/N_{Co} = 0.11$ %. These values are striking, particularly the $\Delta E$ of 0.5 meV which is very close to the 0.6 meV observed at $T \geq 20$-50 K by INS [13,15] and ESR [10]. It is natural to associate the observed $\Delta E$ with the transition from the singlet state to doublet states from the excited states, as mentioned in the previous section. However, given the small $n/N_{Co}$ value of 0.11 %, we propose such an excitation is driven by defects instead of being thermally excited since it persists to low temperature (as low as 2 K). At 2 K, thermal excitation across a 10 meV gap separating ground and first excited states should result in an excited population of $10^{-26}$, indicating that these finite-spin $Co^{3+}$ are not thermally excited. Rather, the dilute quantities are consistent with stabilization of finite spin-states at defects (e.g. oxygen point defects [19,21-23]). $LaCoO_{3-\delta}$ with $\delta$ as small as 0.0005 is sufficient to explain our results. This interpretation is reinforced by measurement of additional samples. Four $LaCoO_3$ samples were measured; two single crystals (one grown at Argonne, one at Princeton, both shown in zero field in Fig. 3.3), and two polycrystals (data not shown). *All* samples exhibited a Schottky anomaly with $\Delta E \approx 0.5$ meV, but with slightly varied $n/N_{Co}$, consistent with variable oxygen defect densities, as expected. The $T < 0.6$ K tail was also present in all samples (but with widely varying magnitude), and is eliminated in high $B$ (Fig. 3.3), suggestive of paramagnetism from a low density of impurities.

Additional information was obtained from the $B$ dependence of $C_P^{Mag}(T)$ (Figs. 3.4 (a)-(c)), which shifts to higher $T$ with increasing $B$. The energy level scheme supported by ESR [10,11] and INS [13] is reproduced in Fig. 3.5(a). The first excited state is a spin-orbit triplet, trigonal crystal field split (by 0.6 meV) into a singlet and doublet lying 10-15 meV above the LS ground state (not shown). ESR data reveal a weakly anisotropic $g$-factor in the range 3.35-3.55 [10], consistent with the predicted value of ~3.5 [14]. An average $g$-factor of 3.45 provides the three level scheme shown in Fig. 3.5 (a) for $B = 3$

and 6 T, indicating expected Zeeman splitting of 1.08 and 2.16 meV, respectively. To determine if this is consistent with our measured $C_P^{Mag}(T,B)$, the data were fitted to a Schottky anomaly with three energy levels (i.e. equation (1) modified to include two splittings, $\Delta E_1(B)$ and $\Delta E_2(B)$, as illustrated in Fig. 3.5(a)), and shown below:

$$C_P^{Mag}(T) = \left(\frac{n}{N_{Co}}\right) \times R \times [(\Delta E_1 / k_B T)^2 \left(\frac{\nu_1}{\nu_0}\right) \exp(-\Delta E_1 / k_B T) + (\Delta E_2 / k_B T)^2 \left(\frac{\nu_2}{\nu_0}\right) \exp(-\Delta E_2 / k_B T)$$
$$+((\Delta E_2 - \Delta E_1)/k_B T)^2 \left(\frac{\nu_1}{\nu_0}\right) \exp(-\Delta E_1 / k_B T) \left(\frac{\nu_2}{\nu_0}\right) \exp(-\Delta E_2 / k_B T)] \qquad (3.7)$$
$$\div \left[1 + \left(\frac{\nu_1}{\nu_0}\right) \exp(-E_1 / k_B T) + \left(\frac{\nu_2}{\nu_0}\right) \exp(-E_2 / k_B T)\right]^2$$

where $\nu_0$, $\nu_1$, and $\nu_2$ are the degeneracies for the low energy level, immediate energy level, and high energy level, respectively. The extracted $\Delta E_{1,2}$ are shown in Figs. 3.5 (b), (c), and the Zeeman splitting is plotted vs. $B$ in Fig. 3.5(b), along with the expectation based on $g = 3.45$.

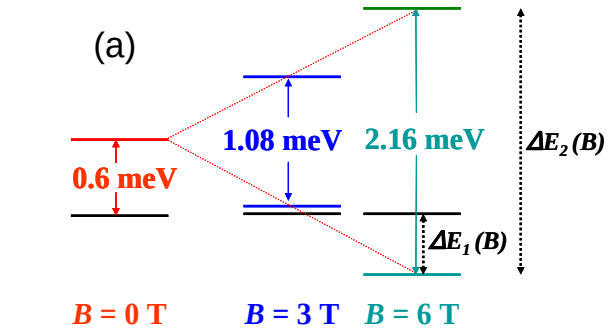


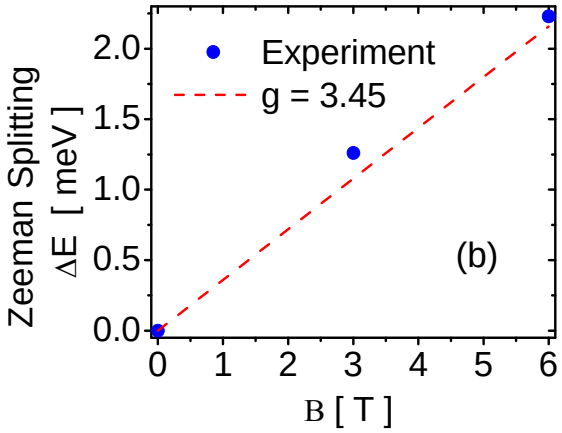


**Fig. 3.5 (a)** Proposed energy level scheme as a function of magnetic field. **(b)** Zeeman splitting vs. field. The dotted line is based on a *g*-factor of 3.45, as discussed in the text.

The agreement is satisfactory, proving that these low $T$ finite spin states, in addition to having zero field splitting close to 0.6 meV and expected degeneracy ratio, also have a $g$-factor consistent with the HS spin orbit triplet. It is remarkable that these trapped finite spin-states have such similar energy levels and $g$-factor to the thermally excited states.

We propose that these defect-stabilized $T = 0$ finite spin Co ions are associated with the magnetic excitons forming around oxygen defect-induced localized carriers, stabilizing HS states on neighboring $Co^{3+}$ ions, and creating magnetic entities with effective spin, $S$ = 10-15 [20-23]. This scenario is consistent with the dilute concentration of the finite-spin states, and the fact that their zero field splitting and g-factor are close to those of the conventional (thermally excited) HS states. In agreement with Kozlenko *et al* [32], we believe that the spin-orbit HS triplet is natural at low concentrations of excited states, as in our defect stabilization picture. At higher $T$, increased population of excited $Co^{3+}$ ions may lead to stabilization of IS (via Co – O hybridization) [4], a scenario that could resolve some of the conflicting observations regarding IS and HS states.

In summary, in this chapter, magnetic Schottky contributions to the specific heat of $LaCoO_3$ reveal finite spin $Co^{3+}$ ions even in the low temperature limit. Instead of being driven thermally to finite spin states, we propose for the first time that they can also be driven by defects such as oxygen deficiency at low temperature. The zero field splitting and $g$-factor of these sates is consistent with the spin-orbit HS triplet observed in prior work. The dilute concentration of these finite spin-states leads us to conclude that we are observing oxygen defect-stabilized HS states, likely associated with magnetic excitons.

# Chapter 4
# Phase separation above the Curie temperature of $La_{1-x}Sr_xCoO_3$

As discussed in section 1.3.2, the existence of phase separation in $La_{1-x}Sr_xCoO_3$ (LSCO) is well established. In this chapter, we systematically study a specific type of phase separation in the ferromagnetic phase in LSCO via small-angle neutron scattering and d.c. susceptibility, which evidence a clustered state above the Curie point forming at a well-defined temperature ($T^*$). Although the existence of preformed clusters above the Curie temperature of the doped perovskite manganites is well established and, in many cases, conforms to the expectations for a Griffiths phase, we will demonstrate that the characteristics of this clustered state in LSCO appear quite unlike those of a Griffiths phase. The deviation from Curie-Weiss (C-W) behavior is opposite to expectations and is field independent, while $T^*$ does not correspond to the undiluted Curie temperature. These results demonstrate that, although the Griffiths model may apply to many systems with quenched disorder, it is not universally applicable to randomly doped transition metal oxides.

## 4.1 Magneto-electronic phase separation in $La_{1-x}Sr_xCoO_3$

As mentioned in section 1.3.2, the existence of magnetic phase separation at low $T$ in LSCO has been demonstrated using transmission electron microscopy (TEM) [1,2], nuclear magnetic resonance (NMR) [3,4], small-angle neutron scattering (SANS) [5], neutron diffraction [1,6], in addition to several indirect techniques [1,7,8]. At low doping the system forms nanoscopic (~ 3 nm) ferromagnetic (F) metallic droplets in a non-F semiconducting matrix [5,6]. As $x$ is increased these clusters increase in density, eventually achieving percolation, and subsequent entry into a long-range ordered F state at $x = 0.18$ [5-8]. Although the phase separation is clear as a function of $x$ at low $T$, the region above $T_C$ has not been investigated in detail.

In this Chapter we examine the possibility of preformed clusters above $T_C$ in the F part of the phase diagram of $La_{1-x}Sr_xCoO_3$ (LSCO). Caciuffo *et al.* [9] observed a deviation from C-W around 305 K in $x = 0.3$ powder which they interpreted as entry into a "cluster-fluctuation regime". SANS data were dominated by chemical scattering but

revealed a weak magnetic Guinier component, which was ascribed to magnetic polarons [9]. The correlation length peaked at 14 Å near $T_C$ (the magnetic intensity also reaches a peak in this region), and the authors concluded that a transition from itinerant to polaronic conduction took place near the Curie point. This was backed up by diffraction data indicating an anomalous thermal expansion in this temperature region. Unfortunately, the SANS data were not acquired to sufficiently high $T$ to observe any possible $T^*$. In this chapter, we provide a full (high $T$) investigation of the behavior above $T_C$ at multiple $x$ ($0.20 \leq x \leq 0.50$) in the F part of the phase diagram, on both poly- and single-crystals. The magnetic SANS intensity, magnetic correlation length, and d.c. susceptibility all show signatures of a well-defined temperature, $T^*$ ($\approx$ 360 K), below which a clustered state is entered as a precursor to full F ordering.

## 4.2 Introduction to the Griffiths-phase

Of the many forms of magnetoelectronic phase separation observed in many transition metal oxides [10-12], as discussed in Section 1.3.2, the concept of "preformation" of F ordered clusters at some well-defined temperature ($T^*$) above the true long-range F ordering temperature ($T_C$) seems to be particularly widely applicable [10,11]. This has been observed in Fs as varied as magnetic semiconductors [13,14], oxides [10-12, 15-21], and magnetocalorics [22]. The explanation for colossal magnetoresistance in certain manganites in terms of field driven expansion of preformed F clusters [10-12,15,17] is an excellent example of the profound impact of this cluster formation, as illustrated in Section 1.2.3.

Preformed clustering also emerges from theoretical descriptions of doped magnetic systems. This includes models developed specifically for the manganites [10,11,23,24], as well as more general treatments of "random" Fs [25-26]. An example of the former is provided by the work of Dagotto *et al.*, where it was shown that disorder at a first order phase transition (e.g. from a F metal to a charge and orbitally ordered antiferromagnetic (AF) insulator) leads to magnetic phase separation below a characteristic temperature $T^*$, in excess of the composition dependent $T_C$ [10,11,23], as shown in Fig. 4.1.

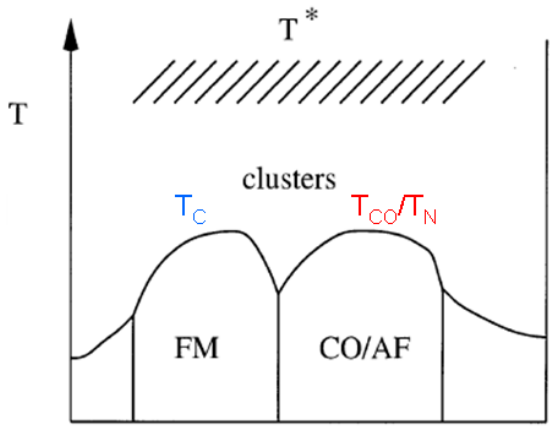


**Fig. 4.1** Schematic illustration of a new temperature scale $T^*$ based on the model specifically developed for manganites. Above the Curie temperatures $T_C$, charge/orbital ordering temperature $T_{CO}$, and Neel temperature $T_N$, a region with coexisting clusters could exist, reproduced from Dagotto *et al.* [11].

The model of Griffiths, originally developed for randomly diluted Ising Fs [25], is a more general treatment that has been found widely applicable to the perovskites [17-20]. Griffiths pointed out that a randomly diluted F with non-magnetic defects will exhibit a suppressed long-range ordering temperature $T_C(x)$ ($x$ is the dilution) and in the region $T_C(x) < T < T_C^{Undiluted}$ the thermodynamic properties (e.g. magnetization) will become non-analytical due to formation of a low density of short-range ordered clusters. $T_C^{Undiluted}$ is therefore the temperature at which this "Griffiths phase" forms and has been coined the Griffiths temperature, $T_G$, analogous to $T^*$. The Griffiths model is viewed as applicable to the manganites as the quenched disorder induced by doping is analogous to random dilution. The original paper of Griffiths [25], and subsequent work [17-20,22,26], has shown that this phase has several characteristics; (i) the susceptibility ($\chi$) deviates from Curie-Weiss (C-W) predictions as $T \rightarrow T_C$ from above (at $T_G$), (ii) this deviation takes the form of an enhanced low field $\chi$ due to the contribution from the F clusters, (iii) the deviation is suppressed in large magnetic field ($H$) due to the polarization of spins outside the clusters, and (iv) $T_G$ can be identified as $T_C^{Undiluted}$, i.e. the maximum $T_C$ in the phase diagram. Numerous magnetic systems [14,17-20,22], including manganites [17,18] and cobaltites [19,20], exhibit these characteristics, although in many cases, these are soft

materials and the Griffiths model doesn't seemingly apply to them since the original Griffiths model was developed for Ising systems, i.e., materials with large anisotropies.

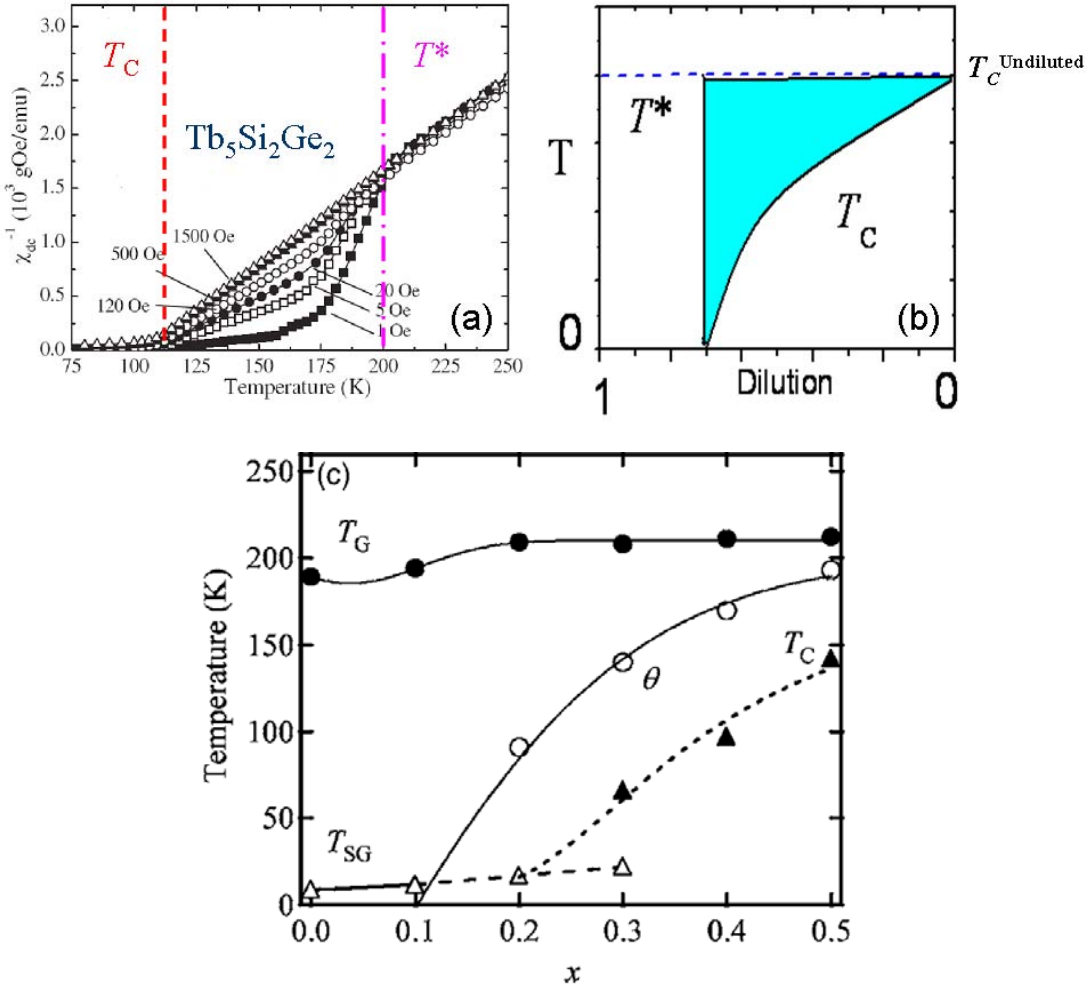


**Fig. 4.2** (a) Temperature dependence of inverse susceptibility in $Tb_5Si_2Ge_2$: An example of Griffiths's phase, reproduced from Magen *et al.* [22], (b) schematic relation between $T^*$ and $T_C$ in a diluted system predicted by Griffiths model, reproduced from Griffiths [25], (c) magnetic phase diagram of $La_{1-x}Sr_{1+x}CoO_4$, $T_G$: Griffiths temperature, θ: Weiss temperature, $T_{SG}$: Spin-glass temperature, $T_C$: Curie temperature, reproduced from Shimada *et al.* [19].

Fig. 4.2 (a) shows an example of Griffiths phase in $Tb_5Si_2Ge_2$, plotted as $\chi^{-1}$ vs. $T$. Since the Griffiths temperature is very close to the Curie temperature of the Si-rich compositions of $Tb_5(Si_{1-x}Ge_x)_4$, the Griffiths phase is proposed to be driven by local

disorder due to the substitution of Ge for Si [22]. The downward deviation from C-W predictions could be seen between $T_C$ and $T^*$. Such a reduced $\chi^{-1}$ in low fields (1-120 Oe) results from the enhanced $\chi$ due to the contributions from the preformed F clusters. It can also be seen that high fields (500 Oe, 1500 Oe) suppress such a downward deviation since they align the spins outside the clusters. As predicted by Griffiths [25], $T^*$ is equal to the maximum $T_C$ of the diluted system (the undiluted $T_C$) and is independent of the dilution level, as shown in Fig. 4.2 (b) [25]. It is also experimentally seen in materials, e.g. $La_{1-x}Sr_{1+x}CoO_4$, as shown in Fig. 4.2 (c) [19].

## 4.3 Experimental evidence of the clustered phase above $T_C$ in $La_{1-x}Sr_xCoO_3$

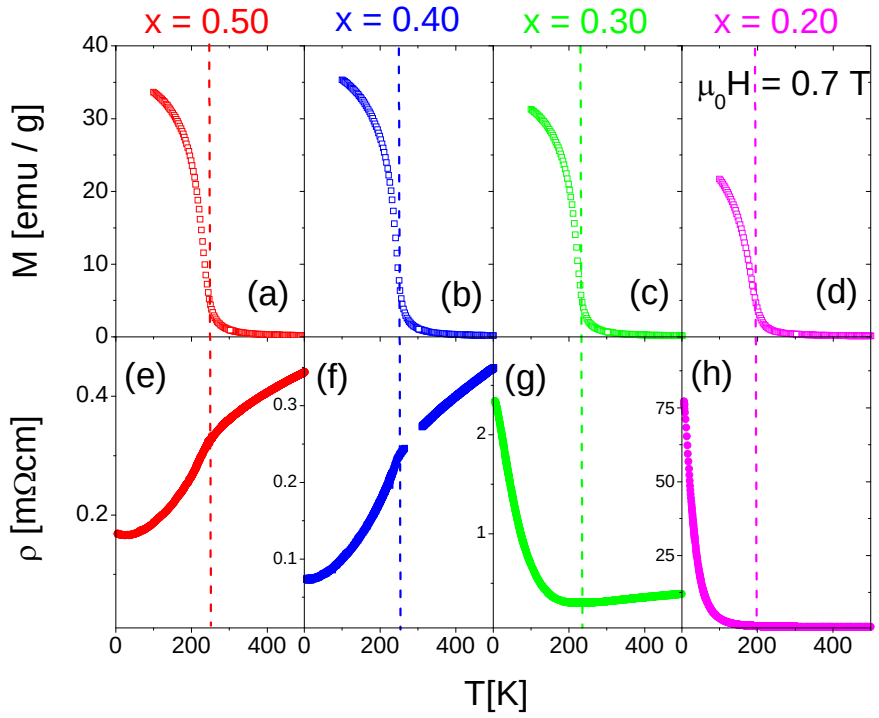


**Fig. 4.3** Temperature dependence of the 0.7 T d.c. magnetization (top panel) and zero field resistivity (bottom panel) of $x$ = 0.50 ((a) and (e)), 0.40 ((b) and (f)), 0.30 ((c) and (g)) and 0.20 ((d) and (h)) polycrystals. The vertical dashed lines mark $T_C$.

Fig. 4.3 provides a global view of the magnetization ($M$) and resistivity ($\rho$) for four F polycrystals ($x$ = 0.20 - 0.50) in the extended range up to 500 K. The data at $T$ < 300 K

are in agreement with prior reports [7,8]. These compositions show F behavior with a $T_C$ that increases gradually with $x$. The $T \rightarrow 0$ extrapolation of the conductivity of all 4 compositions is finite, indicating metallic conductivity [27]. The sign of $d\rho/dT$ at high $T$ (i.e. $T > T_C$) changes between $x = 0.30$ and 0.20, and the compositions with "metallic-like" $d\rho/dT$ show a distinct slope change in the vicinity of $T_C$, as expected [7,8].

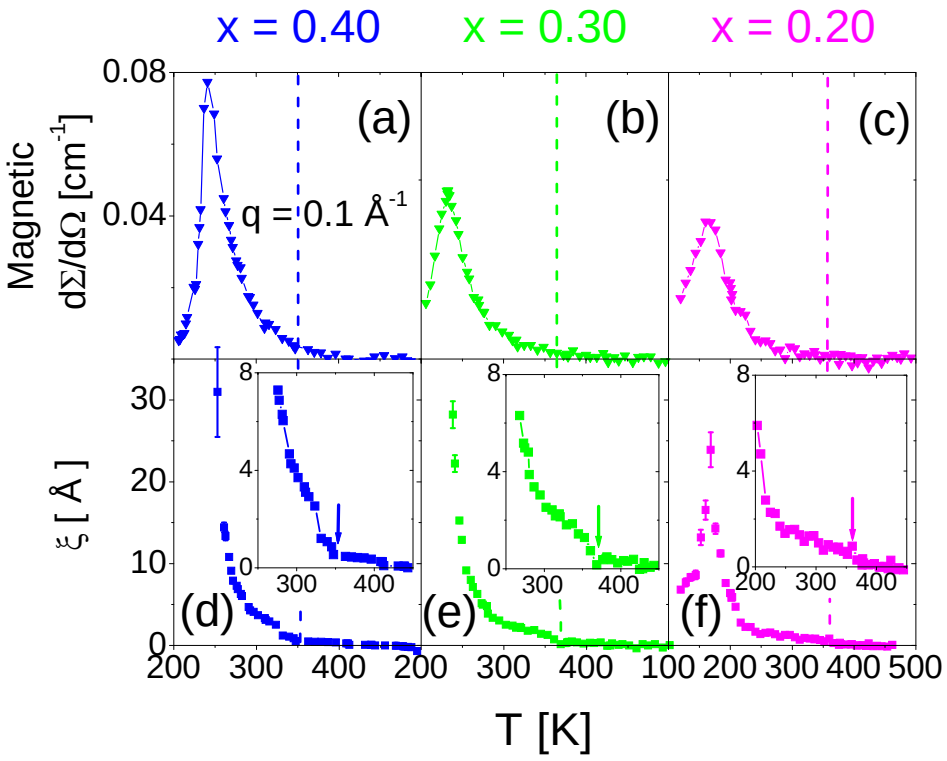


**Fig. 4.4** Temperature dependence of the magnetic part of the absolute small-angle neutron scattering intensity (zero field) at $q = 0.1$ Å$^{-1}$ (top panel), and the correlation length extracted from this scattering (bottom panel). Error bars are included but in some cases are smaller than the points. The insets show the same data in a "close-up" near 360 K. The data are for $x = 0.40$ (left panel), 0.30 (middle panel) and 0.20 (right panel). The vertical dashed lines (and arrows) mark the sharp turn on in correlation length ($T^*$). The small anomaly at 325 K in (d) was not repeatable in other temperature sweeps.

Fig. 4.4 focuses on the regime between 200 and 500 K (i.e. close to, and above, $T_C$) showing the magnetic part of the absolute SANS intensity ($q = 0.1$ Å$^{-1}$), and the magnetic

correlation length ($\xi$) extracted from the SANS, for polycrystals. The magnetic contribution was obtained by subtracting the intensity at the highest temperatures (400-500 K), a procedure which is validated by the fact that the magnetic intensity is negligible until $T$ is decreased down to ~ 360 K. Below this temperature, which is independent of doping, the magnetic intensity rises, reaching a peak at the (doping dependent) $T_C$. Such "critical scattering" would typically be ascribed to quasi-elastic scattering from the short-range spin correlations that increase in prominence as $T_C$ is approached. The $q$ dependence follows the Lorentzian form, $I = I_0 / (q^2 + (1/\xi)^2)$, where $I_0$ is a constant. At a conventional F transition, $\xi$ is expected to show a smooth increase from zero at high $T$, diverging as $T \rightarrow T_C$. $\xi(T)$ extracted from fitting to the Lorentzian form is shown in Figs. 4.4 (d)-(f). The data depart from simple expectations. $\xi(T)$ shows a distinct, sharp onset in the range 346 K (for $x = 0.40$) $< T <$ 369 K (for $x = 0.20$), as opposed to a gradual increase, indicating the sharp onset of spin correlations at a well defined temperature, $T^*$ (dotted lines and arrows in Fig. 4.4). In agreement with prior work on other materials, we interpret this temperature at which a sharp increase in $\xi$ occurs as the point at which F clusters emerge. (Note that prior La NMR data at $x = 0.30$ [4] showed a F signal extending above $T_C$ (the highest temperature measured was 280 K), further evidence for preformation of F clusters). It is worth pointing out that we attempted to fit our data to a Guinier form (following [9]) but it was clear that the Lorentzian form provided a far better description of the data.

Figs. 4.5 (d)-(f) show that the inverse susceptibility also reflects this cluster formation at $T^*$; $\chi^{-1}$ is C-W-like at high $T$ but shows departures from C-W at $T >> T_C$. The solid lines are fits to C-W between 400 and 500 K, and extrapolation to lower $T$ yields temperatures at which deviations occur of ~ 360 K, very close to the $T^*$ values determined from $\xi(T)$. Note that the data deviate *upwards* from the C-W prediction on a $\chi^{-1}$ vs. $T$ plot, i.e. towards lower $\chi$. It should be pointed out that such upward deviations are common in conventional Fs. However, in this case, the close agreement between the temperature at which a discontinuity in $\xi(T)$ occurs and the one at which we observe deviations from C-W suggests that the two are related [9]. As shown in Figs 4.5 (a)-(c), the zero field $\rho(T)$ does not show a large anomaly near 360 K (there may be evidence for

a subtle change in slope), which is consistent with the very small F cluster size at these temperatures. $T^*$ is also present in crystals. Fig. 4.5 (f) displays $\chi^{-1}(T)$ for an $x = 0.30$ single crystal, which is practically indistinguishable from the corresponding polycrystals.

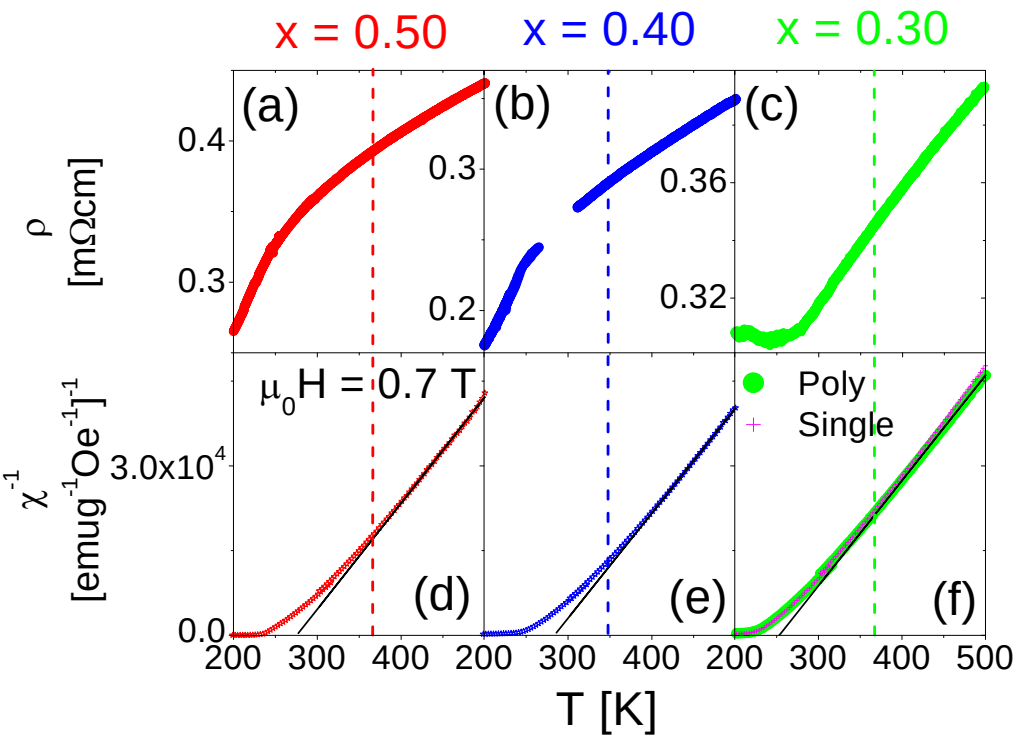


**Fig. 4.5** Temperature dependence of the zero field resistivity (top panel), and the inverse d.c. susceptibility ($H/M$) at 0.7 T (bottom panel). The data are for $x = 0.50$ (left panel), 0.40 (middle panel) and 0.30 (right panel). For the $x = 0.30$ case the (almost indistinguishable) susceptibility data are shown for both polycrystals and single crystals. Solid lines in (d), (e) and (f) are Curie-Weiss fits to the high temperature behavior. The vertical dashed lines mark the sharp turn on in correlation length ($T^*$).

## 4.4 Non-Griffiths-like characteristics of the clustered phase and revised phase diagram

From the data presented thus far, the existence of $T^*$ in LSCO is clear. In terms of determining whether the clustered state has the characteristics of a Griffiths phase, $\chi(T)$ is

of particular interest. As already mentioned, the upward deviation from C-W (Figs. 4.6 (d)-(f)) is at odds with the Griffiths model [25,26] as well as multiple experimental observations [16-20,22]. $\chi$ is expected to increase over C-W, at least at low $H$, where the susceptibility of the clusters is dominant, as shown in Fig. 4.2 (a). The $H$ dependence of $\chi^{-1}(T)$ is therefore important and is examined in detail in Fig. 4.6 for a representative polycrystalline sample ($x$ = 0.40). The data at applied fields of 0.07, 0.7 and 7 T overlap down to $T \approx T_C$, showing the same upward deviation from C-W at the same $T$* of 350 K. Data were acquired at fields down to only 1 mT, showing no change in form, no change in $T$*, and no evidence for any downward deviation from C-W in $\chi^{-1}$ vs. $T$. These data are in stark contrast to the predictions of the Griffiths model (e.g. Fig. 4.2 (a)), a point that will be returned to later.

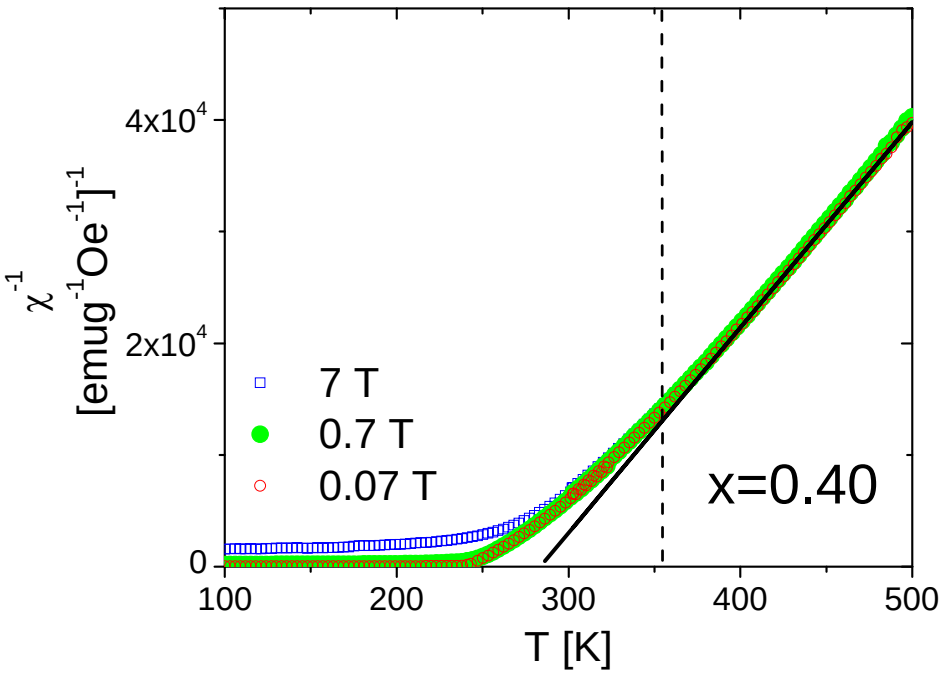


**Fig. 4.6** Temperature dependence of the inverse d.c. susceptibility ($H/M$) of an $x$ = 0.40 polycrystal for applied fields of 7 T, 0.7 T, and 0.07 T. The vertical dotted line denotes $T$*.

Taking the $T^*$ determined from our most sensitive probe (i.e. $\xi(T)$) and adding them to our previously determined magnetic phase diagram [8], we obtain Fig. 4.7. This figure highlights the doping independence of $T^*$, in addition to the fact that $T^*$ does not correspond to the maximum $T_C$. Although precise determination of $T_C^{Max}$ is hindered by the difficulty in preparing fully oxygenated specimens at $x > 0.5$-0.7, the maximum values reported (280-320 K [28-30]) are far below our observed $T^*$ of ~360 K. From the data of Figs 4.4-4.7 we can draw two firm conclusions; (i) a clustered state occurs below a well-defined temperature in the F portion of the phase diagram, with a clear signature in SANS, $\chi(T)$, and NMR and (ii) the characteristics of this state differ significantly from the Griffiths predictions. We therefore conclude that although the Griffiths model seems to apply to many doped magnetic systems [14,17-20,22], it is not universally applicable to the doped oxides.

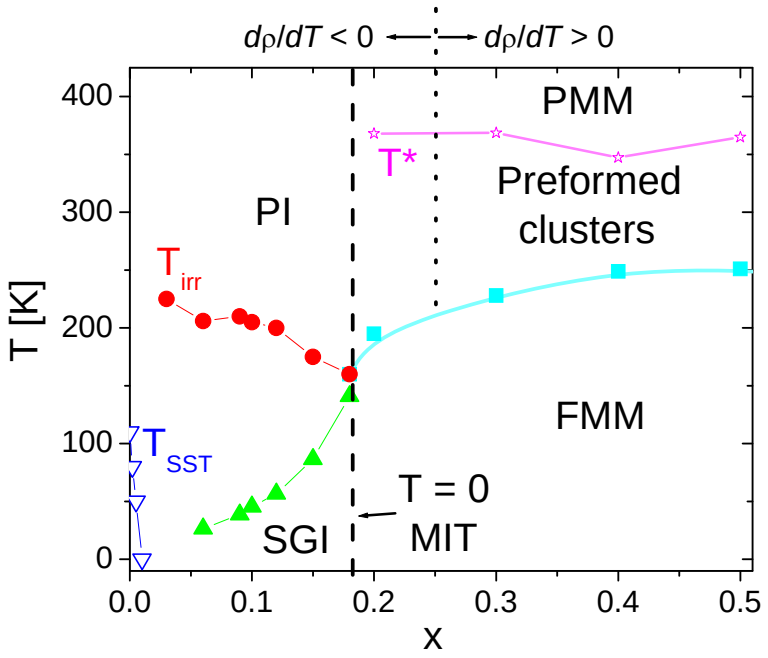


**Fig. 4.7** Revised magnetic phase diagram of $La_{1-x}Sr_xCoO_3$ showing the new regime between $T^*$ and $T_C$ where preformed magnetic clusters exist. $T_{irr}$, and $T_{SST}$ (see ref [8]) are the irreversibility temperature and spin-state transition temperature, respectively. PMM, FMM, PI, SGI and MIT denote paramagnetic metal, ferromagnetic metal, paramagnetic insulator, spin/cluster-glass insulator and metal-insulator transition.

## 4.5 Open questions

One puzzling aspect of this observation is the fact that the cobaltites might be considered better candidates than the manganites for direct comparisons to the Griffiths model. This is because the Griffiths model was originally developed for Ising systems, i.e. hard materials, as mentioned in section 4.2, and cobaltites have much larger magnetocrystalline anisotropies (as will be discussed in Chapter 6) compared to the manganites, which are usually very soft. Although we cannot provide definitive explanations for all aspects of this clustered state, the existence of $T^*$ is certainly in agreement with many phase separation scenarios, and we can speculate on the origin of some of the observed features. For instance, the upward deviation from C-W in the $\chi^{-1}(T)$ data (also seen in other work [9,15]) could be due to AF interactions, which would favor antiparallel alignment of neighboring clusters, suppressing $\chi$. In fact, recent muon spin relaxation measurements on $LaCoO_3$ [31] indicate AF coupling between magnetic excitons (which are thought to be the precursors to F clusters in LSCO) and the surrounding matrix. In addition, the possible dynamic nature of this regime [9] may have to be taken into account to understand $\chi(T)$. In terms of a proposed origin for the phase separation that occurs on cooling below $T^*$, the stochastic fluctuations in local composition that must occur in any randomly doped system at such short length scales (see Figs. 4.4 (d)-(f)) should not be ignored, which will be discussed in great detail in Chapter 5 and is proposed to be the origin of nanoscopic phase separation in LSCO. We believe that it is possible that the local ordering temperature in Sr rich clusters at global compositions of order $x = 0.5$, which are fully oxygenated, could exceed that seen in much higher doped samples, which are difficult to fully oxygenate, leading to a $T^*$ in excess of the apparent $T_C^{Max}$, as observed.

In summary, in this chapter we have presented neutron scattering and magnetometry data on the canonical doped perovskite cobaltite, LSCO, revealing the formation of short-range ordered ferromagnetic clusters at a well-defined temperature of 360 K. Although not fully understood, this phase separated state exhibits behavior quite distinct from that of a Griffiths phase, demonstrating that the Griffiths model is not universally applicable to complex oxides exhibiting preformed ferromagnetic clusters, despite its success in describing the behavior of many randomly doped oxides.

# Chapter 5
# Origin of magneto-electronic phase separation (MEPS) in $La_{1-x}Sr_xCoO_3$ single crystals and a revised phase diagram

In this chapter, we attempt to determine the origin of MEPS in $La_{1-x}Sr_xCoO_3$ (LSCO) by applying a variety of experimental techniques including heat capacity, small angle neutron scattering, transport and magneto-transport. It is found that there exists a finite doping range over which MEPS occurs. The doping range determined from different experimental techniques is found to be in good agreement. Also, this same doping range is reproduced by statistical simulations incorporating local compositional fluctuations. The excellent agreement between experimental data and statistical simulations leads to the conclusion that the MEPS in LSCO is driven solely by inevitable local compositional fluctuations at nanoscopic length scales, as first mentioned in Chapter 4. Such a conclusion indicates that nanoscopic MEPS is doping fluctuation-driven rather than electronically-driven in LSCO. Such a model might also be applicable to the nanoscopic MEPS in other randomly doped materials. Besides that, an abundance of new information obtained via heat capacity, including a discontinuity in Debye temperature accompanying the insulator-metal transition, and a large electron mass enhancement in the metallic state is also discussed in detail. The effect of microscopic magneto-electronic phase separation on electrical transport in LSCO is also studied. It is demonstrated (i) that the $T = 0$ metal-insulator transition can be quantitatively understood using double exchange-modified percolation theory, and, (ii) that the onset of a phase-pure low $T$ ferromagnetic state at high $x$ has a profound effect on the *high T* transport due to a crossover in the nature of the spin fluctuations.

## 5.1 MEPS limits determined from heat capacity in LSCO

As mentioned in section 1.2 and 1.3, due to its observation in a large number of materials and the key role it plays in some of their most attractive properties (e.g. colossal magnetoresistance [1-3] and high temperature superconductivity [4]), MEPS is an active research area in complex oxides [5,6]. As discussed in section 1.3.2 and Chapter 4, the LSCO system has been studied intensively by numerous techniques (e.g. neutron

diffraction (ND) [7], nuclear magnetic resonance (NMR) [8-11], small-angle neutron scattering (SANS) [12-14], and inelastic neutron spectroscopy (INS) [15-17], as well as bulk probes such as magnetometry [18-23], transport and magnetotransport [13,18,19,23-28], thermopower [18,29], etc.), many of which have been applied to single crystals. Specific heat ($C_P$) is a bulk probe that has been studied in less detail, particularly for crystals.

As mentioned in section 1.3.1 and Chapter 3, heat capacity provides vital direct information on lattice dynamics, conduction electrons, magnetism, etc., (as aptly demonstrated by the work on the manganites [1-3,6,30]), however, it has been studied only sporadically in the cobaltites. Undoped polycrystalline $LaCoO_3$ was studied via heat capacity [31-33] to probe the well-known spin-state transition [34], as discussed in detail in Chapter 3. Scattered reports at specific doping values of $Ln_{1-x}AE_xCoO_3$ ($Ln$ = lanthanide, $AE$ = Sr or Ca) compounds have appeared [35-37], but systematic heat capacity work on $La_{1-x}Sr_xCoO_3$ is limited, and, to the best of our knowledge, restricted to polycrystalline samples [38,39]. Detailed studies on the highest quality single crystals available are advantageous in terms of unambiguously determining intrinsic magnetic phase separation effects, particularly given the evidence of extrinsic chemical segregation effects in polycrystals at low processing temperatures [40,41].

In this section we provide a detailed and systematic study of the specific heat of LSCO single crystals over a wide temperature ($0.35\ \text{K} \leq T \leq 270\ \text{K}$) and magnetic field range (up to 9 T), at a total of 11 doping values ($0.00 \leq x \leq 0.30$), i.e., $x = 0.00$, 0.05, 0.10, 0.15, 0.17, 0.18, 0.19, 0.20, 0.22, 0.25 and 0.30. A comprehensive analysis of the data provides a wealth of new information, particularly with respect to the MEPS, which turns out to be directly probed by specific heat. The various contributions to $C_P(T)$ can be tracked with $x$, providing a detailed picture of the evolution of the phase-separated state with doping. Most importantly, the data provide unequivocal evidence for the surprising result that the MEPS in LSCO is confined solely to a well-defined doping range ($0.04 < x < 0.22$). This observation is consistent with recent NMR studies [42] and other techniques including SANS [28] and magnetotransport, which will be discussed in detail in section 5.2 and 5.5.

### 5.1.1 Global temperature behavior in the heat capacity of LSCO

The global temperature dependence (1.8 K ≤ $T$ ≤ 270 K) of the zero magnetic field $C_P$ is shown in Fig. 5.1 for all 11 doping values studied. The overall shape of $C_P(T)$ is as expected, the high $T$ limiting value being consistent with the classical value of 3$R$ per atomic site in the formula unit, where $R$ is the molar gas constant. The most notable high $T$ feature is the clear "lambda anomaly" at $T_C$ for the higher dopings, as expected for long-range ordered FMs [44,45]. Surprisingly, a noticeable feature is found *only* for $x$ = 0.30, 0.25 and 0.22 samples. $x$ = 0.20, 0.19, and 0.18 samples show no large anomaly at the ordering temperature [46] despite the fact that they exceed the critical doping for long-range FM order ($x_C$ = 0.17-0.18), and apparently exhibit a well-defined $T_C$ in bulk magnetometry [26].

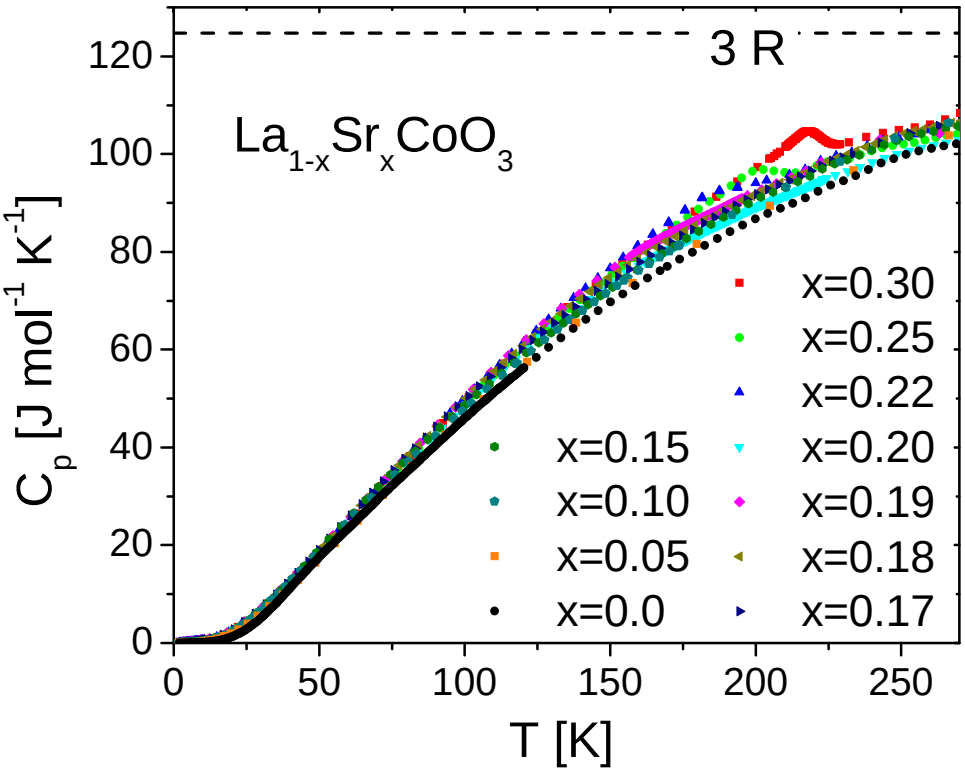


**Fig. 5.1** Temperature dependence of the zero field specific heat (1.8 K ≤ $T$ ≤ 270 K) of 11 $La_{1-x}Sr_xCoO_3$ single crystals with 0.00 ≤ $x$ ≤ 0.30. The horizontal dashed line indicates the value of 3R per atom.

To demonstrate this behavior of the "lambda anomaly" more clearly, Fig. 5.2 (a) shows a "close-up" of the region 100 K $\leq T \leq$ 275 K for $x$ = 0.30, 0.25 and 0.22, illustrating that the $C_P$ anomaly becomes progressively weaker as $x$ decreases, eventually becoming indistinguishable from the "background" at $x < 0.22$. This is seen more clearly by subtracting a smooth background (excluding the region around $T_C$) using a third-order polynomial, to extract the excess magnetic heat capacity, $\Delta C_P(T)$, as shown in Fig. 5.2(b). The systematic decrease in magnitude with decreasing $x$ is evident from this plot and can be quantified by calculating the magnetic entropy associated with the FM ordering transition:

$$S_{Mag} = \int_{T_1}^{T_2} \frac{\Delta C_P}{T} dT \qquad (5.1),$$

where $T_1$ and $T_2$ define a temperature interval straddling $T_C$, e.g. 125 to 275 K (see Fig. 5.2(b)). Such an analysis results in $S_{Mag}$ = 0.60, 0.59 and 0.52 $Jmol^{-1}K^{-1}$ at $x$ = 0.30, 0.25 and 0.22, respectively, all of which are well below the expected full spin entropy of $R \ln(2S + 1)$, where $S$ is the spin of the Co ion. This point will be returned to below. Fig. 5.2 (b) also shows that the anomaly associated with the FM ordering broadens, and becomes more symmetric in shape, as $x$ is decreased. At $x$ = 0.30 the anomaly has the characteristic "lambda" shape associated with a conventional second order FM to paramagnetic phase transition, while at lower $x$ it evolves into an almost symmetric peak. The full width at half maximum of the peak correspondingly increases from 20.1 K at $x$ = 0.30 to 29.7 K at $x$ = 0.22. These trends (i.e. decreasing magnitude [39] and increasing width with decreasing $x$) are also evident in the high $q$ (i.e. $q$ = 0.049 $Å^{-1}$) magnetic SANS cross section, $d\Sigma/d\Omega$ [28]. As first mentioned in section 2.3.4.2, this is the so-called "critical scattering" associated with the increasing spin fluctuations and diverging magnetic correlation length as $T \rightarrow T_C^+$, and the development of long-range order and suppression of spin-wave excitation at $T \leq T_C$ [13,28], which will be discussed in more detail in section 5.2 for each doping. We note that the significant difference between the peak temperatures in $\Delta C_P(T)$ and $d\Sigma/d\Omega(T)$ (e.g. for the same $x$ = 0.30 sample in Figs. 5.2(b,c)) could be due to the relatively poor temperature stability and sample/thermometer coupling in the latter measurement.

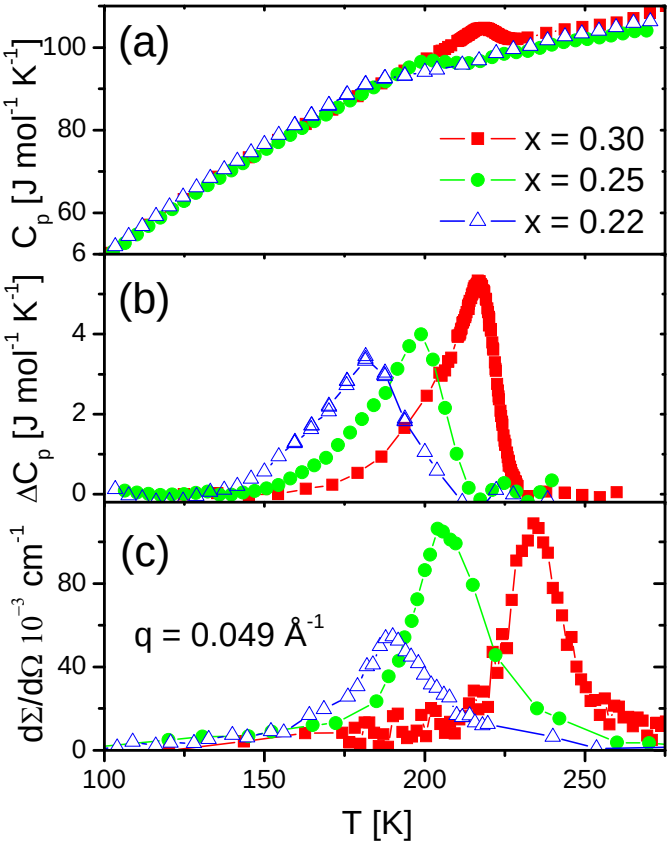


**Fig. 5.2 (a)** Expanded view of the temperature dependence of the specific heat (Fig. 5.1) for $x$ = 0.22, 0.25 and 0.30 single crystals (i.e. those that exhibit anomalies at $T_C$). **(b)** Excess (magnetic) specific heat extracted from the data in (a) by subtracting a smooth background as described in the text. **(c)** High $q$ ($q$ = 0.049 Å$^{-1}$) small-angle neutron scattering absolute magnetic cross section for comparison.

These observations from Figs. 5.1 and 5.2 clearly reveal two regimes of behavior separated by a critical doping value of $x$ = 0.22. Samples with $x >> 0.22$ exhibit a large $C_P$ anomaly at $T_C$ with the classical lambda form, and a sharp well-defined critical scattering peak in SANS, i.e. they exhibit features associated with conventional FMs. At $x$ = 0.22 we observe a smaller, broader, feature in both $C_P$ and SANS, while at $x < 0.22$ the anomaly in $C_P$ is very weak [46]. As discussed in more detail below, we believe that these data indicate that $x$ = 0.22 marks an upper limit for the magneto-electronic phase

separation in LSCO, i.e. a phase-pure FM state exists at $x \geq 0.22$, which is in agreement with our recent SANS analysis [28] and will be discussed in section 5.2. Samples with $x \geq 0.22$ thus exhibit a clear lambda anomaly, although the spin entropy removed through the ordering transition is reduced in comparison to the expected value due to pre-formation of FM clusters as observed in our prior SANS work [14], and discussed in Chapter 4. In the interval $0.18 < x < 0.22$ long-range FM order certainly exists (the magnetic correlation length is still observed to diverge as $T \rightarrow T_C^+$ [28]) but the FM phase fraction is below 100 %, i.e. MEPS is active and the system forms a percolated FM network in a non-FM (isolated cluster containing) background. This picture explains both the decrease in the magnitude of the peak value of $\Delta C_P$ and the peak width as $x$ is decreased. When the FM phase fraction is less than one, coexistence of the long-range order in the percolated FM network with short-range order in the isolated FM clusters naturally leads to a broad distribution of local ordering/freezing temperatures, resulting in weaker, broader, features in $C_P(T)$ and $d\Sigma/d\Omega(T)$. This is also consistent with the broad distribution in local internal hyperfine fields in recent NMR investigations [42]. We will see in the next section that analysis of the low $T$ specific heat provides further evidence for an upper limit for the phase-separated regime at $x = 0.22$.

### 5.1.2 Low temperature behavior in the heat capacity of LSCO

The lower $T$ region ($1.8 \text{ K} \leq T \leq 10 \text{ K}$) is shown in more detail in Fig. 5.3 for 8 representative samples, although all 11 were measured. As is done in chapter 3, the data are plotted as $C_P/T$ vs. $T^2$ to test for a temperature dependence of the form:

$$C_P(T) = \gamma T + \beta T^3 \qquad (5.2),$$

i.e. only electronic ($\gamma T$) and lattice ($\beta T^3$) contributions to $C_P$. The electronic contribution, $\gamma$, is given in a free electron model by $\gamma = \pi^2 k_B^2 N(E_F)/3$, where $N(E_F)$ is the density-of-states at the Fermi level, and the lattice contribution, $\beta$, is given in the Debye model by $\beta = 234 N k_B/\Theta_D^3$, where $N$ is the number of ions/mole and $\Theta_D$ is the Debye temperature. It is clear from Fig. 5.3 that at $x = 0.30$, i.e. deep in the FM metallic state, Eq. (5.2) is indeed a good description of the data. We found that addition of a $T^5$ term to the lattice part of $C_P(T)$ was not required to achieve an adequate fit. (Note that the highest temperature used in this analysis (10 K) is a factor of 40-50 below $\Theta_D$). The observed intercept (i.e. $\gamma$) is

very large, as will be discussed in detail below. This situation changes rapidly as $x$ is decreased. The electronic contribution decreases as $x$ decreases, as expected due to the approach to the metal-insulator transition, but this is accompanied by increasingly obvious systematic deviations from Eq. (5.2). In fact, it can be seen from Fig. 5.3 that the data deviate downwards from simple linear behavior on the $C_P/T$ vs. $T^2$ plot, suggesting an additional contribution to $C_P(T)$ with a $T$ dependence weaker than $T^3$. This feature is in fact visible in previously published data on polycrystals but was not discussed in detail [38,39]. As the simplest possible means to quantify this additional contribution we attempted to fit the data by adding a single power law term to Eq. (5.2), i.e. we added a term of the form $CT^n$, $n$ (and $C$) being allowed to vary with $x$. This was found to provide a good fit to the data with $n$ = 2.10 ± 0.16 for $x$ values of 0.05, 0.10, 0.15 and 0.17, suggestive that $n$ = 2, i.e. these data can be described with an additional $BT^2$ term in $C_P(T)$. The solid lines in Fig. 5.3 are thus fits to:

$$C_P(T) = \gamma T + BT^2 + \beta T^3 \qquad (5.3),$$

where $B$ is a constant for a given doping value. This is found to describe the data very well for $0.05 \leq x \leq 0.30$.

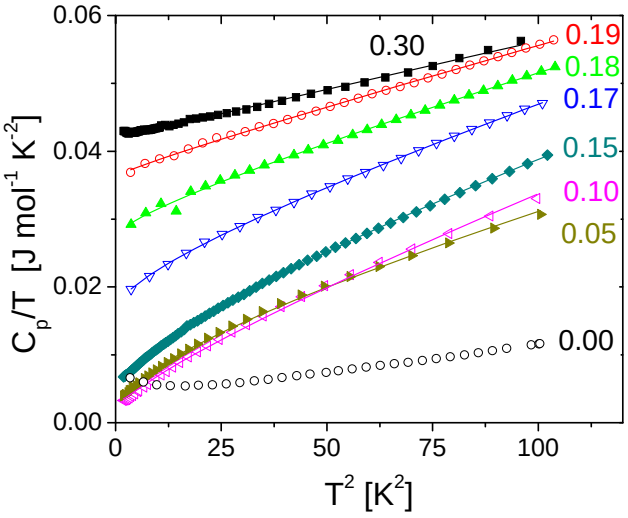


**Fig. 5.3** Temperature dependence of the specific heat (1.8 K ≤ $T$ ≤ 10 K) of 8 representative $La_{1-x}Sr_xCoO_3$ single crystals plotted as $C_P/T$ vs. $T^2$. The solid lines are fits to $C_P(T) = \gamma T + BT^2 + \beta T^3$, a model that is described in detail in the text. The resulting parameters are plotted as a function of doping in Fig. 5.4.

Before continuing to discuss the $x$ dependence of the parameters γ, $B$, and β, and the origin of the $BT^2$ term, we should note that $C_P(T)$ at $x = 0.00$ (the end-member, $LaCoO_3$), is fundamentally different from all of the doped samples [47], as discussed thoroughly in Chapter 3. As a final note on the data of Fig. 5.3, it is important to point out that an FM spin-wave contribution (often found to be of the form $T^{3/2}$) was not required to fit the data up to 10 K. We believe that this is consistent with the significant magnetocrystalline anisotropy in LSCO [26] which should lead to a gapped spin-wave dispersion relation, and the likely absence of significant magnon excitation at such low $T$, as will be discussed in Chapter 6.

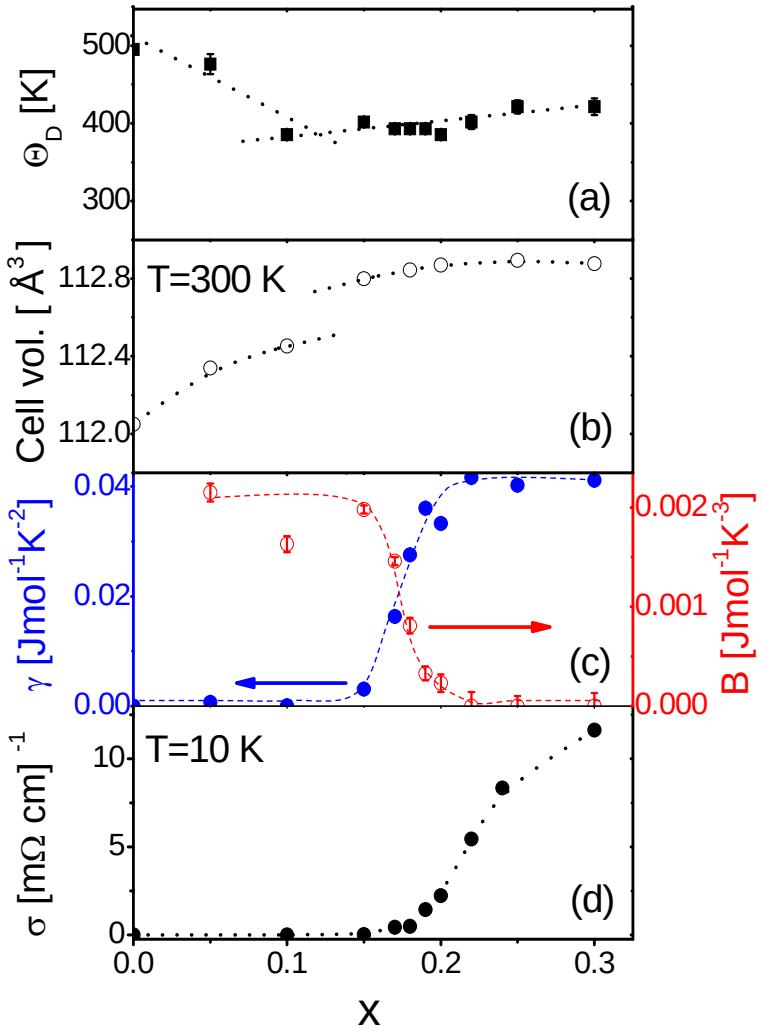


**Fig. 5.4** Doping dependence of **(a)** the Debye temperature, **(b)** the 300 K rhombohedral unit cell volume (from X-ray diffraction), **(c)** the electronic (γ) and $T^2$ contributions ($B$) to the specific heat, and **(d)** the 10 K conductivity. Dashed lines are guides to the eye.

The doping dependence of the three contributions to $C_P(T)$, i.e. $\Theta_D$, $\gamma$, and $B$, are shown in Figs. 5.4(a) and (c). Considering $\Theta_D(x)$ first, we see that the overall magnitude (380 – 500 K) is typical for perovskite oxides of this type and is in accord with measurements on comparable manganites such as $La_{1-x}Sr_xMnO_3$ [1,3,48,49], particularly single crystals [1,49]. The most surprising feature is the discontinuity in slope between $x$ = 0.10 and 0.15. For comparison to $\Theta_D(x)$, the doping dependence of the room temperature unit cell volume of the crystals studied is also shown in Fig. 5.4(b), as first shown in section 2.2.1, the discontinuity in the slope of $\Theta_D(x)$ clearly occurring at a similar $x$ value to the discontinuity in cell volume, which suggests a significant change in lattice structure around $x$ = 0.125. It is natural to correlate this with the known discontinuity in unit cell parameters between $x$ = 0.10 and 0.15 (for both the lattice parameter, $a$, and rhombohedral angle, $\alpha$), which was noticed as early as 1968 by Raccah and Goodenough [50]. In light of the proximity to the critical doping value for the insulator-metal transition, and the crossover to true long-range FM order, Goodenough [50] interpreted the discontinuity in lattice parameters as evidence for coexistence of hole-rich FM metallic and hole-poor non-FM insulating regions, the two phases having distinct lattice parameters. We now know from direct measurements [8,13,16,17] that such magnetic phase separation does indeed take place, although the original interpretation in terms of gross segregation of Sr dopants is too literal. We mention parenthetically that the other obvious origin of such a lattice discontinuity would be the well-known spin-state transition of the $Co^{3+}$ ion, which alters the $t_{2g}/e_g$ orbital occupancy and hence the lattice parameters. However, at 300 K the $Co^{3+}$ ions are already excited from the LS state to a finite spin-state meaning that the spin-state transition is unlikely to dominate the room temperature $x$ dependence of the cell volume. When the cell volume is examined as a function of doping at low $T$ (e.g. 2 K [7]) a large discontinuity *is* observed at low $x$ (between $x$ = 0.00 and 0.10), consistent with the known stabilization of the finite spin-states of the $Co^{3+}$ ion with only light doping. Although it is tempting to suggest that it is the same lattice anomaly which gives rise to the discontinuities in Figs. 5.4(a) and (b), it is not clear how one then understands the details of the observed $\Theta_D(x)$. The $\Theta_D(x)$ we observe is however similar to that seen in $La_{1-x}Sr_xMnO_3$ single crystals [1,49], where it was interpreted in terms of lattice softening induced by dynamical short-range Jahn-

Teller distortions. Such distortions have also been implicated in LSCO [15,16] and could well play the key role in determining $\Theta_D(x)$. Finally, although the correlation between Figs. 5.4(a) and (b) is quite convincing it should be mentioned that a small, low $T$ Schottky contribution to $C_P(T)$, as discussed in Chapter 3, would provide additional specific heat at low $T$ perhaps resulting in extraction of an erroneously high $\Theta_D$ and providing an alternative explanation for Fig. 5.4(a).

We now turn to the doping dependence of the electronic contribution as shown in Fig. 5.4(c) (left axis, solid points). As expected, $\gamma \approx 0$ at low $x$ (due to the non-metallic nature of low doped LSCO), then increases near the MIT before abruptly saturating at $x = 0.22$. The first point to be made about these data is that the saturation of $\gamma$ at $x = 0.22$ is further evidence for the onset of a phase pure FM metallic state at $x = 0.22$ with essentially 100 % FM phase fraction. These data are therefore consistent with the analysis of the FM ordering anomaly presented above (i.e. Figs. 5.1 and 5.2). We will see below that there exists even further evidence for the validity of this picture. The second noteworthy point about $\gamma(x)$ is that it provides further, very direct, evidence of the percolative nature of the MIT, which is expected in the phase separation model [19,26] and will be discussed in detail in section 5.5. This is seen clearly by comparing the doping dependence of the low $T$ conductivity ($\sigma(x)$ [26], Fig. 5.4(d)) with $\gamma(x)$. The more rapid increase in $\gamma(x)$ beyond the critical doping value results in a region near $x = 0.18$ (i.e. just beyond $x_C$) where $\gamma$ is high (67 % of its saturation value) while the conductivity remains very low (only 4% of its value at $x = 0.30$). Such a large electronic contribution to the specific heat in a system with low conductivity clearly argues for a spatially inhomogeneous charge carrier distribution with hole-rich regions embedded in an insulating matrix, consistent with the accepted MEPS picture for LSCO.

The next point to discuss is the very large magnitude of $\gamma$ at high $x$, i.e. in the region where we are dealing with a homogeneous phase-pure FM metallic state. Above $x = 0.22$, $\gamma$ reaches 41 $mJmol^{-1}K^{-2}$, an order of magnitude larger than similar manganite values, e.g. 3.5 $mJmol^{-1}K^{-2}$ in $x = 0.30$ $La_{1-x}Sr_xMnO_3$ single crystals [1,49]. The observed $\gamma$ in highly-doped LSCO is in fact well within the range of what would typically be considered a heavy fermion system. It should be noted though that our value is quite consistent with other reports on polycrystalline LSCO which found $\gamma$ = 41-43 $mJmol^{-1}K^{-2}$ at $x$ = 0.3

[38,39], $\gamma = 48$ mJmol$^{-1}$K$^{-2}$ at $x = 0.33$ [35], and $\gamma = 46$ mJmol$^{-1}$K$^{-2}$ at $x = 1.0$ [51], as well as a solitary single crystal measurement of 49 mJmol$^{-1}$K$^{-2}$ at $x = 0.3$ [52]. An important point to consider here is whether there is another contribution to $C_P(T)$ that is linear in $T$, i.e. whether $\gamma$ could be composed of two contributions, one electronic, the other of some other origin, leading us to over-estimate the electronic contribution. One obvious source of such an effect is magnetism. It is well-known that spin-glasses can exhibit a linear term in $C_P(T)$ and in fact it has been discussed in prior work on polycrystalline LSCO [38] that this may be responsible for the large $\gamma$. The analysis presented above clearly suggests that for $x \geq 0.22$ (i.e. the region with the largest $\gamma$ values) we have a phase-pure FM metallic state, strong evidence that we are *not* over-estimating $\gamma$ due to an additional spin-glass contribution. Neutron scattering data demonstrate persistence of FM to low $T$ in this region, with no suggestion of a re-entrant spin-glass phase. We would expect any glassy contribution to $\gamma$ to show up in the low $x$ region, where $\gamma$ is in fact negligible. Another source of an additional linear contribution to $C_P(T)$ has been discussed in the context of non-stoichiometric $LaMnO_{3+\delta}$ materials [53], which were found to have large $\gamma$ values (up to 23 mJmol$^{-1}$K$^{-2}$) even though they were electrically insulating. This effect was ascribed to a large density of *localized* states near $E_F$, the charge carriers being localized by magnetic or cationic disorder. This effect is not however a viable explanation for the anomalously large $\gamma$ in LSCO. The full $x$ dependence shown in this section (Fig. 5.4(c)) clearly shows no such effect at low $x$, i.e. $\gamma$ is indeed zero when the system is insulating. All of this analysis argues that the $\gamma T$ contribution to $C_P(T)$ in LSCO is truly electronic in origin.

Applying the free electron formula, $\gamma = \pi^2 k_B^2 N(E_F)/3$, we estimate $N(E_F) \approx 17.5$ states/eV/unit cell for $La_{0.7}Sr_{0.3}CoO_3$, which, although much larger than typical single crystal manganites such as $La_{0.7}Sr_{0.3}MnO_3$ (where $\gamma$ implies $N(E_F) \approx 1.4$ states/eV/unit cell) [1,49], is consistent with the low $T$ spin-lattice relaxation rate measured by NMR [11], where the conduction electrons contribute via the orbital relaxation mechanism. First principles electronic structure calculations predict much smaller $N(E_F)$ for LSCO however [54], and $\gamma = 7.5$ mJmol$^{-1}$K$^{-2}$ [51]. All of this indicates a significant mass enhancement, as will be calculated below.

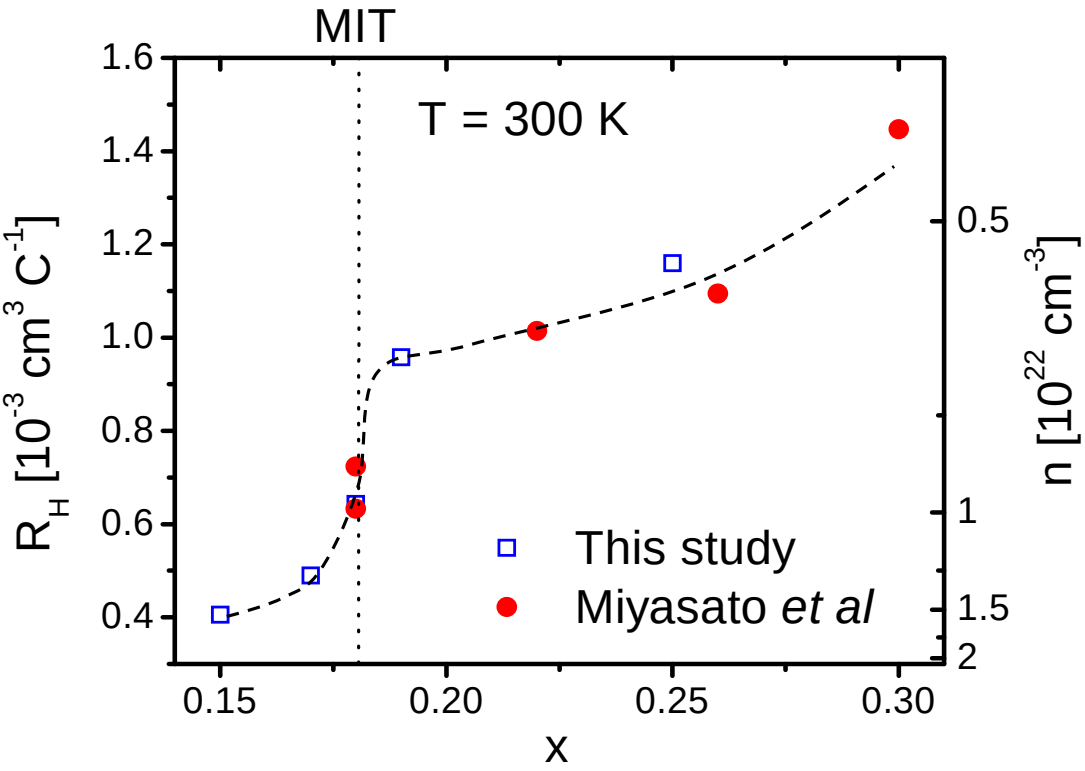


**Fig. 5.5** Doping dependence of the 300 K ordinary Hall coefficient of $La_{1-x}Sr_xCoO_3$ single crystals. Open squares are from this study and the solid circles are taken from Miyasato *et al* [52]. The right axis shows the equivalent electron density, estimated from $n = 1/R_He$. The dotted line is a guide to the eye.

In order to further quantify this we performed room temperature measurements of the ordinary Hall coefficient in order to directly estimate the charge carrier density, which, when combined with the $N(E_F)$ from γ, provides an estimate of the effective mass, $m^*$. The $x$ dependence of the 300 K ordinary Hall coefficient, $R_H$, is shown in Fig. 5.5, along with similar data from the work of Miyasato *et al* [52] on LSCO single crystals [55]. Note that the sign of the Hall coefficient corresponds to hole conduction, as expected. The data reveal a striking change in character near the critical doping value for the insulator-metal transition. Below this value, $R_H$ is small and strongly $x$-dependent, while above it, $R_H \approx 1.0 - 1.4 \times 10^{-3}$ cm$^3$C$^{-1}$, weakly dependent on $x$ and in reasonable agreement with prior work on manganites [1,3]. It is clear from these data that the

ordinary Hall effect is suppressed below the percolation threshold, likely due to the known magneto-electronic phase separation effects, which result in strongly inhomogeneous conduction paths [55-59]. We believe that interpretation of the Hall data at low $x$ will therefore require a detailed study of the interplay between the Hall coefficient, the phase separation, and the inhomogeneous current distribution, which is beyond the scope of this section. Focusing on the high $x$ region we see that the $R_H$ values correspond to carrier densities, $n = 1/R_H e$ of 4-7 $\times$ $10^{21}$ $cm^{-3}$, corresponding to ~ 0.3 holes per Co ion, in reasonable agreement with other perovskites at similar doping levels [1,3]. Using the free electron relation between $N(E_F)$ and $n$, then gives $m^* = \hbar^2 \pi^{4/3} N(E_F)/(3n)^{1/3}$, leading to $m^* \approx 43 m_e$ for $x = 0.3$. In agreement with the work of Balamurugan *et al* on $SrCoO_3$ [51], we interpret this as being due to electron correlation effects in the relatively narrow $\sigma^*$ band, similar to $SrRuO_3$ [60]. It should be noted that $\gamma(x)$ shows no evidence of an enhancement confined to the region near the insulator-metal transition in Fig. 5.4(c), indicating that we are not simply dealing with mass renormalization in the critical region, as often observed in doped Mott insulators [1].

The final discussion point from Fig. 5.4 is the doping dependence of the $T^2$ term, i.e. $B(x)$, as shown in Fig. 5.4(c). The most important insight into the origin of this contribution to $C_P(T)$ comes from the comparison between $B(x)$ and $\gamma(x)$. $B$ remains high out to doping values approaching the MIT ($x \approx 0.17$), beyond which it decreases smoothly to zero at $x = 0.22$. It is clear from these data that $B(x)$ and $\gamma(x)$ exhibit what is essentially a reciprocal relationship, the obvious implication being that $B(x)$ is associated with the non-FM phase. What we observe in Fig. 5.4(c) is thus phase conversion from insulating non-FM to metallic FM with increasing $x$. Such a conversion indicates $\gamma(x)$ and $B(x)$ must scale with the fraction of FM and non-FM phase, respectively, as will be used in section 5.4. Note that the signature of the non-FM phase (i.e. $B$) goes to zero at exactly $x = 0.22$, the point at which the signature of the metallic FM phase ($\gamma$) saturates. As we have argued in section 5.1.1 from $C_P$ anomaly, this is the point where the magnetically phase-separated regime ends and a phase-pure FM metallic state is entered.

The physical mechanism in the non-FM phase giving rise to the $T^2$ contribution to $C_P(T)$ warrants further discussion. Such $T^2$ terms have been observed before in manganites, particularly undoped $LaMnO_3$ [48]. $LaMnO_3$ is known from neutron

diffraction to be an A-type antiferromagnet (AF) (i.e. sheets of FM spins coupled AF) and it was shown that a reasonable form for the spin wave dispersion relation in such a spin structure does indeed lead to a $T^2$ contribution to $C_P(T)$ [48], and this was therefore taken as a plausible origin of this effect. This interpretation is not directly applicable to our case as undoped $LaCoO_3$ does not exhibit A-type, or any other type, of AF order, and $B$ remains finite even for $x > 0$. However, at least at $x = 0$, thermal excitation of simultaneous F and AF spin fluctuations has been observed in LSCO by INS [16], a simple interpretation being the existence of A-type AF fluctuations [16], as mentioned in Chapter 3. It is possible that these fluctuations are the origin of the $BT^2$ term we observe. Although these fluctuations were detected only at $x = 0$ in INS [16], signal to noise issues could have obscured them in lightly doped samples. Cornelius *et al* [61] also observed a $T^2$ contribution to $C_P(T)$ in electron doped $CaMnO_3$. As an extension of the idea presented by Woodfield *et al* [48] they interpreted the $T^2$ term as being due to long-wavelength excitations with both FM and AF components, due to the magnetic phase separation into nanometric FM droplets known to exist in that system [62]. This is very similar to our own situation and it is clear that additional theoretical work aimed at calculating $C_P(T)$ in systems of nanoscopic FM clusters in a non-FM matrix would be valuable. In terms of magnetism, the only other clear possibility would be the incommensurate behavior discovered by Phelan *et al* [17] and interpreted in terms of 7 site magnetopolarons. Observations of similar polarons [63,64] or excitons [65,66] have been made at light doping by several groups and it is likely that such entities exist in the non-FM regions at higher $x$. It is clear that a theoretical study of the possible contribution of such magnetic entities to $C_P(T)$ is urgently required, but in the absence of such work we are unable to make definitive comments on the plausibility of this explanation.

As a final comment we note that it is also possible that the $T^2$ term arises from some non-magnetic feature of the non-FM phase. Application of a 9 T magnetic field has little influence on $C_P(T)$, the change being 1.5 % at 1.8 K and -0.8 % at 10 K for $x = 0.10$, as shown in Fig. 5.6. This suggests that the $BT^2$ contribution is either non-magnetic in origin or arises from a magnetic mechanism that is not significantly modified by a 9 T magnetic field. Fields of this order have been observed to induce some level of FM cluster coalescence, and an accompanying increase in FM phase fraction, but isolated clusters

remain. This has been observed both in INS [67] and SANS [68] experiments. The absence of a strong field dependence does not therefore immediately rule out small clusters/polarons as the origin of the $T^2$ term. In any case, although the exact mechanism leading to the $T^2$ contribution to $C_P(T)$ remains unclear we can be definitive in ascribing it to the non-FM phase. The data of Fig. 5.4(c) therefore show that specific heat provides a very direct probe of the evolution of the MEPS with doping, the most important conclusion being the clear indication of an upper limit for phase separation at $x = 0.22$.

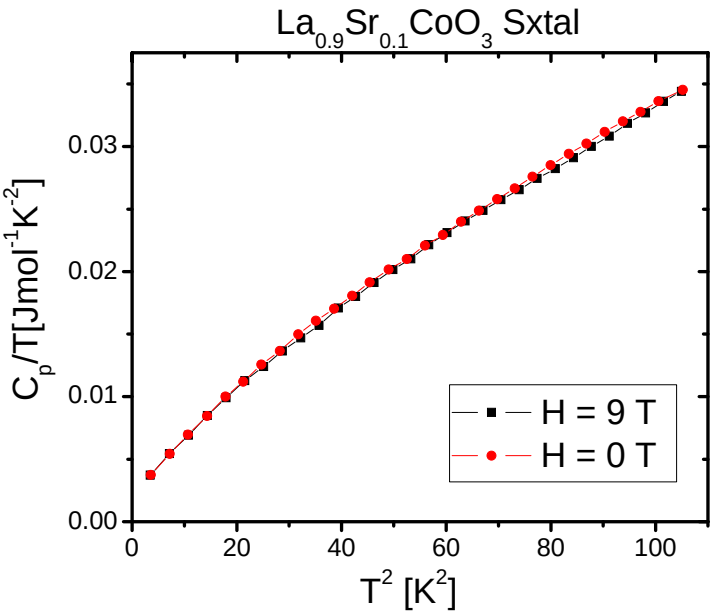


**Fig. 5.6** Temperature dependence of the specific heat (1.8 K ≤ $T$ ≤ 10 K) of a $La_{0.9}Sr_{0.1}CoO_3$ single crystal at fields of 0, and 9 T plotted as $C_P/T$ vs. $T^2$

### 5.1.3 Hyperfine contribution in the heat capacity of LSCO

Fig. 5.7 shows that extending the $T$ range of the measurement to 0.35 K provides considerable additional information. These data are again plotted as $C_p/T$ vs. $T^2$, using $x$ = 0.10 and 0.30 as representative compositions, although all samples with $x \geq 0.05$ show such an effect. Applied magnetic fields of 0, 3 and 9 T are shown. Note that $C_P$ increases with $H$ at low $T$, a point which will be returned to later. The important feature in the data is the large increase in $C_P(T)$ at the lowest temperatures, a feature which is in fact common in magnetic materials and has been observed in manganites [30,48,61,69]. This

feature is understood to be the high $T$ tail of a Schottky anomaly due to splitting of the nuclear energy levels. This is observable at these relatively high temperatures in magnetically ordered materials due to the large values of internal magnetic field present.

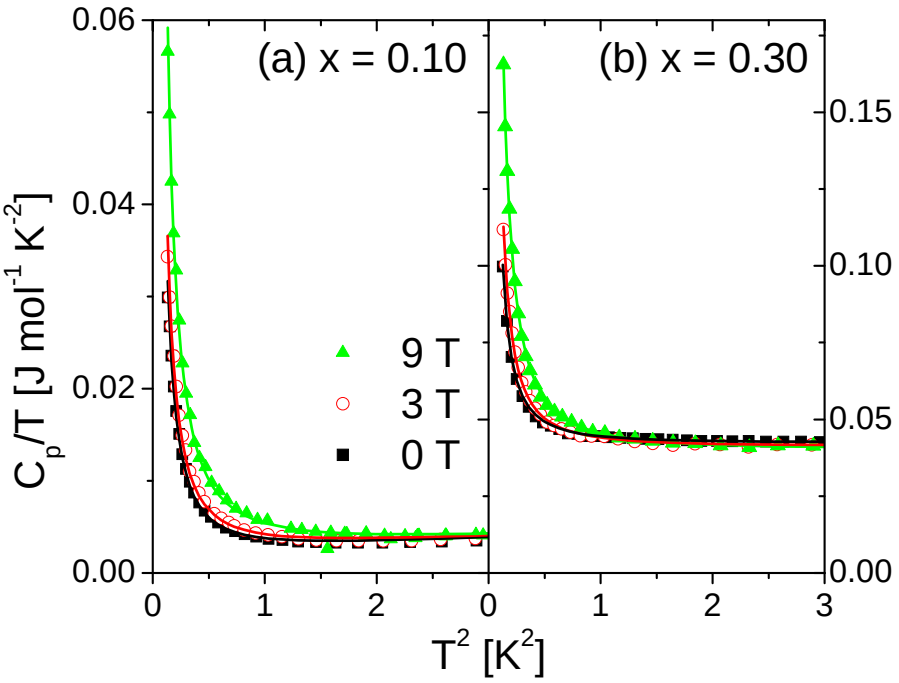


**Fig. 5.7** Temperature dependence of the specific heat (0.35 K ≤ $T$ ≤ 1.8 K) of **(a)** $x$ = 0.10, and **(b)** $x$ = 0.30 $La_{1-x}Sr_xCoO_3$ single crystals plotted as $C_P/T$ vs. $T^2$, in applied magnetic fields of 0, 3, and 9 T. The solid lines are fits to the model described in the text.

In essence the internal magnetic fields generated by the electron system generate a nuclear energy level splitting, which results in a two energy level system with $\Delta E = 2\mu_{Nuc}H_{hf}$ (we have used a nuclear spin, $I$ = 1/2 for the purposes of simple illustration), where $\mu_{Nuc}$ is the nuclear moment and $H_{hf}$ is the hyperfine field. The resulting two level system leads to a nuclear Schottky contribution to the specific heat ($C_P^{Nuc}$) of the form [70,71]:

$$C_P^{Nuc} = R\left(\frac{\Delta E}{k_B T}\right)^2 \frac{g_0}{g_1} \frac{\exp(\Delta E / k_B T)}{\left[1+\left(\frac{g_0}{g_1}\right)\exp(\Delta E / k_B T)\right]^2} \qquad (5.4),$$

where $g_0$ and $g_1$ are the degeneracies of the lower and higher energy levels and $\Delta E$ is the energy gap between these two levels. Such an equation is similar to Eq. (3.5) as mentioned in Chapter 3, except that the energy separation is driven by nuclear field in this case. This equation predicts a peak in $C_P(T)$ in the vicinity of 10 mK, meaning that the data of Fig. 5.7 are simply the high $T$ tail of this feature. In the limit $T >> \Delta E$, Eq. (5.4) reduces to $C_P^{Nuc} \approx A/T^2$, where the constant $A$ is related to $H_{hf}$ by [30,61,69,72]:

$$A = \frac{R}{3}\left(\frac{I+1}{I}\right)\left(\frac{\mu_{Nuc} H_{hf}}{k_B}\right)^2 \qquad (5.5).$$

Note that $I = 7/2$, and $\mu_{Nuc} = 4.64$ nuclear magnetons for $^{59}$Co, and that $H_{hf}$ is the hyperfine field at the Co site. The important point here is that the parameter $A$ provides a direct measure of the local internal field, allowing us to probe the magnetic ordering as a function of $x$. Addition of this nuclear Schottky contribution to Eq. (5.3) results in:

$$C_P(T) = \gamma T + BT^2 + \beta T^3 + \frac{A}{T^2} \qquad (5.6),$$

which generates the solid lines shown in Fig. 5.7, confirming that it is indeed a good description of the data. Note that although we now have four distinct contributions to $C_P(T)$, the final term in Eq. (5.6) is so dominant at low $T$ (for example, it contributes about 96 % of the heat capacity at 0.39 K for $x = 0.10$), the parameter $A$ can still be reliably determined.

The doping and magnetic field dependence of the $H_{hf}$ values extracted from $A$ (using Eq. (5.5)) are illustrated in Fig. 5.8. The field dependence rules out the possibility of paramagnetic impurities as the origin of this Schottky anomaly since in that case, application of magnetic fields of the order of 9 T should strongly suppress the heat capacity, exactly opposite to our observations. Previous zero field NMR measurements probing the $^{59}$Co nucleus revealed a broad peak centered at a frequency of approximately 172 MHz corresponding to an internal field of 17.1 T in the FM phase [8]. This is in good agreement with the value of $H_{hf}$ of 15.9 T at $x = 0.30$ (Fig. 5.8), demonstrating that at high $x$ the data of Fig. 5.8 are quantitatively consistent with the known features of the long-range FM ordering. The intriguing aspect of the data is the behavior in the lower $x$ region. Decreasing $x$ from 0.30 results in a decrease in $H_{hf}$ due to the weakening of the FM ordering, as expected, but we observe no clear feature at the critical doping value of $x$

= 0.17-0.18. Clearly this is due to the persistence of short-range FM ordering well below the critical composition, consistent with the general phase separation picture. The surprising feature of the data is the apparent vanishing $H_{hf}$ at a well defined doping value, estimated by extrapolation to be $x \approx 0.04$. This suggests that the short-range magnetic order from the FM clusters disappears abruptly at $x \approx 0.04$. We have already argued in section 5.1.1 and 5.1.2 that there exists a well-defined upper limit to the region over which phase separation occurs at $x \approx 0.22$, which is in fact qualitatively consistent with the theoretical work of Suzuki *et al* showing a crossover from a phase-separated to homogeneous state at high doping [73]. The data of Fig. 5.8 additionally suggest a *lower* limit of $x \approx 0.04$, defining an interval, $0.04 < x < 0.22$ over which MEPS is active. Complementary SANS data on the same crystals also show a clear onset of high $q$ scattering intensity around $x = 0.04$ [28], which will be further discussed in section 5.2. In section 5.4, we will use this unanticipated result that the phase separation is confined to a precise doping range as they key piece of evidence to argue that the phase separation is doping-fluctuation driven rather than being true electronic phase separation.

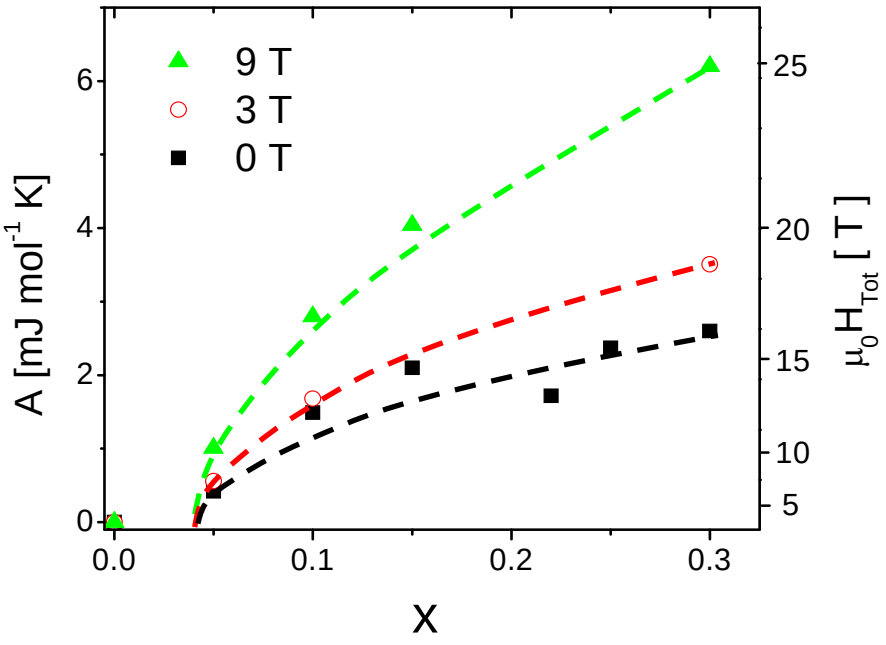


**Fig. 5.8** Doping dependence of the hyperfine field extracted from the nuclear contribution to the specific heat ($A$), as described in the text. Data are shown for applied magnetic fields of 0, 3, and 9 T. The dotted lines are guides to the eye.

There are certain aspects to this observation of a well-defined range over which phase separation occurs which warrant further discussion. The first of these is the lower limit of $x = 0.04$. A significant number of investigations, using techniques such as NMR [42], INS [64], muon spin relaxation [65,66], and susceptibility [63] have concluded that local magnetic entities are certainly present below this limit. These local magnetic entities have been given a variety of labels such as "magnetopolarons" [17], "spin polarons" [42], "magnetic excitons" [65,66] and "spin-state polarons" [64] but it is clear that they all describe magnetic inhomogeneity at low or zero doping. We do not believe that this is contradictory to the results presented in this chapter. It is our hypothesis that these entities are precursors [65,66] to the strongly FM correlated clusters observed in SANS and heat capacity, which are apparently only present in large enough quantities to be detected by SANS above $x \approx 0.04$. It is not currently clear exactly how the evolution from "polaron" to "cluster" takes place or exactly what the distinctions are between the two terms, although the presence, or otherwise, of magnetocrystalline anisotropy could play an important role. It could also be that the detection limits of the various experimental techniques is a factor that contributes significantly to this confusion, and this is obviously an area that would benefit from additional work. Another important point is that the range over which phase separation occurs in *polycrystalline* LSCO is distinctly larger than for single crystals. NMR studies suggest that the range in polycrystals could be as high as $0.00 < x < 0.50$ [8], significantly widened in comparison to the single crystals studied here. We believe that this is likely due to additional, extrinsic, Sr doping inhomogeneity due to incomplete solid-state reaction. It has been observed in prior work that the signatures of magnetic phase separation weaken with increasing firing temperature in polycrystalline samples [40,41], which fits with this picture. The single crystals, where the magnetic phase separation limits can be understood within the picture of purely random Sr distributions [28] are the ultimate limit of such studies.

## 5.2 MEPS limits determined from SANS in LSCO

As mentioned in section 2.3.4, SANS is a powerful tool in exploring the structure of materials on various length scales. As a direct technique, SANS is a sensitive probe in

detecting the phase fraction and therefore is extensively used to explore the MEPS in LSCO [12-14, 28]. In order to determine MEPS limits, samples of 8 doping values were measured by SANS at the NIST Center for Neutron Research at a wavelength of 6-8 Å, in the wave-vector range 0.003 $Å^{-1} < q < 0.2$ $Å^{-1}$. The doping evolution of two types of magnetic scattering, i.e. Porod scattering and Lorentzian scattering, as mentioned in section 2.3.4.2, were analyzed as below. The magnetic correlation length is also extracted from SANS, which will be used for the statistical simulation performed in section 5.3.

### 5.2.1 *q* dependence of SANS intensity in LSCO

Fig. 5.9 shows the $q$ dependence of the absolute cross-section at some typical temperatures for two representative dopings: (a) $x = 0.30$, i.e. deep in FM phase, which was first shown in Fig. 2.32 in section 2.3.4, and (b) $x = 0.15$, i.e. below the critical composition $x_C \approx 0.17$-$0.18$. Starting from $x = 0.30$ as shown in Fig. 5.9 (a), it can be seen that the scattering can be split into two parts: Porod scattering corresponding to long-range ordering at low $q$ proportional to $q^{-4}$, as illustrated by the dashed line, and Lorentzian scattering corresponding to short-range spin-correlations at high $q$. It can be seen that with decreasing temperature, long-range magnetic scattering at low $q$ (Porod scattering) starts to turn on at $T_C$ above the chemical background (scattering due to long-range defects such as twins), and becomes dominant at low temperature (20 K), indicating a long-range magnetic ordered state. On the other hand, with decreasing temperature, one can see that the Lorentzian scattering reaches a maximum at about $T_C$ and goes back to the high temperature value (303 K) at low $T$ (20 K). This is due to critical scattering, as discussed in section 2.3.4.2. The correlation length can be extracted from the Lorentzian fitting with Eq. (2.25), as mentioned in section 2.3.4 and shown in blue lines in Fig. 5.9. For both types of scattering, the magnetic contribution was isolated by subtracting the scattering at the highest temperatures (> 300 K).

For $x = 0.15$ as shown in Fig. 5.9 (b), the scenario is quite different. In the Porod scattering regime, there is no temperature dependence, suggesting there is no long-range magnetic ordering at this doping. On the other hand, strong temperature dependence: i.e. increasing scattering with decreasing temperature, can be seen in Lorentzian scattering, suggesting the existence of short-range magnetic ordering, possibly due to FM clusters.

To illustrate the full temperature dependence of these two types of scattering, two representative $q$ values from each type of scattering were chosen to demonstrate the tendency, as discussed below.

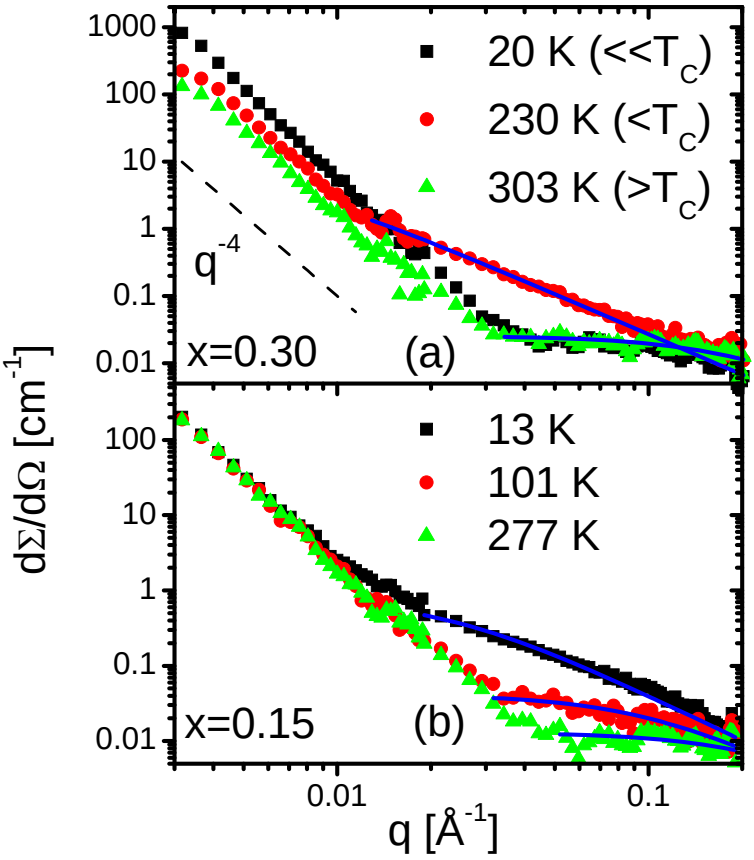


**Fig. 5.9** $q$ dependence of SANS intensity in $La_{1-x}Sr_xCoO_3$ for (a) $x$ = 0.30 at $T$ = 20 K, 230 K, and 303 K, (b) $x$ = 0.15 at $T$ = 13 K, 101 K, and 277 K. The black dash line is an illustration of $q^{-4}$dependence in the Porod scattering. The blue solid lines are fits to Lorentzian scattering, as described in the text.

### 5.2.2 *T* dependence of SANS intensity in LSCO

Figs. 5.10(a)-(f) plot the $T$ dependence of the low scattering wavevector ($q$ = 0.007 Å$^{-1}$) intensity ($[d\Sigma/d\Omega]_{low\ q}$), high $q$ (0.049 Å$^{-1}$) scattering intensity ($[d\Sigma/d\Omega]_{high\ q}$), and magnetic correlation length, $\xi$, for 8 single crystal samples. Crystals of $x$ = 0.30, 0.24,

0.22, and 0.20 show the onset of low $q$ scattering and a peak in $[d\Sigma/d\Omega]_{high\ q}$ at the Curie temperature, $T_C$. $[d\Sigma/d\Omega]_{low\ q}$ follows the Porod form ($d\Sigma/d\Omega \propto q^{-4}$) due to scattering from domains of size $D$, in the limit $q >> 2\pi/D$ [12]. Adherence to this form down to $q$ = 0.003 Å$^{-1}$ immediately implies that the domains exceed 2000 Å, i.e. truly long-range FM order [12,16,17], as mentioned in section 2.3.4.2. (We plot $x$ = 0.24, and 0.20 on the right axis for clarity purpose due to a scale issue; we believe the anomalously large $[d\Sigma/d\Omega]_{low\ q}$ at $x$ = 0.24 is not a pure magnetic contribution due to the existence of microcracks in the sample.) $[d\Sigma/d\Omega]_{high\ q}$ on the other hand is Lorentzian $d\Sigma/d\Omega \propto 1 / (q^2 + (1/\xi)^2)$, enabling extraction of the magnetic correlation length [12], as discussed in section 2.3.4.2. As shown in Fig. 5.10 (c), for $x$ = 0.30, 0.24, 0.22, and 0.20, $\xi$ diverges as $T \rightarrow T_C^+$, as expected in a long-range ordered FM. At $x$ = 0.17, which is very close to the percolation threshold, $x_C$, $\xi$ diverges as $T \rightarrow T_C^+$ and the low $q$ scattering shows a clear onset, but $[d\Sigma/d\Omega]_{high\ q}$ has only a bump at $T_C$ with significant intensity at low $T$.

The $x$ = 0.15, 0.10, and 0.05 crystals ($x < x_C$) are radically different. For $x$ = 0.15, $[d\Sigma/d\Omega]_{low\ q}$ is negligible, while $[d\Sigma/d\Omega]_{high\ q}$ shows an onset around 150 K, becoming intense at low $T$. Similar behaviors were also observed for $x$ = 0.10 and 0.05 crystals: $[d\Sigma/d\Omega]_{low\ q}$ is negligible and $[d\Sigma/d\Omega]_{high\ q}$ turns on at low temperature. We want to point out that the close analysis of the seemingly non-zero $[d\Sigma/d\Omega]_{low\ q}$ indicates that it is actually due to a small, and very weakly temperature dependent, background that is *not* magnetic scattering from the sample. Therefore, after subtracting the background, the magnetic contribution from $[d\Sigma/d\Omega]_{low\ q}$ for $x \leq 0.15$ is still negligible due to the absence of long-order magnetic ordering, as expected. Consistent with the negligible low $q$ scattering, $\xi$ at $x$ = 0.15 does not diverge. Apparently spin correlations emerge at ~150 K, grow in range with decreasing $T$, but are limited to ~2.5 nm by the physical size of the magnetic clusters. We thus use $\xi$, which strictly provides a measure of the characteristic spatial extent of the spin correlation function, as an approximate measure of the FM droplet size. The validity of this procedure is borne out by the reasonable agreement with the $\xi$ values derived from elastic neutron scattering peak widths [16].

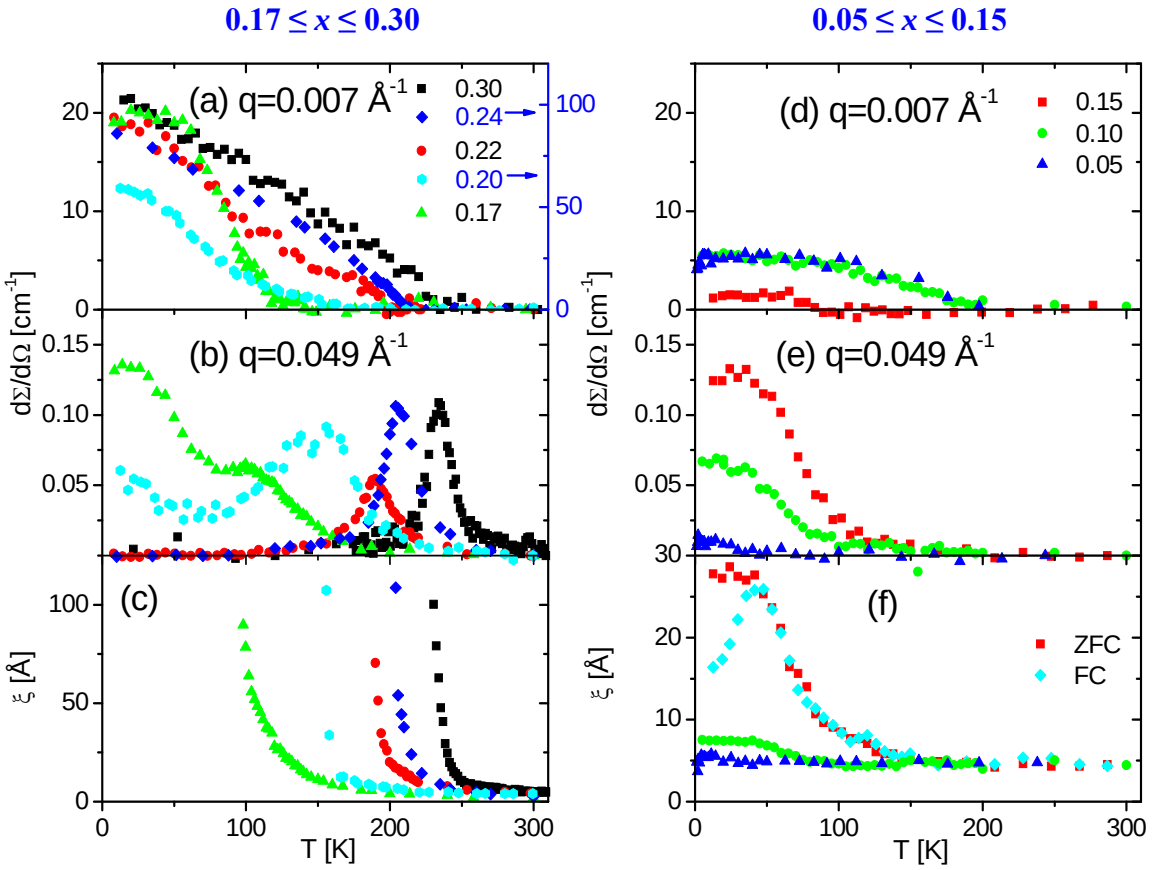


**Fig. 5.10** $T$ dependence of the magnetic SANS intensity (absolute cross-section) at $q$ = 0.007 Å$^{-1}$ (a) and (d), $q$ = 0.049 Å$^{-1}$ (b) and (e), and the extracted magnetic correlation length (c) and (f) for $x$ = 0.05, 0.10, 0.15, 0.17, 0.20, 0.22, 0.24 and 0.30 single crystals. For $x$ = 0.20, and 0.24 in panel (a), right axis was used due to a scale issue.

For $x \leq 0.15$, $\xi(T)$ shows a splitting between field cooled (FC) and zero field cooled (ZFC) curves close to the "spin-glass" freezing temperature [27], $\xi(T)$ after FC being smaller than $\xi(T)$ after ZFC. Similar behavior was also observed at $[d\Sigma/d\Omega]_{high\ q}$ for $x \leq$ 0.15. Such a suppression of $\xi(T)$ and $[d\Sigma/d\Omega]_{high\ q}$ after FC seems counterintuitive at the first glance since one would expect the FM clusters to grow after FC, resulting in increased $\xi(T)$ and $[d\Sigma/d\Omega]_{high\ q}$. However, after careful examination, such a behavior could be understood quite naturally as below: FC will induce some coalescence of large FM clusters and keep the original small isolated clusters. Therefore, the coalescence of large FM clusters will contribute to magnetic scattering at lower $q$, giving rise to

decreased magnetic scattering at original high $q$, which only comes from the left over non-coalesced small clusters. Correspondingly, $\xi(T)$, which is determined from Lorentzian scattering from the high $q$ window, will decrease since some of the original larger clusters now coalesce and shift out of the high $q$ window to the low $q$ region. Such a coalescence of large FM clusters resulting in decreased $\xi(T)$ is also observed by INS experiments under high field [67].

### 5.2.3 Doping dependence of SANS intensity and magnetic correlation length in LSCO

In order to determined the active MEPS doping limits from SANS, doping evolution of $[d\Sigma/d\Omega]_{low\ q}$, $[d\Sigma/d\Omega]_{high\ q}$, and magnetic correlation length $\xi$ at low $T$ (10 K) is plotted in Fig. 5.11. Fig. 5.11 (a) shows the low $T$ (10 K) $[d\Sigma/d\Omega]_{low\ q}$ vs. $x$ is negligible at low $x$ due to the absence of long-range FM, but turns on at $x$ = 0.17, i.e. at percolation. A maximum occurs at $x$ = 0.20 due to formation of a percolated network with maximum contrast between FM and non-FM phases. Significantly, $[d\Sigma/d\Omega]_{low\ q}$ becomes roughly constant above $x$ = 0.22, at a lower value than at $x$ = 0.20. The surprising implication is that a uniform single-phase FM state is entered at $x \geq 0.22$, at which point $[d\Sigma/d\Omega]_{low\ q}$ comes only from domains. Thus the determined upper doping limit from SANS, i.e. $x$ = 0.22 for active MEPS is consistent with the limits determined from lamda anomaly, electronic contribution, and $T^2$ contribution from heat capacity measurements, as discussed in section 5.1.

The doping dependence of $[d\Sigma/d\Omega]_{high\ q}$ (Fig. 5.11(b)) strengthens this argument. It can be seen that $[d\Sigma/d\Omega]_{high\ q}$ vanishes at $x$ = 0.22 (the point at which $[d\Sigma/d\Omega]_{low\ q}$ flattens), again in agreement with the upper doping limit for MEPS determined from heat capacity. Also, it can be noticed that the lower extrapolation doping value for $[d\Sigma/d\Omega]_{high\ q}$ to approach zero is $x \approx 0.04$, i.e. the same lower doping limit for MEPS determined from the hyperfine contribution to the heat capacity, as discussed in section 5.1.3. The FM-correlated nanoscopic clusters apparently first form at statistically significant density at $x$ = 0.04, increase in scattering intensity up to $x$ = 0.15, decrease beyond $x$ = 0.17 due to coalescence, then become negligible at $x$ = 0.22 when uniform FM is established. Fig. 5.11(c) shows the doping dependence of $\xi$ for both single- and poly-crystals. It shows a

weak increase with increasing $x$, from ~2 unit cells (6-8 Å) at $x = 0.05$ up to ~ 6 unit cells (20-25 Å) at $x = 0.15$, an important point for the analysis presented below.

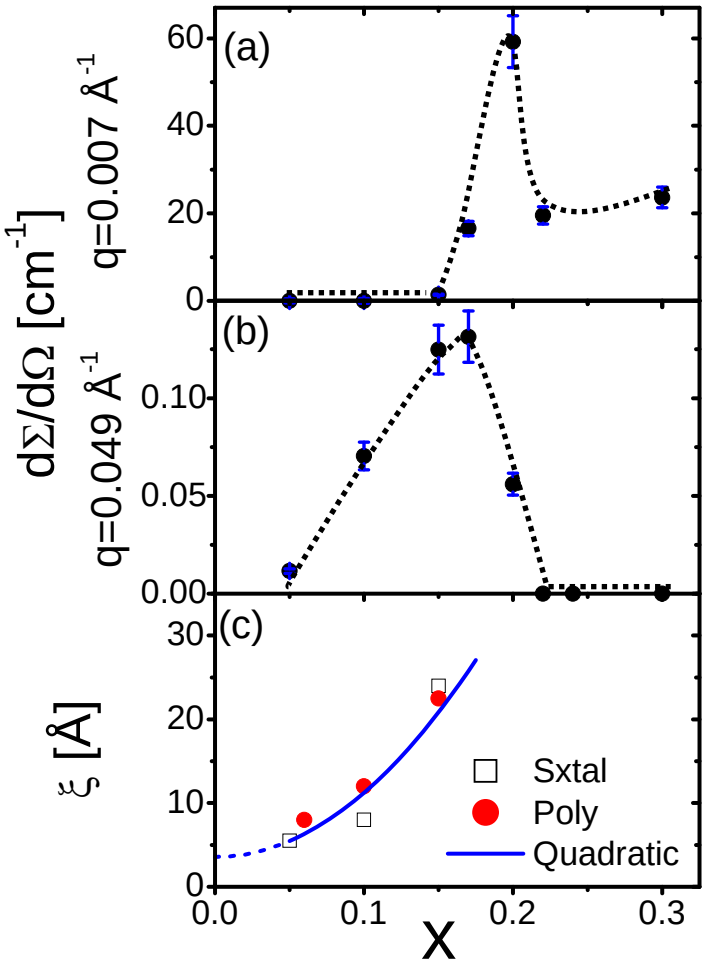


**Fig. 5.11** Doping dependence of magnetic SANS intensity (absolute cross-section) at (a) $q = 0.007$ Å$^{-1}$ and (b) $q = 0.049$ Å$^{-1}$, and (c) magnetic correlation length for both single- and poly-crystals at 10 K. The dotted lines are guides to the eye while the solid line is a fit as described in the text.

## 5.3 MEPS limits determined from statistical simulation in LSCO

Given such clear evidence of localization of the phase separated region to a specific range of doping determined from different experimental techniques, simulations were performed to determine if this finite range could possibly be accounted for by local doping fluctuations. A 240 x 240 x 240 array of La ions was considered, as shown in Fig.

5.12. Doping was achieved by assigning a probability $x$ of occupation of a given site with Sr and the lattice was broken up into sampling volumes $L^3$ (= 4/3 $\pi\xi^3$), playing the role of the nanoscopic clusters. The distribution in local dopings on the sampling length scale $L$, $P(x_{local})$, was then collected at multiple global doping values, $x$.

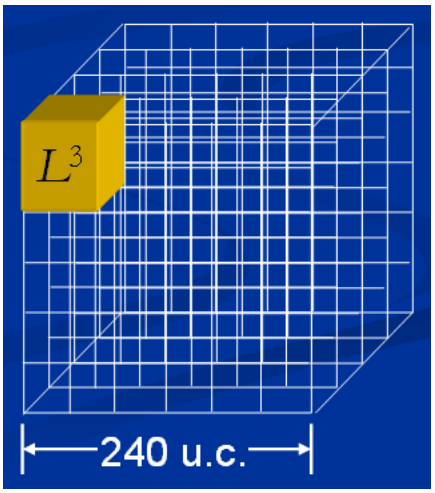


**Fig. 5.12** Schematic of a 240 x 240 x 240 array of La ions doped with Sr by assigning a probability $x$ of occupation of a given site. Sampling volumes $L^3$ ($L$ in the unit of unit cell) was chosen to compute the local doping distribution for a given global doping value $x_{global}$.

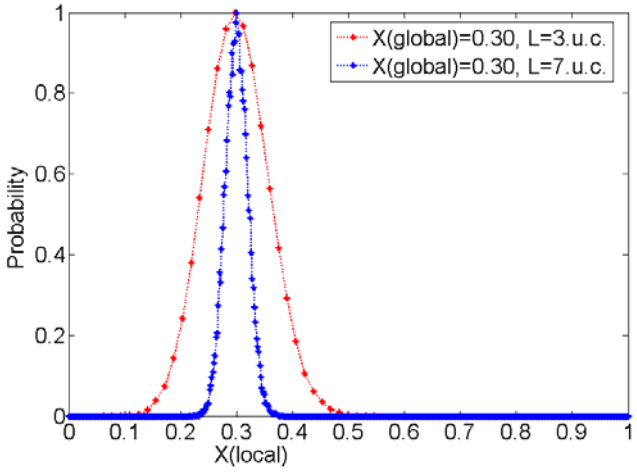


**Fig. 5.13** Local doping distributions for $x_{gloabl}$ = 0.30 at $L$ = 3, and 7 u.c.

As a simple illustration, Fig 5.13 shows the local doping distributions $P(x_{local})$ at a fixed global doping value $x_{global}$ = 0.30 for two different sampling volumes, $L^3$ = (3 u.c.)$^3$ and (7 u.c.)$^3$. It can be seen the local doping distribution is centered at the global doping value for each sample volume. It can also be seen clearly that the width of these

distributions is dependent on the sampling volume, decreasing with increased sample volume, which is expected since a larger sample volume reduces the local fluctuation and results in a narrower distribution. Now, if such a plot is extended for all global doping values $x_{global}$ for a fixed sample volume, a 3 dimensional distribution will be given with the height representing the local doping probability, as shown in Fig. 5.14 for the sample volume $L^3$ = (3 u.c.)$^3$ and (7 u.c.)$^3$.

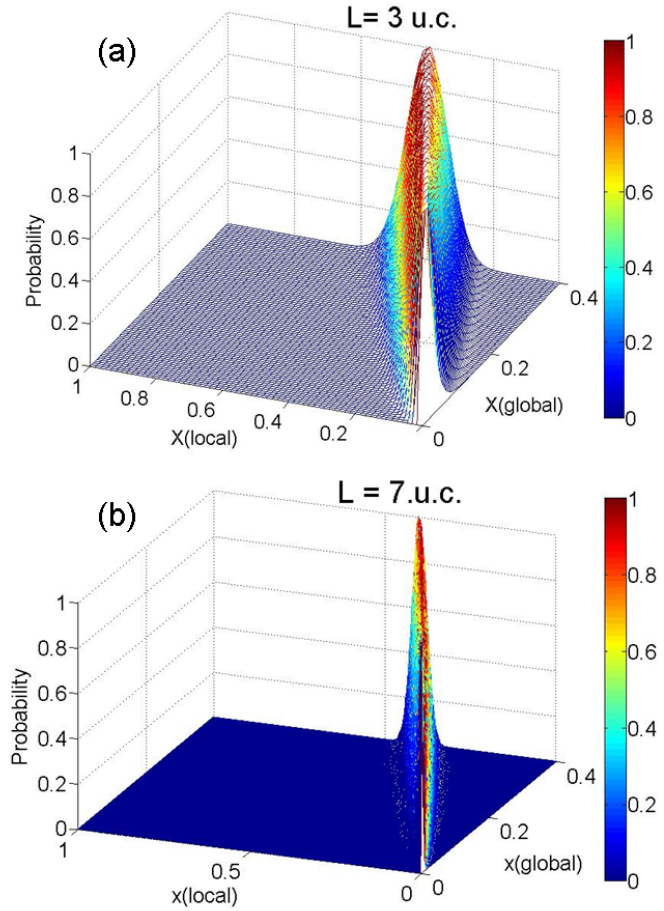


**Fig. 5.14** Three dimensional local doping distribution at (a) $L$ = 3 u.c. and (b) $L$ = 7 u.c.

To better visualize the 3 dimensional plot, a contour plot was used, i.e. a projection of the probability on to a 2 dimensional plane, as shown in Fig. 5.15. The distributions arising for sampling volumes of 3 unit cells cubed and 11 unit cells cubed are shown as color plots in Figs. 5.15 (a) and (b). As a result, vertical cuts through these figures are the $P(x_{local})$ distributions at that particular global $x$ value, as mentioned before and shown in Fig. 5.13.

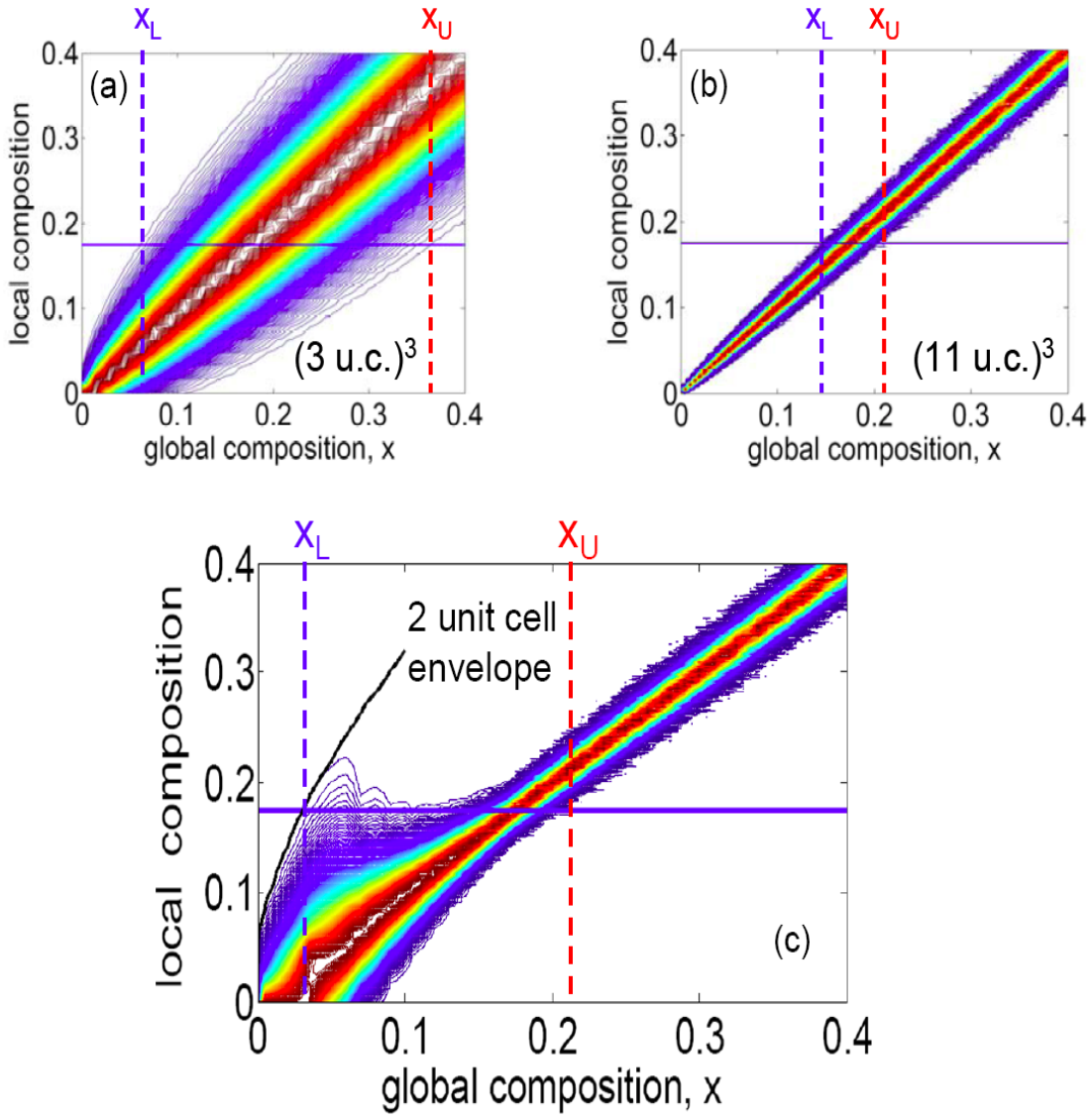


**Fig. 5.15** Contour plot of calculated distribution of local doping as a function of the global doping, $x$, for sampling volumes of (a) 3 unit cells cubed, (b) 11 unit cells cubed, and (c) the experimentally determined ($x$-dependent) magnetic correlation volume. The vertical lines indicate the upper and lower limits for the phase separation, i.e. the points where the distributions intersect the horizontal line at $x = 0.18$.

Consider the intersection of these distributions with the horizontal line $x_{local} = 0.18$, i.e. $x_C$ from the *bulk* phase diagram. Assuming that in any region with $x_{local} \geq 0.18$ FM order is stable (leading to nucleation of a short range FM cluster), and in any region with $x_{local} < 0.18$ FM order is unstable, leads to prediction of a finite range for MEPS. The lower

intersection point, $x_L$, is the point at which the entire distribution is below $x_{local} = 0.18$ (a uniform non-FM state), and the upper intersection point, $x_U$, is the point at which the entire distribution lies above $x_{local} = 0.18$ (a uniform FM state). For the doping value between $x_L$ and $x_U$, the system is made of a mixture of FM state and non-FM state, in other words, the doping limits for MEPS active region is $x_L$ and $x_U$. Figs. 5.15 (a) and (b) thus predict $x_L = 0.06$, $x_U = 0.36$, and $x_L = 0.14$, $x_U = 0.21$, respectively, neither of which agrees with experiment. This is because, as shown in Fig. 5.11(c), the actual experimentally determined sampling length scale (i.e. the magnetic correlation length) is itself dependent on global doping. $\xi(x)$ was therefore fitted to a simple function (a quadratic, Fig. 5.11 (c)) in order to compute the relevant sampling length at any $x$ as an input for the simulations. As an aside note that, (i) a quadratic describes $\xi(x)$ better than a linear function, and (ii) finite $\xi(x \rightarrow 0)$ can be rationalized in terms of non-zero spin states in magnetic excitons [65,74] or spin-state polarons [64], which could be the precursors to the FM correlated clusters we observe at $x \geq 0.04$. Local magnetic entities such as polarons [17,64] or magnetic excitons [65,74] likely exist at very low (even zero) $x$, but strongly FM-correlated spin clusters apparently first form at $x \approx 0.04$. The results from these final simulations are shown in Fig 5.15 (c). The unusual shape of the distribution is due to the form of $\xi(x)$. (At low $x$ the distribution is wide due to the small sampling volume (~2 unit cells cubed); while at high $x$ it is narrow due to the larger sampling volume.) From Fig. 5.15 (c) we predict $x_L = 0.03$, $x_U = 0.21$, remarkably close to the experimental values (0.04 and 0.22). Note that this agreement is achieved with no adjustable parameters, using the experimentally determined $\xi(x)$.

## 5.4 Origin of MEPS in LSCO: Local compositional fluctuations

The summarized experimental data from different techniques are plotted in Fig. 5.16. The doping limits determined from SANS and heat capacity are almost identical, i.e. $x_L = 0.04$ and $x_U = 0.22$. Magnetotransport (Fig. 5.16 (e)) provides further confirmation. As described previously [26], the magnetoresistance can be simply decomposed into "metallic" and "insulating" contributions, which will be discussed in more detail in section 5.5. The insulating contribution disappears at $x = 0.22$, at which point the metallic contribution becomes constant, confirming once more the onset of uniform FM beyond $x =$

0.22. This conclusion is also consistent with La NMR showing a saturation of the center field of the resonance near $x = 0.22$ [42], as shown in Fig. 5.16 (f).

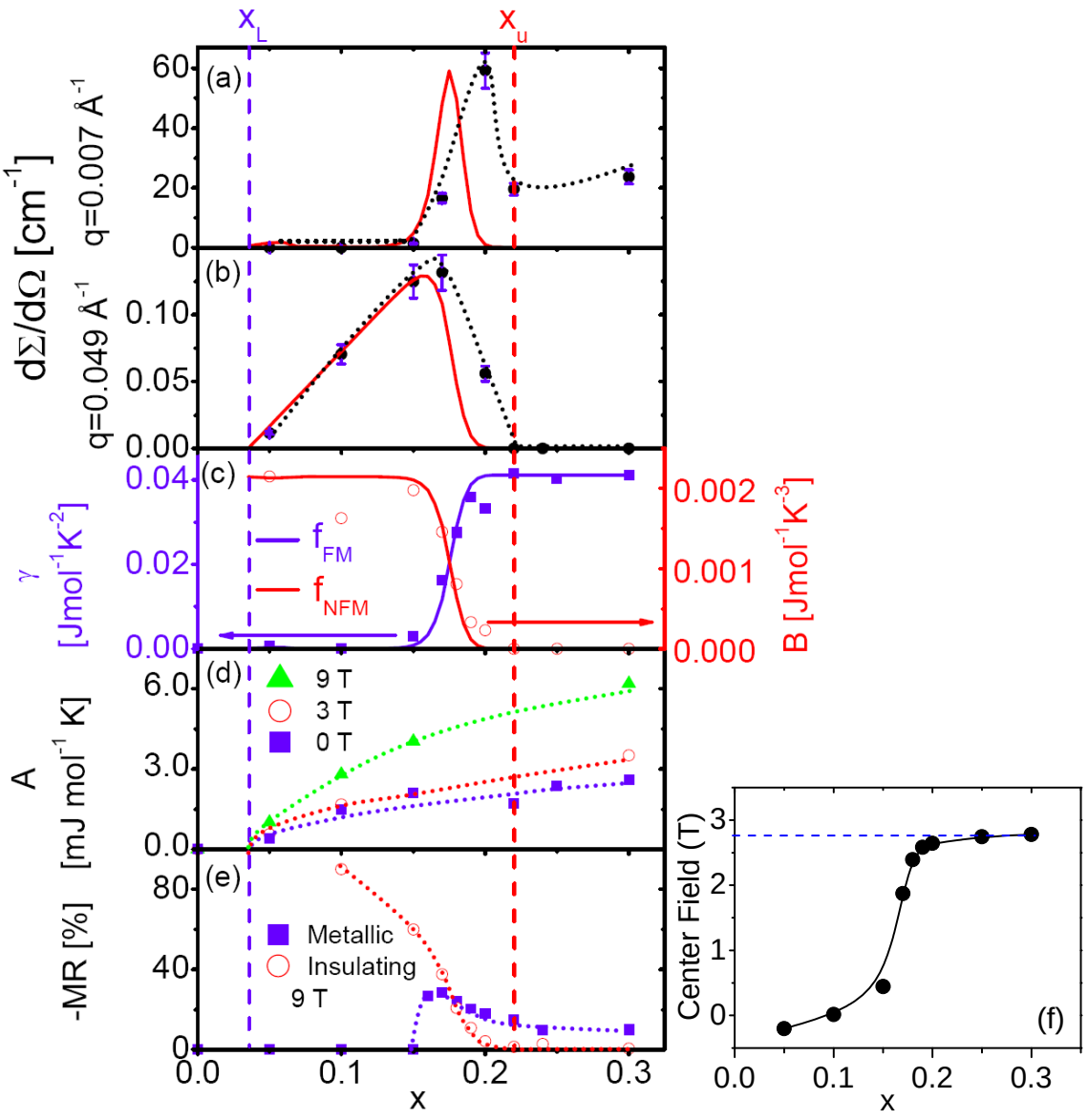


**Fig. 5.16.** Doping dependence of the 10 K magnetic SANS intensity (absolute cross-section) at (a) $q = 0.007$ Å$^{-1}$ and (b) $q = 0.049$ Å$^{-1}$. Doping dependence of the electronic and $T^2$ contributions to the specific heat (c), the nuclear hyperfine contribution to the specific heat (d), and the 9 T magnetoresistance (e). The dotted lines are guides to the eye while the solid lines are fits to the models described in the text. The vertical dashed lines indicate the upper and lower limits for the phase separation, $x_U$ and $x_L$. (f) Central field, $\langle H_{hf} \rangle$ of $La_{1-x}Sr_xCoO_3$ at 4.2 K from $^{139}$La NMR spectrum. Reproduced from Ref. 42.

Meanwhile, statistical simulations reproduced almost the same doping limits as experimental values, as just discussed in section 5.3. Actually, the validity of the model can be further verified by extracting the phase fractions, $f_{FM}$ (of the long-range-ordered FM phase) and $f_{NFM}$. These are shown in Fig. 5.16 (c), normalized to, and overlaid on, $\gamma(x)$ and $B(x)$, which, we have argued in section 5.1, must scale with $f_{FM}$ and $f_{NFM}$. The agreement is satisfactory. The $x$ dependence of $[d\Sigma/d\Omega]_{high\ q}$ (Fig. 5.16 (b)) can also be modeled. $[d\Sigma/d\Omega]_{high\ q}$ must be proportional to the phase fraction of the non-long-range-ordered regions ($f_{NFM}$) and the density of clusters within these regions, which we observed to increase linearly with $x$ beyond $x = 0.04$, i.e. $[d\Sigma/d\Omega]_{high\ q} = C(x - 0.04)f_{NFM}(x)$, where $C$ is a constant. As shown in Fig. 5.16 (b) the agreement with experiment is reasonable. $[d\Sigma/d\Omega]_{low\ q}$ is of the Porod type and is thus proportional to the specific area of contact between FM and non-FM phases. This can be crudely approximated as $[d\Sigma/d\Omega]_{low\ q} \approx C' f_{FM}(x) f_{NFM}(x)$ ($C'$ is a constant) [75], which is exact as $f_{FM} \rightarrow 0,1$. As shown in Fig. 5.16 (a) the simulation (solid line) faithfully reproduces the onset at $x = 0.15$, and the peak near percolation, but is incapable of modeling the constant intensity at $x \geq 0.22$, which arises from domains.

The fact that different experimental techniques give rise to the same doping limits for MEPS which can be perfectly reproduced by a simple statistical simulation, as well as the striking agreement between experiment and these simple statistical simulations, directly implies that the phase-separated state in LSCO can be explained solely on the basis of unavoidable local doping fluctuations in a randomly doped crystal, with no need to invoke electronic phase separation. It is important to stress that electronic inhomogeneity is of course still present. It is simply driven by doping fluctuations as opposed to an electronically driven phase separation mechanism. The long-range Coulomb interaction likely plays a key role in limiting the phase-separation length scale [see ref. 76 for example], making these local compositional fluctuations extremely important. It is clear that longer length scale inhomogeneities, (which seem to occur in some manganites for example) cannot be described by this model, as can be seen from the rapid decrease in distribution width with sampling volume. As a final comment note that a key feature of this analysis is that the critical doping level for the onset of FM order in the *bulk* phase

diagram ($x$ = 0.18) apparently applies at surprisingly short length scales, of the order of only 2 unit cells.

## 5.5 Transport signatures of percolation and electronic phase homogeneity in LSCO

As discussed in the previous sections, MEPS in LSCO is now reasonably well understood [7-19,28,42] and is believed to be driven by local doping fluctuations and confined to a specific doping range $0.04 < x < 0.22$. In this section, we will try to understand the relationship between the nature of the phase separation on a *microscopic* level, and the behavior of *macroscopic* properties such as electronic transport in LSCO. On the *microscopic* level, the system forms nanoscopic hole-rich ferromagnetic (FM) clusters in a hole-poor non-FM insulating matrix at low $x$. The range of the FM spin correlations is isotropic, so the FM clusters can be viewed as spherical droplets [16]. As $x$ is increased to a critical value ($x_c \approx$ 0.17-0.18) a transition from insulator to metal and short- to long-range FM occurs, qualitatively consistent with percolation of metallic FM droplets [19]. Detailed studies [7-19,28,42] have provided a relatively complete picture of the evolution of this inhomogeneity with $x$. The goal of this section is to take this knowledge on the *microscopics* of the phase-separated state in LSCO and establish to what extent it enables us to understand the *macroscopic* electronic properties, specifically resistivity ($\rho$). We reach two main conclusions. First, that established percolation theory, modified to include double exchange (DE), provides a quantitative understanding of the low $T$ conductivity and the critical doping value. Second, that the onset of a phase-pure low $T$ FM metallic state above $x$ = 0.22 has a strong influence on the nature of the *high temperature* resistivity, due to a crossover in the characteristic time scale for the spin correlations associated with the phase separation.

### 5.5.1 Percolation nature of metal-insulator transition in LSCO

We first consider the phase separated state at low $x$, i.e. on approach to percolation. As discussed in section 5.2, the SANS-derived low $T$ magnetic correlation length, $\xi(x)$, as shown again in Fig. 5.17(a), provides a good measure of the FM cluster size, which increases from 5-10 Å at $x \approx 0.05$ to ~ 20 Å at $x$ = 0.15.

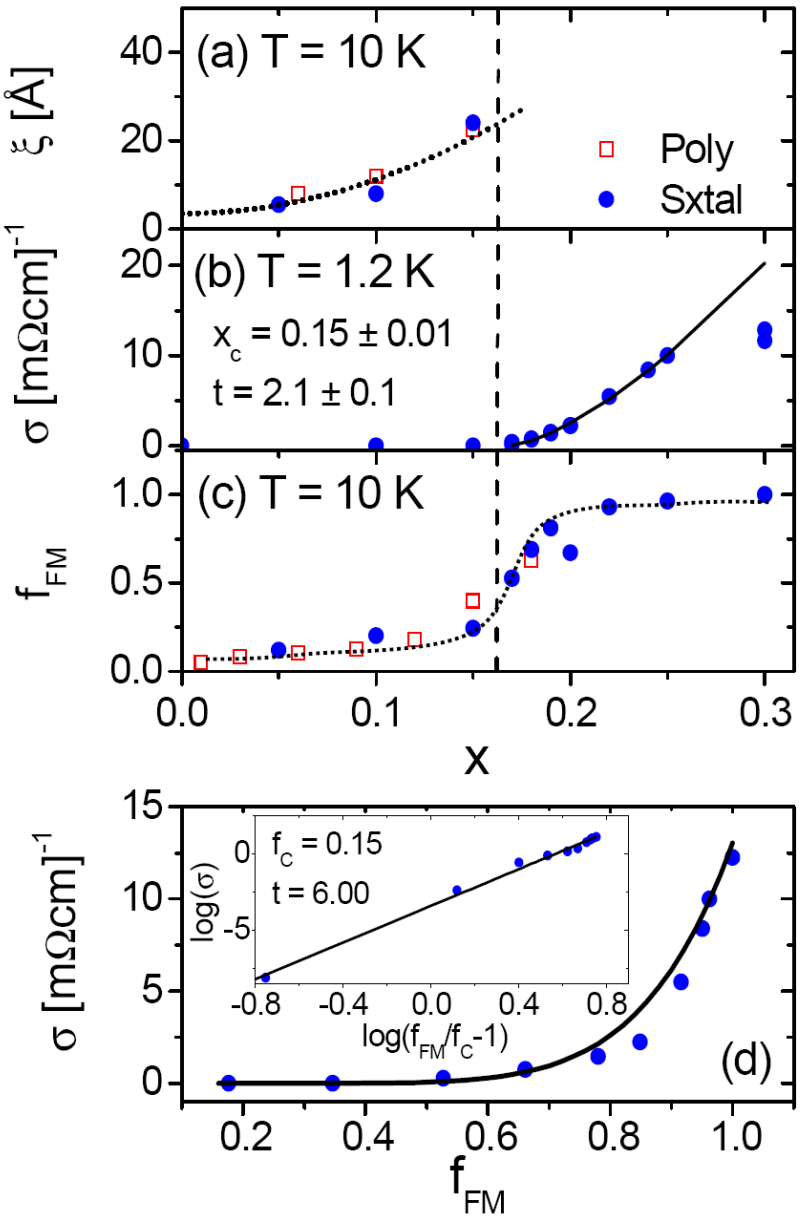


**Fig. 5.17** Top panel: Doping dependence of **(a)** the 10 K magnetic correlation length, **(b)** the 1.2 K conductivity, and **(c)** the 10 K ferromagnetic phase fraction. Dotted lines are guides to the eye. The solid lines are fits to the models described in the text. The vertical dashed line marks the percolation threshold. Bottom panel **(d)**: 1.2 K conductivity as a function of ferromagnetic phase fraction. **Inset:** Data re-plotted on a log scale to facilitate the analysis discussed in the text. Solid lines are fits, as described in the text.

Fig. 5.17(b) shows the corresponding low $T$ (1.2 K) conductivity, σ, which we will show is *quantitatively* consistent with established percolation theory [77-79]. In the

random continuum percolation model (RCPM) the random placement of a variable volume fraction of metallic clusters in an insulating medium leads, in the critical region, to:

$$\sigma(T \to 0) = \sigma_0 \left( \frac{x'}{x'_c} - 1 \right)^t \qquad (5.7),$$

where $\sigma_0$ is a constant, $x'$ is the metallic volume fraction, $x'_c$ is the threshold value for percolation, and $t$ is a critical exponent. The 3D value of $x_c$ is dependent on assumptions but lies in the range 0.15 – 0.29 [77-79]. For the exponent, early work predicted $t$ = 1.6-2.0 [77,78] while later studies suggested a universal value of 2 [79]. It is interesting to note that direct application of Eq. (5.7) to the data of Fig. 5.17(b), equivalent to assuming $x' \approx x$, provides an excellent fit (solid line in Fig. 5.17 (b)) with $x_c = 0.15 \pm 0.01$ and $t = 2.1 \pm 0.1$, very close to expectations [80]. As we will see below, this is essentially fortuitous.

A more meaningful analysis requires knowledge of the metallic volume fraction. As in prior work on manganites [81-83] the volume fraction of FM phase ($f_{FM}$) can be estimated by taking the ratio of the FM (i.e. saturating) magnetization at any $x$, to the saturation magnetization deep in the FM phase ($x$ = 0.30), where $f_{FM} = 1$. The raw data of the hysteresis loops for 10 singly crystals at 10 K are shown in Fig. 5.18 (a). The intercept of the linear fitting of the high field data gives rise to the FM magnetization at any $x$, as shown in Fig. 5.18 (b) using $x$ = 0.17 as an example. The determined $f_{FM}$ is shown in Fig. 5.17 (c). It can be seen that $f_{FM}$ increases linearly with $x$ up to $x$ = 0.15 then rises rapidly, reaching values close to 1 above $x$ = 0.22. $\sigma(x)$ (Fig. 5.17(b)) and $f_{FM}(x)$ (Fig. 5.17(c)) can then be combined to plot $\sigma(f_{FM})$ (Fig. 5.17(d)). Associating the FM regions with metallic conductivity (justified by the DE mechanism and the known phase behavior) gives $x' = f_{FM}$, enabling use of Eq. (5.7). The best fit was obtained from log-log plots of $\sigma$ vs. ($f_{FM}/f_C$ -1) (inset to Fig. 5.17(d)), determining the value of $f_C$ which minimizes $\chi^2$. The result (solid line) is $f_C = 0.15 \pm^{0.09}_{0.03}$ and $t = 6.0 \pm 0.20$, i.e. an $f_c$ value within the expected range and an exponent that is, at first sight, anomalous. However, such large exponents have a solid theoretical basis in DE systems. As discussed by Xiong *et al* [84] the additional link between $\sigma$ and FM spin alignment in DE materials necessarily leads to a

stronger zero field $\sigma(x)$ than standard percolation. Combining real space renormalization with resistor network computations they predicted $t$ = 5.3 in zero magnetic field [84], compared to a measured value of 6.9 in $La_{5/8-y}Pr_yCa_{3/8}MnO_3$ [85]. Our value of $t$ = 6.0 is thus in very reasonable agreement with theoretical predictions, demonstrating that the low $T$ $\sigma(x)$ in LSCO can be quantitatively understood in terms of DE-modified RCPM. A successful percolation description of the metal-insulator transition also provides a simple explanation for one of the major features of the phase behavior; the onset of metallicity and long-range FM around 17 % doping, close to the expected 3-D percolation threshold.

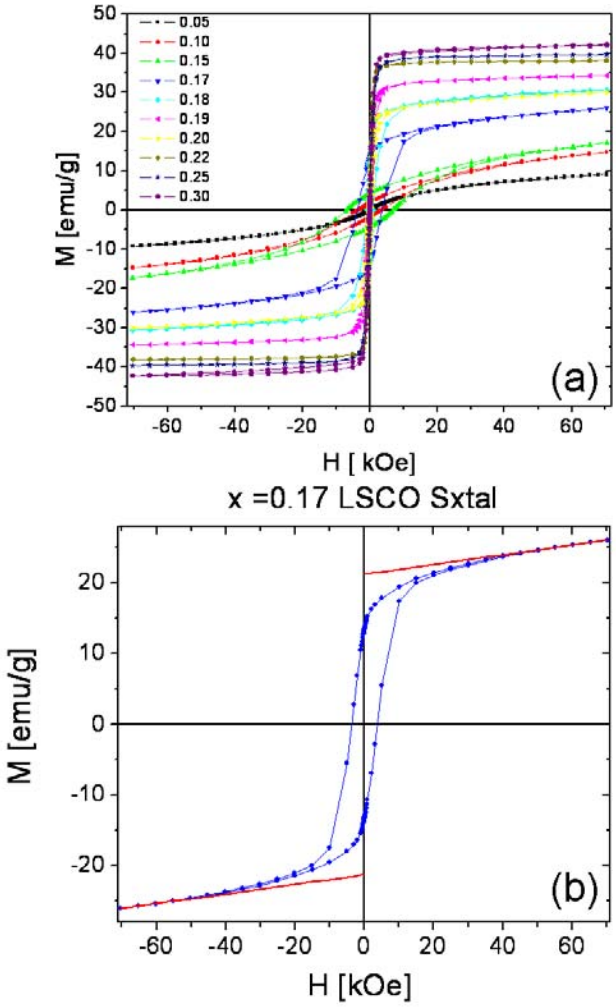


**Fig. 5.18 (a)** Hysteresis loops at 10 K for $x$ = 0.05, 0.10, 0.15, 0.17, 0.18, 0.19, 0.20, 0.22, 0.25, and 0.30 $La_{1-x}Sr_xCoO_3$ single crystals **(b)** Illustration of extraction of FM volume fraction from high field fitting (solid red lines) for a $x$ = 0.17 $La_{1-x}Sr_xCoO_3$ single crystal.

### 5.5.2 Effect of low *T* electronic phase homogeneity on high *T* transport at higher doping in LSCO

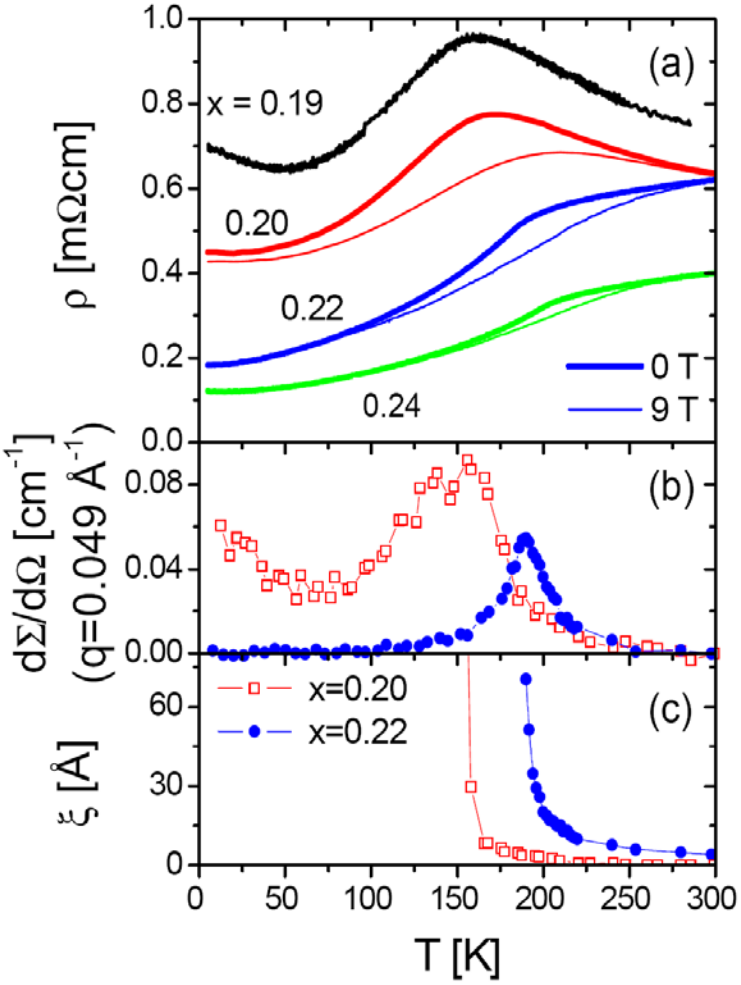


**Fig. 5.19** Temperature dependence of **(a)** the resistivity in zero field (heavy lines) and 9 T (light lines) for $x$ = 0.19, 0.20, 0.22 and 0.24, **(b)** the $q$ = 0.049 Å$^{-1}$ SANS intensity (with the 300 K value subtracted), and **(c)** the magnetic correlation length. For (b) and (c) the data are shown for $x$ = 0.20 and 0.22.

The established features of the phase-separated state also provide insight into the transport at higher doping. As discussed in the previous sections, at $x$ = 0.22, phase-separation ends and a phase-pure FM metallic phase is entered at low $T$ [28]. This can even be seen in Fig. 5.17 (c), where $f_{FM}$ abruptly saturates (at a value close to 1) at $x$ = 0.22. Surprisingly, a close inspection of ρ($T$) in this $x$ range, as shown in Fig. 5.19 (a)

reveals a subtle indication of this special doping point, unnoticed in prior work. At $x \geq 0.22$ $d\rho/dT$ is positive above and below $T_C$, indicating a metallic-like $\rho(T)$ in both the low $T$ FM and high $T$ paramagnetic phases. A kink occurs at $T_c$ along with a modest negative MR [26] due to field-induced suppression of spin disorder. For $x < 0.22$ however, $d\rho/dT$ is positive below $T_C$, reflecting the expected metallicity due to DE, but reverses sign at $T > T_C$. The fact that the sign change in high $T$ $d\rho/dT$ occurs exactly at $x = 0.22$ indicates, quite remarkably, that the onset of a phase-pure FM metallic state *below* $T_c$ has a strong influence on $\rho(T)$ *above* $T_c$. This is shown more clearly in Figs. 5.20(a,b) which plot the $x$ dependence of $d\rho/dT$ at 250 K, and the residual resistivity ratio ($\rho$(300 K) / $\rho$(10 K)). The abrupt change at $x = 0.22$ is very clear, and is also evident in the $x$ dependence of the MR at $T_c$, as mentioned in section 5.4 and shown Fig. 5.20(c), which is strongly enhanced for $x < 0.22$.

We believe that the FM spin correlations above $T_C$ play a key role in this behavior. Figs. 5.19 (b,c) show the high $q$ (0.049 Å$^{-1}$) SANS cross-section [$d\Sigma/d\Omega(T)$] and $\xi(T)$ for $x = 0.20$ and 0.22 to illustrate this point. Consider $x = 0.20$. The high $q$ $d\Sigma/d\Omega$ is non-zero as $T \rightarrow 0$ (due to scattering from nanoscopic FM clusters when the long-range FM volume fraction is less than 1, as discussed thoroughly in section 5.2), and exhibits broad critical scattering around $T_C$. The $x = 0.22$ data are radically different. The high $q$ $d\Sigma/d\Omega$ vanishes at low $T$ (due to the phase pure long-range FM ordered state), and the critical scattering peak sharpens [86], as mentioned in section 5.2. $\xi(T)$ is also very different in these two cases; at $x = 0.20$ $\xi$ is small at high $T$ and diverges as $T \rightarrow T_C^+$, while for $x = 0.22$ $\xi(T)$ has a long high $T$ tail, indicating that short-range range spin correlations persist much further above $T_C$. This is broadly consistent with prior SANS data on high $x$ polycrystals [12,14], as discussed in Chapter 4, which suggested pre-formation of FM clusters at a well-defined temperature, $T^*$ ($> T_c$). Following this interpretation, these single crystal data indicate an abrupt change in the pre-formed cluster state at $x = 0.22$, coinciding with the fundamental change in the low $T$ magnetic state. For $x \geq 0.22$ $T^*$ greatly exceeds $T_C$ with strong FM spin correlations occurring above $T_C$, while at $x < 0.22$ $T^*$ decreases dramatically, with distinctly weaker high $T$ spin correlations. The abrupt change in the high $T$ transport at $x = 0.22$ can then be simply explained by considering the

relative time scales for the FM spin fluctuations and the transport. We propose that the $x$ = 0.22 crossover to a phase-pure long-range FM state below $T_c$, with strong FM spin correlations above $T_c$, also marks a transition from a dynamic to static (on the time scale relevant to electronic transport) clustered state at $T > T_c$. At $x \geq 0.22$ the FM spin correlations within the pre-formed clusters are static on the time scale relevant for the electronic transport enabling DE interactions to establish weakly metallic transport (positive $d\rho/dT$). At $x < 0.22$ on the other hand, the FM spin correlations are sufficiently dynamic on the transport time scale to render DE ineffective. The onset of static FM spin correlations at $T_C$ then leads to a sign change in $d\rho/dT$, a strong competition between metallic and insulating phases, enhanced MR, and a consistent interpretation of $\rho(T,x)$.

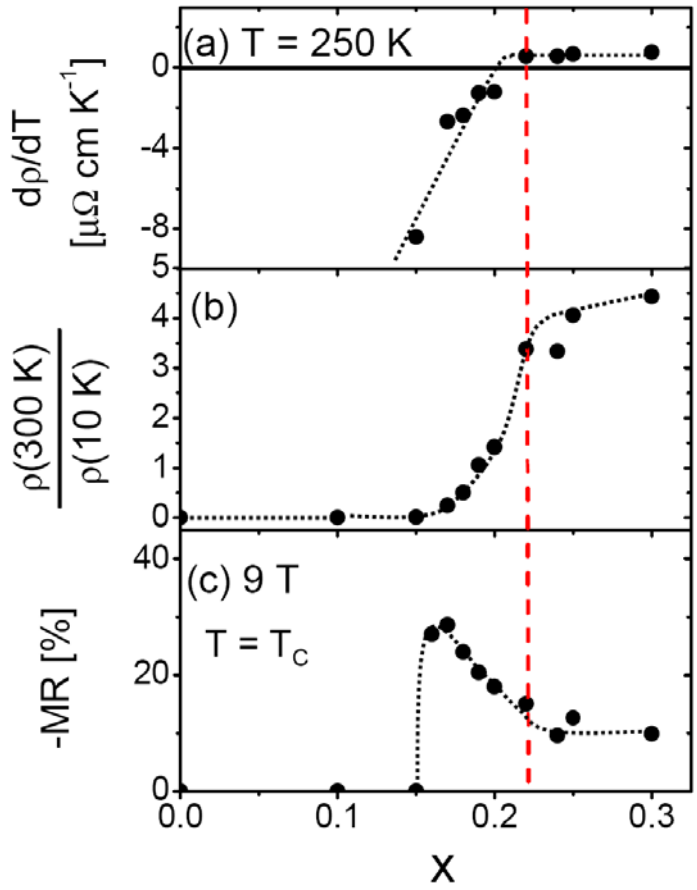


**Fig. 5.20** Doping dependence of **(a)** the 250 K temperature derivative of the resistivity, **(b)** the residual resistivity ratio (RRR), and **(c)** the 9 T magnetoresistance $[(\rho(H)-\rho(0))/\rho(0)]$ at the magnetic ordering temperature. Dotted lines are guides to the eye. The horizontal dashed line marks the special doping value ($x$ = 0.22) discussed in the text.

## 5.6 Revised phase diagram

Combining all of the experimental data obtained from single crystals, a revised magnetic phase diagram can be established, as shown in Fig. 5.21. Starting from $x = 0$ ($LaCoO_3$), $T_{SST}$ indicates the temperature scale of the spin-state transition from a low spin state to a finite spin state (intermediate / high spin) for $Co^{3+}$, as discussed in detail in Chapter 3.

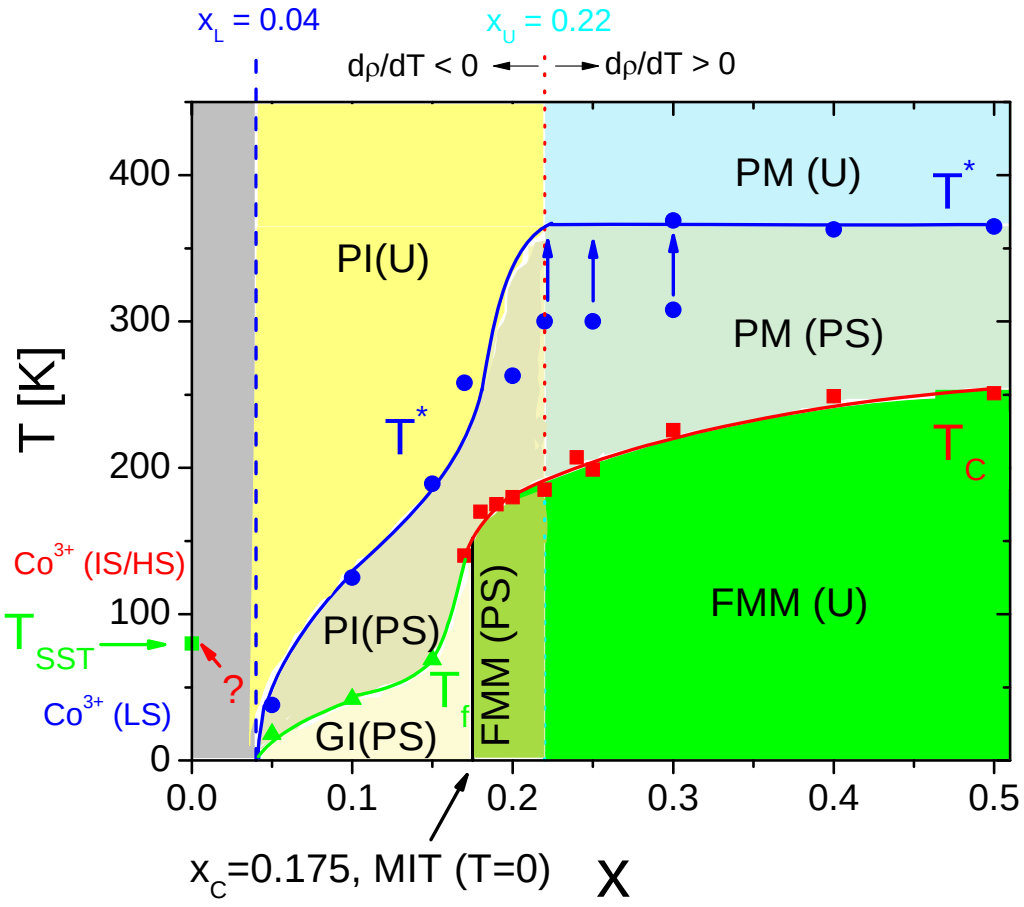


**Fig. 5.21** Revised magnetic phase diagram of $La_{1-x}Sr_xCoO_3$. Acronyms defined as follows. $T_C$ (red squares): Curie temperature. $T^*$ (blue circles): Preformed-clusters temperature. $T_f$ (green triangles): Freezing temperature for spin glass. $T_{SST}$ (green square): Spin-state transition temperature for $LaCoO_3$. GI: Glassy insulator. PI: Paramagnetic insulator. PM: Paramagnetic metal. FMM: ferromagnetic metal. MIT: Metal-insulator transition. U indicates it is a uniform state while PS indicates it is a phase separated state.

At higher doping ($0.04 \leq x < 0.175$), isolated FM clusters start forming (without percolation or coalescence) in the non-FM insulating matrix while the system forms glassy insulating state at low temperature ($T < T_f$: The freezing temperature). $x = 0.04$ indicates the lower doping limit for active MEPS, as discussed in the previous sections 5.1-5.4. $T_f$ is determined from magnetization measurements and the glassy behavior at low temperature was well established by J. Wu *et al.* on polycrystalline samples [19,27]. With increasing temperature ($T_f < T < T^*$: Preformed-cluster temperature), the system enters a paramagnetic insulating state. In this temperature range, FM clusters still exist in the non-FM matrix although their spin orientation fluctuates instead of staying frozen, which is the scenario for low temperature ($T < T_f$). Therefore, $T_f$ can be treated as a blocking temperature of these clusters, which possess superparamagnetic nature. At even higher temperature ($T > T^*$), there is no existence of FM clusters and the system is in a uniform paramagnetic insulating state.

At even higher doping ($0.175 \leq x < 0.22$), the FM clusters formed in the non-FM matrix begin coalescing, resulting in a percolated FM metallic network, which enables the system to enter a metallic long range FM ordered state at low temperature ($T < T_C$: The Curie temperature). $x = 0.175$ corresponds to the critical composition in single crystals, indicating the non-FM to FM transition as well as the metal-insulator transition. The long range FM-ordering is evidenced from SANS, as discussed in section 5.2, and the metallicity is shown in electronic transport measurements in single crystals by J. Wu *et al.* [13]. It is important to point out that in spite of the coalesce of the clusters, there are still some isolated FM clusters, leading to coexistence of short-range and long range ordering, as witnessed in SANS and indicated by heat capacity, as discussed in sections 5.1 and 5.2.

At higher temperature ($T_C < T < T^*$), the system enters a paramagnetic insulating state with the existence of preformed-FM clusters. $T^*$ is determined from SANS, indicating the onset temperature of preformed-clusters with non-Griffiths characteristics, as discussed in Chapter 4. As pointed out in section 5.5, in spite of the existence of these FM clusters, the FM spin correlations within the clusters are sufficiently dynamic on the transport time scale, leading to ineffective DE and insulating transport (negative $d\rho/dT$). The clusters

disappear at higher temperature ($T > T^*$), resulting in a uniform paramagnetic insulating state.

At high doping ($x \geq 0.22$), all FM clusters percolate without any remaining isolated FM clusters and the system enters a phase-pure metallic long range FM ordered state at $T < T_C$. The phase-pure property, i.e. pure long-range FM ordering without short-range spin correlations, is demonstrated through heat capacity, SANS, and simple statistical simulation, as discussed in sections 5.1-5.3. Therefore, $x = 0.22$ corresponds to the higher doping limit for active MEPS. At $T_C < T < T^*$, the system enters a paramagnetic metallic state (positive $d\rho/dT$) with the presence of preformed-FM clusters with non-Griffiths characteristics. The fact that the metal-insulator transition at high temperature occurs at exactly the same doping limit as the entry to pure phase state at low temperature, as shown in section 5.5, indicates the nanoscopic MEPS at low temperature has a strong impact on the macroscopic transport property at this higher temperature. Such a phenomenon is understood in terms of the characteristic time scale for the spin correlations. We propose that at $x \geq 0.22$ the time scale for the FM spin correlations within the pre-formed clusters is static relative the electronic transport, which enables DE interactions to establish weakly metallic transport, as explained in section 5.5. A uniform paramagnetic metallic state is entered at $T > T^*$ without the existence of clusters. A note to the phase diagram: Due to the inaccessibility of single crystals at high doping, i.e. $x = 0.40$ and 0.50, the polycrystal values of $T_C$ and $T^*$ was adopted.

In summary, in this chapter, we have provided a detailed study of the nanoscale magneto-electronic phase separation in single crystal LSCO through heat capacity, SANS and transport measurements, revealing the existence of a specific range over which it occurs. This exact doping range, the doping dependence of the phase fractions, and the doping dependence of the small-angle neutron scattering, as well as the electronic contribution, and a newly-discovered $T^2$ contribution, can all be reproduced by simple statistical simulations incorporating the local compositional fluctuations that must occur on nanoscopic length scales. We therefore believe that the magneto-electronic phase separation is driven by spatial fluctuations in doping rather than true electronic phase separation. Similar mechanisms could be at work in other randomly doped oxides exhibiting magneto-electronic inhomogeneity (e.g. cuprates and manganites), provided

that the coexisting phases have sufficiently small free energy differences, and, crucially, that the inhomogeneities occur on truly nanoscopic length scales.

In addition, from the heat capacity and ordinary Hall effect in LSCO single crystals, we found evidence for a softening of the lattice at intermediate doping values, strong additional evidence for the percolation nature of the insulator-metal transition, and a large electron mass enhancement due to strong electron-electron correlations in the ferromagnetic metallic state. The transport measurements cast a clear light on the interplay between the macroscopic electronic transport and the microscopic nature of the magnetically phase-separated state in LSCO. We conclude, (i) that the low temperature conductivity can be understood in terms of double exchange-modified percolation theory, and (ii) that the anomalous high temperature transport at high doping can be explained on the basis of a crossover from a dynamic to static pre-formed cluster state above the Curie point. The results demonstrate that the electronic transport in LSCO single crystals can be thoroughly understood on the basis of the current knowledge of the phase-separated state. Finally, a revised phase diagram incorporated the newly discovered doping limits for active MEPS is established.

# Chapter 6
# Magneto-crystalline anisotropy in highly doped $La_{1-x}Sr_xCoO_3$ single crystals

As first mentioned in Chapter 4, highly doped ($x \geq 0.175$) $La_{1-x}Sr_xCoO_3$ (LSCO) crystals are relatively hard magnetic materials with large coercivities, which could be treated within the Ising model. However, information about the magneto-crystalline anisotropy, such as the easy magnetization axis, the hard magnetization axis, and the anisotropy constants is still missing in spite of the fact that such information will benefit studies in LSCO. These include the determination of the blocking temperature of ferromagnetic (FM) clusters at low doping in LSCO, as well as the comparison of anisotropy constants between bulk and thin films LSCO. This is important as films appear to have unexpectedly large coercivities. In this chapter, we document a systematic study of magneto-crystalline anisotropy in highly doped LSCO single crystals via d.c. magnetometry, and small-angle neutron scattering (SANS), with the goal of qualitatively determining the easy and hard magnetization axis. Torque magnetometry is required to quantitatively determine the anisotropy constants of highly doped LSCO, which will be discussed in Chapter 7.

## 6.1 Introduction

Although the magneto-electronic phase separation in LSCO has been extensively studied in the past decade, as discussed in the previous chapters, little knowledge was accumulated on the magneto-crystalline anisotropy of LSCO. As far as we know, no experiment has been done to directly determine the anisotropy constants of LSCO in the ferromagnetic (FM) phase ($x \geq 0.175$). There was one estimation of the (assumed uniaxial) anisotropy constant $K_U$, which turns out to be in the range $3\times10^5$ to $1\times10^6$ erg/cm$^3$, done by H.M. Aarbogh *et al.* based on the blocking temperature and the determined cluster size from $x = 0.15$ LSCO single crystals [1]. However, a direct determination of $K$ is missing.

In spite of the lack of the information about the anisotropy constants, such a study can be very beneficial for the study of LSCO. One benefit is to properly understand the

blocking temperature $T_B$ of the FM clusters, which have been observed via different experimental techniques, as discussed in the previous chapters, at low dopings. Such a goal can be achieved via estimating 4/3 $\pi\xi^3 K$ ($\approx k_B T_B$), where $\xi$ is the cluster size, which is well established, and $K$ is the anisotropy constant, which remains unknown. In essence, we can check self-consistency between FM cluster sizes, anisotropies, and thermal stabilities. Another benefit of such a study would be the comparison of anisotropy constants between bulk and thin films LSCO. As reported by M.A. Torija *et al.* [2], the coercivities of $x$ = 0.50 LSCO thin films are largely enhanced compared to the corresponding bulk materials, which could be a strain-induced anisotropy effect. Prior to determining the anisotropy constants in LSCO thin films and performing the subsequent quantitative comparison between bulk and thin films, knowledge of the bulk anisotropy constants is obviously required.

Before showing the experimental data of LSCO single crystals, it is important to have a brief introduction about the magneto-crystalline anisotropy energy $E$. For FMs, the natural direction of spontaneous magnetization below the Curie temperature ($T_C$) is referred to as the easy axis of magnetization. The origin of magneto-crystalline anisotropy is the spin-orbit coupling. Because of the large magneto-static energy associated with uniform magnetization in a crystal, the crystal has the tendency to split into many small volumes of uniform magnetization, called domains, to minimize magneto-static energy. As a compromise, finite numbers of domains are formed to reach a minimal sum of magneto-static energy and domain wall energy. When a low field is applied, the domain walls will move to form larger domains to reduce the magneto-static energy. Under a large enough field, a large domain will form by rotating each individual domain magnetization to the field direction. The energy stored in the crystal by keeping the magnetization of the crystal along the field direction (not necessarily the easy magnetization orientation) is called the magneto-crystalline anisotropy energy, $E$.

In cubic crystals, it was first shown by N. S. Akulov [3-6] and was later generally accepted that the magneto-crystalline anisotropy energy $E$ can be expressed as below [7-9]:

$$E = K_0 + K_1(\alpha_1^2\alpha_2^2 + \alpha_2^2\alpha_3^2 + \alpha_3^2\alpha_1^2) + K_2\alpha_1^2\alpha_2^2\alpha_3^2 \qquad (6.1),$$

where $K_0$, $K_1$, and $K_2$ are magneto-crystalline anisotropy constants for some cubic crystal, usually expressed in ergs/cm$^3$, and $\alpha_1$, $\alpha_2$, and $\alpha_3$ are the cosines of the angles between the magnetic field and the principle axes in a cubic system. It can be seen that the first term $K_0$ in Eq. (6.1) is independent of the orientation, i.e. an isotropic term; therefore, it is usually dropped for anisotropy analysis since it has nothing to do with magneto-crystalline anisotropy. $K_1$ and $K_2$ are usually referred to as anisotropy constants in cubic materials. Higher power terms in Eq. (6.1) are generally not needed [9].

For high symmetry crystallographic orientations, such as [100], [100], and [111] in a cubic system, $E$ can be reduced to a simpler formula by straightforward calculations, as shown in Table 6.1(a) [9]. By comparing the $E$ along different orientations, easy, medium, and hard magnetization axes can be determined, as shown in Table 6.1(b). In simple terms, the easy magnetization axis corresponds to the minimum anisotropy energy while the hard magnetization axis corresponds to the maximum anisotropy energy at a given magnetic field. For example, when $K_1$ is positive and $K_2$ varies between -9/4 $K_1$ and $+\infty$, $E_{<100>} < E_{<110>} < E_{<111>}$, indicating <100> is the easy magnetization axis and <111> is the hard magnetization axis.

**Table 6.1**(a) Magneto-crystalline anisotropy energy for various crystallographic orientations for a cubic crystal. Reproduced from Ref. 9. (b) Easy, medium, and hard magnetization axes with different rang of anisotropy constants for a cubic crystal. Reproduced from Ref. 10.

(a)

| $[uvw]$ | $a$ | $b$ | $c$ | $\alpha_1$ | $\alpha_2$ | $\alpha_3$ | $E$ |
|---|---|---|---|---|---|---|---|
| [100] | 0 | 90° | 90° | 1 | 0 | 0 | $K_0$ |
| [110] | 45° | 45° | 90° | $1/\sqrt{2}$ | $1/\sqrt{2}$ | 0 | $K_0 + K_1/4$ |
| [111] | 54.7° | 54.7° | 54.7° | $1/\sqrt{3}$ | $1/\sqrt{3}$ | $1/\sqrt{3}$ | $K_0 + K_1/3 + K_2/27$ |

(b)

| $K_1$ | + | + | + | − | − | − |
|---|---|---|---|---|---|---|
| $K_2$ | $+\infty$ to $-9K_1/4$ | $-9K_1/4$ to $-9K_1$ | $-9K_1$ to $-\infty$ | $-\infty$ to $9\lvert K_1\rvert/4$ | $9\lvert K_1\rvert/4$ to $9\lvert K_1\rvert$ | $9\lvert K_1\rvert$ to $+\infty$ |
| Easy | ⟨100⟩ | ⟨100⟩ | ⟨111⟩ | ⟨111⟩ | ⟨110⟩ | ⟨110⟩ |
| Medium | ⟨110⟩ | ⟨111⟩ | ⟨100⟩ | ⟨110⟩ | ⟨111⟩ | ⟨100⟩ |
| Hard | ⟨111⟩ | ⟨110⟩ | ⟨110⟩ | ⟨100⟩ | ⟨100⟩ | ⟨111⟩ |

In this chapter, we will determine the easy and hard magnetization axes of LSCO via two methods: (i) angle-dependent magnetometry, and (ii) a study of domain formation via SANS.

## 6.2 Magnetometry

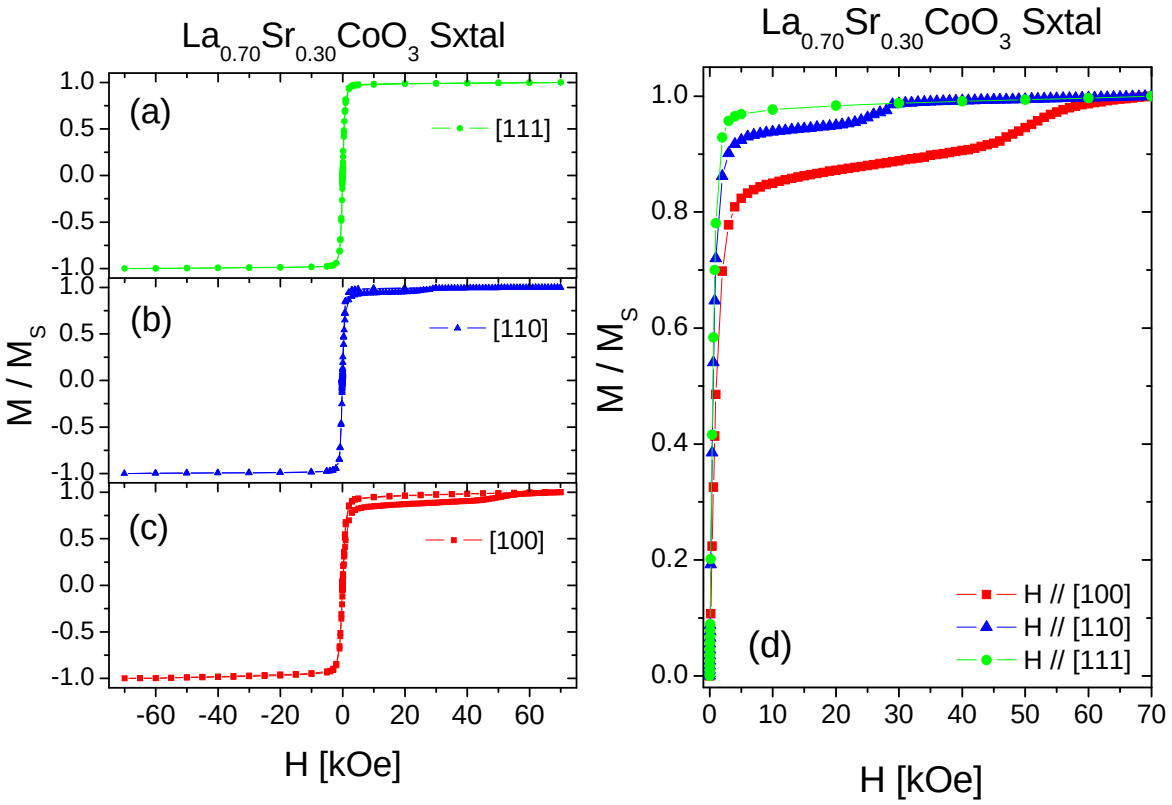


**Fig. 6.1** Normalized magnetization hysteresis loops of a $La_{0.7}Sr_{0.3}CoO_3$ single crystal at 10 K for applied magnetic field *H* along (a) [111], (b) [110], (c) [100] orientations, and (d) the normalized virgin curves.

Figs. 6.1(a)-(c) show the normalized magnetization hysteresis loops of an $x = 0.30$ $La_{1-x}Sr_xCoO_3$ single crystal at 10 K with applied field along three high symmetry crystallographic orientations, [111], [110], and [100], which were aligned through Laue X-ray diffraction. The corresponding virgin curves for each configuration are shown in Fig. 6.1(d). After zero field cooling, the field sweeps (Figs. 6.1 (a)-(c)) started from zero field, increased to 70 kOe, decreased to -70 kOe, and went back to 70 kOe. From Fig. 6.1(d), it can be seen that for [100], the domain rotation and thus the saturated magnetization is achieved at a much larger field (around 55 kOe), than in the [110]

(around 25 kOe) and the [111] (around 2~3 kOe), clearly indicating that for $x$ = 0.30 $La_{1-x}Sr_xCoO_3$ crystals, [100], [110], and [111] are the hard, medium, and easy magnetization axes, respectively. Such a conclusion is also reinforced by comparing the magnetization curves to that of a well understood ferromagnetic material, for example, faced centered cubic nickel, with <111> easy axis, as shown in Fig. 6.2. The qualitative similarity between these two sets of magnetization curves is clear.

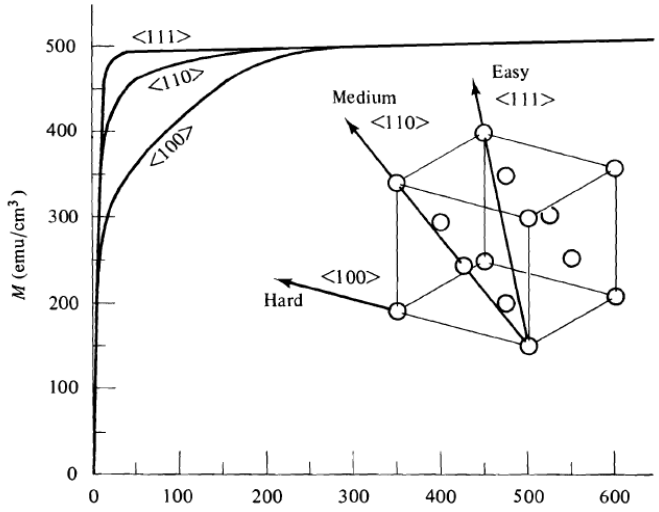


**Fig. 6.2** Magnetization virgin curves of nickel crystal. Reproduced from Ref. 9,11.

However, it is surprising that the magnetization saturation of the virgin curves occurs at such a large field for the medium and hard magnetization axes. One possible origin is the isolated non-FM phases existing in the system, i.e. magnetic inhomogeneities. Although these non-FM phases were argued to be absent for $x$ > 0.22 crystals, as discussed in Chapter 5, they may still exist in minute quantities in the system. Such a hypothesis is in agreement with the non-saturation of the torque observed in the recent experiments on the same doping, which will be discussed in Chapter 7.

Such a hypothesis is also strengthened by the hysteresis loops of an $x$ = 0.20 $La_{1-x}Sr_xCoO_3$ single crystal, as shown in Fig. 6.3. We believe that the increased phase fraction of the isolated non-FM phases at decreased Sr doping drives the saturation field to a much larger field for each crystallographic orientation than for $x$ = 0.30 . For [111], it can be seen that the saturation field is promoted to a range of 10-60 kOe, while for [110] and [100], we believe that the saturation fields are far beyond the maximum field applied (70

kOe). As a side note, it is worthwhile to point out that the absence of a goniometer while carrying out the magnetometry measurement may result in slight misalignment of the samples to some extent, and introduce some systematic errors. However, the tendency of increased saturation fields with decreased doping in highly doped LSCO seems clear. At the very least, it is safe to conclude from magnetometry measurements that in highly doped $La_{1-x}Sr_xCoO_3$ single crystals, <100>, <110>, and <111> are the hard, medium, and easy magnetization axes, respectively.

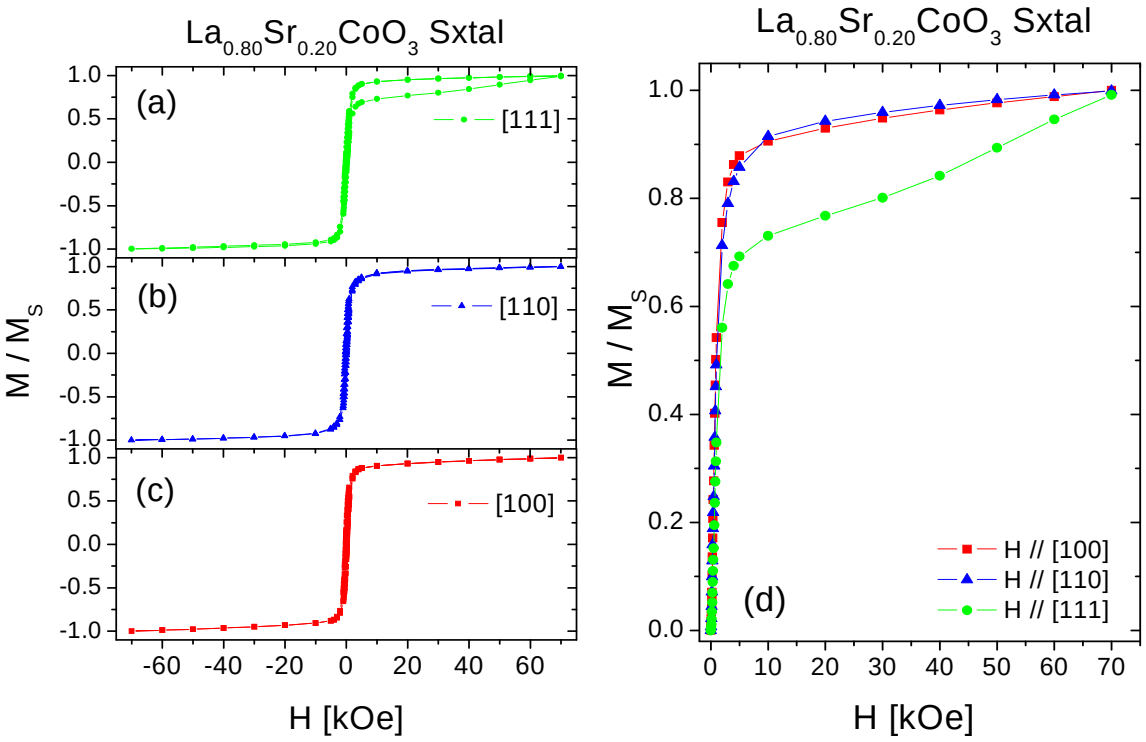


**Fig. 6.3** Normalized magnetization hysteresis loops of a $La_{0.8}Sr_{0.2}CoO_3$ single crystal at 10 K for applied magnetic field *H* along (a) [111], (b) [110], (c) [100] orientations, and (d) the normalized virgin curves.

## 6.3 Anisotropic SANS

We also discovered that SANS can be used to explore the magneto-crystalline anisotropy in highly doped LSCO crystals. When the crystal is cooled below the Curie temperature at zero field, the preferred orientations of the spontaneously formed domains will point along the easy magnetization axes. As discussed in section 2.3.4.2, since the

scattering intensity $\frac{d\Sigma}{d\Omega}$ is proportional to $\sin^2(\theta)$ ($\theta$ is the angle between the magnetization in the sample and some specific orientation on the detector), the preferred magnetization along the easy axes will produce an anisotropic scattering pattern on the detector. By examining the anisotropic SANS pattern on the detector, the magneto-crystalline anisotropy in the crystals can be investigated.

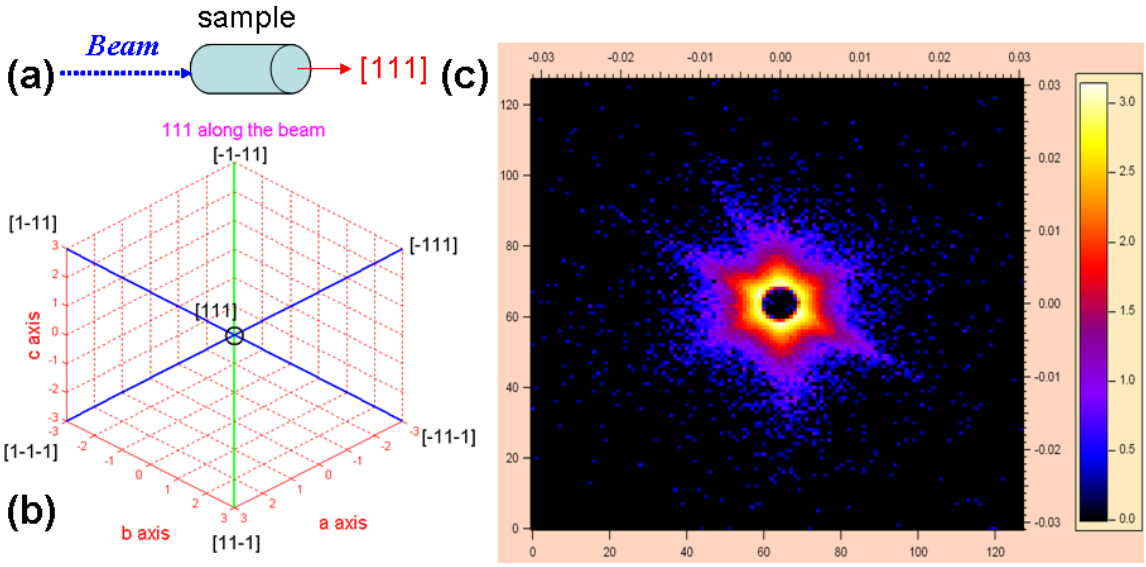


**Fig. 6.4** (a) Sample alignment for a $La_{0.8}Sr_{0.2}CoO_3$ single crystal with one of <111> axes parallel to neutron beam, (b) schematic diagram of the rest <111> axes in the view of neutron beam, and (c) the SANS scattering pattern on the two dimensional detector for the above sample alignment at 12.6 K in the low $q$ (0.003 $Å^{-1} \leq q \leq$ 0.03 $Å^{-1}$) configuration, scale bar indicates the scattering intensity with a log scale.

If <111> are the easy magnetization axes, when the sample is aligned with one of the <111> axes along neutron beam, as shown in Fig. 6.4(a), since the magnetizations *visible* to neutron beam are only the components perpendicular to neutron beam, as discussed in section 2.3.4.2, only the magnetizations along the rest of the six <111> axes should be detected and reflected on the detector. As can be seen from Fig. 6.4(b), the rest of the six <111> axes are equally separated. The simple schematic diagram indicates the SANS scattering pattern should have a six-fold symmetry. Such a prediction is verified by an experiment performed at 12.6 K after zero field cooling of a $La_{0.8}Sr_{0.2}CoO_3$ single crystal aligned with one of the <111> axes along neutron beam, as shown in Fig. 6.4 (c). The six

fold symmetry is evident from the scattering pattern, which is in perfect agreement with the prediction. Above the Curie temperature, as expected, the six-fold symmetry disappears and the SANS scattering pattern becomes isotropic, as shown in Fig. 6.5.

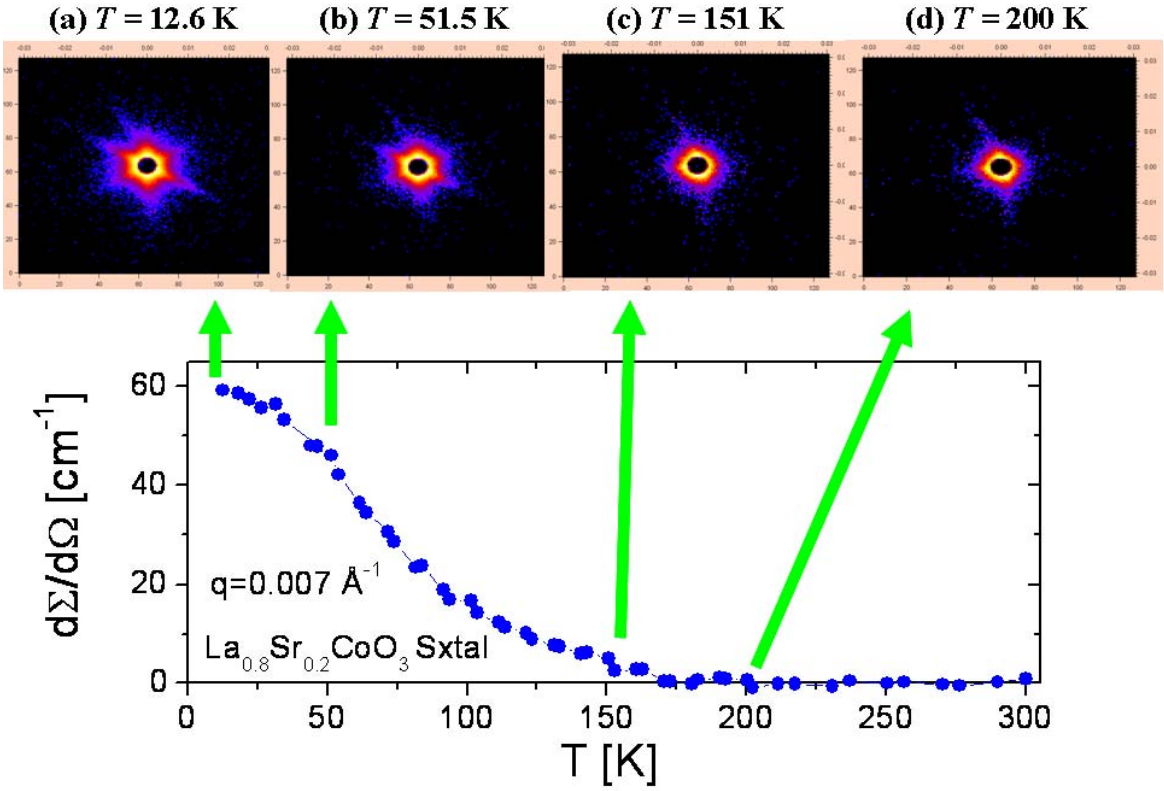


**Fig. 6.5** Temperature dependence of the SANS scattering pattern on the detector for the same sample alignment shown in Fig. 6.4. The bottom panel shows the corresponding temperature dependence of low $q$ scattering ($q$ = 0.007 Å$^{-1}$).

It becomes even clearer by examining the angular dependence of the intensity after subtracting the room temperature background at some specific $q$ value with a small width. Such an angular dependence is shown in Fig. 6.6, which is achieved by subtracting the high temperature absolute cross section and integrating the intensity at different angle over a ring with $q$ centered at 0.006 Å$^{-1}$ and a width 0.001 Å$^{-1}$. The six fold symmetry is clearly seen. It is worthwhile to point out that such a small $q$ value indicates the domains really possess long-range scale, on the order of 1000 Å, as mentioned in section 2.3.4.2. The data can actually be reasonably fitted with two-fold and six-fold cosine functions, as shown in Fig. 6.6. The two-fold cosine function is added to produce the 2 predominantly

peaks, which may be due to the fact that the real structure is rhombohedrally distorted along two of the <111> axes instead of being perfect cubic, as discussed in Chapter 1. Alternatively, the small remnant field in the SANS instrument could have preferably aligned two of the <111> axes.

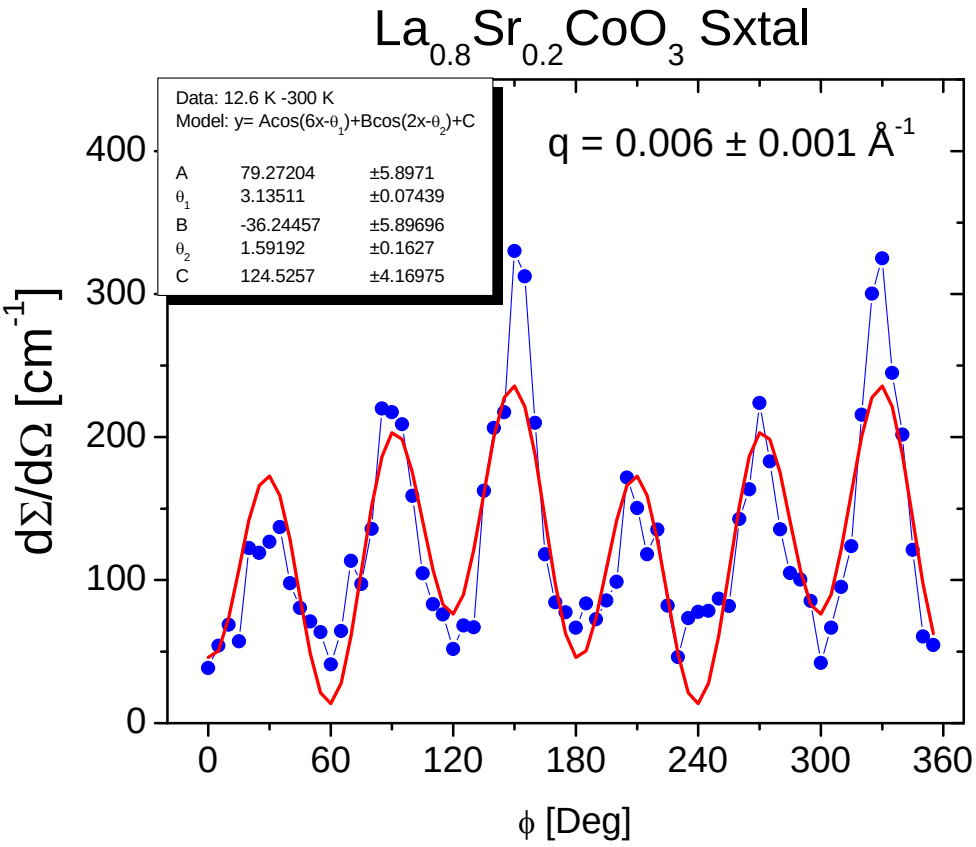


**Fig. 6.6** Angular dependence of SANS magnetic scattering at 12.6 K for a $La_{0.8}Sr_{0.2}CoO_3$ single crystal (as shown in Fig. 6.4.) after subtracting the high temperature background. The integration ring is centered at $q$ = 0.006 Å$^{-1}$ with a width of ± 0.001 Å$^{-1}$. The red line represents the fit, as discussed in the text.

Although the SANS experiments on a $La_{0.8}Sr_{0.2}CoO_3$ single crystal strongly suggests that <111> are the easy magnetization axes, one may argue that it is possible that <100> are the easy axes since a six-fold symmetry can also be produced under the same sample alignment configuration (<111> along neutron beam). Therefore, the SANS experiment with <111> aligned along the neutron beam alone does not seem to rule out the possibility of <100> being the easy axes. To discriminate these two possibilities, one

experiment that can be done is to align <111> along the vertical direction (the beam direction is defined as horizontal), i.e. perpendicular to the beam direction, as shown in Fig. 6.7(a). Under this sample alignment configuration, the possibility of <111> being the easy axis will produce an eight-fold symmetry with not necessarily equal separation, as shown in Fig. 6.7(b), or a six-fold symmetry (the scattering components of two sets of <111> axes in the are both aligned along vertical direction). However, the possibility of <100> being the easy axis will produce a four-fold symmetry (one set of <100> axes are aligned with neutron beam), or a six-fold symmetry. Under no circumstances, will <100> being the easy axis produce an eight-fold symmetry. The experimental evidence of an eight-fold symmetry at 10 K on a $La_{0.7}Sr_{0.3}CoO_3$ single crystal can be seen in Fig. 6.7(c). Such an eight-fold symmetry becomes even clearer in the plot of angular dependence of the intensity at some specific $q$ value with a small width, as shown in Fig. 6.8. This angular dependence is achieved by integrating the intensity at different angle over a ring with $q$ centered at 0.008 $Å^{-1}$ and a width 0.001 $Å^{-1}$. The eight fold symmetry is self-evident. Therefore, the observation of such an eight-fold symmetry in the SANS scattering pattern unambiguously pins down the easy magnetization axes to <111>.

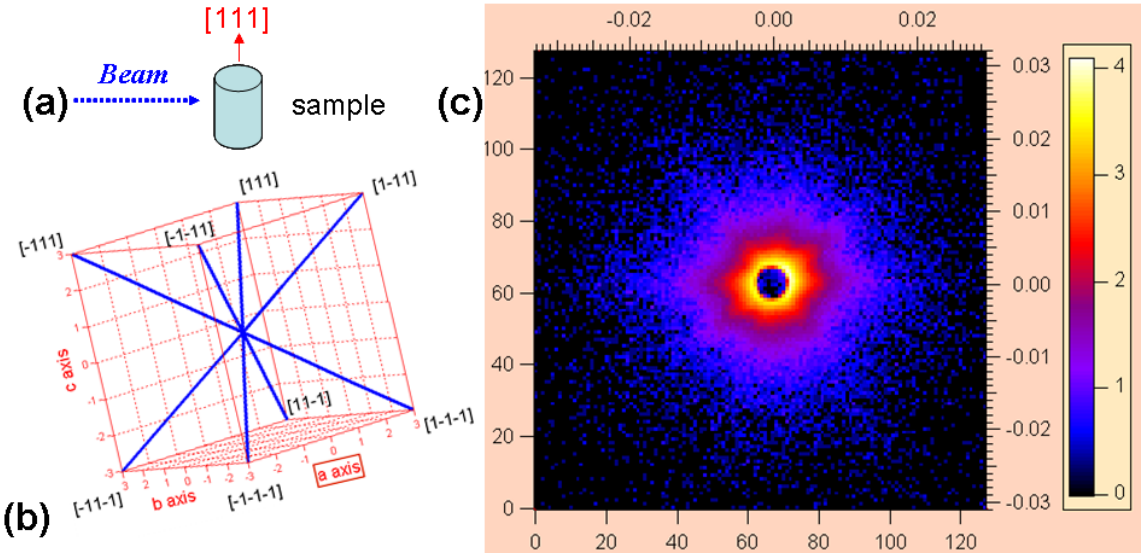


**Fig. 6.7** (a) Sample alignment for a $La_{0.7}Sr_{0.3}CoO_3$ single crystal with one of <111> axes perpendicular to neutron beam, (b) schematic diagram of all <111> axes in the view of neutron beam, and (c) the SANS scattering pattern on the two dimensional detector for the above sample alignment at 10 K in the low $q$ ($0.003\ Å^{-1} \leq q \leq 0.03\ Å^{-1}$) configuration, scale bar indicating the scattering intensity with a log scale.

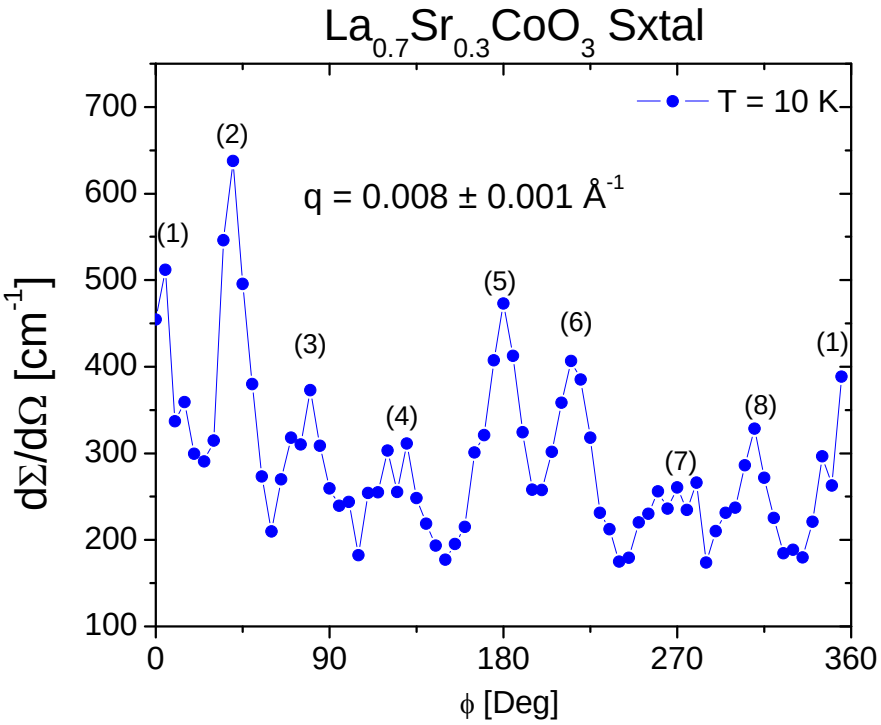


**Fig. 6.8** Angular dependence of SANS magnetic scattering at 10 K for a $La_{0.7}Sr_{0.3}CoO_3$ single crystal (as shown in Fig. 6.7.). The integration ring is centered at $q$ = 0.008 Å$^{-1}$ with a width of ± 0.001 Å$^{-1}$.

In summary, in this chapter, the efforts of determining the magnetic anisotropy in highly doped LSCO are made. The experiments performed on two different dopings of LSCO in the FM phase through magenetometry and SANS lead to the conclusion that in highly doped LSCO, the easy and hard magnetization axes are <111> and <100>, respectively. Such an easy magnetization axis may be due to the rhombohedra structure of the crystals, which will split the equal Co-O bond length of an octahedron in a perfectly cubic structure into two sets, i.e. a short Co-O bond length set and a long Co-O length set. This bond length splitting will further affect the strength of double exchange (DE) in the Co-O-Co chains. Somehow, due to the Co-O length splitting, the spin-orbit coupling along <111> axes favors <111> being the easy magnetization axis. More theoretical work is required to fully understand the origin. In addition to that, the quantitative determination of the anisotropy constants requires the usage of torque magnetometry, as will be discussed in Chapter 7.

# Chapter 7
# Summary, conclusions, and future work

In this thesis, magneto-electronic phase separation in the perovskite $La_{1-x}Sr_xCoO_3$ single crystals was extensively studied through complementary experimental techniques including heat capacity, small angle neutron scattering, magnetometry, and transport, as well as via statistical simulations. Not only was the evolution of phase separation with doping and temperature thoroughly investigated, but also the fundamental origin for such a phenomenon was explored. In addition, the spin state transition in $LaCoO_3$ at low temperature, the percolation nature of metal-insulator transition in doped $La_{1-x}Sr_xCoO_3$ (LSCO), and the magnetic anisotropy in highly doped LSCO were examined carefully, as summarized in detail below.

Through heat capacity, a new origin for finite spin Co ions in $LaCoO_3$ was revealed, which even persists to low temperature ($T\rightarrow$ 0 K). This was detected via a Schottky Anomaly in the heat capacity, which was not previously known. The determined dilute concentration of about 0.11% for these finite spin states indicates they are not driven by thermal excitation, but by defects such as oxygen vacancies. The additional field dependent experiments established that these excited states have a zero field splitting about 0.5 meV and a *g* factor of about 3.5, which is consistent with the spin-orbit high spin (HS) triplet scheme observed in prior work. Such a discovery casts a new understanding of the spin state at low temperature, which was generally accepted as low spin (zero spin), despite the highly-debated nature of the spin state transition occurring at higher temperature.

Via small-angle neutron scattering and d.c. susceptibility, a specific type of phase separation in the ferromagnetic (FM) phase in LSCO was thoroughly studied. Such a study reveals the formation of short-range ordered FM clusters below a well-defined temperature ($T^*$) of about 360 K. It was demonstrated that the characteristics of this clustered state in LSCO appear quite unlike those of a Griffiths phase, although many of the features of preformed clusters above the Curie temperature in other doped perovskites conform to the expectations for a Griffiths phase. The deviation from Curie-Weiss (C-W) behavior is opposite to expectations and is field independent, while $T^*$ does not

correspond to the undiluted Curie temperature. These results illustrate that the Griffiths model may not be universally applicable to randomly doped transition metal oxides.

Through a variety of experimental techniques including heat capacity, small angle neutron scattering, transport and magneto-transport, the origin of MEPS in LSCO single crystals was explored. It was discovered that there exists a finite doping range over which MEPS occurs. Such a doping range is unambiguously determined from different experimental techniques, turning out to be $0.04 < x < 0.22$. Also, the same doping range was perfectly reproduced by statistical simulations based on local compositional fluctuations at the experimentally determined magnetic correlation length scale. This excellent agreement leads to the conclusion that the phase separation in LSCO is driven solely by inevitable local compositional fluctuations at nanoscopic length scales. Such a conclusion indicates that nanoscopic phase separation is doping fluctuation-driven rather than electronically-driven in LSCO. This mechanism might also be applicable to the nanoscopic phase separation in other randomly doped materials. In addition, from the heat capacity and ordinary Hall effect in LSCO single crystals, the evidence for a softening of the lattice at intermediate doping values, strong additional evidence for the percolation nature of the insulator-metal transition, and a large electron mass enhancement due to strong electron-electron correlations in the FM phase was found. Finally, the effect of microscopic phase separation on the macroscopic electrical transport in LSCO was also studied. It was demonstrated that (i) the $T = 0$ metal-insulator transition can be quantitatively understood within the double exchange-modified percolation framework, and, (ii) due to a crossover in the nature of the spin fluctuations, the onset of a phase-pure low $T$ FM state at high doping has a profound effect on the *high* $T$ transport.

Finally, through magenetometry and SANS, the magneto-crystalline anisotropy of highly doped LSCO was studied. The experiments done on two crystals at different dopings clearly indicate that in highly doped LSCO, the easy and hard magnetization axes are the <111> and <100> axes, respectively. However, a quantitative determination of the anisotropy constants of highly doped LSCO is elusive.

In spite of the intensive study of LSCO in the current work, some important questions remained unanswered. One of them, as mentioned above, is the magneto-crystalline

anisotropy constant of highly doped LSCO. Although the easy and hard magnetization axes were determined through magnetometry and small angle neutron scattering, the quantitative determination of the anisotropy constants is still not available. Such important information can be achieved through torque magnetometry measurements. Preliminary experiments have been done on highly doped samples and revealed some significant difficulties including non-saturation of the torque and complications with alignment of small crystals. Recent work in conjunction with C. Keppel provided a reliable route to avoid the first problem via separation of FM and non-FM components. In future work, careful alignment procedures should enable reliable measurements.

For future work, there are some other things worthwhile for further exploration, as discussed below. Some preliminary work has been done in each of these areas:

(i) Phase separation in $La_{1-x}Sr_xCoO_3$ thin films.

As revealed by the experiments on LSCO single crystals, the phase separation occurs at the nanoscopic scale. It is interesting to explore what will happen in LSCO thin films with thickness on the order of a few nm due to size confinement. A series of thin films with various thickness for $x$ = 0.50 and 0.22 have been grown by our group. The magnetometry and transport experiments carried out by our group suggest there exists a critical thickness for $x$ = 0.50, below which unexpected phase separation occurs. Such a suggestion was confirmed by the recent small angle neutron scattering (SANS) experiments in conjunction with M. Torija. A systematic study aiming to uncover the doping and thickness evolution of the phase separation in LSCO thin films is underway in our group.

(ii) Layered perovskite compounds $La_{2-x}Sr_xCoO_4$

Being a quasi-2D system, $La_{2-x}Sr_xCoO_4$ illustrates fascinating features like CMR, Griffiths-like behavior, and the spin-state transitions, etc. Considering the non-Griffiths-like behavior observed in perovskite $La_{1-x}Sr_xCoO_3$, which has a 3D structure, it is intriguing to compare these two compounds and study the dimensionality dependence. Such a quasi-2D system can be used as an ideal model system to understand the phase separation, which can lead to some general conclusions determined solely by dimension. In spite of these benefits, so far little work is done on these compounds, which are only

limited to some specific doping compositions. We have fabricated 11 polycrystalline samples with evenly spaced dopings, aiming to systematically study these compounds. In collaboration with Argonne National Lab, efforts to synthesize single crystals are underway.

(iii) Phase separation in narrow-bandwidth compounds, e.g. $Pr_{1-x}Ca_xCoO_3$.

The exploration of phase separation in these compounds can be used to test the validity of the origin for nanoscopic phase separation, proposed as the most important conclusion of this thesis, i.e. the local doping fluctuation mechanism. If such an origin is correct, it should also explain the active doping limits for phase separation in $Pr_{1-x}Ca_xCoO_3$. Thus far, a series of polycrystalline samples have been made. Preliminary experiments via magnetometry and transport have been done in our group. A major part of the systematic study via heat capacity is completed. Recent SANS experiments in conjunction with S. El-Khatib provided reliable information about the length scale of phase separation in this material. Future work includes fully oxygenating the samples and carrying out the rest of the phase separation exploration in these compounds.

# Bibliography

## Chapter 1


1. D. G. Schlom, S. Guha, and S. Datta, *Gate Oxides Beyond $SiO_2$*, MRS Bulletin, Vol. 33, November 2008, www.mrs.org/bulletin.
2. J.F. Scott, C.A. Paz de Araujo, Science **246**, 1400 (1989).
3. P. Holtappels, U. Vogt, and T. Graule, Advanced Engineering Materials **7**, no.5 292 (2005).
4. M. Viret, M. Drouet, J. Nassar, J.-P. Contour, C. Fermon, and A. Fert, Europhys. Lett., vol. 39, p. 545(1997).
5. M. H. Jo, N. D. Mathur, N. K. Todd, and M. G. Blamire, Phys. Rev. B **61**, R 14905 (2000).
6. M. Bowen, M. Bibes, A. Barthelemy, J.-P. Contour, A. Anane, Y. Lemaitre, and A. Fert, Appl. Phys. Lett. **82**, 233 (2003).
7. M. Bibes, A. Barthelemy, IEEE Trans. Electron. Devices, 54, 1003 (2007).
8. R. Ramesh, and D. G. Schlom, *Whither Oxide Electronics?* MRS Bulletin, Vol. 33, November 2008, www.mrs.org/bulletin.
9. E. Dagotto, *Nanoscale phase separation and colossal magnetoresistance*, Springer, New York (2002).
10. E. Dagotto, T. Hotta and A. Moreo, Phys. Rep. **344** 1 (2001).
11. P.A. Lee, N. Nagaosa, X. G. Wen, Rev. Mod. Phys. **78** 17 (2006).
12. Y. Tokura and Y. Tomioka, J. Mag. Mag. Mat. **200** 1 (1999).
13. J.M.D. Coey, M. Viret, and S. von Molnár, Adv. in Phys. **48** 167 (1999).
14. M.B. Salamon and M. Jaime, Rev. Mod. Phys. **73** 583 (2001).
15. K. Rabe, J.-M. Triscone, and Ch. H Ahn, *Physics of Ferroelectrics: A modern perspective*. Springer (2007).
16. R. Ramesh and N. A. Spaldin, Nature Materials **6**, 21 (2007).
17. R. von Helmolt, J. Wecker, B. Holzapfel, L. Schultz, and K. Samwer, Phys. Rev. Lett. **71**, 2331 (1993).
18. J. Volger, Physica **20**, 49 (1954).

19. M. Fath, S. Freisem, A.A. Menovsky, Y. Tomioka, J. Aarts, and J.A. Mydosh, Science **285**, 1540 (1999).
20. A. N. Pasupathy *et al*., Science **320**, 196 (2008).
21. G. R. Blake, L. Chapon, P. G. Radaelli, D. N. Argyriou, M. J. Gutmann, and J. F. Mitchell, Phys. Rev. B **66**, 144412 (2002).
22. E.Granado, C. D.Ling, J. J.Neumeier, J. W. Lynn, and D. N. Argyriou, Phys. Rev. B **68** 134440 (2003).
23. J.W. Lynn, R.W. Erwin, J.A. Borchers, Q. Huang, A. Santoro, J.-L. Peng, and Z.Y. Li, Phys. Rev. Lett. **76** 4046 (1996).
24. M. Hennion, F. Moussa, G. Biotteau, J. Rodriguez-Carvajal, L. Pinsard, and A. Revcolevschi, Phys. Rev. Lett. **81** 1957 (1998).
25. Ch. Simon, S. Mercone, N. Guiblin, C. Martin, A. Brulet, and G. Andre, Phys. Rev. Lett. **89** 207202 (2002).
26. G. Papavassiliou, M. Fardis, M. Belesi, T. G. Maris, G. Kallias, M. Pissas, D. Niarchos, C. Dimitropoulos, and J. Dolinsek, Phys. Rev. Lett. **84** 761(2000).
27. G. Papavassiliou, M. Belesi, M. Fardis, and C. Dimitropoulos, Phys. Rev. Lett. **87** 177204 (2001).
28. M. Belesi, G. Papavassiliou, M. Fardis, M. Pissas, J. E. Wegrowe, and C. Dimitropoulos, Phys. Rev. B **63**, 180406 (2001).
29. P.L. Kuhns, M.J.R. Hoch, W.G. Moulton, A.P. Reyes, J. Wu and C. Leighton, Phys. Rev. Lett. **91** 127202 (2003).
30. D. Phelan, D. Louca, S. Rosenkranz, S.-H. Lee, Y. Qui, P.J. Chupas, R. Osborn, H. Zheng, J.F. Mitchell, J.R.D. Copley, J.L. Sarrao, and Y. Moritomo, Phys. Rev. Lett. **96** 027201 (2006).
31. D. Phelan, D. Louca, K. Kamazawa, S.-H. Lee, S.N. Ancona, S. Rosenkranz, Y. Motome, M.F. Hundley, J.F. Mitchell, and Y. Moritomo, Phys. Rev. Lett. **97** 235501 (2006).
32. B.F. Woodfield, M.L. Wilson, and J.M. Byers, Phys. Rev. Lett. **78** 3201 (1997).
33. A.L. Cornelius, B.E. Light and J.J. Neumeier, Phys. Rev. B. **68** 014403 (2003).

34. M. Paraskevopoulos, J. Hemberger, A. Krimmel, and A. Loidl, Phys. Rev. B. **63** 224416 (2001).
35. R. Mahendiran and P. Schiffer, Phys. Rev. B. **68** 024427 (2003).
36. S. Tsubouchi, T. Kyômen, M. Itoh, and M. Oguni, Phys. Rev. B **69** 144406 (2004).
37. K. Muta, Y. Kobayashi, and K. Asai J. Phys. Soc. .Jpn. **71** 2784 (2002).
38. S. Tsubouchi, T. Kyomen, and M. Itoh, Phys. Rev. B. **67** 094437 (2003).
39. T. Asaka, Y. Anan, T. Nagai, S. Tsutsumi, H. Kuwahara, K. Kimoto, Y. Tokura and Y. Matsui, Phys. Rev. Lett. **89** 207203 (2002).
40. M. Tokunaga, Y. Tokunaga, and T. Tamegai, Phys. Rev. Lett. **93** 037203 (2004).
41. Y. Tokura, *Physics Today*, 50 July (2003)
42. M. Gerloch, R.C. Slade , *Ligand-Field Parameters*, (1973).
43. K. Yoshida, *Theory of Magnetism*, (1996).
44. C. Herring, in *Magnetism*, edited by J. Rado and H. Suhl (Academic, New York, 1965), Vol. 2.
45. Y. Okimoto, T. Katsufuji, T. Ishikawa, A. Urushibara, T. Arima, and Y. Tokura, Phys. Rev. Lett. **75**, 109 (1995)
46. A. J. Millis, B. I. Shraiman, and R. Mueller, Phys. Rev. Lett.**77**, 175 (1996).
47. M. Quijada, J. Cerne, J. R. Simpson, H. D. Drew, K. H. Ahn, A. J. Millis, R. Shreekala, R. Ramesh, M. Rajeswari, and T. Venkatesan, Phys. Rev. B **58**, 16093 (1998).
48. A. Machida, Y. Moritomo, and A. Nakamura, Phys. Rev. B **58**, 12540 (1998).
49. S. Satpathy, Z. S. Popovic, and F. R. Vukajlovic, Phys. Rev. Lett.**76**, 960 (1996).
50. C. Zener, Phys. Rev. **82**, 403 (1951).
51. P. G. de Gennes, Phys. Rev. **118**, 141 (1960).
52. P. W. Anderson and H. Hasegawa, Phys. Rev. **100**, 675 (1955).
53. H. A. Jahn, and E. Teller, *Stability of Polyatomic Molecules in Degenerate Electronic States. I. Orbital Degeneracy*. (1937).
54. J. Kanamori, J.Appl. Phys.Suppl. **31**, 14s (1960).
55. D.S. Dessau, and Z.-X. Shen, *Contribution to Colossal Magnetoresistance Oxides, Monographs in Condensed Matter Science*. Gordon & Breach, London. 1999.

56. M. Imada, A. Fujimori, and Y. Tokura, Rev. Mod. Phys. **70**, 1039 (1998).
57. W. E. Pickett and D. J. Singh, Phys. Rev. B **53**, 1146 (1996).
58. H. Y. Hwang, S. W. Cheong, P. G. Radaelli, *et al.*, Phys. Rev. Lett. **75**, 914 (1995).
59. Y. Tomioka, Y. Tokura, Metal-insulator phenomena relevant to charge/orbital-ordering in perovskite-type manganese oxides. 1999.
60. A. J. Millis, P.B. Littlewood, and B.I. Shraiman, Phys. Rev. Lett.**74**, 5144 (1995).
61. H. Roder, J. Zang, and A. R. Bishop, Phys. Rev. Lett. **76** 1356 (1996).
62. A. S. Alexandrov and A. M. Bratkovsky, Phys. Rev. Lett. **82**, 141 (1999).
63. A. J. Millis, Nature **392**, 147 (1998).
64. J. Wu. Ph.D Thesis, *Magneto-electronic phase separation in* $La_{1-x}Sr_xCoO_3$, University of Minnesota, U.S.A. September 2006.
65. S. Yunoki, J. Hu, A. L. Malvezzi, A. Moreo, N. Furukawa, and E. Dagotto, Phys. Rev. Lett. **80**, 845 (1998).
66. S. Yunoki and A. Moreo, Phys. Rev. B **58**, 6403 (1998).
67. S. Yunoki, A. Moreo, and E. Dagotto, Phys. Rev. Lett. **81**, 5612 (1998).
68. K.I. Kugel, A.L. Rakhmanov and A.O. Sboychakov, Phys. Rev. Lett. **95** 267210 (2005).
69. M.Yu. Kagan, D.I. Khomskii, and M. Mostovoy, Eur. Phys. J. B **12**, 217(1999).
70. D.I. Khomskii, Physica B **280**, 325 (2000).
71. S-Q. Shen and Z.D. Wang, Phys. Rev. B **58**, R8877 (1998); F. Zhong and Z.D. Wang, Phys. Rev. B **60**, 11883 (1999); B. M. Letfulov, Eur. Phys. J. B **14**, 19 (2000).
72. C. Perroni, G. De Filippis, V. Cataudella, and G. Iadonisi, cond-mat/0106588, preprint 2001;Y. Motome and M. Imada, ISSN 0082-4789, preprint.
73. J. Burgy, M. Mayr, V. Martin-Mayor, A. Moreo and E. Dagotto, Phys. Rev. Lett. **87** 277202 (2001).
74. K.H. Ahn, T. Lookman and A.R. Bishop, Nature **428** 401 (2004).
75. M.Uehara, S.Mori, C.H.Chen, and S.-W.Cheong, Nature **399**, 560(1999).
76. K. H. Kim, M. Uehara, V. Kiryukhin, S.-W. Cheong, *Multi-Scale Phase Modulations in Colossal Magnetoresistance Manganites*, Kluwer Academic Publishers, (2004).
77. W. C. Koehler and E. O. Wollan, J. Phys. Chem. Solids **2**, 100 (1957).

78. R. R. Heikes, R. C. Miller, and R. Mazelsky, Physica (Amsterdam) **30**, 1600 (1964).
79. P.M. Raccah and J.B. Goodenough, J. Appl. Phys. **39** 1209 (1968).
80. P.M. Raccah and J.B. Goodenough, Phys. Rev. **155** 932 (1967).
81. S. R. English, J. Wu, and C. Leighton, Phys. Rev. B **65**, 220407(R) (2002).
82. V.G. Bhide, D. S. Rajoria, G. R. Rao, and C. N. R. Rao, Phys. Rev. B **6**, 1021 (1972).
83. K. Asai, O. Yokokura, N. Nishimori, H. Chou, J. M. Tranquada, G. Shirane, S. Higuchi, Y. Okajima, and K. Kohn, Phys. Rev. B **50**, 3025 (1994).
84. For a short review see, M. Imada, A. Fujimori, and Y. Tokura, Rev. Mod. Phys. **70**, 1039 (1998), pp. 1235–1239.
85. S. Yamaguchi, Y. Okimoto, H. Taniguchi, and Y. Tokura, Phys. Rev. B **53**, R2926 (1996).
86. K. Asai, A. Yoneda, O. Yokokura, J. M. Tranquada, G. Shirane, and K. Kohn, J. Phys. Soc. Jpn. **67**, 290 (1998).
87. S. Yamaguchi, Y. Okimoto, and Y. Tokura, Phys. Rev. B **55**, R8666 (1997).
88. K. Asai, P. Gehring, H. Chou, and G. Shirane, Phys. Rev. B **40**, 10 982 (1989).
89. Y. Kobayashi, N. Jujiwara, S. Murata, K. Asai, and H. Yasuoka, Phys. Rev. B **62**, 410 (2000).
90. M. Itoh, M. Sugahara, I. Natori, and K. Motoya, J. Phys. Soc. Jpn. **64**, 3967 (1995).
91. M.A. Korotin, S. Yu. Ezhov, I.V. Solovyey, V.I. Anisimov, D.I. Khomskii and G.A. Sawatzky, Phys. Rev. B. **54** 5309 (1996).
92. C. Zobel, M. Kriener, D. Bruns, J. Baier, M. Gruninger, T. Lorenz, P. Reutler and A. Revcolevschi, Phys. Rev. B. **66** 020402(R) (2002).
93. G. Maris, Y. Ren, V. Volotchaev, C. Zobel, T. Lorenz and T.T.M. Palstra, Phys. Rev. B. **67** 224423 (2003).
94. G. Vanko, J.-P. Rueif, A. Mattila, Z. Nemeth and A. Shukla, Phys. Rev. B. **73** 024424 (2006).
95. R.F. Klie, J.C. Zheng, Y. Zhu, M. Varela, J. Wu, and C. Leighton, Phys. Rev. Lett. **99** 047203 (2007).
96. S. Noguchi, S. Kawamata, K. Okuda, H. Nojiri, and M. Motokawa, Phys. Rev. B. **66** 094404 (2002).

97. M.J.R. Hoch, S. Nellutla, J. van Tol, E.S. Choi, J. Lu, and J.M. Mitchell, Phys. Rev. B. **79** 214421 (2009).

98. M.W. Haverkort, Z. Hu, J.C. Cezar, T. Burnus, H. Hartmann, M. Reuther, C. Zobel, T. Lorenz, A. Tanaka, N.B. Brookes, H.H. Hsoeh, H.-J. Lin, C.T. Chen, and L.H. Tjeng, Phys. Rev. Lett. **97** 176405 (2006).

99. A. Podlesnyak, S. Streule, J. Mesot, M. Medarde, E. Pomjakushina, K. Conder, A. Tanaka, M.W. Haverkort, and D.I. Khomskii, Phys. Rev. Lett. **97** 247208 (2006).

100. Z. Ropka and R.J. Radwanski, Phys. Rev. B. **67** 172401 (2003).

101. D. Louca and J.L. Sarrao, Phys, Rev. Lett. **91** 155501 (2003)

102. N. Sundaram, Y. Jiang, I.E. Anderson, D.P. Belanger, C.H. Booth, F. Bridges, J.F. Mitchell, Th. Proffen, and H. Zheng, Phys. Rev. Lett. **102** 026401 (2009).

103. R. Caciuffo, D. Rinaldi, G. Barucca, J. Mira, J. Rivas, M.A. Señarís Rodríguez, P.G. Radaelli, D. Fiorani, and J.B. Goodenough, Phys. Rev. B **59,** 1068 (1999)

104. P. Ravindran, P. A. Korzhavyi, H. Fjellvag, and A. Kjekshus, Phys. Rev. B **60**, 16423 (1999)

105. J. Wu and C. Leighton, Phys. Rev. B **67**, 174408 (2003).

106. M.J.R. Hoch, P.L. Kuhns, W.G. Moulton, A.P. Reyes, J. Wu, and C. Leighton, Phys. Rev. B. **69** 014425 (2004).

107. M.J.R. Hoch, P.L. Kuhns, W.G. Moulton, A.P. Reyes, J. Lu, J. Wu, and C. Leighton, Phys. Rev. B. **70** 174443 (2004).

108. M.J.R. Hoch, P.L. Kuhns, W.G. Moulton, A.P. Reyes, M.A. Torija, J.F. Mitchell and C. Leighton, Phys. Rev. B. **75** 104421 (2007).

109. R. Caciuffo, J. Mira, J. Rivas, M.A. Senaris-Rodriguez, P.G. Radaelli, F. Carsughi, D. Fiorani and J.B. Goodenough, Europhys. Lett. **45** 399 (1999).

110. J. Wu, J.W. Lynn, C. Glinka, J. Burley, H. Zheng, J.F. Mitchell and C. Leighton, Phys. Rev. Lett. **94** 037201 (2005).

111. M.A. Senaris-Rodriguez and J.B. Goodenough, J. Solid State Chem. **118** 323 (1995).

112. D.N.H. Nam, K. Jonason, P. Nordblad, N.V. Khiem and N.X. Phuc, Phys. Rev. B. **59** 4189 (1999).

113. S. Mukherjee, R. Ranganathan, P.S. Anilkumar and P.A. Joy, Phys. Rev. B. **54** 9267 (1996).

114. I. Fita, R. Szymczak, R. Puzniak, I.O. Troyanchuk, J. Fink-Finowicki, Y.M. Mukovskii, V.N. Varyukhin, and H. Szymczak, Phys. Rev. B. **71** 214404 (2005).

115. M. Kriener, C. Zobel, A. Reichl, J. Baier, M. Cwik, K. Berggold, H. Kierspel, O. Zabara, A. Freimuth, and T. Lorenz, Phys. Rev. B. **69** 094417 (2004).

116. K. Berggold, M. Kriener, C. Zobel, A. Reichl, M. Reuther, R. Muller, A. Freimuth, and T. Lorenz, Phys. Rev. B. **72** 155116 (2005).

117. D. Louca, J. L. Sarrao, J. D. Thompson, H. Rőder, and G. H. Kwei, Phys. Rev. B **60**, 10378 (1999).

118. S. Sankar, D. Dender, J.A. Borchers, D.J. Smith, R.W. Erwin, S.R. Kline, and D.J. Smith, J. Magn. Magn. Mater. **221** (2000).

119. S. Sankar, A. E. Berkowitz, and D.J. Smith, Phys. Rev. B **62**, 14 273 (2000).

120. S. Barzilai, Y. Goldstein, I. Balberg, and J. S. Helman Phys. Rev. B **23**, 1809 (1981).

121. J. Q. Xiao, J. S. Jiang, and C. L. Chien, Phys. Rev. Lett **68**, 3749 (1992).

122. J. Wu, H. Zheng, J. F. Mitchell, and C. Leighton, Phys. Rev. B **73**, 020404 (2006).

123. D. Phelan, D. Louca, S.N. Ancona, S. Rosenkranz, H. Zheng, and J.F. Mitchell Phys. Rev. B **79** 094420 (2009).

124. T. Miyasato, N. Abe, T. Fujii, A. Asamitsu, S. Onoda, Y. Onose, N. Nagaosa, Y. Tokura, Phys. Rev. Lett. **99** 086602 (2007).

125. Y. Onose and Y. Tokura, Phys. Rev. B. **73** 174421 (2006).

## Chapter 2

1. William D. Callister, Jr., *Materials science and engineering: An introduction*, 5th edition, New York, Chichester, Weinheim, Brisbane, Singapore, Toronto, 2000.
2. E. A. Brandes, and G. B. Brook (Editors), *Smithells metals reference book*, 7th edition, Butterworth-Heinemann, Oxford, 1992.
3. M. Palcut, K. Wiik, and T. Grande, J. Phys. Chem. *B*, 111 (9), 2299(2007).
4. H. Taguchi, M. Shimada, and M. Koizumi, J. Solid State Chem.**29**, 221(1979).

5. H. Taguchi, M. Shimada, and M. Koizumi, Mater. Res. Bull. 15, 165 (1980).
6. P. Bezdicka, A. Wattiaux, J. C. Grenier, M. Pouchard, and P. Hagenmuller, Z. Anorg. Allg. Chem. **619**, 7 (1993).
7. A. Nemudry, P. Rudolf, and R. Schöllhorn, *Chem. Mater*. 8, 2232(1996).
8. S. Kawasaki, M. Takano, and Y. Takeda, J. Solid State Chem.**121**, 174 (1996).
9. H. M. Aarbogh, J. Wu, L. Wang, H. Zheng, J. F. Mitchell, and C. Leighton Phys. Rev.B **74,** 134408 (2006).
10. S. M. Koohpayeh, Ph.D thesis, *Crystal growth of functional oxides using an image furnace,* University of Birmingham, U. K. July 2007.
11. H. Zheng, J. F. Mitchell, *Crystal growth of* $La_{1-x}Sr_xCoO_3$ *specimens*. Argonne National Laboratory Cobalt Oxides Workshop, Argonne, IL, July 2007
12. J. F. Mitchell, D. N. Argyriou, J. D. Jorgensen, D. G. Hinks, C. D. Potter, and S. D. Bader, Phys. Rev.B **55**, 63 (1997).
13. N.W. Ashcroft, N. Mermin, *Solid State Physics,* 1976.
14. P. M. Raccah and J. B. Goodenough, Phys. Rev. **155**, 932 (1967).
15. R. Caciuffo, D. Rinaldi, G. Barucca, J. Mira, J. Rivas, M.A. Señarís Rodríguez, P.G. Radaelli, D. Fiorani and J.B. Goodenough, *Phys. Rev. B* **59,** 1068 (1999)
16. P. M. Raccah, R. J. Bouchard, and A. Wold, J. Appl. Phys. **37**, 1436 (1966)
17. P. M. Raccah and R. J. Arnott, Phys. Rev. **153**, 1028 (1967)
18. N. Closset, R.van Doorn, H. Kruidhof, and J. Boeijsma, Powder Diffraction, v11, p31 (1996)
19. Private communication with J. F. Mitchell, Argonne National Laboratory, Argonne, IL.
20. P.M. Raccah and J.B. Goodenough, J. Appl. Phys. **39** 1209 (1968)
21. *Manual of Bruker-AXS Microdiffractometer,* IT Chareterization facility at University of Minnesota, MN.
22. B. D. Josephson, Phys. Lett. **1**, 251 (1962)
23. P.W. Anderson and J. M. Rowell, Phys. Rev. Lett. **10**, 230 (1963).
24. T. Hirano, T. Nagaishi and H. Itozaki, Supercond. Sci. Technol. **12**, 759(1999).

25. Magnetic Property Measurement System (MPMS XL) Hardware Reference Manual, Quantum Design, San Diego, CA, 2005.
26. C. Leighton, John Kern, and Suzanne R. English, Rev. Sci. Instrum. **73**, 2364 (2002)
27. Janis Research company 9T NbTi magnet in an ultralow loss Dewar with a Janis Supervaritemp variable temperature insert.
28. J.H. Kim *et al.*, Physica C 412 – 414 (2004).
29. L. J. V. d. Pauw, Philips. Res. Repts. **13**, 1(1958).
30. L. J. V. d. Pauw, Phili. Tech. Rev. **20**, 220(1958).
31. http://www.qdusa.com/pdf/brochures/ppms_9_06.pdf.
32. Physical Property Measurement System Heat Capacity Option User's Manual, Part Number 1085-150F, 7th edition, San Diego, CA, USA 2000.
33. Physical Property Measurement System Helium-3 Refrigerator System User's Manual, Part Number 1092-100C, 3th edition, San Diego, CA, USA 2002.
34. Physical Property Measurement System Torque Magnetometer Option User's Manual, Part Number 1084-150B, 3th edition, San Diego, CA, USA 1999.
35. R. Pynn, *Neutrons Scattering: A Primer* (Los Alamos Neutron Science Center)
36. J. M. Carpenter (University of Rome), *Introduction to Theory of Neutron Scattering*, National Laboratory, February, 2006.
37. R. Pynn, *Neutron Scattering: Small Angle Scattering* (Los Alamos National Laboratory).
38. http://www.ncnr.nist.gov/instruments/ng7sans/
39. S. M. Choi, *SANS Experimental Methods*, NCNR Summer School, June 2000.
40. S. Kline, *Fundamentals of Small-Angle Neutron Scattering*, NCNR Summer School, June 2000**.**
41. SANS Data Reduction Tutorial, NIST, (2003).
42. J. Wu, J. W. Lynn, C. J. Glinka, J. Burley, H. Zheng, J. F. Mitchell, and C. Leighton, Phys. Rev. Lett. **94**, 037201 (2005).
43. J. W. Lynn, L. Vasiliu-Doloc, and M. A. Subramanian,Phys. Rev. Lett. **80**, 4582 (1998).

44. C. Yaicle, C. Martin, Z. Jirak, F. Fauth, G. Andre, E. Suard, A. Maignan, V. Hardy, R. Retoux, M. Hervieu, S. Hebert, B. Raveau, Ch. Simon, D. Saurel, A. Brulet, and F. Bouree, Phys. Rev. B **68**, 224412 (2003).
45. Ch. Simon, S. Mercone, N. Guiblin, C. Martin, A. Brûlet, and G. André, Phys. Rev. Lett. **89**, 207202 (2002).
46. J. W. Lynn, R. W. Erwin, J. A. Borchers, Q. Huang, A. Santoro, J.-L. Peng, and Z. Y. Li,Phys. Rev. Lett. **76**, 4046 (1996).
47. R. M. Moon, T. Riste, and W. C. Koehler, Phys. Rev. **181**, 920 (1969).
48. O. Halpern, and M.H. Johnson, Phys. Rev. **55**, 898 (1939).
49. A. Michels, and J. Weissmüller, Rep. Prog. Phys. **71** 066501 (2008).

## Chapter 3

1. P.M. Raccah and J.B. Goodenough, Phys. Rev. **155** 932 (1967).
2. For a short review see p1235-1239 in M. Imada, A. Fujimori and Y. Tokura, Rev. Mod. Phys. **70** 1039 (1998).
3. K. Asai, O. Yokokura, N. Nishimori, H. Chou, J.M. Tranquada, G. Shirane, S. Higuchi, Y. Okajima and K. Kohn, Phys. Rev. B. **50** 3025 (1994).
4. M.A. Korotin, S. Yu. Ezhov, I.V. Solovyey, V.I. Anisimov, D.I. Khomskii and G.A. Sawatzky, Phys. Rev. B. **54** 5309 (1996).
5. S. Yamaguchi, Y. Okimoto and Y. Tokura, Phys. Rev. B. **55** R8666 (1997).
6. C. Zobel, M. Kriener, D. Bruns, J. Baier, M. Gruninger, T. Lorenz, P. Reutler and A. Revcolevschi, Phys. Rev. B. **66** 020402(R) (2002).
7. G. Maris, Y. Ren, V. Volotchaev, C. Zobel, T. Lorenz and T.T.M. Palstra, Phys. Rev. B. **67** 224423 (2003).
8. G. Vanko, J.-P. Rueif, A. Mattila, Z. Nemeth and A. Shukla, Phys. Rev. B. **73** 024424 (2006).
9. R.F. Klie, J.C. Zheng, Y. Zhu, M. Varela, J. Wu and C. Leighton, Phys. Rev. Lett. **99** 047203 (2007).
10. S. Noguchi, S. Kawamata, K. Okuda, H. Nojiri and M. Motokawa, Phys. Rev. B. **66** 094404 (2002).

11. M.J.R. Hoch, S. Nellutla, J. van Tol, E.S. Choi, J. Lu and J.M. Mitchell, Phys. Rev. B. **79** 214421 (2009).
12. M.W. Haverkort, Z. Hu, J.C. Cezar, T. Burnus, H. Hartmann, M. Reuther, C. Zobel, T. Lorenz, A. Tanaka, N.B. Brookes, H.H. Hsoeh, H.-J. Lin, C.T. Chen and L.H. Tjeng, Phys. Rev. Lett. **97** 176405 (2006).
13. A. Podlesnyak, S. Streule, J. Mesot, M. Medarde, E. Pomjakushina, K. Conder, A. Tanaka, M.W. Haverkort and D.I. Khomskii, Phys. Rev. Lett. **97** 247208 (2006).
14. Z. Ropka and R.J. Radwanski, Phys. Rev. B. **67** 172401 (2003); R.J. Radwanski and Z. Ropka, Physica B **359-361** 1354 (2005).
15. D. Phelan, D. Louca, S. Rosenkranz, S.-H. Lee, Y. Qui, P.J. Chupas, R. Osborn, H. Zheng, J.F. Mitchell, J.R.D. Copley, J.L. Sarrao and Y. Moritomo, Phys. Rev. Lett. **96** 027201 (2006).
16. D. Louca and J.L. Sarrao, Phys, Rev. Lett. **91** 155501 (2003).
17. N. Sundaram, Y. Jiang, I.E. Anderson, D.P. Belanger, C.H. Booth, F. Bridges, J.F. Mitchell, Th. Proffen and H. Zheng, Phys. Rev. Lett. 102 026401 (2009).
18. J.-Q. Yan, J.-S. Zhou and J.B. Goodenough, Phys. Rev. B. 70 014402 (2004).
19. E.L. Nagaev and A.I. Podelshchikov, J. Phys. Cond. Mat. **8** 5611 (1996).
20. S. Yamaguchi, Y. Okimoto, H. Taniguchi and Y. Tokura, Phys. Rev. B. **53** R2926 (1996).
21. S.R. Giblin, I. Terry, S. Clarke, T. Prokscha, A.T. Boothroyd, J. Wu and C. Leighton, Europhys. Lett. **70** 677 (2005).
22. S.R. Giblin, I. Terry, D. Prabhakaran, A.T. Boothroyd, J. Wu and C. Leighton, Phys. Rev. B. **74** 104411 (2006).
23. S.R. Giblin, I. Terry, D. Prabhakaran, A.T. Boothroyd, and C. Leighton, unpublished (2008).
24. A. Podlesnyak, M. Russina, A. Furrer, A. Alfonsov, E. Vavilova, V. Kataev, B. Buchner, Th. Strassle, E. Pomjakushina, K. Conder and D.I. Khomskii, Phys. Rev. Lett. **101** 247603 (2008).

25. D. Phelan, D. Louca, K. Kamazawa, S.-H. Lee, S.N. Ancona, S. Rosenkranz, Y. Motome, M.F. Hundley, J.F. Mitchell and Y. Moritomo, Phys. Rev. Lett. **97** 235501 (2006).
26. B.F. Woodfield, M.L. Wilson, and J.M. Byers, Phys. Rev. Lett. **78** 3201 (1997).
27. N.W. Ashcroft, N. Mermin, *Solid State Physics*, 1976.
28. E.S.R. Gopal, *Specific heats at low temperatures*, Plenum Press, New York (1966).
29. S. Stolen, F. Gronvold, H. Brinks, T. Atake and H. Mori, Phys. Rev. B. **55** 14103 (1997).
30. T. Kyomen, Y. Asaka and M. Itoh, Phys. Rev. B. **67** 144424 (2003).
31. C. He, S. Eisenberg, C. Jan, H. Zheng, J.F. Mitchell, and C. Leighton, unpublished (2009).
32. D.P. Kozlenko, N.O. Golosova, Z. Jirak, L.S. Dubrovinsky, B.N. Savenko, M.G. Tucker, Y. Le Godec and V.P. Glazkov, Phys. Rev. B. **75** 064422 (2007)

**Chapter 4**

1. R. Caciuffo, D. Rinaldi, G. Barucca, J. Mira, J. Rivas, M.A. Sĕnarís- Rodríguez, P.G. Radaelli, D. Fiorani and J. B. Goodenough, Phys. Rev. B **59**, 1068 (1999).
2. J.Mira, J. Rivas, G. Baio, G. Barucca, R. Caciuffo, D. Rinaldi, D. Fiorani and M.A. Sĕnarís- Rodríguez, J. Appl. Phys. **89**, 5606 (2001).
3. P.L. Kuhns, M.J.R. Hoch, W.G. Moulton, A.P. Reyes, J. Wu and C. Leighton, Phys. Rev. Lett. **91**, 127202 (2003); M.J.R. Hoch, P.L. Kuhns, W.G. Moulton, A.P. Reyes, J. Wu and C. Leighton, Phys. Rev. B. **69** 014425 (2004).
4. M.J.R. Hoch, P.L. Kuhns, W.G. Moulton, A.P. Reyes, J. Lu, J. Wu and C. Leighton, Phys. Rev. B. **70** 174443 (2004).
5. J. Wu, J.W. Lynn, C. Glinka, J. Burley, H. Zheng, J.F. Mitchell and C. Leighton, Phys. Rev. Lett. **94** 037201 (2005).
6. D. Phelan, D. Louca, S. Rosenkranz, S.-H Lee, Y.Qiu, P.J. Chupas, R. Osborn, H. Zheng, J.F. Mitchell, J.R.D. Copley, J.L. Sarrao and Y. Moritomo, Phys. Rev. Lett. **96**, 027201 (2006).
7. M.A. Senaris-Rodriguez and J.B. Goodenough, J. Sol. Stat. Chem. **118** 323 (1995).

8. J. Wu and C. Leighton, Phys. Rev. B. **67** 174408 (2003).
9. R. Caciuffo, J. Mira, J. Rivas, M.A. Senaris-Rodriguez, P.G. Radaelli, F. Carsughi, D. Fiorani and J.B. Goodenough, Europhys. Lett. **45** 399 (1999).
10. E. Dagotto, Nanoscale phase separation and colossal magnetoresistance, Springer (2002).
11. E. Dagotto, T. Hotta and A. Moreo, Phys. Rep. **344** 1 (2001).
12. J. M. D. Coey, M. Viret and S. von Molnar, Adv. Phys., **48**, 167 (1999).
13. A.P. Li, J. Shen, J.R. Thompson and H.H. Weitering, Appl. Phys. Lett. **86** 152507 (2005)
14. V.M. Galitski, A. Kaminski and S. Das Sarma, Phys. Rev. Lett. **92** 177203 (2004); A. Kaminski and S. Das Sarma, Phys. Rev. Lett. **88** 247202 (2002).
15. J.M. de Teresa, M.R. Ibarra, P.A. Algarabel, C. Ritter, C. Marquina, J. Blasco, J. Garcia, A. del Moral and Z. Arnold, Nature **386** 256 (1997).
16. O. Chauvet, G. Goglio, P. Molinie, B. Corraze and L. Brohan, Phys. Rev. Lett. **81** 1102 (1998).
17. M.B. Salamon, P. Lin and S.H. Chun, Phys. Rev. Lett. **88** 197203 (2002).
18. J. Deisenhofer, D. Braak, H.-A. Krug von Nidda, J. Hemberger, R.M. Eremina, V.A. Ivanshin, A.M. Balbashov, G. Jug, A. Loidl, T. Kimura and Y. Tokura, Phys. Rev. Lett. **95** 257202 (2005).
19. Y. Shimada, S. Miyasaka, R. Kumai and Y. Tokura, Phys. Rev. B. **73** 134424 (2006).
20. S. Huang, K. Ruan, Z. Lv, L. Zhuang, P. Wei, H. Wu, M. Li, J. Zhang, Y. Chai, H. Yang, L. Cao and X. Li, Phys. Rev. B. **73** 094431 (2006).
21. Z. Sun, J.F. Douglas, A.V. Fedorov, Y.-D. Chuang, H. Zheng, J.F. Mitchell and D.S. Dessau, in press, Nature Physics (2006).
22. C. Magen, P.A. Algarabel, L. Morellon, J.P. Araujo, C. Ritter, M.R. Ibarra, A.M. Pereira and J.B. Sousa, Phys. Rev. Lett. **96** 167201 (2006).
23. J. Burgy, M. Mayr, V. Martin-Mayor, A. Moreo and E. Dagotto, Phys. Rev. Lett. **87** 277202 (2001).
24. M. Gulacsi, A. Bussman-Holder and A.R. Bishop, Phys. Rev. B. **71** 214415 (2005).
25. R.B. Griffiths, Phys. Rev. Lett. **23** 17 (1969).

26. A.J. Bray, Phys. Rev. Lett. **59** 586 (1987); A.J. Bray and M.A. Moore, J. Phys. C. **15** L765 (1982).
27. The sign reversal in $d\rho/dT$ at low $T$ occurs at higher $x$ in polycrystals than in single crystals due to grain boundary effects.
28. H. Taguchi, M. Shimada and M. Koizumi, J. Sol. Stat. Chem. **29** 221 (1979).
29. S. Kawasaki, M. Takano and Y. Takeda, J. Sol. Stat. Chem. **121** 174 (1996).
30. S. Balamurugan, K. Yamaura, A.B. Karki, D.P. Young, M. Arai and E. Takayama-Muromachi, Phys. Rev. B. **74** 172406 (2006).
31. S.R. Giblin, I. Terry, D. Prabhakaran, A.T. Boothroyd, J. Wu and C. Leighton, Phys. Rev. B. 74 104411 (2006).

## Chapter 5

1. Y. Tokura and Y. Tomioka, J. Mag. Mag. Mat. **200** 1 (1999).
2. J.M.D. Coey, M. Viret and S. von Molnár, Adv in Phys. **48** 167 (1999).
3. M.B. Salamon and M. Jaime, Rev. Mod. Phys. **73** 583 (2001).
4. P.A. Lee, N. Nagaosa, W. Xiao-Gang, Rev. Mod. Phys. **78** 17 (2006).
5. For a review see: E. Dagotto, T. Hotta and A. Moreo, Phys. Rep. **344** 1 (2001).
6. E. Dagotto, Nanoscale phase separation and colossal magnetoresistance, Springer, New York (2002).
7. R. Caciuffo, D. Rinaldi, G. Barucca, J. Mira, J. Rivas, M.A. Senaris-Rodriguez, P.G. Radaelli, D. Fiorani and J.B. Goodenough, Phys. Rev. B. **59** 1068 (1999).
8. P.L. Kuhns, M.J.R. Hoch, W.G. Moulton, A.P. Reyes, J. Wu and C. Leighton, Phys. Rev. Lett. **91** 127202 (2003).
9. M.J.R. Hoch, P.L. Kuhns, W.G. Moulton, A.P. Reyes, J. Wu and C. Leighton, Phys. Rev. B. **69** 014425 (2004).
10. M.J.R. Hoch, P.L. Kuhns, W.G. Moulton, A.P. Reyes, J. Lu, J. Wu, and C. Leighton, Phys. Rev. B. **70** 174443 (2004).
11. M.J.R. Hoch, P.L. Kuhns, W.G. Moulton, A.P. Reyes, M.A. Torija, J.F. Mitchell and C. Leighton, Phys. Rev. B. **75** 104421 (2007).

12. R. Caciuffo, J. Mira, J. Rivas, M.A. Senaris-Rodriguez, P.G. Radaelli, F. Carsughi, D. Fiorani and J.B. Goodenough, Europhys. Lett. **45** 399 (1999).
13. J. Wu, J.W. Lynn, C. Glinka, J. Burley, H. Zheng, J.F. Mitchell and C. Leighton, Phys. Rev. Lett. **94** 037201 (2005).
14. C. He, M.A. Torija, J. Wu, J.W. Lynn, H. Zheng, J.F. Mitchell and C. Leighton, Phys. Rev. B. **76** 014401 (2007).
15. D. Louca and J.L. Sarrao, Phys, Rev. Lett. **91** 155501 (2003).
16. D. Phelan, D. Louca, S. Rosenkranz, S.-H. Lee, Y. Qui, P.J. Chupas, R. Osborn, H. Zheng, J.F. Mitchell, J.R.D. Copley, J.L. Sarrao and Y. Moritomo, Phys. Rev. Lett. **96** 027201 (2006).
17. D. Phelan, D. Louca, K. Kamazawa, S.-H. Lee, S.N. Ancona, S. Rosenkranz, Y. Motome, M.F. Hundley, J.F. Mitchell and Y. Moritomo, Phys. Rev. Lett. **97** 235501 (2006).
18. M.A. Senaris-Rodriguez and J.B. Goodenough, J. Solid State Chem. 118 323 (1995).
19. J. Wu and C. Leighton, Phys. Rev. B **67** 174408 (2003).
20. D.N.H. Nam, K. Jonason, P. Nordblad, N.V. Khiem and N.X. Phuc, Phys. Rev. B. **59** 4189 (1999).
21. S. Mukherjee, R. Ranganathan, P.S. Anilkumar and P.A. Joy, Phys. Rev. B. **54** 9267 (1996).
22. I. Fita, R. Szymczak, R. Puzniak, I.O. Troyanchuk, J. Fink-Finowicki, Y.M. Mukovskii, V.N. Varyukhin and H. Szymczak, Phys. Rev. B. **71** 214404 (2005).
23. M. Kriener, C. Zobel, A. Reichl, J. Baier, M. Cwik, K. Berggold, H. Kierspel, O. Zabara, A. Freimuth and T. Lorenz, Phys. Rev. B. **69** 094417 (2004).
24. R. Mahendiran and A.K. Raychaudhuri, Phys. Rev. B. **54** 16044 (1996).
25. V. Golovanov, L. Mihaly and A.R. Moodenbaugh, Phys. Rev. B. **53** 8207 (1996).
26. H.M. Aarbogh, J. Wu, L. Wang, H. Zheng, J.F. Mitchell, and C. Leighton Phys. Rev. B. **74** 134408 (2006).
27. J. Wu, H. Zheng, J.F. Mitchell and C. Leighton, Phys. Rev. B. **73** 020404(**R**) (2006).
28. C. He, S. El-Khatib, J. Wu, J.W. Lynn, H. Zheng, J.F. Mitchell, and C. Leighton, in press, Europhys Lett. (2009).

29. K. Berggold, M. Kriener, C. Zobel, A. Reichl, M. Reuther, R. Muller, A. Freimuth and T. Lorenz, Phys. Rev. B. **72** 155116 (2005).
30. J.J. Neumeier and A.L. Cornelius in Nanoscale phase separation and colossal magnetoresistance, E. Dagotto, Springer, New York (2002), pp251.
31. S. Stolen, F. Gronvold, H. Brinks, T. Atake and H. Mori, Phys. Rev. B. **55** 14103 (1997).
32. T. Kyomen, Y. Asaka and M. Itoh, Phys. Rev. B. **71** 024418 (2005).
33. M. Tachibana, T. Yoshida, H. Kawaji, T. Atake, and E. T. Muromachi, Phys. Rev. B **77** 094402 (2008).
34. For a brief review see M. Imada, A. Fujimori and Y. Tokura in Metal-Insulator Transitions, Rev. Mod. Phys. **70** 1039 (1998). pp 1235.
35. M. Paraskevopoulos, J. Hemberger, A. Krimmel and A. Loidl, Phys. Rev. B. **63** 224416 (2001).
36. R. Mahendiran and P. Schiffer, Phys. Rev. B. **68** 024427 (2003).
37. S. Tsubouchi, T. Kyômen, M. Itoh, and M. Oguni, Phys. Rev. B **69** 144406 (2004).
38. K. Muta, Y. Kobayashi, and K. Asai J. Phys. Soc. .Jpn. **71** 2784 (2002).
39. S. Tsubouchi, T. Kyomen and M. Itoh, Phys. Rev. B. **67** 094437 (2003).
40. J. Mira, J. Rivas, G. Baio, G. Barucca, R. Caciuffo, D. Rinaldi, D. Fiorani, and M.A. Senaris Rodriguez, J. Appl. Phys. **89** 5606 (2001).
41. D. Samal, K. Balamurugan, C. Shivakumara and P.S. Anil Kumar, J. Appl. Phys. **105** 07E320 (2009).
42. R.X. Smith, M.J.R. Hoch, P.L. Kuhns, W.G. Moulton, A.P. Reyes, G.S. Boebinger, J. Mitchell, and C. Leighton, Phys. Rev. B **78** 092201 (2008).
43. These are the same single crystals used in refs [13,15-17,26-28].
44. D. Kim, B. Revaz, B.L. Zink, F. Hellman, J.J. Rhyne and J.F. Mitchell, Phys. Rev. Lett. **89** 227202 (2002).
45. J.E. Gordon, S.D. Bader, J.F. Mitchell, R. Osborn and S. Rosenkranz, Phys. Rev. B. **60** 6258 (1999).

46. Close analysis of the field dependent part of $C_P(T)$ reveals weak features associated with the magnetic ordering transitions all the way down to x = 0.10 [39]. This does not alter our argument for a distinct difference in behavior between x = 0.20 and 0.22.
47. C. He, H. Zheng, J.F. Mitchell, M.L. Foo, R.J. Cava and C. Leighton, Appl. Phys. Lett., **94** 102514 (2009).
48. B.F. Woodfield, M.L. Wilson, and J.M. Byers, Phys. Rev. Lett. **78** 3201 (1997).
49. T. Okuda, A. Asamitsu, Y. Tomioka, T. Kimura, Y. Taguchi, and Y. Tokura, Phys. Rev. Lett. **81** 3203 (1998).
50. P.M. Raccah and J.B. Goodenough, J. Appl. Phys. **39** 1209 (1968).
51. S. Balamurugan, K. Yamaura, A. B. Karki, D. P. Young, M. Arai, and E. Takayama,Muromachi, Phys. Rev. B **74** 172406 (2006).
52. T. Miyasato, N. Abe, T. Fujii, A. Asamitsu, S. Onoda, Y. Onose, N. Nagaosa, Y. Tokura, Phys. Rev. Lett. **99** 086602 (2007).
53. L. Ghivelder, I. Abrego Castillo, M.A. Gusmao, J.A. Alonso and L.F. Cohen, Phys. Rev. B. **60** 12184 (1999).
54. P. Ravindran, H. Fjellvag, A. Kjekshus, P. Blaha, K. Scwarz and J. Luitz, J. Appl. Phys. **91** 291 (2002).
55. Y. Onose and Y. Tokura, Phys. Rev. B. **73** 174421 (2006).
56. V. Orlyanchik, M.B. Weissman, M.A. Torija, M. Sharma and C. Leighton, Phys. Rev. B. **78** 094430 (2008).
57. Similar effects have been suggested as the origin of an enhanced anomalous Hall coefficient in La1-xCaxCoO3 crystals and films [58,59].
58. S.A. Baily, M.B. Salamon, Y. Kobayashi and K. Asai, Appl. Phys. Lett. **80** 3138 (2002).
59. A.V. Samoilov, G. Beach, C.C. Fu, N.-C. Yeh and R.P. Vasquez, Phys. Rev. B. **57** R14032 (1998).
60. J. Okamoto, T. Mizokawa, A. Fujimori, I. Hase, M. Nohara, H. Takagi, Y. Takeda and M. Takano, Phys. Rev. B. **60** 2281 (1999).
61. A.L. Cornelius, B.E. Light and J.J. Neumeier, Phys. Rev. B. **68** 014403 (2003).

62. E. Granado, C.D. Ling, J.J. Neumeier, J.W. Lynn and D.N. Argyriou, Phys. Rev. B. **68** 134440 (2003).
63. S. Yamaguchi, Y. Okimoto, H. Taniguchi and Y. Tokura, Phys. Rev. B. **53** R2926 (1996).
64. A. Podlesnyak, M. Russina, A. Furrer, A. Alfonsov, E. Vavilova, V. Kataev, B. Buchner, Th. Strassle, E. Pomjakushina, K. Conder and D.I. Khomskii, Phys. Rev. Lett. **101** 247603 (2008).
65. S.R. Giblin, I. Terry, S. Clarke, T. Prokscha, A.T. Boothroyd, J. Wu and C. Leighton, Europhys. Lett. **70** 677 (2005).
66. S.R. Giblin, I. Terry, D. Prabhakaran, A.T. Boothroyd, J. Wu and C. Leighton, Phys. Rev. B. **74** 104411 (2006).
67. D. Phelan, D. Louca, S.N. Ancona, S. Rosenkranz, H. Zheng and J.F. Mitchell, Phys. Rev. B. 79 094420 (2009).
68. J. Wu, J.W. Lynn and C. Leighton, unpublished.
69. M.R. Lees, O.A. Petrenko, G. Balakrishnan and D. McK. Paul, Phys. Rev. B. **59** 1298 (1999).
70. E.S.R. Gopal, Specific heats at low temperatures, Plenum Press, New York (1966).
71. H.M. Rosenberg, Low temperature solid state physics, Oxford Press, Oxford, (1963).
72. H. Kopferman: Nuclear moments, Academic Press, New York (1958).
73. R. Suzuki, T. Watanabe and S. Ishihara, arXiv:0905.1389v1.
74. S.R. Giblin, I. Terry, D. Prabhakaran, A.T. Boothroyd and C. Leighton, Phys. Rev. B. **79** 174410 (2009).
75. Similar results are obtained in lattice models of microemulsions for example (D. Andelman, M.E. Cates, D. Roux and S.A. Safran, J. Chem. Phys. **87** 7229 (1987).
76. K.I. Kugel, A.L. Rakhmanov and A.O. Sboychakov, Phys. Rev. Lett. **95** 267210 (2005).
77. B.I. Shklovskii and A.L. Efros, *Electronic properties of doped semiconductors*, Springer-Verlag, New York, 1979, pp 94.
78. S. Kirkpatrick, Rev. Mod. Phys. **45** 574 (1973).

79. M. Sahimi, Applications of percolation theory, Taylor and Francis, London, 1994; M. Sahimi, Phys. Rep. **306** 213 (1998).
80. The data were fitted only in the critical region $x < 0.25$. Deviations are to be expected at higher $x$.
81. K.H. Kim, M. Uehara, C. Hess, P.A. Sharma and S.-W. Cheong, Phys. Rev. Lett. **84** 2961 (2000)
82. V. Hardy, A. Wahl and C. Martin, Phys. Rev. B. **64** 064402 (2001).
83. D. Niebieskikwiat, R.D. Sanchez, L. Morales and B. Maiorov, Phys. Rev. B. **66** 134422 (2002).
84. Y. Xiong, S-Q. Shen and X.C. Xie, Phys. Rev. B. **63** 140418(R) (2001).
85. M. Uehara, S. Mori, C.H. Chen and S.-W. Cheong, Nature **399** 560 (1999).
86. Similar behavior is seen in the specific heat anomaly at $T_c$, which also clearly reveals the special doping point at $x = 0.22$. See: C. He, S. Eisenberg, C. Jan, H. Zheng, J.F. Mitchell and C. Leighton, unpublished (2009).

## Chapter 6

1. H.M. Aarbogh, J. Wu, L. Wang, H. Zheng, J.F. Mitchell, and C. Leighton, Phys. Rev. B. **74** 134408 (2006).
2. M.A. Torija, M. Sharma, M. R. Fitzsimmons, M. Varela, C. Leighton, J. Appl. Phys. **104** 023901 (2008).
3. N. S. Akulov, Zeits. f. Physik **52**, 389 (1928).
4. N. S. Akulov, Zeits. f. Physik **59**, 254 (1930).
5. N. S. Akulov, Zeits. f. Physik **67**, 794 (1931)
6. N. S. Akulov, Zeits. f. Physik **100**, 197 (1936).
7. R. M. Bozorth, Phys. Rev. **50**, 1076 (1936).
8. J. H. van Vleck, Phys. Rev. **52**, 1178 (1937).
9. B. D. Cullity, *Intorduction to magnetic materials*, Addison-Wesley, Meno Park, California (1972).
10. R. M. Bozorth, *Ferromagnetism*, New York: Van Nostrand (1951).

11. S. Kaya, *On the magnetization of single crystals of nickel*, Sci. Reports Tohoku Univ., **17**, 639-663 (1928).